DEVELOPMENT OF A CHEMICAL DOSIMETER FOR ELECTRON BEAM FOOD IRRADIATION

A Thesis

by

RAMIRO RIVADENEIRA

Submitted to the Office of Graduate Studies of
Texas A&M University
in partial fulfillment of the requirements for the degree of

MASTER OF SCIENCE

May 2005

Major Subject: Biological and Agricultural Engineering

DEVELOPMENT OF A CHEMICAL DOSIMETER FOR ELECTRON BEAM FOOD IRRADIATION

A Thesis

by

RAMIRO RIVADENEIRA

Submitted to the Office of Graduate Studies of
Texas A&M University
in partial fulfillment of the requirements for the degree of

MASTER OF SCIENCE

Approved as to style and content by:

Rosana Moreira
(Chair of Committee)

Elena Castell-Perez
(Member)

Leslie A. Braby
(Member)

Gerald Riskowski
(Head of Department)

May 2005

Major Subject: Biological and Agricultural Engineering

ABSTRACT

Development of a Chemical Dosimeter
for Electron Beam Food Irradiation. (May 2005)
Ramiro Rivadeneira, B.S., Texas A&M University
Chair of Advisory Committee: Dr. Rosana Moreira

A chemical solution composed of paraffin wax, chloroform, and methyl yellow biological indicator was shaped into a solid 3-D apple phantom to determine absorbed dose from e-beams and X-rays. The purpose of this research was to determine the most uniform irradiation treatment on apple-phantoms (a complex shaped target) and GAFCHROMIC® HD-810 films using electron beams from (1) a 2 MeV Van de Graaff (VDG) accelerator, (2) a 10 MeV Linear Accelerator (LINAC), and (3) X-rays from a 5 MeV LINAC.

Irradiation with the VDG accelerator confirmed that tilting the apple-phantom y-axis towards the e-beam source by 90 degrees, 45, and 22.5 degrees resulted in more uniform treatment in both the methyl yellow apple phantom and HD-810 film. The phantoms were over-exposed at the top and bottom regions when their y-axis was oriented exactly parallel to the e-beam at 22.5-degrees. The 45-degree orientation ensured uniformity throughout the whole apple surface without overexposing it at the top and bottom. In contrast, the 90-degree orientation resulted in the least effective treatment with the bottom and top region not receiving any radiation.

A 10 MeV dual e-beam showed uniform penetration from top to bottom in the HD-810 film and apple phantoms. The HD-810 film responded linearly with doses up to 1.5 kGy while the methyl yellow response was non-linear up to 0.5 kGy maximum. The X-ray irradiation completely penetrated the apple phantoms from top to bottom showing excellent lateral uniformity at different penetration depths.

DEDICATION

I dedicate my thesis to:

My parents, Ramiro Rafael Rivadeneira, and Luz E. Elvira Pinos

My brother, Juan Carlos Rivadeneira

My sister, Maria Fernanda Rivadeneira

And my love, Maria de los Angeles Vinueza

Thanks to all of your love, support, and words of wisdom

that inspired me to give my best.

ACKNOWLEDGMENTS

I would like to thank and acknowledge Dr. Rosana Moreira, my advisor, for providing me with the opportunity to challenge myself as an individual and a professional, and for providing the friendship and financial support to complete this work. Thanks to Dr. Elena-Castell for her words of encouragement and for being an outstanding role model as a teacher.

Very special thanks to Dr. Leslie Braby for his continued technical advice and support throughout the project's course. Also, very special thanks to Jongsoon Kim for his friendship, work commitment, and positive attitude to complete this project. I am thankful to Mr. Tony Restivo for his patience, for keeping us motivated and for his work experience which always came in handy.

Special thanks to Mr. John Shumbera from the Texas A&M Cyclotron Institute for his technical expertise and support in helping us troubleshoot our vacuum systems. In addition, thanks to Mr. Richard Epting for providing us with his help and support throughout the project's construction phase. I am also thankful to Dr. James Morgan, Department of Civil Engineering for helping us evaluate the project structural safety.

Finally, I want to thank all my friends: Claudia, Maria, Paulo, Carmen, Lou, Fernando, Esteban, Juan, Adolfo, Dario, Jeijoon, Jongsoon, Nont, my brother Juan Carlos, and Angy for making my life and stay at College Station worthwhile.

TABLE OF CONTENTS

CHAPTER Page

LIST OF FIGURES

Page

Page

Page

LIST OF TABLES

CHAPTER I

INTRODUCTION

Food irradiation is a non-thermal treatment used to enhance food safety and preservation. The process results in reproductive lethality in microorganisms responsible for foodborne illness. Gamma rays and electron beams are the two most common methods for irradiating food products. Specifically, gamma rays produced from elements such as ^{60}Co and ^{137}Cs (McMurray et al., 1998) are used to deeply penetrate a food product in any direction. Electronic accelerators produce high energy, 1 to 10 mega electron volts (MeV) electrons with less penetration power, higher efficiency, and relatively low-cost than gamma rays. These machines provide an excellent alternative for fruit and vegetable surface pasteurization compared to gamma rays.

For any irradiation treatment, it is critical to control the absorbed dose, i.e., the energy absorbed per unit mass of irradiated material, to provide uniform radiation treatment. In fruits and vegetables, for example, it is important to deliver radiation uniformly throughout the product to achieve bacterial reduction, quarantine control, shelf-life extension, or any specific purpose.

This thesis follows the style and format of the *Transactions of the ASAE*.

Different radiation sensors or dosimeters such as thermo luminescence dosimeters (TLD), semiconductors, radiochromic film, and chemical compounds reactive to radiation are available for relative dosimetry measurements on irradiated products (Butson et al., 2003). Indeed, a dosimetry system is required to measure absorbed radiation and find the best product configuration to deliver a specific treatment dose.

For instance, radiochromic film is used typically in food irradiation to map dose distributions at specific locations in products with predefined packaging and uniform geometries. However, complex shaped and non-homogenous foods with respect to their 3-D mass distribution make it difficult to produce complete dose map distributions using radiochromic film (Borsa et al., 2002). Hence, there is a need to develop a dosimetry system capable of easily producing a complete and accurate 3-D dose map distribution to establish adequate radiation treatment.

The objective of this study was to produce a solid state chemical mixture that works not only as a radiation indicator, but would also provide the possibility of relatively measuring ionizing radiation in food products. An apple-phantom, a three-dimensional representation of an apple made of an equivalent biological material, was used as the sample product geometry for electron beam irradiation. Such phantom was composed of a mixture of paraffin, chloroform, and methyl yellow as used earlier for clinical research (Potsaid and Irie, 1961, 1963).

Extensive research has been performed in the medical field using chemical solutions for dosimetry measurements under low dose irradiations of X-rays (Clark and

Bierdstet, 1955), gamma rays (Wakabayashi et al., 1963; Yoshino et al., 1979), and electron beams (McLaughlin et al., 1991). Through the use of a phantom, absorbed dose distributions in fruits and vegetables can be determined by relating the radiation induced color change to a specific dose through a calibration curve. As a result, it is possible to establish optimal product orientation to ensure uniform irradiation.

The development of a solid chemical dosimeter will enable visually detection of ionizing radiation in a 3-D object and thus establish quantitative measurement based on relative absorbed dose distributions within the phantom. For instance, during radiation processing with electronic beams, it is of extreme importance to be able to "see" where electrons hit in a product after the exposure. In that way, it is possible to determine the best orientation of the product relative to the source to obtain the most uniform dose distribution in the individual or bulk of products.

With the help of a flatbed desktop scanner, it is possible to record in a computer a two dimensional image that shows the color change resulting from irradiation. As a result, a phantom would offer the capability of detecting radiation in a 3-D manner by slicing the phantom in any particular direction (Wolodzko et al., 1999; Tarte et al., 1997). Advances in computer graphics and data processing methods make it possible to ingrate the flatbed scanner as an inexpensive and reproducible technique (Aydarous et al., 2001; Bazioglou and Kalef-Ezra, 2001; Alva et al., 2002) for relative radiation measurement.

Therefore, an apple phantom together with a flatbed scanner and image processing methods were studied to find the optimal relative dose distribution in a food product with the purpose of establishing uniform radiation treatment. Specifically, the objectives of this study were:

1. To develop a radiation sensitive indicator shaped like a complex food product such as an apple, and calibrate it as a relative dosimeter with a flatbed desktop scanner and image processing techniques.
2. To develop dose deposition and dose depth distributions in GAFCHROMIC® HD-810 film and the apple phantom using a:
   a. 2 MeV e-beam from Van de Graaff electron accelerator
   b. 10 MeV dual e-beam Linear Accelerator (LINAC)
   c. 5 MeV LINAC with X-ray converter.
3. To compare the apple phantom dose deposition and dose depth distributions to those obtained with the GAFCHROMIC® HD-810 radiochromic film.

CHAPTER II

LITERATURE REVIEW

Radiation detection systems have been developed in the area of radiation therapy to accurately predict a point dose or map dose distributions using several measuring methods such as radiochromic films, alanine, chemical solutions, and thermoluminescence (Bazioglou and Kalef-Ezra, 2001; Tarte et al., 1997; Butson et al., 2003; Kovacs et al., 2002). Today, radiochromic film and alanine dosimetry have been implemented to irradiation of food products to map absorbed dose distributions using a scanner as a readout technique (Alva et al., 2002; Aydarous et al., 2001). However, there is a need to develop a detection mechanism that not only predicts point doses, but can describe relatively absorbed dose distributions in complex shaped and non-homogenous food products to insure radiation uniformity.

2.1 Electron Interactions with Matter

The discussion that follows explains the interactions that occur when charged particles travel through a specific medium. It is of great importance to understand these mechanisms, which are the basis of radiation detection devices. In particular, radiation interactions produced by charged particles such as electrons are emphasized. Other types of charged particles include alphas, positrons, protons, and other heavy ions.

When a charged particle interacts with a medium it can produce ionization events in the material along with some excitation producing an *ion-pair*. The minimum threshold energy required for a charged particle to create an ion-pair is between 3 to 4 eV (Knoll 1999). In fact, radiation interactions that create ion-pairs are called *ionizing radiations*.

Sources of energetic electrons include those emitted from nuclear reactions, which are called beta particles or beta rays, while electrons resulting from interactions of X-rays or gamma photons with matter are referred to as secondaries. Some interactions of high energy electrons or other charged particles result in additional electrons called delta-rays (Knoll 1999). In addition, electrons may be produced upon emission from a heated surface and accelerated to high velocities through a potential difference or electric field.

As energetic charged particles interact with the bound electrons and positive nuclei within a material, most of the energy is transferred to the medium by coulomb interactions. Some losses to radiative emissions known as *bremsstrahlung* emissions can also occur from any position along the electron track (Alpen 1998). Indeed, a photon is produced when a fast or secondary electron loses its energy due to an inelastic interaction with a nucleus in the absorbing atom material.

Electrons travel forward along tracks away from the initial beam direction when penetrating through a specific medium. These deviations from the incident beam direction result from elastic and inelastic scattering processes. The process continues with emission of secondary electrons along their tracks producing a cascade effect until the energy is dissipated, in excitation and thermal losses, at very low energies (IAEA 2002).

2.1.1 Stopping Power

By definition, the energy dissipated in a material or absorber of atomic number *Z*, by a charged particle, *Y*, with kinetic energy *T*, is called *stopping power* $(dT/dx)_{Y,T,Z}$. Dividing the stopping power by the material density yields a quantity known as *mass stopping power* $(dT/\rho dx)_{Y,T,Z}$ (Attix, 1986). In particular, the total mass stopping power of a medium is defined as the sum of its *mass collision* and mass *radiative stopping power* as follows:

$$\left(\frac{dT}{\rho\,dx}\right) = \left(\frac{dT}{\rho\,dx}\right)_{collision} + \left(\frac{dT}{\rho\,dx}\right)_{radiative} \tag{2.1}$$

For electrons, the mass collision stopping power in terms of its kinetic energy, *T* (MeV), and rest mass, m_oc^2, can be expressed as:

$$\left(\frac{dT}{\rho\,dx}\right)_{collision} = k\left[\ln\left(\frac{\tau^2(\tau+2)}{2\left(I/m_oc^2\right)^2}\right) + F^{\pm}(\tau) - \delta - \frac{2C}{Z}\right] \tag{2.2}$$

Here, τ is defined as: $\tau \equiv T/m_oc^2$ and $F^{-}(\tau) \equiv 1-\beta^2+\frac{\tau^2/8-(2\tau+1)\ln 2}{(\tau+1)^2}$, for electrons. The term, *C/Z*, is a shell correction factor accounting for error in the stopping power equation and is the same for all charged particles of velocity, β. In addition, δ, is a second correction factor accounting for polarization or density effect.

The *radiative mass stopping power* according to Bethe and Heitler (Attix, 1986) is approximated by:

$$\left(\frac{dT}{\rho\, dx}\right)_{radiative} = \sigma_o \frac{N_A Z^2}{A}\left(T + m_o c^2\right)\overline{B}_r \tag{2.3}$$

where, σ_o, is the differential atomic cross section (cm^2/atom) and B_r is a function of Z and T. The amount of radiation losses due to radiative processes such as bremsstrahlung is expressed as the ratio of radiative to collisional stopping power and is approximated by (Attix, 1986):

$$\frac{\left(dE/dx\right)_{radiative}}{\left(dE/dx\right)_{collision}} \cong \frac{TZ}{700} \tag{2.4}$$

Radiative losses are a small fraction of the losses due to ionization and excitation for electrons and secondary electrons with energies of a few MeV, and become important only in absorbers with high atomic numbers (Knoll, 1999).

It is possible to obtain the stopping power for a chemical composition or mixture through the Bragg's Rule, which tells that atoms contribute almost independently to the stopping power making their effects additive (Turner, 1996). Given the weight fraction,

f, for each of the constituents, $n=1,2,3...$ with their respective atomic number, Z, then the mass stopping power in the mixture is defined as (Attix, 1986):

$$\left(\frac{dT}{\rho\, dx}\right)_{mixture} = f_{z,1_1}\left(\frac{dT}{\rho\, dx}\right) + f_{z,2}\left(\frac{dT}{\rho\, dx}\right) + ... + f_{z,n}\left(\frac{dT}{\rho\, dx}\right) \qquad (2.5)$$

For a given mixture it also follows from the Bragg-Kleeman Rule that:

$$\frac{Z}{A}\ln I = \sum_i \left[f_{z_i}\left(\frac{Z}{A}\right)_i \ln I_i \right] \qquad (2.6)$$

where, I (eV) is the compound's mean excitation potential and $(Z/A)_i = \sum f z_i\, (Z/A)$ for the compound.

2.1.2 Electron Range and Penetration Depth

As discussed earlier, electrons follow a tortuous path through absorbing materials due to electron-electron and sometimes electron-nuclear interactions that can suddenly produce changes in the penetration direction. In particular, the range of penetration measured along the electron path in a medium is described by the *continuous slow down approximation (CSDA) range* and is defined as (Attix, 1986):

$$R_{CSDA} \equiv \int_0^{To} \left(\frac{dT}{\rho dx}\right)^{-1} dT \qquad (2.7)$$

where T_o is the initial particle kinetic energy (MeV) and $dT/\rho\, dx$ the mass stopping power (MeV cm^2/g). The definition of range above is considered as the expectation value of the path length, *l*, that an electron follows until it comes to rest (Attix, 1986) as shown in Figure 2-1.

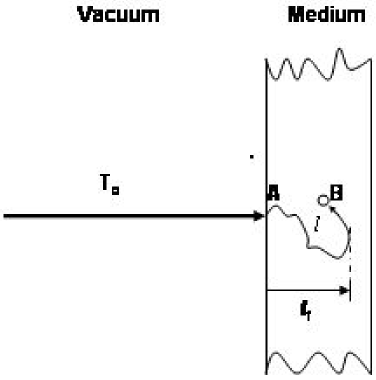

Figure 2-1. Range for individual electron traveling through pathlength, *l*. Farthest depth of penetration is t_f as electron travels from A to B. (Attix, 1986).

Notice that the quantity, t_f , called the farthest depth of penetration, does not account for the stochastic nature of radiative processes as well as $R_{(CSDA)}$. For low *Z* materials the CSDA range may be approximated to the expectation value of the path length, *l*, as considered above, while for high *Z* materials, penetration is larger because of the increase in stopping power with increasing atomic number.

2.2 Electron Accelerators

2.2.1 Van de Graaff Electrostatic Accelerator

Physicists in the early 1900’s have started developing machines called particle accelerators to study particle interactions. Accelerators made it possible to produce streams of elementary particles of equal energy to those on natural radioactive sources. In 1931, the American scientist Van De Graaff built an *electrostatic accelerator*, which was capable of producing a beam of electrons using high voltage sources rather than radioactive ones (Takács, 1997). Quickly, the *Van de Graaf (VDG) electrostatic accelerator* became an inexpensive and reliable research tool, which nowadays has found several practical applications in the areas of low-energy nuclear physics, radiation therapy, food processing, and many others (Wilson, 2001).

Typically, electrostatic accelerators are based on a single potential drop configuration where a high voltage potential is obtained by means of mechanical transfer of charge from ground to the high voltage terminal (Chao and Tigner, 1999). The basic components of an electrostatic accelerator include: a charging system, a support column, and an acceleration tube. Figure 2-2 shows the typical configuration of a Van De Graaff electrostatic accelerator.

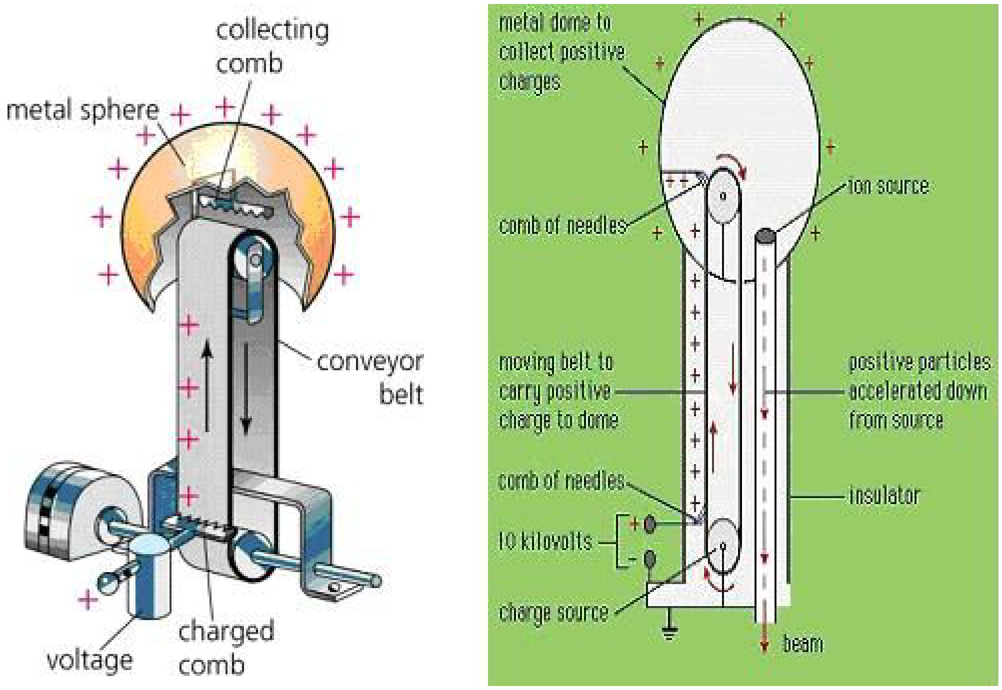

Figure 2-2. Van de Graaff electrostatic accelerator configuration scheme (Wilson, 2001).

In a VDG accelerator the electrons are sprayed onto a moving belt via a corona discharge or physical rubbing in gas using a dc-power generator as an electron source. The belt is made of plastic rubber with high dielectric strength and immersed in an insulating gas at high pressure.

The electrons or charge collected in the moving belt is transported against the potential gradient to a high voltage metal terminal where no electric field other than that from the charge on the belt exists. The charge is collected at the high voltage terminal upon contact with a metal brush, and further is accelerated back to ground (Humphries, 1986).

From a physical standpoint, the key idea to charged particle acceleration is to recognize the forces required to make this acceleration possible. To increase the kinetic energy, *T*, of a charged particle it is necessary to change its momentum, *p*. This change is possible only if a force, *F*, acts upon the charged particle, thus:

$$\frac{dp_x}{dt} = F_x = qT_x \tag{2.8}$$

Figure 2-3 below shows the movement of a charged particle within a *uniform* electric field between two parallel plates at a potential difference *V*.

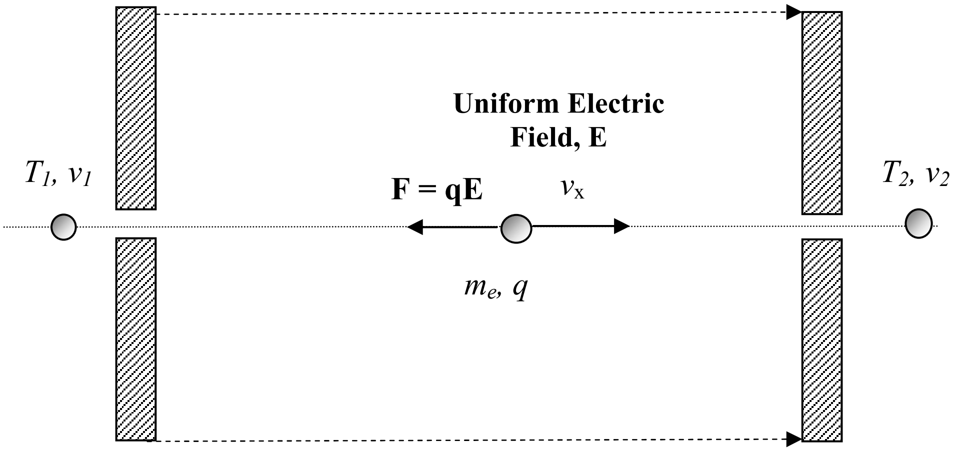

Figure 2-3. Electron acceleration in a uniform electric field E between two parallel plates (Humphries, 1986).

As electrons move in the direction of the uniform electric field *E*, their potential energy increases up to the potential difference V_1-V_2 = *V*. In fact, for oppositely charged parallel plates the potential difference is proportional to the distance between the two plates by *E* (Young and Freedman, 1996):

$$V_1 - V_2 = Ed \tag{2.9}$$

where *d*, is the distance between plates. For a VDG accelerator, the two parallel plates are the high voltage terminal and the tank that connects to ground. The motion of charged particles within a uniform electric field is analogous to the motion of a free body falling into earths' gravitational field Scharf (1994).

The maximum charge density, σ_{max} (C/cm^2), collected on the belt depends on the dielectric strength of the environment. For a flat belt, the maximum charge density is given by:

$$\sigma_{\max} = 2\varepsilon_o \varepsilon \, E_{\max} \tag{2.10}$$

Here, ε_o, is an electric constant (electric flux/m), ε is the permissivity of the environment surrounding the conveyor belt, and E_{max} is the breakdown strength of the electric field (V/m). The maximum possible voltage V_{max} is dependent on E_{max}, then for an electron traveling between two parallel plates separated by a distance *d* (m):

$$V_{\max} = E_{\max} d \tag{2.11}$$

2.2.2 Radio Frequency (RF) Linear Accelerators (LINAC)

Linear accelerators are the most powerful and efficient electron accelerators. The newest LINAC's differ from earlier electrostatic machines in that they use electric fields alternating at radio frequencies to accelerate the particles as a substitute for high voltage acceleration (Humphries, 1986).

In a RF LINAC the kinetic energy of the electrons is increased when injected into an accelerating structure. Typical injection energies range from tens of kilo-electron volts and leave with energies of several million electron-volts (electrons are accelerated near the speed of light with concurrent changes in their mass). The kinetic energy increase in a LINAC is provided from pulses of microwave power injected to the accelerating structure using a klystron RF amplifier. The main components in a LINAC system include (Titan Scan TB-10/15 LINAC Operation and Maintenance Manual):

1. Electron source
2. RF system
3. Linear Electron Accelerator Section

Figure 2-4 shows the basic scheme layout of a radio frequency linear accelerator.

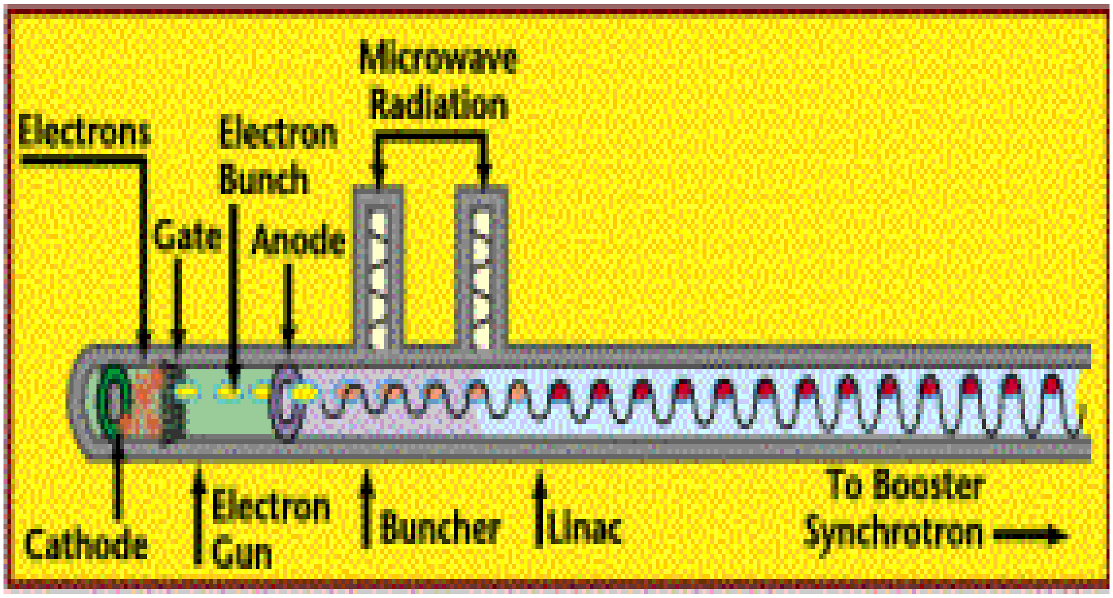

Figure 2-4. Radio frequency linear accelerator scheme (Takács, 1997).

During operation, electrons are extracted from the cathode surface of a dispenser made of tungsten and impregnated with barium that works as the electron source. Next, they are passed into the accelerator structure that is evacuated at a high vacuum (between 10^{-7} and 10^{-8} Torr) where the electron gun and RF system reside. First, the electrons enter the "buncher" section of the acceleration tube that is designed to couple energy more efficiently to the slowest moving electrons. At this stage, the RF phase velocity is adjusted to "bunch" the electrons together and increase their velocity near the speed of light (Wilson, 2001).

Next, the electrons enter a constant velocity region where they continue to gain energy (by gaining mass) as they travel through an accelerating wave guide. Once the beam leaves the accelerating wave guide, it is passed through a magnetic quadrupole and scanning magnet (Livingston and Blewett, 1962; Wilson, 2001). As a result, the e-beam increases its cross sectional area and can be scanned across a products surface.

2.3 Phantoms for Radiation Detection

Development of imaging technologies in medicine such as Computer Tomography (CT) Scans and Magnetic Resonance Imaging (MRI) led to the idea of radiation detection in 3-D.

The advances in medical imaging technology make it possible for radiation therapists to map absorbed radiation dose distributions in human body models known as anthropogenic *phantoms*. In particular, phantoms are 3-D geometric representations of any anatomy for study. For instance, a human body phantom is a model sectioned transversally into slices simulating different human-tissues with holes for insertion of radiation detectors (Alderson et al., 1962). Unfortunately, the nature of such detectors makes it difficult to produce accurate 3-D dose distributions due to non tissue-equivalent materials, large volumes, and dependence on radiation qualities.

The idea of a 3-D phantom capable of measuring radiation dose distributions was based on the findings that aqueous gel solutions uniformly dispersed chemical compounds affecting NMR parameters (longitudinal $T1$ and transverse $T2$ relaxation time) (Gore et al., 1996). Many researchers then adapted this method to produce absorbed dose distributions using MRI. Hence, it is possible to map radiation dose distributions since a radiation induced effect may be proportional to the absorbed radiation dose. Nowadays, two types of gel compounds are used in clinical dosimetry phantoms to determine absorbed dose distributions, Fricke-gel, and poly-acrylamide gel.

Phantoms may be cast of any materials; however, for clinical dosimetry studies most of them are made of tissue-equivalent materials such as pure gels of gelatin, agar, polyvinyl alcohol, silicone, organic dopped gels, paramagnetically dopped gels, and reverse micelle solutions (Hornak, 1996).

2.4 Dosimeter Systems

To measure absorbed dose in any material, a *dosimetry system* needs to be implemented. A dosimetry system is formed of two basic elements: (1) a radiation induced effect, and (2) a device capable of quantifying the induced change in the dosimeter.

For instance, consider irradiation of a solid material that changes color due to a radiation induced chemical reaction. Such color change may be measured quantitatively via colorimetry and related to specific absorbed doses. As a result, the color change (radiation induced effect) can be measured with a colorimeter (dosimeter measuring device) using a well defined color scale established in colorimetry standards and methods.

Consequently, any radiation effect or response that may be quantified in a reproducible manner using a well defined measuring device shall be used as a dosimeter. Several types of dosimeters permit absorbed dose measurement based on two methods. *Absolute dosimetry* is a method by which absorbed dose is measured directly and no calibration is required from a known radiation field (Attix, 1986). *Relative dosimetry* is a method by which a reference or absolute point is defined and all measurements that follow are referenced to that particular absolute (Butson et al., 2003).

The following is a brief description of common dosimeter systems, as described in the *ASTM E170 Terminology Relating to Radiation Measurements and Dosimetry,* classified according the two methods above.

2.4.1 Absolute Dosimeters

These types of dosimeters are known as *primary standard dosimeters*. They enable to measure directly the absolute absorbed dose based on fundamental units and physical constants, and is maintained and operated by a national standard laboratory that provides the basic standard for a country. Typical primary standard dosimeters used in absolute dosimetry include: calorimeters, ionization chambers, and alanine dosimeters.

2.4.1.1 Calorimeters

The absorbed doses of ionization radiation may be measured directly using a device called a calorimeter. In general, the energy dissipation or heat is measured as a function of the absorbing material thermal properties throughout observation of any temperature increase or decrease when ionizing radiation interacts with the medium (Eichholz and Poston, 1979).

In particular, graphite calorimeters have been widely investigated because its radiation absorption characteristics are similar to that of water (Shani, 2001). As a result, they are used in electron beam processing facilities where they provide key parameters related to the characteristics of the electronic beam (IAEA 2002). The temperature increase or decrease in a material is measured in terms of an electric current via thermocouples or thermistors given a known amount of energy absorbed. Ideally, adiabatic conditions should exist to prevent energy losses.

2.4.1.2 Ionization Chambers

Ionization chambers are gas-filled detectors that can sense an ionization event when exposed under radiation. In general, when charged particles travel through a gas, molecules can be excited or ionized along the particle path. Ionization chambers work on the principle of charge collection resulting from ionization through a potential difference or electric field. As a result, an output signal relates the charge to the absorbed dose. Ionization chamber as described in this context refers explicitly to a detector in which ion-pairs of electrons are collected from gases (Knoll, 1999).

When a neutral gas molecule is ionized with charged particles a free electron and a positively charged ion result, i.e., an ion-pair. Ion-pairs can result either from direct interaction with the incident particle or through delta rays processes. The ion-pair production mechanism is not relatively important, but the number of ion-pairs that can be used as an output signal.

The least energy required to produce an ion-pair in gas-filled detectors is between 10 and 25 eV (Knoll, 1999). Incident particles within a gas may not create any ion-pairs thus losing their energy mainly by exciting electrons to higher levels without removal. As a result, incident particles lose more energy in average to form ion-pairs. This loss of energy per ion-pair formed is known as the *W-value*. A typical value for *W* lies between 25-35 eV/ion pair (Attix, 1986) and is larger than the gas ionization energy.

When a potential difference exists in a gas, the motion of positive ions and free electrons represents an electron current that is the basis for the gas-filled ionization chamber. Indeed, consider a volume of gas under steady state irradiation conditions. For an infinitesimally small sample volume the rate of ion-pair formation should balance the rate at which ion-pairs exit the volume, thus the rate of ion-pair formation is constant. When negligible recombination conditions exist and all charges are collected then the steady state current is a direct measure of the ion-pairs formed (Attix, 1986).

For a large enough voltage, recombination becomes negligible and all the charges created within the gas volume add to the ion-current. However, all charges will collect to a certain voltage threshold where the rate of ion-pair formation is constant. This is known as the ion *saturation region* (Eichholz and Poston, 1979). For air-filled ionization chambers, increases in humidity will raise the recombination volume rate. Knoll (1999) describes that to minimize ion current losses due to diffusion and recombination it is helpful to determine the true saturated current by plotting $1/I$ vs. $1/V$. Extrapolation of $1/V$ to zero predicts the saturated current value.

2.4.1.3 Alanine Dosimeters

These dosimeters are composed of L-α-alanine and small amounts of a binder polymeric material such as paraffin. Their shape is of a small circular pellets or rods between of 3-5 mm in diameter. When exposed to radiation, the crystalline forms of L-α-alanine are transformed into free radicals, which are detected using electron spin resonance spectroscopy (ESR). Because the free radical concentration formed in the crystal structure is proportional to the ESR signal obtained, the alanine crystals can be used as a dosimeter (Regulla and Deffner, 1982). The dose range of alanine dosimeters is 1-10^5 Gy with saturation at 5x10^5 Gy, and linearity up to 3x10^3 Gy.

The crystalline structure of alanine dosimeters is tissue equivalent material that counteracts the recombination of free radicals resulting in a 4% signal loss for the first year after irradiation for dose values above 3 kGy. The non-destructive characteristics of the readout method make alanine dosimeters usable multiple times. Typically, alanine dosimeters may be used in different applications such as radiation therapy, food irradiation, quality control, and others where there is a need to precisely verify the radiation dose (Olsson and Bergstrand, 2001).

2.4.2 Relative Dosimeters

Relative dosimeters are usually *routine working dosimeters*. They require calibration against a primary reference standard. Working dosimeters are used to perform day to day dose measurements, may not be stable to specific weather conditions and could show significant variations from batch to batch. The following are used typically for relative dosimetry.

2.4.2.1 Radiochromic Film (RCF)

Radiochromic film dosimeters are a type of radiation detection device that changes in color upon irradiation. Color change occurs due to interaction of charged particles that react with a sensitive component of the film (Shani, 2001). Typically, dyes of biological materials contain specific chemical groups sensitive to radiation.

For instance, Pararosaniline cyanide (PRC), Hexapararosaniline cyanide (HHEVC), and New fuschin cyanides (NFC) are radiation sensitive dyes that can be transformed into solutions for radiation detected (ISO/ASTM 51540: 2002. Standard Practice for Used of a Radiochromic Liquid Dosimetry System).

Radiochromic dosimeters may be developed as liquids, gels, or films. There is a wide color response spectrum for radiochromic dosimeters for several doses ranging as low as 0.1 up to 10^6 Gy (Butson et al., 2003). Next, we discuss radiochromic film physical characteristics and existing methods to evaluate absorbed dose.

Absorbed dose in RCF relates to a quantity known as optical density (OD). In turn, OD is a measure of the change in color that occurs upon irradiation. In particular, RCF optical density is proportional to absorbed dose. This proportionality is revealed physically in the film as shadows of a specific color develop under irradiation. Indeed, increasing absorbed dose values yield darker shadows, i.e., higher optical density. Films exposed to low doses yield low optical density and lighter shadows (Shani, 2001; Gann, 1999; Fulton, 1996).

During irradiation, radiochromic film becomes darker attenuating part of the visible light transmitted. At this point, the film is said to be developed and light attenuation produces the change in color or dark shadows. In consequence, only part of the visible light transmits through the film. Optical density is described as a measure of the amount of light transmitted through the film in terms of a particular darkness or intensity at any point of the film:

$$OD = \log\left(\frac{I_o}{I}\right) \tag{2.12}$$

Here I_o is the unexposed film light intensity and I the film light intensity after irradiation. The above equation shows an inversely proportional relationship between light intensity and optical density. Consequently, films with high optical density values correspond to low light intensities, and vice versa. Equation 2.12 shows the logarithm of the ratio (Io/I) follows a linear relationship to dose making it possible to predict any dose if the optical density is known.

Radiochromic film attributes provide major advantages over several dosimetry systems. For instance, RCF's are relatively insensitive to visible light, and offer low-energy spectral sensitivity. RCF processing is convenient and fast since it is self-developing and no chemical processing is required. Handling is really simple and can be performed under normal room light for short periods of time. However, it has been shown that film is sensitive to ultraviolet light so sunlight must be avoided at all times (Stevens et al., 1996).

Indeed, RCF's so far are widely used as the standard to perform dosimetry in medicine, electronics, and most recently in food processing (Miyahara et al., 2002a; Borsa et al., 2002; Miyahara et al., 2002b; Ouattara et al., 2002). RCF high spatial resolution makes it possible to detect dose at any point or map dose distributions in a two dimensional plane.

Dosimetry is typically performed with film digitizers, spectrophotometers, and transmission densitometers. Now, traditional computer scanners are being used to read

RCF's optical density and extend its useful dose range (Alva et al., 2002; Aydarous et al., 2001; Bazioglou and Kalef-Ezra, 2001; Stevens et al., 1996).

Several types of RCF are available in the market for wide dose range applications such as the FWT-60 (FarWest Technology, Goleta, CA, USA) with a range of 0.5 – 200 kGy, GEX B3 WINdose (GEX Corporation, Colorado, USA) with a range of 1 kGy – 300 kGy, GAFCHROMIC® HD-810 (Advanced Materials Group, International Specialty Products (ISP), NJ, USA) with a range of 100 Gy to 500 Gy, GAFCHROMIC® MD-55 with a linear range up to 50 Gy.

Every film possesses a characteristic light absorption spectrum where optical density can be maximized at a particular wavelength. Film sensitivity and linear response to dose depends on the light emitted from the read out system to perform measurement. For instance, GAFCHROMIC® HD-810 spectra shows two absorption peaks located at 615 nm and 675nm attenuating the yellow and red parts of the spectrum, respectively (International, 2003). Performing optical density measurements with a readout system that emits light close to any desired peak will optimize the response as is the case of a laser He-Ne densitometer emitting light at 633 nm (Shani, 2001). For instance, it has been reported that the sensitivity of HD-810 RCF dose range was improved up to $5.5\text{x}10^3$ Gy using a color desktop scanner as a readout technique (Zhongli et al., 2003; Stevens et al., 1996; Aydarous et al., 2001).

The use of a flatbed scanner in conjunction with RCF provides a quick, reliable, and inexpensive dosimetry system that has been exploited nowadays mainly in clinical dosimetry (Aydarous et al., 2001; Zonghli et al., 2003; Alva et al., 2002; Stevens et al., 1996). The radiochromic film sensitivity improvements using a desktop scanner make it an ideal candidate for the detection of radiation distributions for food irradiation.

2.4.2.2 Thermoluminescent Dosimeters

When radiation energy strikes certain inorganic crystals, electrons are removed from their stable energy states becoming trapped in lattice imperfections of the crystalline solid and leaving positive electron holes or holes in the vacant positions. If the crystal temperature is raised, electrons escape from lattice traps releasing energy in the form of emitted light. This phenomenon is known as *thermoluminescence (TL)* and permits detecting the amount of radiation imparted to a crystalline material from its light emission under a controlled increase of temperature (Eichholz and Poston, 1979).

The intensity of the light emitted is measured with a photomultiplier tube for different temperatures. This is known as a *glow curve*, and it is unique to every crystal. For dosimetry purposes, thermoluminescent materials should be able to "glow" or produce enough light output for over reasonable periods of time and heating (Shani, 1991).

The light emission process in inorganic crystals strictly depends on energy states of the crystal lattice structure. Insulators and semiconductors are the only materials in which electrons have available discrete energy bands defined known as the valance, conduction and forbidden bands (Knoll, 1999; Loveland et al., 2000). Electrons sitting on the lower energy band, valence band, are directly bound to the crystal lattice structure. On the other hand, some electrons carry sufficient energy to move freely through the crystal lattice, these correspond to the conduction band. The forbidden gap corresponds to an energy region where no electron may exist in the pure crystal (Schaffer et al., 2000).

Ionizing radiation exposure to the crystal produces electrons to be excited from the valence to the conduction band producing an electron-hole pair. When electrons come back to their valence band, they recombine with the created hole and the energy of the light photon emitted may be too high to be seen in the visible range. To improve these processes impurities known as *activators* are added to the pure crystal producing special lattice sites with defined energy levels in the forbidden gap. As a result, photons of light emitted from electron de-excitement could be seen because the energy at each specific site is less to that of the full forbidden gap. These new defined lattice sites within the forbidden gap are known as *recombination* or *luminescence centers* (Knoll, 1999), or *color centers* (Murphy et al., 2002) and its energy spectrum is defined from their energy structure in the crystalline lattice.

For the case of TLD’s, it is desired to create as many luminescent centers as possible to prevent electron-hole recombination. If the amount of energy of the luminescence center is much greater to that of the valence band then at room temperature electrons have a less chance to fall back to their de-excited state. The process is analogous and holes can also be trapped; thus a measure of the number of electron-hole pairs provides an idea of the radiation exposure.

The number of electron-hole pairs shall be obtained upon reheating the sample material to a high enough temperature, characteristic of each color center, where the trapped electrons fall-back to the conduction band. Upon recombination with a hole, a photon of light is emitted if the temperature is low enough to prevent holes to be released. The same idea is true for released holes that recombine with trapped electrons to emit a photon of light if the temperature to release electron is not exceeded. Thus, the number of photons emitted (ideally one per trapped electron-hole pair released) provide an indication of the electron-hole pairs created initially, and the basis for the signal used in TLD detectors.

Common thermoluminescent materials include calcium sulfate $CaSO_4$ with Mn as the activator, Calcium Fluoride CaF_2 with Mn, Lithium Fluoride LiF with Mg or Ti where, Mn, Mg, and Ti are impurities added to the crystal lattice. Today, the most widely recognized TLD is lithium borate because of its close resemblance to tissue equivalent material and its wide energy range response for gamma rays (Shani, 2001).

However, electron beam dosimetry is more challenging due to the individual dose vs. depth response for incident electron beam energies. As electrons travel through a material they lose energy so that both energy and dose vary with material depth making it more difficult to accurately measure dose.

A different readout mechanism known as Optically Stimulated Luminescence (OSL) for TLD dosimeters is based on a strong light source such as a laser or light emitting diode that promotes charge de-excitation through defined luminescence states instead of conventional heating. The Sunna film dosimeter (Sunna Systems Corporation, Washington, USA) contains a microcrystalline LiF dispersion based on a polymer matrix of 0.240 mm thickness providing a useful dose range of 0.01-100 kGy. Lately, this technique has been applied to the irradiation of meats and disinfestations for doses above and below 1kGy (Kovacs, 2002) under electron beams and gamma irradiations.

2.4.2.3 Chemical Dosimeters

Radiation measurement can be obtained from yield of a known chemical reaction in a medium such as a liquid, solid or gas (Attix, 1986). The following, provides a brief description of some chemical systems such as organic aqueous solutions and non-aqueous solutions that may be used for dosimetry purposes.

The oxidative–reduction of ferrous ions to ferric ions in acidic solutions led to the measurement of absorbed doses in water (IAEA, 2002). This chemical mechanism has been well investigated and is known as the Fricke dosimeter which is widely accepted as a reference standard dosimeter.

Indicator solutions of biological dyes, including methylene blue (Kovacs et al., 1998), phenolphthalein, bromophenol blue, methyl red (Barakat et al., 2001)**,** and methyl yellow (Yoshino et al., 1981; Clark, 1963) have also been studied as possible dosimeters. For instance, Clark and Bierdstedt (1955) analyzed the radiation sensitivity of a non-aqueous solvent dye, methyl yellow, in organic liquids such as chloroform and carbon tetrachloride to suggest a possible aqueous chemical dosimeter.

Under soft X-ray irradiation with doses between 5-50 Gy, it was found that hydrogen chloride (HCl) was produced in chloroform-methyl yellow solutions and showed high *G* values (number of acid molecules formed per 100 eV). Radiation yield coefficient was used as a direct method of determining the dosimeter sensitivity to absorbed dose; however color analysis have also been performed typically via densitometry to determine dose distributions.

Potsaid and Irie (1961) developed a solid state chemical dosimeter when mixing melted paraffin wax with chloroform-methyl yellow solutions to study low dose distributions in radiotherapy. Paraffin wax showed miscible with chloroform-methyl yellow solutions providing excellent visual color changes from yellow to red after irradiation. Nonetheless, color patterns where not uniform due to excessive flaking and internal cracking; such problems were easily solved by adding small quantities (0.2%-1%) of refined waxes (Clark, 1963) such as microcrystalline wax which showed improved color patterns without affecting the dosimeter sensitivity.

Several other researchers (Wakabayashi et al., 1963; Yoshino et al., 1979) extensively studied the chemical interactions of chloroform-methyl yellow solutions in paraffin wax under gamma or X-rays radiation using spectrophotometry. Methyl Yellow solutions in chloroform presented an absorbance spectrum with two major and minor peaks located at 305 and 407nm respectively, with increasing intensity as methyl yellow concentration increased. After irradiation exposure, the solutions color shifted from yellow to red showing a new absorption band around 515-540 nm, and increased intensity for higher radiation doses. However, when higher amounts of paraffin wax were added to the solution, shorter absorption wavelengths resulted. Such wavelengths suggested intermolecular interactions between the paraffin and the dye.

Noticeably, higher amounts of different molecular weight paraffin waxes (C_6 to C_{36}) in irradiated samples showed increased radiation yield values for hydrogen chloride.

Yoshino et al. (1979) proposed that hydrogen molecules from paraffin or hydrogen atoms react via a radical mechanism with a chlorine radical, formed in the radiolysis of chloroform (HCl_3), to increase the hydrogen chloride (HCl) yield in the dosimeter system. Surprisingly, it was also found that different paraffin molecular weights did not influence the radiation yield of HCl in the dosimeter. The above discussion shows the use of halogenated hydrocarbons embedded in a polymeric matrix for radiotherapy purpose using soft X-rays between 5 and 50 Gy.

It is of interest to further study the possibility of using a biological indicator with chloroform in a polymer matrix to model relative absorbed dose distributions using low energy electrons in a food product. Specifically, a paraffin-chloroform-dye apple, an *"apple phantom"*, could provide not only a qualitative method to visually determine absorbed radiation (indicator), but also a quantitative approach to relative dose measurement to determine radiation uniformity.

2.5 Image Processing

2.5.1 Structure of a Computer Image

An image may be defined as a function of light intensity values that are located at a given point in a two-dimensional plane. If f is the light intensity function at any point (x,y) on a 2-D plane, then $f(x,y)$ is the intensity value at that position that is proportional to its brightness or gray level of the image at that point. Thus, a digital image may be represented in a matrix form where the location of each row and column stores an intensity value (Gonzalez and Woods, 1992). Each intensity value at a particular position is called a *pixel* or *picture element*.

2.5.2 RGB Color Model

The idea of a color model is to facilitate the representation of color in a general standard accepted way. Several color models exists each one designed for a specific purpose, e.g., CIELAB model tries to approximate human vision using three standard parameters.

On the other hand, the RGB color model represented with points of red, green, and blue is mostly used as a standard for color monitors and printers (Gonzalez and Woods, 1992). As a result, a digitized computer image can be split into its spectral red, green, and blue *components* or *color planes*.

The RGB color subspace is defined in Cartesian coordinates with a unit cube where the color primaries, *red*, *green*, and *blue* are located on the *x, y, z* axis, respectively of the unit cube, and *cyan*, *magenta* and *yellow* colors are located at the remaining corner positions as shown in Figure 2-5 below.

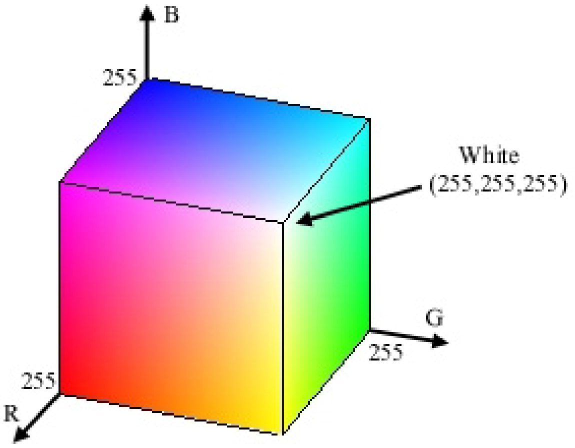

Figure 2-5. Representation of RGB color space (Gonzalez and Woods, 1992)

Black color is defined as the origin of the unit cube, and white color is located at the furthest distance from the origin. In this system, color values are defined as a point on or inside the cube by joining two vectors extending from the origin. Also, *gray-scale* is defined as points from black to white joined by these two points.

In a computer, each color point is represented under the RGB format using a *pixel* or *picture element* that contains particular information of red, green, and blue data values. These three components of red, green and blue are represented as three 8-bit numbers for an individual pixel in the base two or binary system used in computers (Burdick, 1997). In this system, an 8-bit byte can have 256 possible values ranging from 0 to 255, i.e., $2^8 = 256$ as in the sequence, 2^1, 2^2, 2^3, 2^4, 2^5, 2^6 2^7, 2^8. As a result, colors in each plane for each pixel are represented from its lowest intensity or zero to its maximum intensity 255.

For instance, pure white is defined as [255,255,255] and pure black [0,0,0]. A pure yellow is combination of pure red and pure green values [255, 255, 0]. Values of gray have the property of equal RGB values. A value of [10, 10, 10] represents a darker gray than [200,200,200] which shows a lighter gray. Higher bit numbers can store more representations of the same color, e.g., 10-bit produces $2^{10} = 1024$ combinations for a single intensity value. However, increasing the bit-number comes with the expense of greater amounts of computer power and storage. The number of bits needed to define a pixel intensity value is defined as an image *depth-resolution* (Burdick, 1997). Images acquired with 8-bit of depth resolution are very natural to its original and are called *truecolor* images. In the RGB color model each 8-bit color layer (1-byte), i.e., red, green, or blue, yields a possible 256 colors per layer so a total of 256x256x256 = 16.7 million color combinations are possible with 24-bit true color image.

2.6 Radiochromic Readers for Image Processing

2.6.1 Desktop or Flatbed Scanners

A desktop of flat bed scanner is a device capable of acquiring an image of an object and convert it to digital light intensity data for computer processing. Hardware resolution and color pixel depth are the two main considerations for comparison of image data between scanners. However, individual scanner properties such as the type of lamp used for scanning, the quality of the image sensing device or charged coupled device (CCD), dynamic range control, and optics system determine also image quality. The following, is a brief discussion as described by Gann (1999) on the anatomy of the scanner components and how these factors impact image quality.

A CCD is a collection of miniature light-sensitive diodes that convert light (photons) into electrons or electrical charge. They record the lightness intensity which is proportional to the number of photons captured per unit time. Light intensity may be defined in terms of the amount of light reflected or transmitted by an object. Particularly, white is the highest color intensity while black is the lowest. As a result, the CCD has a linear relationship to the amount of light intensity reflected or transmitted by an object. Light intensity data recorded, or accumulated electrical charge in the CCD is yet not a digital signal, so it has to be passed through an analog to digital (A/D) converter so the computer can read it. A typical scanner with an 8-bit A/D converter captures 3 colors (red, green, blue) which in turn produce a 24-bit image.

Next, the scan object light spectrum in reflection or transmission mode plays a key role in the quality of its color appearance. Based on the object spectrum it is possible to determine the best absorption regions, and thus this information could be used to closely match an illumination method in a particular scanner. As a result, the scanner's light source is of fundamental importance to best match an object true color as perceived by the human eye.

Several light sources are common with today's scanners, for instance fluorescent, xenon gas discharge, and the most popular cold-cathode fluorescent lamps. Each type of lamp has particular advantages/disadvantages depending upon the specific scanning needs; however, in most cases lamp intensity changes considerably with lamp temperature. Most scanners include a feedback loop which maintain lamp intensity uniformity from scan to scan, and assure lamp stability.

Because each scanner lamp has a unique absorption spectrum, scans of an object with different lamps will not reproduce exactly the same color. Most scanner lamps try to closely reproduce the sunlight spectrum which is the most common and stable light source. The daylight *6500K* or D_{65} standard, a statistical average of measurements of actual daylight around the world, is a good model that scanner lamps try to follow. Of course, not all lamps reproduce exactly the D_{65} standard but some are similar such as fluorescent light sources. Figure 2-6 shows different scan light sources compared to daylight D_{65} standard.

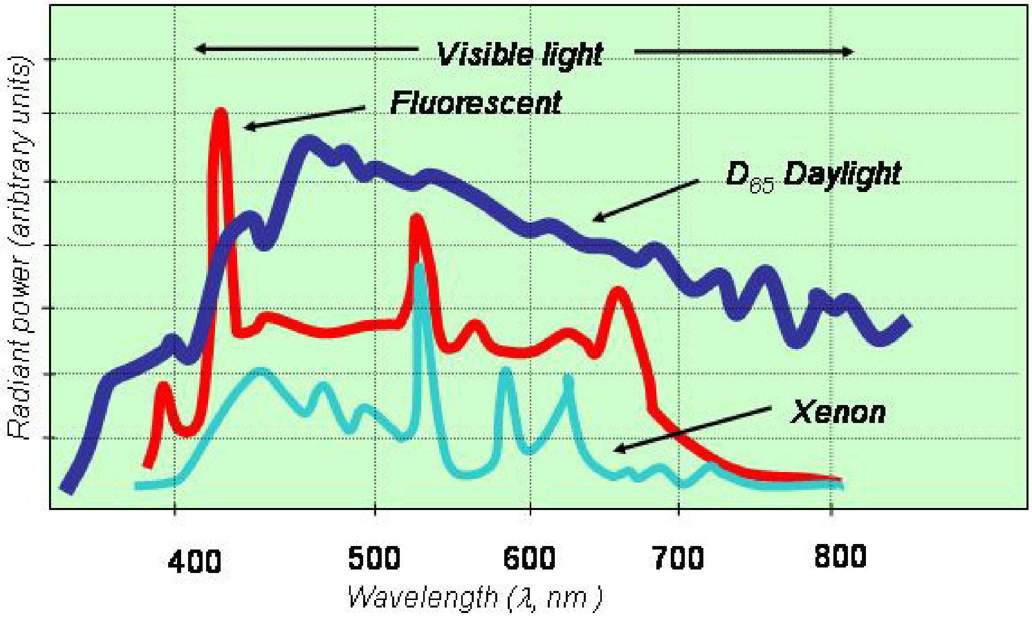

Figure 2-6. Spectra for various light sources (Gann, 1999).

Figure 2-6 shows that specific light sources over or under emphasize particular colors at different wavelengths for which intensity values may be too high or low resulting in corrupted color in those spectral regions. Even though scanners with different lamps reproduce color differently they can be designed for specific applications, e.g., film scanning, in which the use of a particular lamp enhances image quality.

Dynamic range is a measure of the image density or OD from image intensity data. Density is defined from a 0 to 4 scale, where a value of 4 means the image is completely dark and 0 means a pure white. Dynamic range scale is the inverse of the intensity scale, i.e., more density values means less intensity values. From the discussion on radiochromic films, optical density (OD) or density is defined in a logarithm scale. For instance, a density value of 3.0 is 10 times more intense than a density of 2.0. In turn, an intensity of 100:1 is a density range of 2.0, and an intensity of 1000:1 is a density of 3.0. While the theoretical maximum of density may be obtained for any intensity, the practical limit is 4.0 because no scan yet could result in a density of four (Fulton, 1996).

In a typical scanner dynamic range, D_{range}, may be expressed in terms of the maximum, D_{max}, and minimum, D_{min}, density values as follows:

$$D_{range} = D_{\max} - D_{\min} \tag{2.13}$$

Large dynamic range values result in better detail of the image dark shadow areas for positive films, prints or slides. The amount of detail in the dark areas of the film may be improved upon the bit-depth at which the scanner works. For instance, for a scanner with an *A/D* converter that produces a 30-bit image, means the scanner uses 10 bits per pixel per color (Gann, 1999). As a result, the theoretical smallest value the *A/D* converter can produce is 1/1024 or 1 10-bit count. Thus, assuming the scanner is able to see a 1-bit image, the density is:

$$D_{\max} = \log\left(\frac{1}{\left(\frac{1}{2^{10}}\right)}\right) = 3.0 \tag{2.14}$$

Reflective materials like photographs and printed pages have a maximum density value of 2.0, and typically about 1.5. This occurs mainly due to the material ability to greatly reflect light, and the gloss of the inks used. Thus, densities of 2.0 in reflective materials are not of importance because such densities do not exist in the originals. However, transmissive materials such as slide films, and negatives are able to produce densities of 3.0 and above (more shadows) in the originals thus requiring scanners that offer higher dynamic range values. In particular, it is desired to use a high-resolution flat bed scanner as a reading device for radiochromic film and apple phantom intensity data to map radiation distributions

CHAPTER III

MATERIALS AND METHODS

This research was composed of three irradiation experiments performed on apple phantoms. Two experiments were performed with electrons and one with X-rays. First, apple phantoms were irradiated with 1.35 MeV electrons using a Van de Graaff electron accelerator Type AK model S (High Voltage Engineering Corporation, Burlington, Massachusetts) at the Biological and Agricultural Engineering Food Engineering Safety Laboratory at Texas A&M University. Next, a 10 MeV (TB-10/15, The Titan Corporation, San Diego, CA) and 5 MeV (TB-5/15, The Titan Corporation, San Diego, CA) LINAC's were used to perform irradiation with electrons and X-rays, respectively, at the Texas A&M University Electron Beam Food Research Facility.

3.1 Experimental Apparatus

3.1.1 Van De Graaff Accelerator

The Van de Graff electron accelerator designed and manufactured by High Voltage Engineering Corporation (Burlington, Massachusetts) is a source of charged particles, similar in energy to those emitted from naturally radioactive materials. The system is capable of accelerating electrons up to 2 MeV. A constant potential is characteristic of the Van de Graaff, belt-type electrostatic method of producing high voltages. The basic generator can be separated into three component parts: the Van de Graaff generator, the vacuum system, and the controls. The Van de Graaff generator consists of a cylindrical device approximately 1.8 m long and 80 cm in diameter set 1 meter above the floor level enclosed in a steel pressure tank. It can generate current up to 250 μA of electrons at specific selected energies between 0.75 and 2 MeV. At the highest energy, 2 MeV, the beam power can be adjusted to 100 watts and delivered to a target area of 100 square centimeters of unit density of material, providing a dose rate of 1.0 kGy/s. Figures 3-1 thru 3-3 show the specific accelerator components.

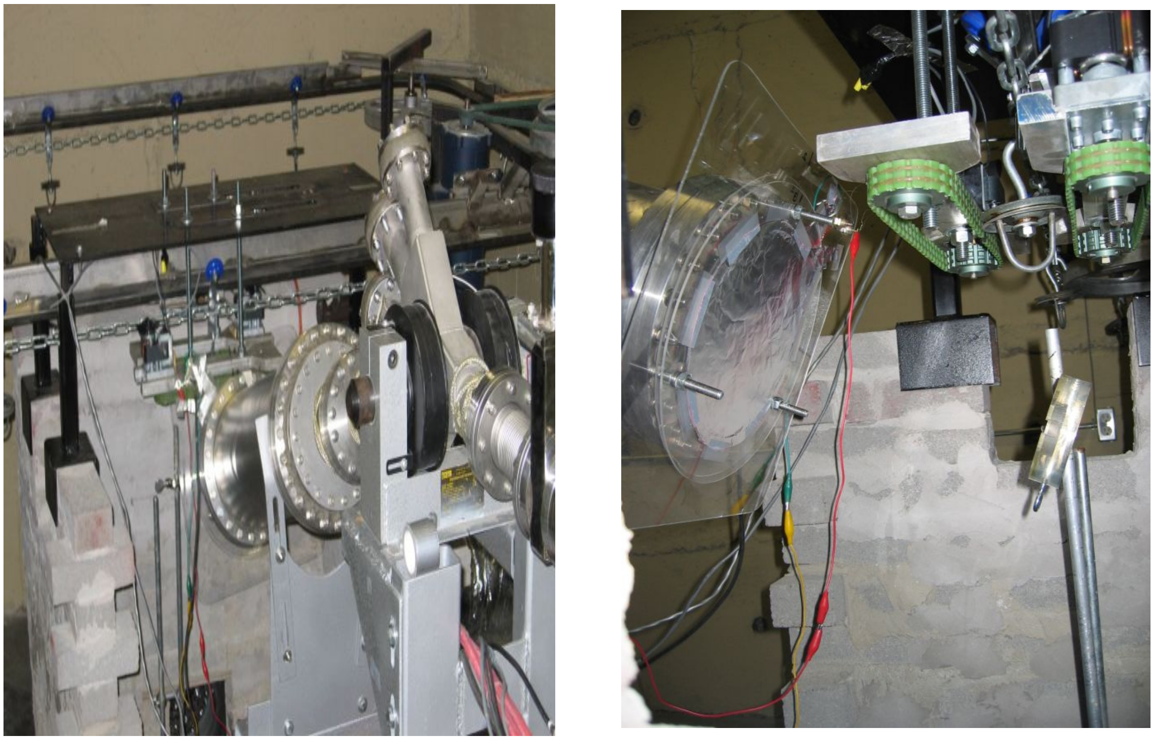

Figure 3-1. E-beam exit window, top view (left). Side view with parallel-plate transmission ionization chamber and Farmer dosimeter holder (right).

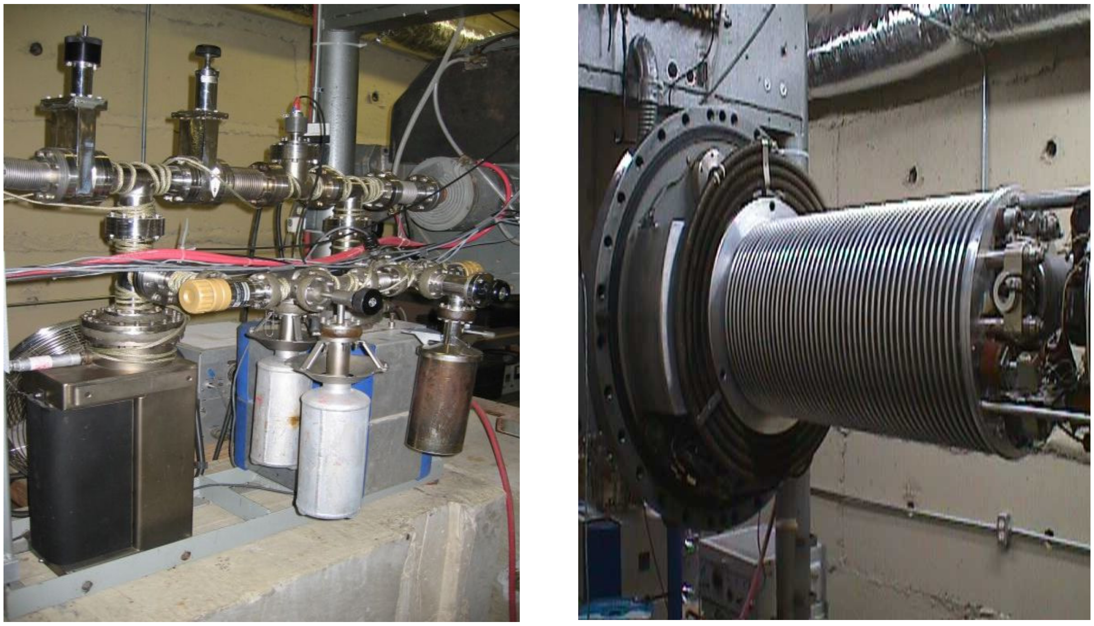

Figure 3-2. Vacuum system with liquid nitrogen roughing pumps (left). Accelerating column without tank (right).

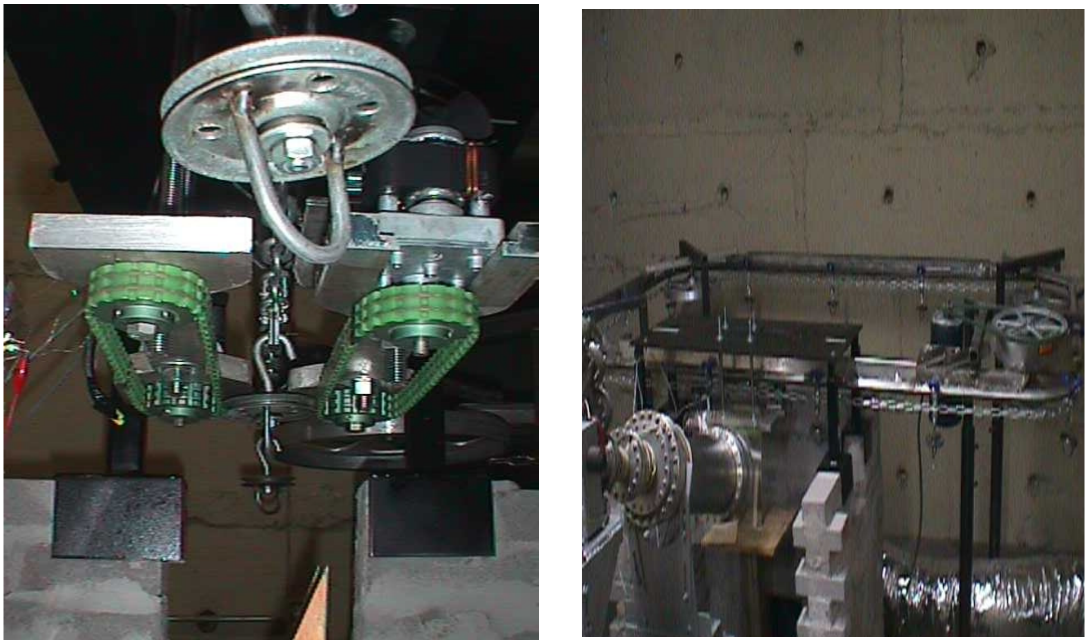

Figure 3-3. Rotating mechanism with turning hook (left). Track and trolley overhead conveyor system (right).

3.1.2 Van de Graaff Accelerator Conveyor System

An overhead conveyor system (Econo Manufacturing Co., Celina, Ohio) was constructed to transport apple phantoms in front of the electron-beam exit window at a height of 1.3 m from the ground and 28.36 cm away from it. The conveyor is a track and trolley arrangement that can transport 14 samples at a time, and is driven by an adjustable speed gear motor. It has a rectangular loop shape with dimensions of 2.6 m length by 1.53 m width. Figure 3-4 below shows the layout of the conveyor system set in front of the exit window.

Figure 3-4. Overhead conveyor system layout for e-beam irradiation using Van de Graaff accelerator.

Apple phantom samples can be suspended on the conveyor with a Y-shaped hanger that fits and travels along the conveyor line. A turning hook that is disc-shaped with a 360 ^{o} swivel bearing allows rotational motion of samples, and is directly hung from the Y-shape hangers. To obtain electron beam profiles of our samples along its rotational axis, a rotational mechanism was mounted in a surrounding rectangular shielding wall (0.9 m x 0.9 m x 0.9 m) in front of the exit window. The rotational mechanism consists of two polyurethane timing belts that constantly rotate in opposite directions by means of two independently driven direct current gear motors rotating at constant speed.

When samples travel in front of the exit window, two timing belts produce the rotational mechanism to activate and samples rotate in its own axis by means of a turning hook during irradiation. The rotational mechanism includes an additional circuit that uses a limit switch that controls the conveyor translational motion to place samples directly in front of the beam at a preset position. At such position, translational motion stops, a sample rotates uniformly for irradiation while a red light in the conveyor control box indicates the sample is in its irradiating position. By means of a push bottom, translational motion can be resumed (light turns off) and the next sample arrives to be placed at the irradiation point where translational motion is turned off again.

These processes are cycled for all the samples to be irradiated, and the light in the conveyor control box is used as a means to track sample locations within the conveyor line. Figure 3-5 shows the rotational mechanism and an irradiated sample.

Figure 3-5 and Figure 3-6 show the rotational mechanism and its layout relative to the e-beam exit window.

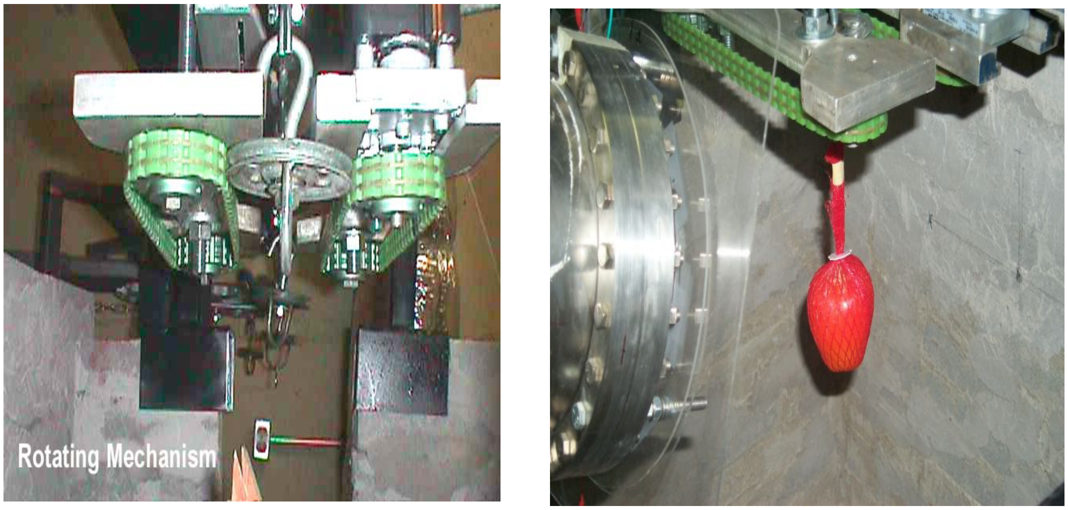

Figure 3-5. Rotational mechanism for e-beam irradiation (left). Apple phantom set up for irradiation (right).

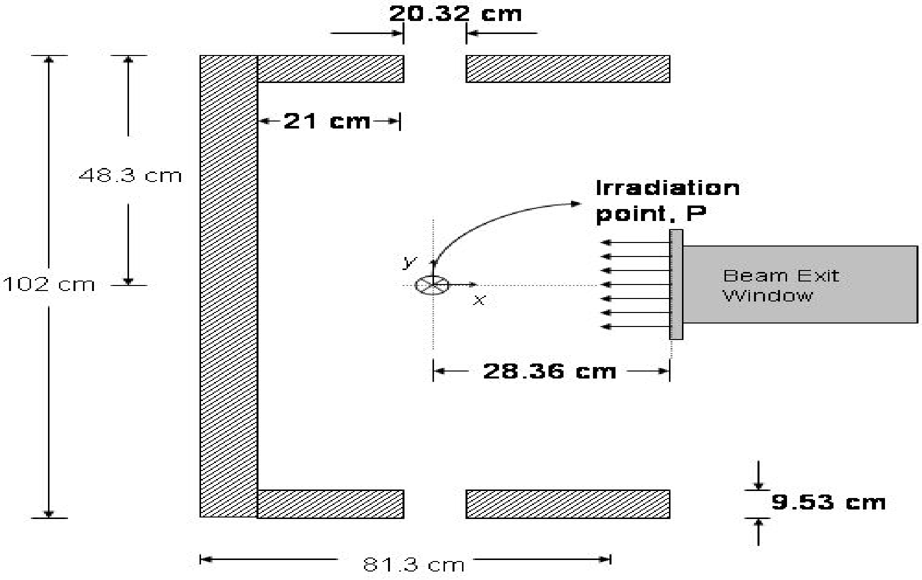

Figure 3-6. Conveyor system layout reference with respect to the Van de Graaff exit window.

3.1.3 SureBeam 10 MeV LINAC

The electron beam linear accelerator in the Food Research Facility at Texas A&M University provides two operation modes, i.e., electrons and X-rays. For electron irradiations two vertically mounted and opposing 10 MeV, 18 Kilowatt LINAC are used to accelerate electrons to near the speed of light using microwaves so they can be targeted into a food product. The electron LINAC can operate in single or dual beam mode so food products receive radiant energy from one or both the upper and lower accelerators so that product flipping is not required. Figure 3-7 below shows the layout of two LINAC's providing dual beam irradiation.

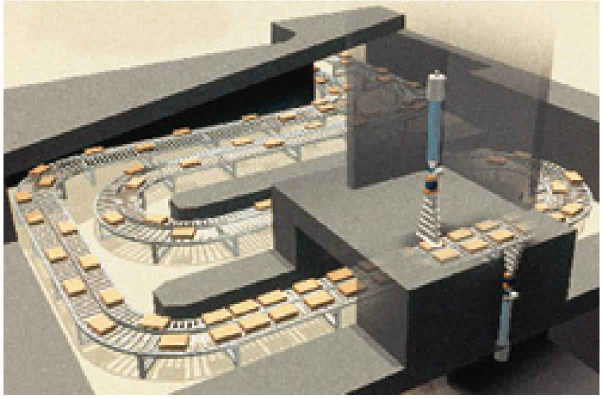

Figure 3-7. Irradiation layout using dual beam LINAC's.

For X-ray irradiation a single horizontally mounted 5 MeV, 15 Kilowatt X-ray Linear Accelerator produces electrons traveling near the speed of light hitting a dense metal target so X-rays are produced. Figure 3-8 show the two 10 MeV electron accelerators and the 5 MeV accelerator used to produce the X-rays. Figure 3-9 shows the conveyor layout for the electron beam and X-ray irradiations.

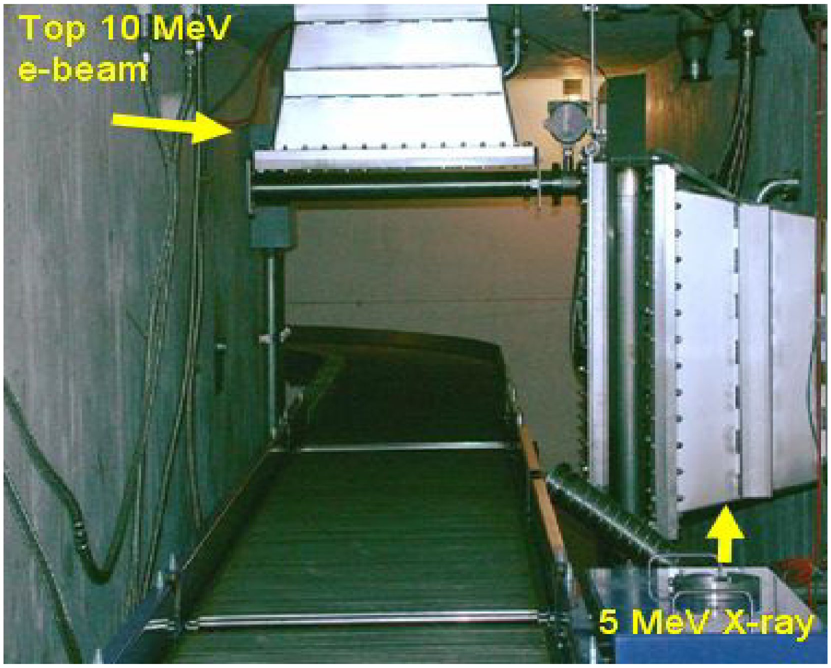

Figure 3-8. Electron accelerators layout (Top: 10 MeV e-beam LINAC, Right: 5 MeV X-ray LINAC).

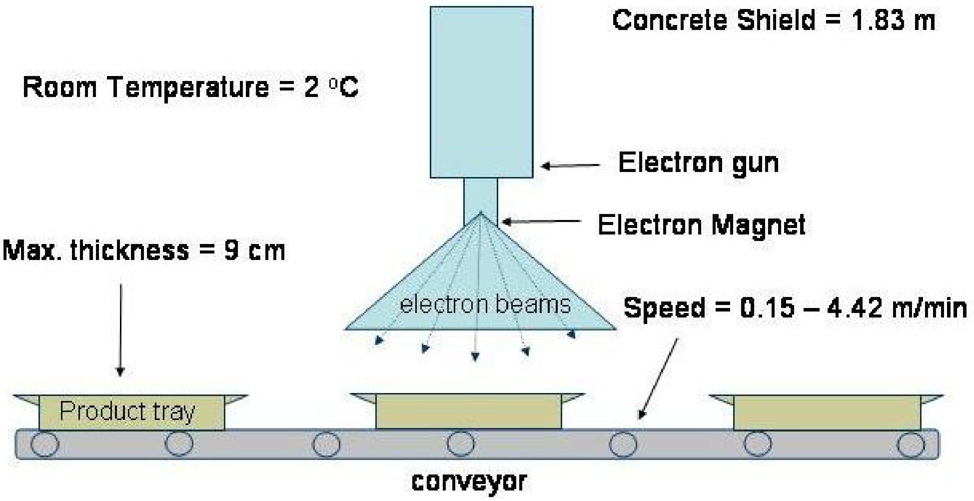

Figure 3-9. Conveyor layout for irradiation with 10 MeV electrons and 5 MeV X-rays.

The Food Research Facility employs a single conveyance system to move the product in and out of the process chamber at a pre-defined speed. All LINACs and conveyors are controlled with Allen Bradley Programmable Logic Control (PLC) software that along with SureBeam's RS View Human Interface software, enables the irradiation process to be virtually automated and very tightly controlled.

3.2 Apple Phantom Development

3.2.1 Apple Mold Development for Phantom Castings

Phantom chemical dosimeters were created using a mold obtained originally by casting one *Red Golden Delicious* apple obtained from a local vendor. The apple shape and geometry were cast exactly every time for the purpose of this research. The casting material used was a synthetic rubber (Reprorubber No. 16131 catalyst and base, FlexBar Machine Corp, NY) that can reproduce exactly the apple geometry. Once both, base and catalyst were mixed using a 1:1 ratio, the casting time before solidification was approximately 7 minutes. One container of catalyst and base, each of 1,075 mL of material, respectively, were used to produce the final casting mold.

3.2.2 Chemical Development of the Apple Phantom

Apple-phantoms were produced in the Food Safety Engineering laboratory at the Department of Biological and Agricultural Engineering at Texas A&M University. Mass calculations for an apple phantom were produced using an apple synthetic rubber mold as described above to assure sample geometrical uniformity. The mold had a capacity of 0.325 Kg of water. The amount of paraffin wax required for each casting was determined from the amount of water in the mold, i.e., 325.0 mL/mold after measurement. The ratio of paraffin to water is 3:3.5 (by wt.). Thus, using water density, 1000 Kg/cm^3, each mold holds 0.325 Kg of water or 0.279 Kg of paraffin wax. The total paraffin wax mass approximately considered was then 0.280 Kg; thus, mass balance calculations for each component were performed using a total mass of 0.280 Kg.

Next, a mass balance shown in Figure 3-10 was performed to obtain specific the concentrations at 20% chloroform at a fixed 1% microcrystalline wax concentration. For instance, at 20% chloroform solution in paraffin wax:

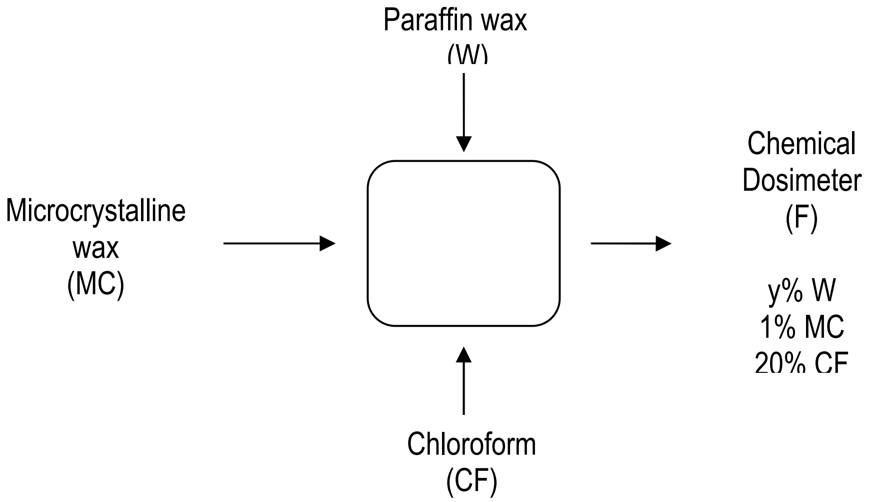

Figure 3-10. Paraffin, chloroform, dye system for apple phantom samples.

A. MC Wax

$$MC = 0.01 * F \tag{3.1}$$

$$MC = 0.01 * F = 0.01 * 0.280\,Kg = 0.0028\,Kg$$

B. Chloroform

$$CF = 0.20 * F \tag{3.2}$$

$$CF = 0.20 * 0.280\,Kg = 0.056\,Kg$$

C. Paraffin Wax

$$MC + W + CF = F \tag{3.3}$$

$$W = F - MC - CF$$

$$W = 0.280\,Kg - (0.0028 + 0.056)\,Kg = 0.221\,Kg$$

Chloroform mass was converted to volume via its density (ρ = 1520 Kg/m^3).

$$CF = \frac{0.056\,Kg}{1520\,\frac{Kg}{m^3}} = 36.84x10^{-6}\ m^3\ = 36.84x10^{-3}\ L \qquad (3.4)$$

Next, the required mass of methyl yellow dye to obtain a concentration of, c_1 = 4*10^{-4} *m,* was obtained as:

$$Molal\,Concentration = \frac{moles\ of\ \ methyl\ \ yellow}{1\,kg\ \ of\ \left(paraffin\,wax + mc\,wax + chloroform\right)} \qquad (3.5)$$

Thus,

$$4*10^{-4}\,m = \frac{n\ moles\,methyl\,yellow}{0.280\,kg\ \ solvent} \qquad (3.6)$$

$$n\ moles\,methyl\,yellow = 0.280\,kg*\left(4*10^{-4}\right)\frac{mol}{kg} = 112*10^{-5}\,mol$$

$$mass(c_1 = 4*10^{-4}\,m) = 112*10^{-6}\,mol*\frac{0.22529\,Kg}{1\ mol} = 25.23*10^{-6}\ \ Kg \qquad (3.7)$$

Table 3-1. Apple-phantom chemical composition (by wt., at 20% chloroform, 4x10^{-4} *m* methyl yellow)

Component	**Mass (Kg)**
Paraffin Wax	0.221
Chloroform	0.056
Methyl Yellow	2.5x10^{-5}
Microcrystalline wax	2.8x10^{-3}
Total Mass	0.280

Table 3-1 above shows the mass required to cast an apple phantom dosimeter specifically at 20% chloroform and 4x10^{-4} *m* methyl yellow concentration.

The dosimeter chemical composition described above provide identical electron density and Z values (atomic number) to that of an actual apple (Appendix B). Although paraffin wax has been used as a common tissue substitute in radiation dosimetry and measurements (ICRU, 1989), it is important to determine how well this material matches the radiation interaction properties of an actual apple for e-beam treatment.

Table 3-2 compares the calculated elemental compositions, density and Z values of the paraffin phantom with those of a *Red Delicious* apple.

Table 3-2. The elemental composition and density of an actual apple and the phantom

	Elemental Composition [%/weight]					Density[2]	Z_{eff}[1]
Material	**H**	**C**	**N**	**O**	**Others**	**[kg/m^3]**	
Phantom	12.99	70.27	0.0168	---	17.72 Cl	1008	7.43
Actual Apple (Red Delicious)	10.28	6.07	0.04	83.47	0.01 Mg, 0.01 Ca, 0.01P, 0.11K	1042	6.58

[1] effective atomic number; calculated as (Tsoulfanidis, 1995):

$$Z_{eff} = \frac{\sum_i (W_i / A_i) Z_i^2}{\sum_i (W_i / A_i) Z_i}$$; where A_i is the atomic mass, Z_i the atomic number, and W_i the weight fraction

[2] At room temperature. Mohsenin (1986).

The phantom contained 70% of carbon (paraffin's hydrocarbon structure - $C_{25}H_{52}$) and 18% of chlorine (from chloroform). No oxygen was present in the phantom. However, the carbon contained in tissue material substitutes the missing oxygen (ICRU, 1989); thus, in average, the phantom has identical electron density and Z value (atomic number) to that of an actual apple.

The total linear stopping power, S, for electrons includes the total energy loss, dE, by collision and bremsstrahlung production for a path length dx in the medium as,

$$S = \frac{dE}{dx} = \left(\left(\frac{dE}{\rho \cdot dx} \right)_{col} + \left(\frac{dE}{\rho \cdot dx} \right)_{rad} \right) \cdot \rho \qquad (3.8)$$

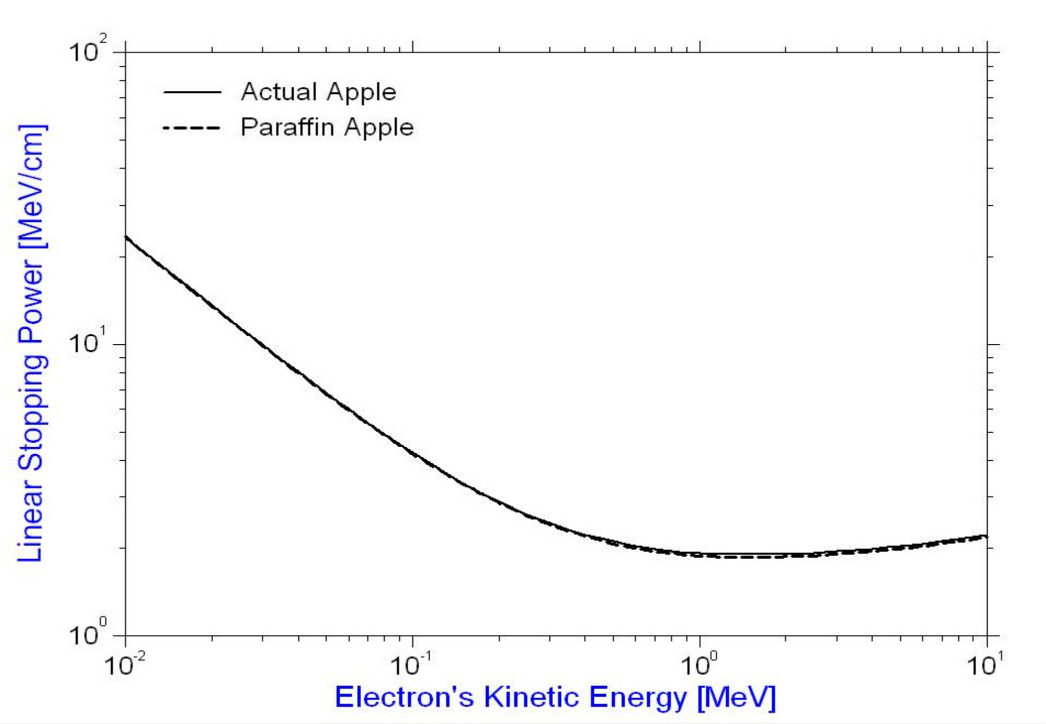

Figure 3-11. Total stopping power (TSP) of an actual apple and the phantom (paraffin apple) with corresponding electron energy.

where ρ is the density of the medium, $(dE/\rho\ dx)_{col}$ is the mass collision stopping power which includes all energy loses in particle collisions that directly produces secondary electrons (delta rays) and atomic excitations and, $(dE/\rho\ dx)_{rad}$ is the mass radiative stopping power which includes all energy losses of the primary electron which lead to bremsstrahlung production (ICRU, 1984).

Figure 3-11 shows that the total stopping power values for both the phantom and the actual apple overlap throughout the entire range of energy. Therefore, the developed phantom can be used for practical studies of e-beam irradiation of an actual apple for an energy source range of 0.01 – 10 MeV.

The practical advantages of paraffin wax are that it is readily available, easily worked, and freely mixed with halogenated hydrocarbons (Potsaid and Irie, 1961). It also provides rigidity to the dosimeter and works as a holding matrix to the chloroform and methyl yellow dye. The small mass percentage of the microcrystalline wax present in the apple phantom also enhances rigidity preventing it from cracking.

3.2.3 Casting of Apple-Phantoms

The apple-phantom chemical solution, as shown in Table 3-1 was uniformly mixed and kept at a temperature of 65 ± 1 ^{o}C in a water bath for about 1 hour before it was poured into each of the molds. Increasing the temperature above 65 ^{o}C resulted in longer cooling times, and non-uniform apple phantoms due to the temperature gradient created between the chemical solution and room temperature (25 ± 1 ^{o}C).

After pouring was completed, each mold was kept in a dark room and removed from its cast after 24 hours. This was necessary to prevent the solution to be exposed to the ultraviolet (UV) light from the fluorescent lamps in the laboratory, and also to allow the chemical mixture to completely solidify before irradiation treatment. Figure 3-12 below shows an apple phantom after it was removed from its cast, ready for cutting, and packaged prior the irradiation treatment.

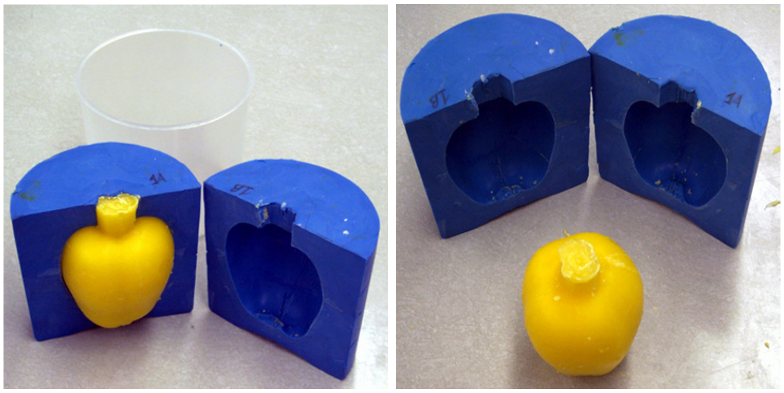

Figure 3-12. Apple phantom sample and its cast.

3.2.4 Cutting Method

The apple phantom was cut in half across their vertical axis, i.e., from the top of the stem to the bottom, using a Delta band saw model 28-276 (Delta Machinery, Jackson, Tennessee) with a 19 mm blade. The center of each apple phantom was determined from the characteristic lines formed upon solidification in each one of the molds. Next, a solid line was drawn across the surface of each phantom before it was cut. Each resulting slice was then referenced as Left and Right Phantom Slices. Figure 3-13 shows an apple phantom before and after being cut in half resulting in its left and right slices.

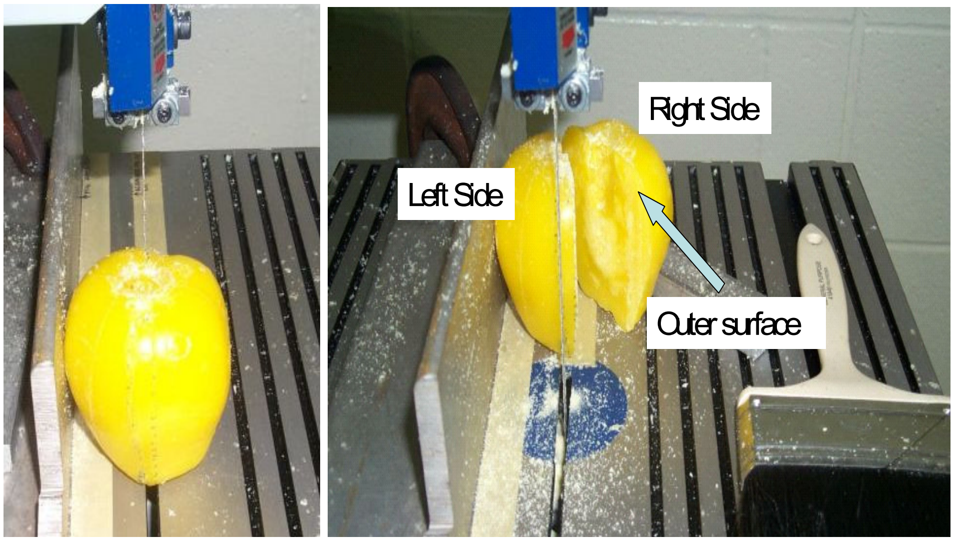

Figure 3-13. Unexposed apple phantom before cut (left). Apple phantom cut results in left and right slices (right).

Next, the GAFCHROMIC® HD-810 (Advanced Materials Group, International Specialty Products (ISP), New Jersey) film was cut with the contour corresponding to the apple phantom right plane slice before being packaged together. The next section describes the preparation of the radiochromic film.

3.2.5 GAFCHROMIC® HD-810 Film Contours

A 210 x 296 mm piece paper (A4 standard white) with the same dimensions of a HD-810 radiochromic film sheet was used as a grid to fit 6 apple contours per sheet of film, and photocopied twice. The flat surface contours corresponding to each one of the right apple phantom slices was reproduced in each particular box to obtain the same apple phantom shape. Next, a 210 x 296 mm sheet of film was placed on top of the grid and held together with small strips of transparent scotch tape to prevent sliding, and individual contour slices were cut. Figure 3-14 shows the paper grid and film sheet before it was cut.

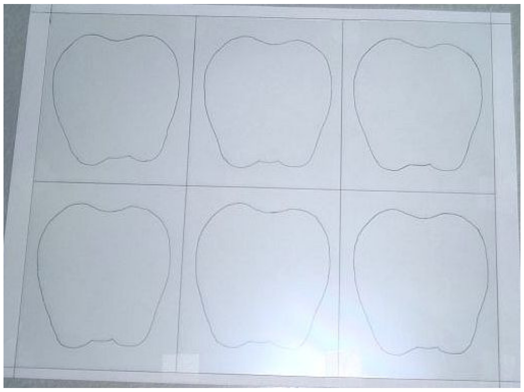

Figure 3-14. HD-810 film layout with apple phantom contours for irradiation.

Each individual apple film slice was cut and held together between two identical paper slices forming a protective envelope for the apple film slice. For protection purposes, each side of the paper protective envelope was completely covered with a thin scotch tape to prevent chloroform migration into the film after vacuum packaging. Each apple phantom slice, left and right, was held together with its corresponding radiochromic film envelope in its center using a full revolution of scotch tape around its latitudinal axis. At this point, the apple phantoms were ready for vacuum packaging.

3.3 Apple-Phantom Vacuum Packaging.

Vacuum packaging was used in all experiments including E-beam, and X-rays. A vacuum sealer system model VS-200 (Black & Decker, Hampstead, Maryland) was used to package apple phantoms. This system included a special roll of 27.94 cm width by 548.64 cm length polyethylene plastic bag for custom made bags.

For irradiation with the VDG accelerator, plastic bags of 27.94 cm width and height were cut so the apple center matched the center spot where the electronic beam is considered uniform. The TOP and BOTTOM regions shown in Figure 3-15 were designed for support only and no vacuum was pulled on those areas. After the phantom samples were vacuum packaged, a distance of 12 cm was measured from the bag's origin to point *a*, where a hole was punched in the bag. The same procedure was performed in point *b*. Each bag was labeled as in Figure 3-15.

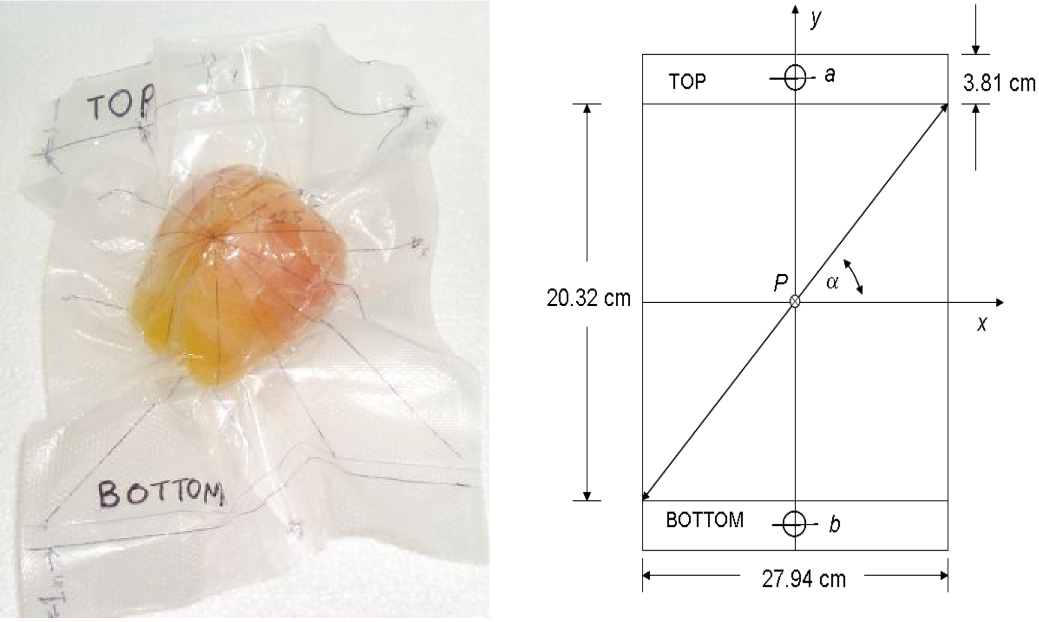

Figure 3-15. Apple phantom at 45 degrees from its vertical axis of rotation (left). Plastic bag configuration for the apple-phantom slices. Alpha denotes the irradiation angle with respect to its horizontal axis (right).

Following apple phantom packaging in vacuum bags, experimental irradiations were conducted as described below.

3.4 Irradiation Experiments

3.4.1 E-Beam Irradiation Experimental Design Using the VDG Accelerator

Apple phantoms were produced in triplicate and irradiated using 1.35 MeV electrons for treatment at $\alpha = 90$, 45, and 22.5 degrees. Doses of 50 and 100 Gy were delivered (Appendix A) respectively for each angle value as shown in Table 3-3.

Table 3-3. Experimental design for Van de Graaff experiment

Dose (Gy)	**Angle, α (Degrees)**		
	90^o	*45^o*	*22.5^o*
50	3	3	3
100	3	3	3

Irradiations were performed in batches ranked accordingly to the irradiation angle and dose. Figure 3-16 shows the layout used for e-beam irradiation with an apple-phantom oriented at α = 90 degrees.

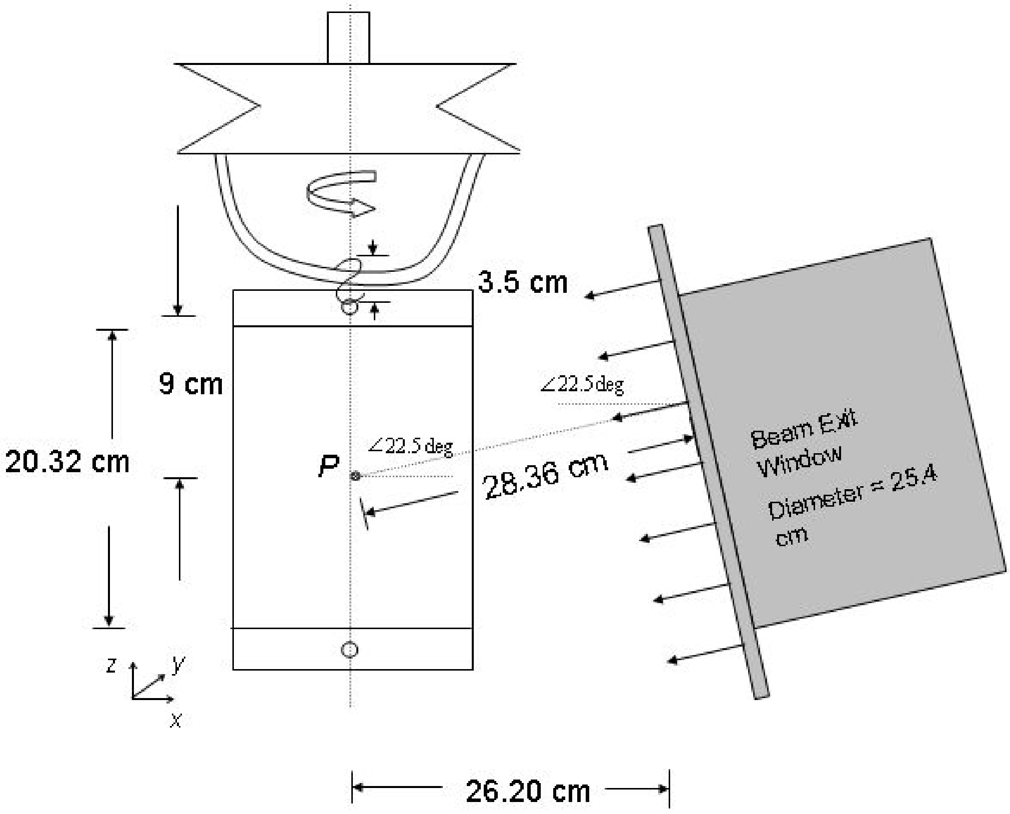

Figure 3-16. Lateral view of irradiation point P in front of exit window.

Analyses were carried out 24 hours after treatment to permit the apple phantom's chemical solution to stabilize as well as HD-810 film contours.

3.4.2 E-Beam Irradiation Experimental Design Using the 10 MeV LINAC

Surface treatment of apple-phantoms was performed with a dual beam of 10 MeV electrons. Target doses of 1, 0.4, 0.2 kGy were delivered to each sample respectively, according to MNCP-5 simulation based on:

1. The thicknesses of Plexiglas attenuators (Section 3.4.2.1) of 3 cm, 4 cm and 4.2 cm.
2. The rolling conveyor system traveling at a speed of 18.3 m/min (60 ft/min).

The attenuating material was utilized so the calibration equations developed for the VDG e-beam irradiation could be used to produce dose deposition and dose depth profiles. As a result, the apple-phantoms were required to be enclosed in secondary packaging to match their respective target doses. Figure 3-17 shows the layout of the configuration used to irradiate the apple-phantoms.

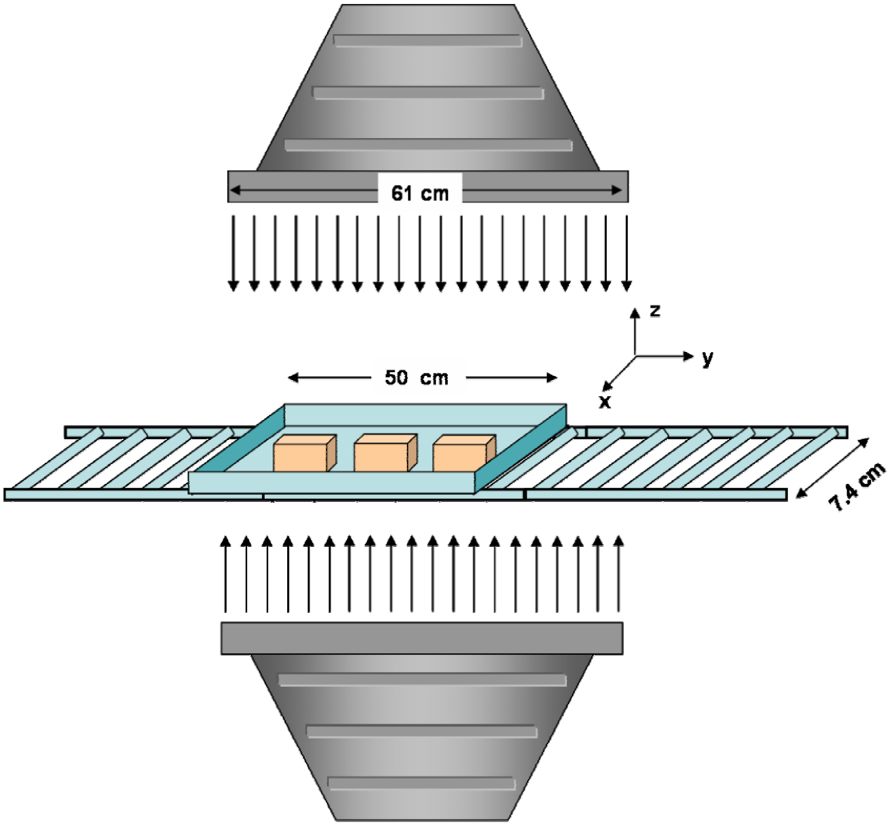

Figure 3-17. Configuration for irradiation treatment of apple-phantoms with 10 MeV electrons.

3.4.2.1 Polystyrene Phantom Holder with Lucite for the 10 MeV E-Beam Irradiation

For the irradiation experiment using the 10 MeV LINAC, individual polystyrene apple holders were constructed for each apple-phantom. Each polystyrene holder was 10 cm in length, 10 cm in width, and 14 cm height with a wall thickness of 1.5 cm. Each holder contained two removable top and bottom Lucite custom made absorbers. The Lucite absorbers were cut perfectly with a milling machine in three different thicknesses of 3.0, 3.2, and 4.0 cm to obtain the desired target doses of 1, 0.4, and 0.2 kGy respectively.

Prior to irradiation, the vacuum apple phantoms were introduced in their respective apple holders sorted by their Lucite absorber thickness. Finally, each apple holder was taped to a cardboard box with 60.9 cm in length, 50.8 cm width, and 10.2 cm height. Figure 3-18 below shows the configuration of an individual 4 cm Lucite apple holder, and the final setup before irradiation.

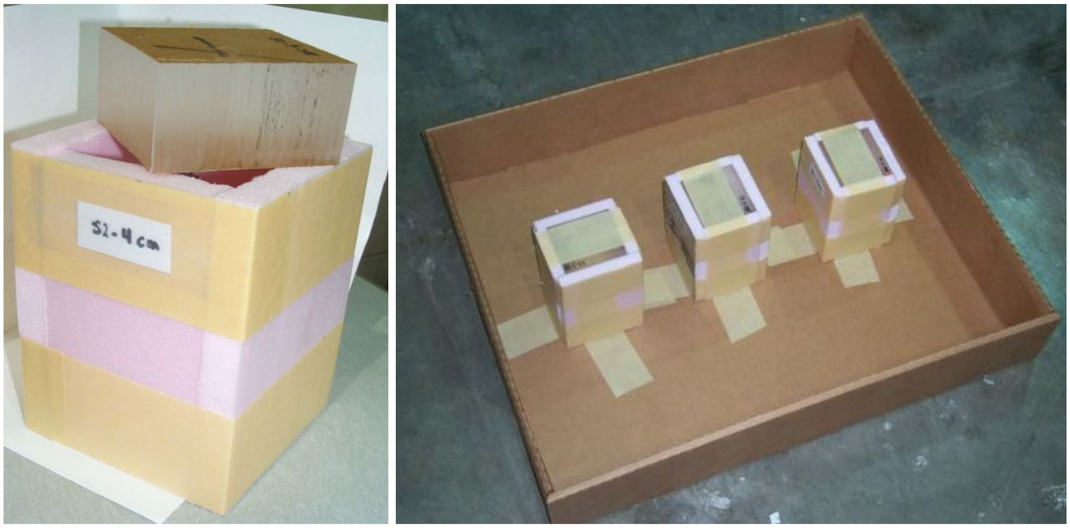

Figure 3-18. Polystyrene holder with 4 cm thick Lucite absorber (left). Apple holders for 4 cm thick Lucite absorber before irradiation treatment.

Apple phantoms were produced in triplicate and irradiated as shown above in the right side of Figure 3-18. Table 3-4 shows experimental design based on the secondary packaging used.

Table 3-4. Experimental design for e-beam irradiation with the 10 MeV LINAC (dual beam). Conveyor speed of 18.3 m/min

Target Dose	**Lucite Absorber Thickness**		
Gy	3 cm	4 cm	4.2 cm
1000	3	-	-
400	-	3	-
200	-	-	3

The irradiations were performed in batches ranked accordingly its Lucite thickness value. The analyses were carried out 24 hours after treatment to permit the apple phantom's chemical solution to stabilize as well as HD-810 film contours.

3.4.3 X-ray Irradiation Experimental Design Using the 5 MeV LINAC

The X-ray irradiation experiment with the 5 MeV LINAC also required a secondary holder for the apple-phantoms. Hence, a custom made polystyrene holder for three phantoms was constructed. Each apple-phantom was separated by a distance of 16.5 cm center to center to prevent scattering effects. The height from the bottom of the holder to the center of the apple was 31 cm where the X-ray beam was located. Every phantom was positioned with its axial center[1] aligned parallel to the X-ray direction. The phantoms top surface (stem) was facing the X-ray beam to expose first the top region of the apple. Each apple-phantom contained its respective radiochromic film slice as described in section 3.1.1. Figure 3-19 shows the arrangement of three apple phantoms used for X-ray irradiation in a cardboard box holder prior to irradiation.

---

[1] Axial center position corresponds to the direction in which the apple was described in Section 3.1.1

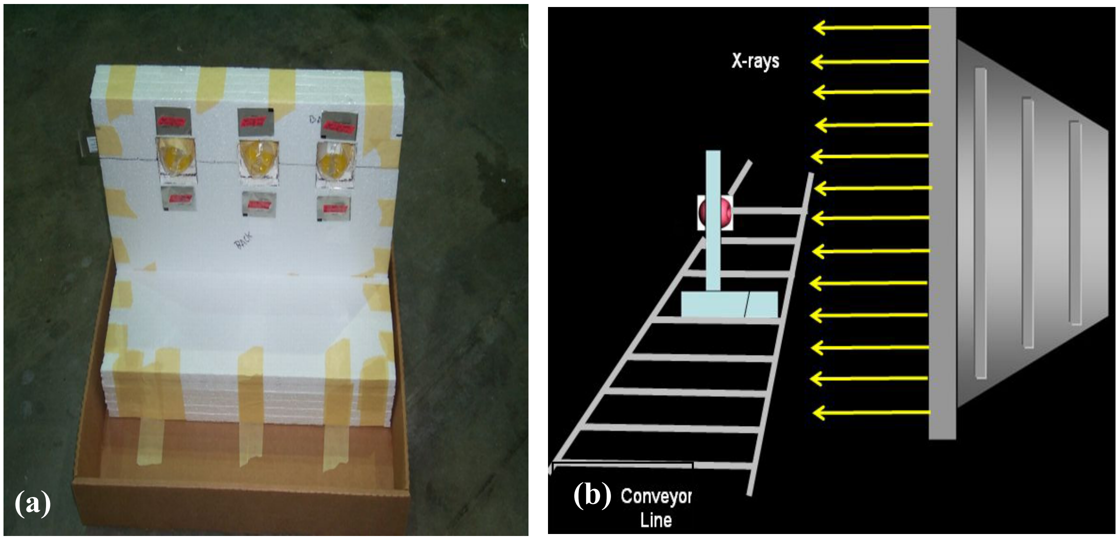

Figure 3-19. (a)Apple phantom holder for the X-ray irradiation experiment. (b) Configuration layout for the apple-phantom irradiation at a conveyor speed of 0.61 m/min (right).

Table 3-5 shows the sample distribution used for the X-ray irradiation experiment.

Table 3-5. Experimental design for X-ray irradiation using a 5 MeV LINAC and a conveyor speed of 0.61 m/min

Target Dose (Gy)	**Apple Phantoms**
600	3

3.5 Apple-Phantom Post Irradiation Handling

After each of the irradiation experiments were completed, the apple phantom samples were pulled out of their vacuum bags to prevent chloroform migration to the HD-810 film placed in between the two halves. All phantom samples and HD-810 film were stored in a dark room for a period of 24 hours prior to analysis with a flatbed transmission scanner. Next, the right side halve of each apple-phantom was used to obtain individual 3.175 mm thick apple contours.

3.5.1 Apple-Phantom Slicing

The band saw described in Section 3.2.4 was adjusted to 3.175 mm thick gap. The gap distance was regulated using a 90 degree aluminum elbow aligned parallel to the cutting saw direction. Two heavy duty clamps were used to secure the aluminum elbow to the bandsaw working table.

In preparation for slicing, the flat face on the right side of each apple-phantom was first supported on a 3.175 mm polystyrene bed aligned parallel to the cut direction. Next, each apple-phantom was slowly moved until a uniform cut resulted. The polystyrene bed was used to prevent and protect from breaking the phantom side closer to the working table. The chemical composition at 20% chloroform and $4\text{x}10^{-4}$ m of methyl yellow (by weight) resulted in very fragile phantoms for handling. Prior to analysis with a transmission flatbed scanner, the edges of each apple slice contour were cleaned of wax debris with a fine scalpel. The apple slice contour thicknesses were measured for each irradiation experiment yielding on average 3.175 ± 0.06 mm values.

3.6 Scanning Preliminary Setup

A Microtek ScanMaker 8700 Pro Series (Microtek USA, Carson, California) was used to perform transmission scans on both radiochromic film and methyl yellow slices. A 7.62 cm x 7.62 cm square perimeter made of transparent tape was delineated in the center of the glass surface of the scanner to use it as a scanning reference.

Next, a preliminary scan of the delineated area was performed and the scanner lamp then warmed for a period of 5 minutes to avoid any temperature differences. The scans corresponding to each irradiation experiment were performed consecutively allowing a 1 minute interval in between to prevent the lamp from warming up. After an individual scan was completed for each irradiation experiment, a lint-free cloth was used to keep the glass surface clean at all times.

3.6.1 GAFCHROMIC® HD-810 Film Scanning

Using the scanning software Scan Wizard Pro v.5, a square image area corresponding to the dimensions of the reference grid was pre-set. The scanner was set to capture an image at 300 pixels per inch (ppi). As a result, 2.64 mega bytes image of 960 pixels x 960 pixels was scanned each time and saved using a Tagged Image File Format (TIFF). The films were scanned using a full range dynamic[2] value. Finally, all apple film contours corresponding to X-rays and e-beam experiments were scanned and saved to a computer.

---

[2] dynamic range corresponding to a value of $D = 4.0 - 0.05$.

3.6.2 Apple-Phantom Contours Scanning

The apple-phantom slice contours described in Section 3.5.1 were scanned using a dynamic range[3] value of 3.2 using the same predefined squared area discussed in Section 3.6. All software correction tools were turned off, and the scan resolution was also set at 300 ppi resulting in an image of 960 x 960 pixels. The apple-phantom slices contours containing both, X-ray and e-beam data from both experiments, were scanned and saved to a computer using TIFF format.

3.7 GAFCHROMIC® HD-810 Film Calibration

The film apple contours of 1 cm x 1 cm were irradiated at the irradiation point *p* using a cylindrical Lucite holder. Specifically, the holder was designed and constructed to fit the round Farmer ionization chamber metal cylinder with the film in front of the ionization window volume. Hence, a direct dose measurement in the beam center, located 28.36 cm away from the exit window was obtained. The holder was supported at the irradiation point using a vertical tripod assembled with an adjustable rod in the horizontal direction where the holder was attached. As a result, height was adjusted exactly to the desired position and the holder positioned at any particular angle with respect to the beam exit window. Figure 3-20 shows the configuration used to calibrate the film at a 22.5 degree angle parallel to the exit window and a distance of 28.36 cm away.

---

[3] dynamic range corresponding to a value of $D = 4.0 - 0.8$.

Figure 3-20. Radiation holder at irradiation point, *P*, for HD-810 film calibration.

A calibration curve for the films was produced at the irradiation point *P* by placing individual film slices and irradiating at specific doses. Each individual film was scanned using the guidelines provided in Section 3.6.1 and 3.6.2. Because the film thickness was extremely small compared to that of a methyl yellow slice, the films were scanned in transmission mode using the full dynamic range scale. Scanning the film under the same dynamic range value of a methyl yellow slice reduced the ability of the film to predict higher doses in all channels. The film intensity data was analyzed for the Green channel and a calibration equation was found between 50 and 1500 Gy. Figure 3-21 shows the calibration results.

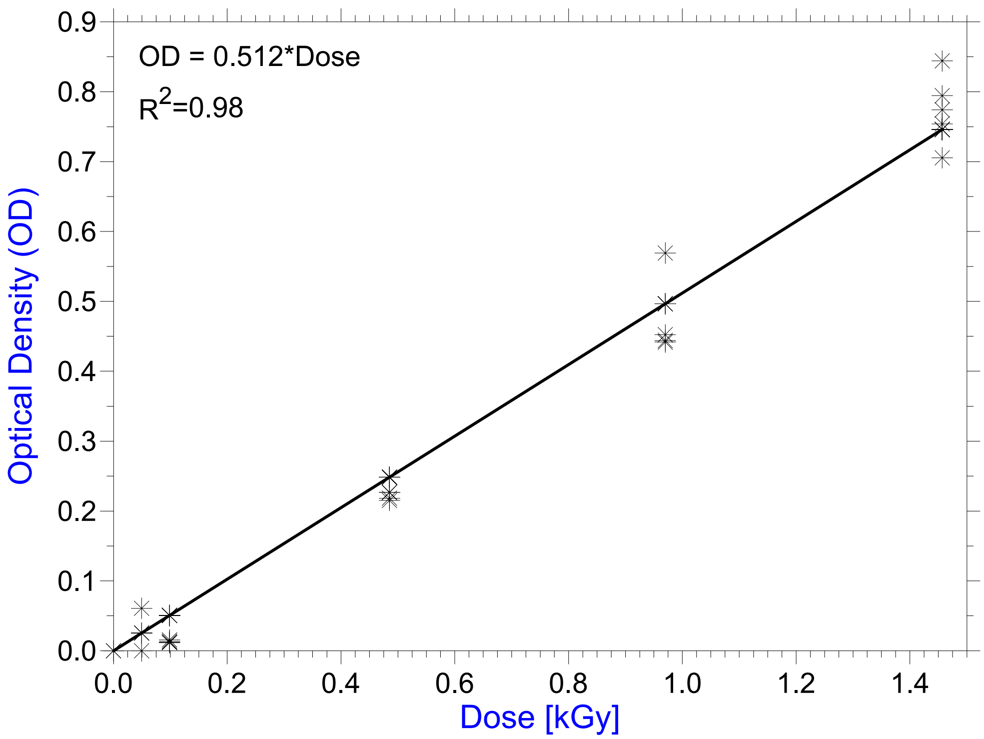

Figure 3-21. GAFCHROMIC® HD-810 film calibration curve (Green Channel) at irradiation point *P*.

The calibration curve shown in Figure 3-21 was used to transform OD data of all images to dose values. The curve works only for green channel data and was used for the e-beam experiments described in sections 3.4.1 and 3.4.2.

3.8 Chemical Dosimeter Calibration with the VDG Accelerator

The methyl yellow, chloroform, and paraffin wax solution using the chemical composition described in Section 3.2.2 was calibrated with circular Petri dishes of 2.54 cm in diameter and 7.6 cm height where the solution was poured. After a 24 hour period, the samples were irradiated with 1.35 MeV electrons using target doses from 0 Gy to 500 Gy. After the irradiations, each sample was cut using the procedure explained in Section 3.2.4, and scanned along the beam direction (Section 3.6.2). Figure 3-22 shows the results for green channel.

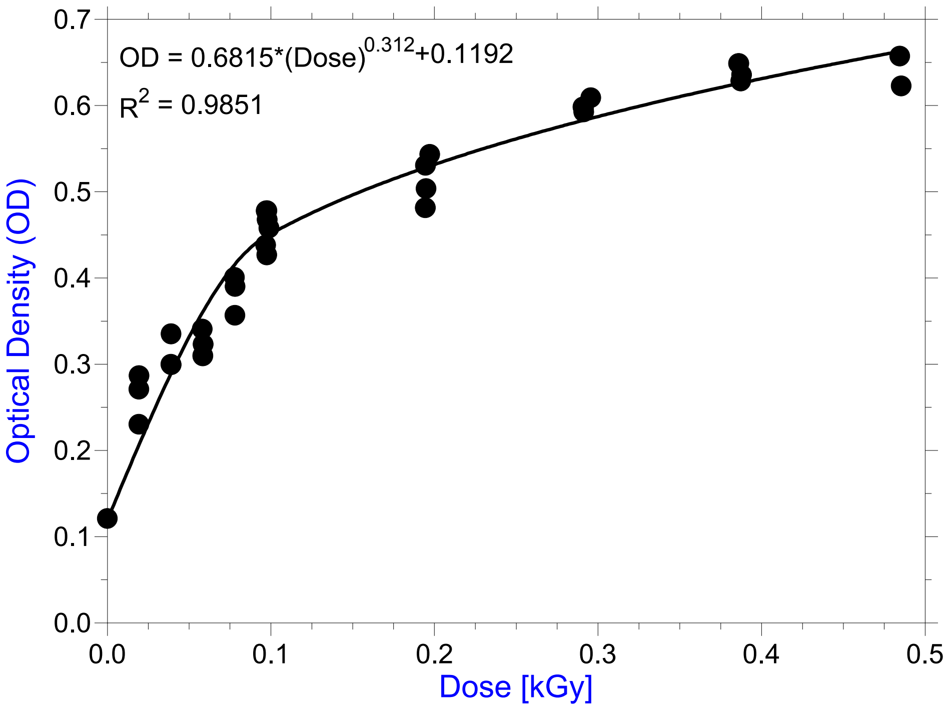

Figure 3-22. Green channel methyl yellow calibration curve using 3.175 mm thick slices and 1.35 MeV electrons.

The calibration curve shown in Figure 3-22 was used to transform OD data of all images to dose values. The curve works only for green channel data and was used for the e-beam experiments described in sections 3.4.1 and 3.4.2.

3.9 Image Processing of GAFCHROMIC® Film and Apple Phantom Contours

A computer code was written using Matlab® (The Mathworks Inc., Natick, Massachusetts) for the HD-810 film and methyl yellow apple contours to extract and analyze the intensity data corresponding to the green channel of each image file. A 960 pixel x 960 pixel square matrix contained all the intensity data measurements for the green channel only. Each data point was transformed to optical density using equation 2.12, and later to dose values using the calibration equations shown in Figure 3-21 and Figure 3-22 for film and methyl yellow respectively.

The dose deposition profiles for the film and methyl yellow apple contours were computed using the Matlab Image Processing Toolbox ® contouring algorithms, and later transformed to grayscale.

The dose depth distribution profiles were produced with a computer algorithm that extracted an intensity data matrix of 65 pixels x 360 pixels. Each point represents the intensity data extracted from the film or phantom surface in the radial direction or depth every 1 degree around the phantom periphery. The intensity data in pixels was scaled to millimeters through the image resolution that was set at 300 pixels per inch for every scan (Section 3.6.1, and 3.6.2). As a result, each image contained 12 pixels per millimeter.

For the e-beam irradiation with electrons using the Van de Graaff accelerator only, the dose uniformity ratio, D_{max}/D_{min}, defined as the maximum to the minimum dose at a penetration depth from the surface along the phantom periphery was obtained by manipulating the dose depth distribution profile matrix.

First, the minimum value in each of the dose matrices for every dose treatment and orientation was defined as all the dose values that were at least 10% above the minimum data point. All dose data satisfying this criteria was used for the analysis, and everything else was replaced with zeroes. Next, the maximum and minimum dose data values for each treatment were obtained from each row (i.e., penetration depth data) along the apple periphery (i.e., 0 to 360 degrees), and the dose uniformity ratio calculated and saved into a tab delimited file for graphing purposes.

CHAPTER IV

EXPERIMENTAL RESULTS

4.1 E-Beam Irradiation Using Van de Graaff Accelerator

4.1.1 Energy Deposition and Dose Depth Distributions

Electron beam irradiation was delivered to the apple-phantom dosimeters developed as described in Sections 3.2 and 3.3, using 1.35 MeV electrons at the irradiation point, *P*, as described in Section 3.7. The absorbed dose distribution for each apple-phantom was obtained using the reference coordinate system described next.

Each apple-phantom was rotated at a constant speed around a fixed vertical plane defined as the conveyor's vertical axis passing through the phantom center point. In addition, each apple-phantom was positioned (Section 3.3) at an angle, α, defined as the horizontal or latitudinal plane passing through the phantom's left to right sides (180 degrees – 0 degrees). The e-beam source was fixed at an angle of 22.5 degrees pointing downwards with respect to the apple-phantom horizontal or latitudinal plane. The dose distributions were obtained for α values of 90, 45 and 22.5 degrees using target doses of 50 Gy and 100 Gy per angle respectively. The experimental dose rate was fixed 4.5 Gy/min and at 7.5 Gy/min.

Figure 4-1 defines the reference coordinate system used to perform the e-beam irradiations described in Section 3.4.1 (E-Beam Irradiation Experimental Design using VDG Accelerator)

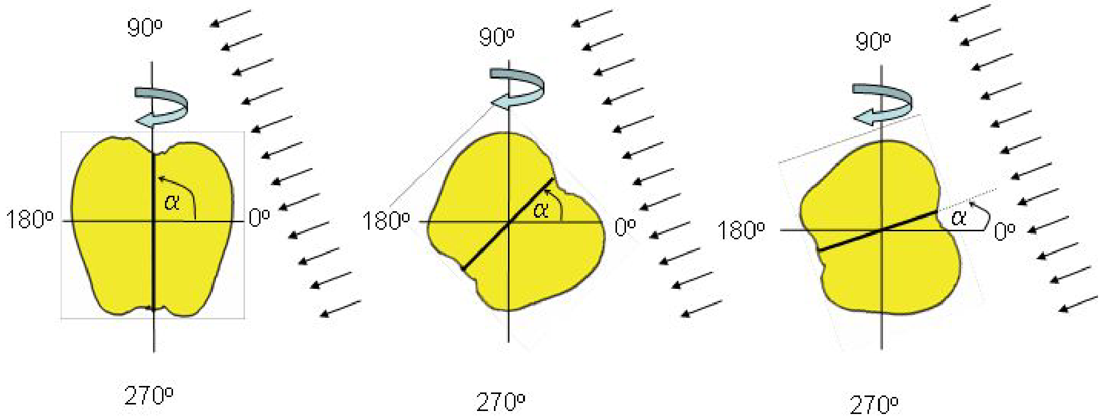

Figure 4-1. Reference coordinate system with α = 90, 45, and 22.5 degrees (left to right) for e-beam irradiation with Van de Graaff accelerator.

Figure 4-2 defines the apple phantom dimensions centered at the irradiation point *P* a distance of 28.36 cm away from the exit window.

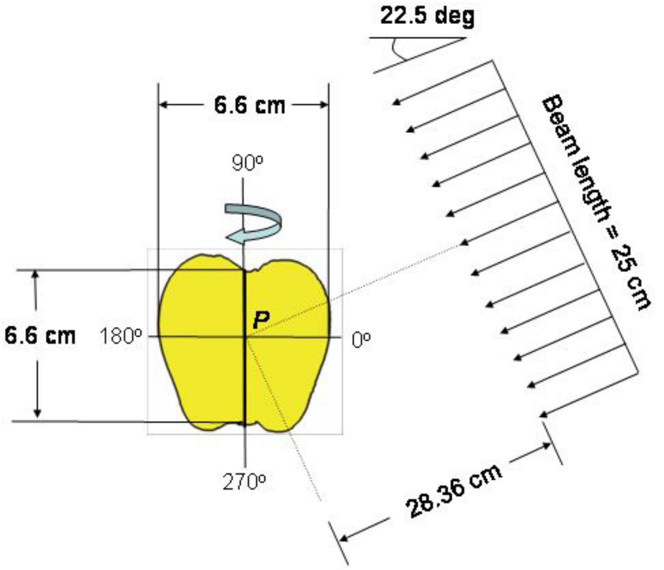

Figure 4-2. Apple-phantom dimensions centered at irradiation point *P*.

Each apple-phantom was irradiated first with its top orientation to half the total target dose at each particular α angle. Next, the apple-phantom bottom was turned over to deliver the remaining dose at the same particular α angle. This process was performed by switching the vacuum packaged apple-phantom polyethylene bag orientation from points *a* to *b* as shown in Figure 3-15 (Section 3.3).

The results that follow show the depth dose distribution in an apple-phantom contour and HD-810 film as a function of angle, θ, from 0 to 360 degrees. The dose data obtained for this experiment was calculated at the plane that traverses the apple-phantom from top to bottom, and divides the phantom in two symmetrical pieces as shown by the apple center lines in Figure 3-15 so the radiochromic film response could be compared to that of the apple-phantom.

It is expected that the dose distributions for both, film and apple-phantom will depend on several common factors such as the electron entrance angle, the distance from the electron exit window to the phantom, the path electrons follow as a result of scattering and the maximum penetration range within the apple-phantom. Dose energy deposition data and dose depth contours were created to provide a visual reference for the different treatments studied for the completion of this research.

4.1.2 GAFCHROMIC® HD-810 Film Contours

The energy deposition profiles and dose depth distributions around the apple-phantom periphery (0-360 degrees), in its vertical plane of symmetry, (i.e., divides the apple in half from top to bottom) are shown in Figure 4-3 to Figure 4-8 and Figure 4-9 to Figure 4-14 for the target doses of 50 Gy and 100 Gy, respectively. Similar results are shown in Appendix D (Figure D-1 thru Figure D-24)

Figure 4-3, shows the energy deposition profile at an orientation of 90 degrees away from the apple longitudinal axis results in a uniform irradiation on the left and right sides of the phantom. However, no irradiation resulted near the top and bottom region located between 70-90 degrees and 240 and 300 degrees as shown in the dose depth profile in Figure 4-4. The maximum penetration depth was approximately 4.57 mm from the surface at 180 degrees.

It can be seen that Figure 4-4 contains a high dose region between 210 and 240 degrees below a depth of 0.76 mm. At the same time, high doses were found between 100 and 240 degrees. These high doses resulted from the continuous irradiation of such particular points due to the geometrical orientation during the irradiation. At 90 degrees apple orientation, no irradiation was found at the top and bottom regions even though the phantom was irradiated from the top and bottom as explained previously in Section 4.1.1.

Also, the high doses present on the left and right bottom sides of the phantom resulted from a higher number of electrons being directed towards these ends due to a shift of the electron beam distribution as shown in Figures A-9 and A-10 Appendix A.

In addition, it was found that a higher energy deposition gradient existed from points at the left and right bottom sides (between 180 and 360 degrees) compared to the left and right top sides (between 0 and 180 degrees) which confirmed that a higher number of electrons struck the apple-phantom at the bottom due the mentioned shift in the electron beam distribution.

The left side of the energy deposition contour in Figure 4-3 shows the greatest penetration depths to that of the right. This behavior was consistent throughout all samples within this treatment (See Appendix Figure D-1 thru Figure D-4). This behavior was due to the swiveling motion of the polyethylene bag (together with its respective apple-phantom) as it hung from the turning hook and rotated around its vertical axis (Figure 3-16).

Only a very small fraction of the normal surface vectors will be parallel with the incident electrons resulting in a direct hit. Such points were expected to receive higher doses and greater penetration depths due to the absence of electron scattering events.

Nonetheless, it was found that due to the beam distribution, higher number of electrons struck the apple-phantom at the left and right bottom parts resulting in greater penetration depths despite of the higher occurrence of scattering events compared to the phantom top.

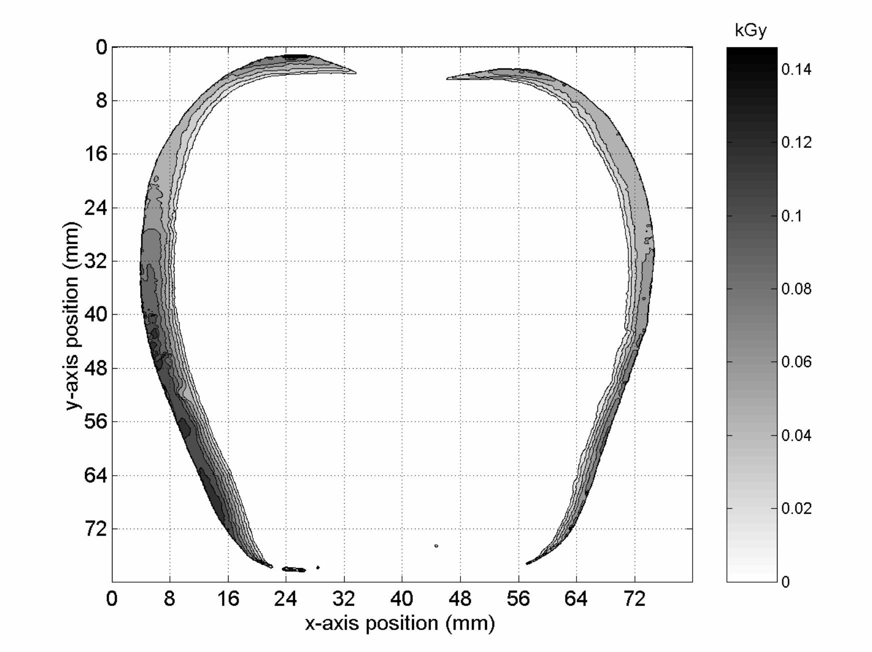

Figure 4-3. HD-810 film dose distribution in the apple-phantom irradiated at 50 Gy with the VDG and α = 90 degrees towards and against a 1.35 MeV plane source.

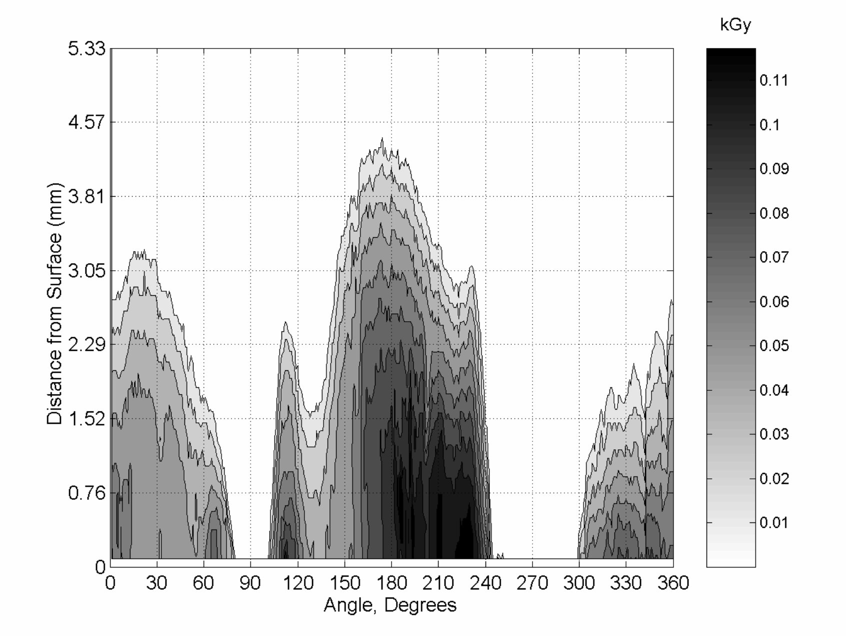

Figure 4-4. HD-810 film dose-depth distribution in the apple-phantom irradiated at 50 Gy with the VDG and α = 90 degrees towards and against a 1.35 MeV plane source.

Figure 4-5 shows that the dose deposition data was more uniform at α=45 degrees compared to α=90 degree orientation angle away from the apple's y-axis. Appendix D (Figure D-9 thru D-12) show similar results. It can be observed that the new orientation angle of 45 degrees produces a more uniform dose deposition in areas located at the top and bottom of the phantom. The bottom region (Figure 4-6) of the phantom, (270 degrees), however, did not show significant dose deposition, but wider regions (between 210 to 270 degrees and 300 to 330) were irradiated compared to those in Figure 4-3.

The penetration depth at α=45 degrees (Figure 4-6) showed more uniformity to that irradiated at α=90 degrees (Figure 4-4). Both orientations showed a maximum penetration depth of approximately 4.57 mm from the surface at different regions, but at the 45 degree orientation larger and more equal penetration depths resulted through the apple-phantom's periphery (Figure 4-5).

High dose regions were minimized compared to the α=90 degree orientation due to a more uniform irradiation. Such uniformity resulted in part due to the geometrical arrangement. In this case, the apple-phantom was oriented closer to the electron beam incident angle resulting in more exposed regions, particularly those in the proximity of 90 and 270 degrees (Figure 4-7).

Even though the results in Figure 4-6 shows high dose distributions at 250 and 300 degrees, the energy deposition gradient appeared more uniform to that at α=90 degrees and penetration depths were similar at both orientations.

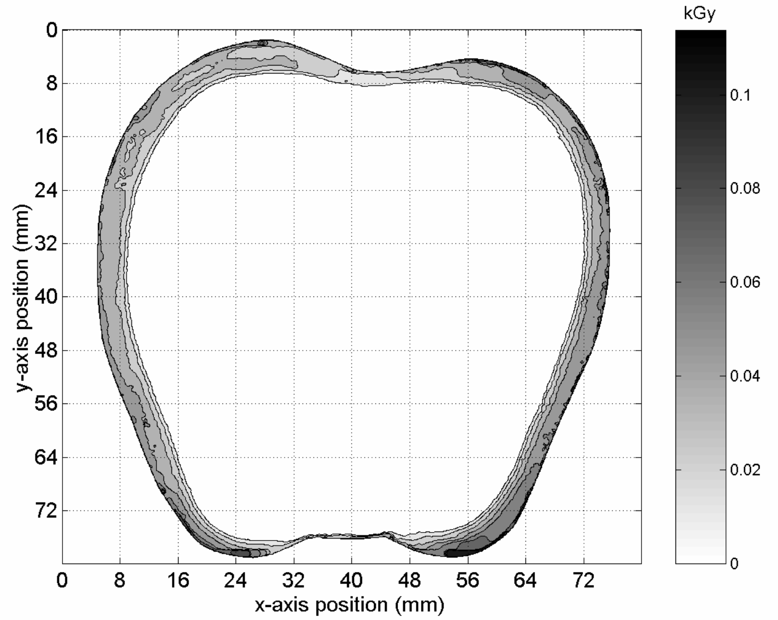

Figure 4-5. HD-810 film dose distribution in apple-phantom irradiated at 50 Gy with the VDG and α = 45 degrees towards and against a 1.35 MeV plane source.

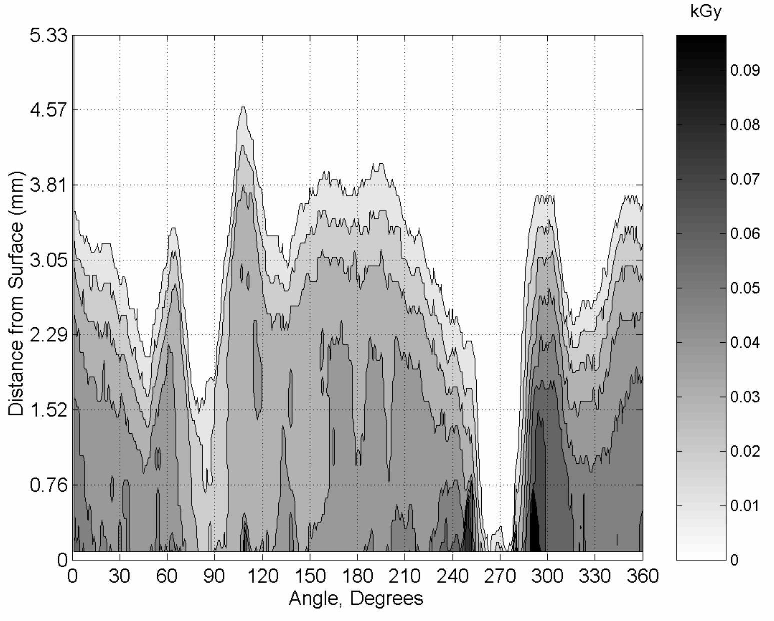

Figure 4-6. HD-810 film dose-depth distribution in the apple-phantom irradiated at 50 Gy with the VDG and α = 45 degrees towards and against a 1.35 MeV plane source.

The apple-phantom orientation parallel to the electron beam at α=22.5 degrees (Figure 4-7) showed very similar results to that of at α=45 degrees. In particular, the top regions at α=22.5 degrees appeared to be uniformly irradiated almost as fine as at α=45 degrees. Clearly, wider regions for α=22.5 degrees were irradiated at the bottom for both orientations compared to the 90 degrees array.

It was expected that the apple-phantom exposure at the same angle to that of the electron beam would result in the best irradiation orientation. In particular, the closer the apple-phantom is aligned to the beam direction wider areas of the apple are exposed. This covers the whole apple's surface. However, problem areas were still located at the top and bottom, where due to geometrical considerations several points were not irradiated at the particular dose of 50 Gy (Figure 4-7). Appendix D shows similar results for the same orientation (Figure D-1 thru Figure D-12).

Figure 4-6 shows that for α=22.5 degrees, the phantom absorbed the highest doses at the top left and right positions located at 60 and 120 degrees respectively. At these locations it is expected that the electron entrance angle be perpendicular to the phantom surface resulting in high dose regions. The largest penetration depths at these positions demonstrate that the electrons penetrated nearly perpendicular to the phantom surface.

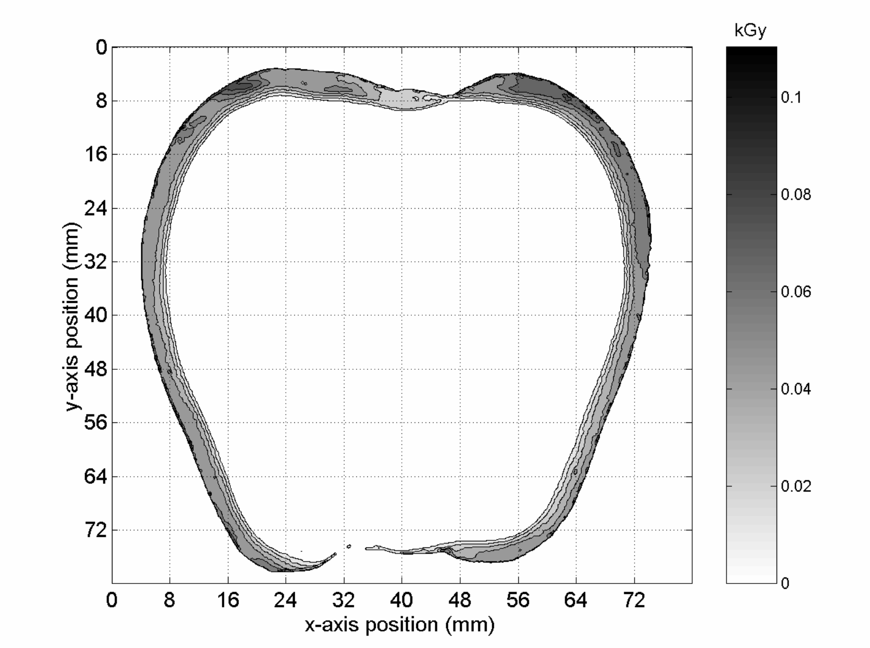

Figure 4-7. HD-810 film dose distribution in the apple-phantom irradiated at 50 Gy with the VDG and $\alpha = 22.5$ degrees towards and against a 1.35 MeV plane source.

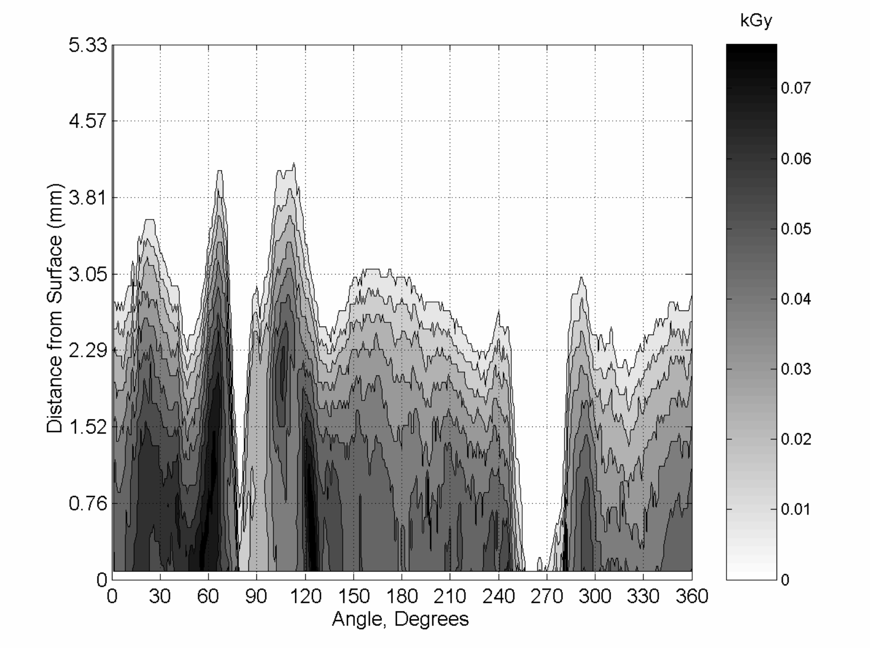

Figure 4-8. HD-810 film dose-depth distribution in the apple-phantom irradiated at 50 Gy with the VDG and $\alpha = 22.5$ degrees towards and against a 1.35 MeV plane source.

The influence of a higher dose in the energy deposition and penetration depth profiles, around the phantom periphery, was studied using the previous apple-phantom orientation with a 100 Gy dose. Appendix D (Figure D-13 thru Figure D-24) shows similar results for the same orientations. The results are discussed next.

Again, high dose values were characteristic at the left and right bottom sides of the apple-phantom as shown in Figure 4-8 between 150 to 240, and 300 to 360 degrees.

Figure 4-9 shows the dose distribution for an apple-phantom irradiated at an orientation of 90 degrees in front of the beam and 100 Gy. Clearly, the irradiation resulted in a more uniform coverage around the phantom periphery compared to that at 50 Gy (Figure 4-3). The electron penetration depth was also well distributed throughout the surface; however, the top and bottom of the phantom remained almost unexposed.

The maximum penetration depth (between 150 to 240 and 300 to 360 degrees) was approximately 4.6 mm from the surface as shown in Figure 4-10. These results show that the overall penetration depth improved in uniformity at the higher dose value compared to the lower one.

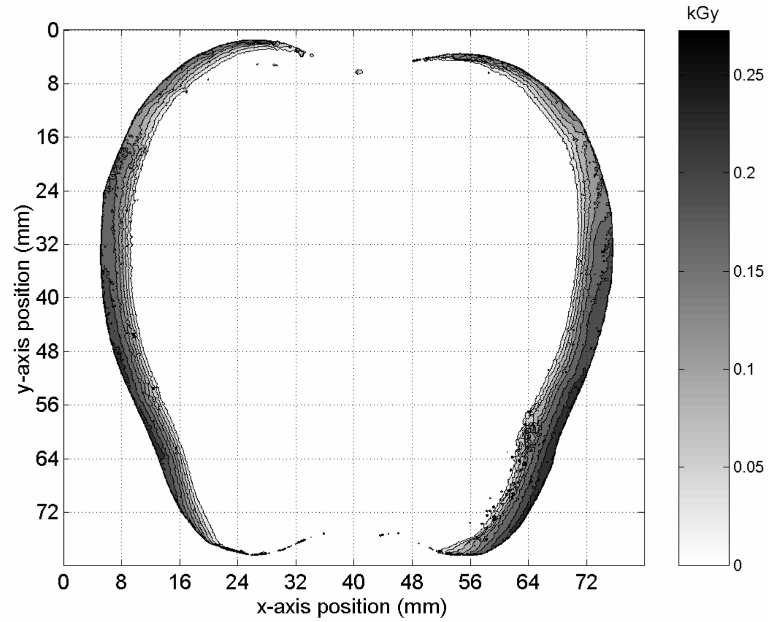

Figure 4-9. HD-810 film dose distribution in the apple-phantom irradiated at 100 Gy with the VDG and α = 90 degrees towards and against a 1.35 MeV plane source.

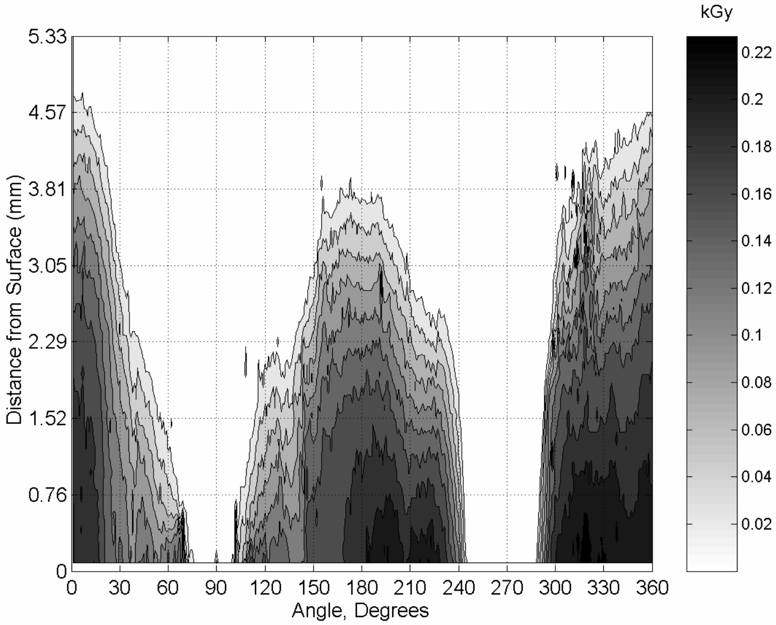

Figure 4-10. HD-810 film dose-depth distribution in the apple-phantom irradiated at 100 Gy with the VDG and α = 90 degrees towards and against a 1.35 MeV plane source.

As the top of apple-phantom was positioned closer to the electron beam plane at 100 Gy, the energy deposition data improved as shown in Figure 4-11 and Figure 4-13 irradiated at α= 45 and α= 22.5 degrees, respectively.

The dose deposition data shown in Figure 4-11 demonstrate that at α= 45 degrees there was complete radiation treatment throughout the phantom periphery (Figure 4-12). The unexposed regions that were found at the lower energies were completely covered using higher doses.

For instance, at the top of the phantom, Figure 4-12 shows that between 80 and 120 degrees the maximum penetration depth was at least 1.6 mm from the surface. At the bottom, between 250 and 300 degrees, the minimum penetration depth was 3.05 mm from the surface compared to less than 0.76 mm at 50 Gy (Figure 4-6).

Figure 4-12 also shows that the apple-phantom received high dose values at the top and bottom right and left corners located at approximately at 45, 135, 225, and 315 degree regions, respectively. At a penetration depth of 2.30 mm from the surface, the dose distribution became more uniform throughout the apple periphery.

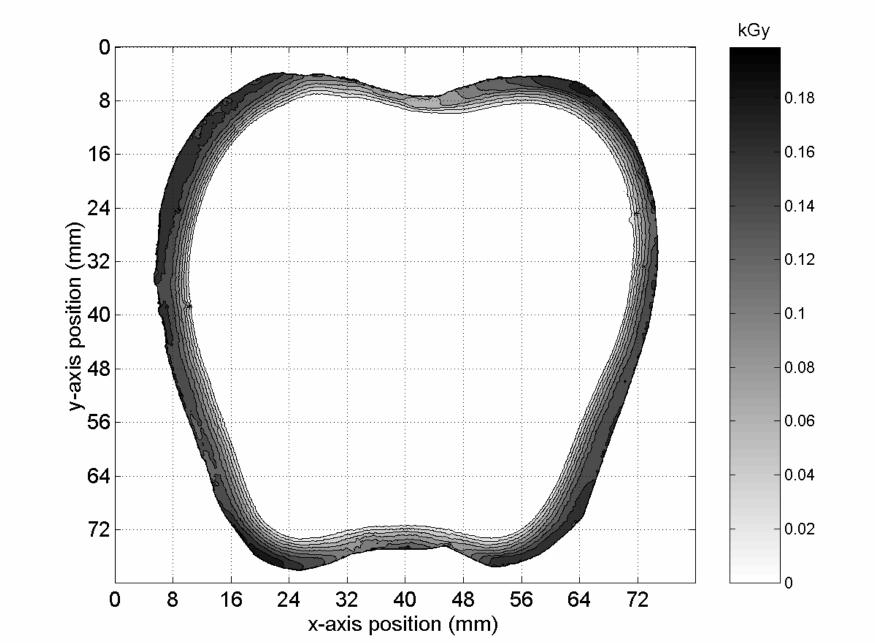

Figure 4-11. HD-810 film dose distribution in the apple-phantom irradiated at 100 Gy with the VDG and α = 45 degrees towards and against a 1.35 MeV plane source.

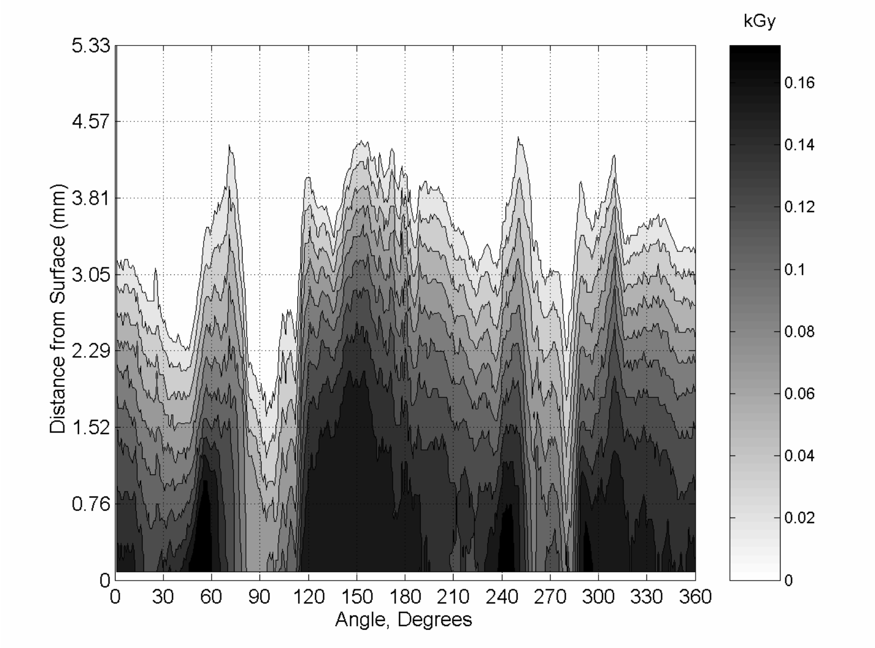

Figure 4-12. HD-810 film dose distribution in the apple-phantom irradiated at 100 Gy with the VDG and α = 45 degrees towards and against a 1.35 MeV plane source.

The final phantom irradiation produced at α=22.5 degrees and 100 Gy showed complete treatment of the apple periphery as the α= 45 degrees (Appendix D Figure D-37 thru Figure D-48). The dose distribution shown in Figure 4-13 and the dose depth distribution shown in Figure 4-14 show the deeper penetration depth (5.33 mm from the surface) compared to the other two treatments at α=45 and α=90 degrees. Nonetheless, it was also found that the apple-phantom absorbed higher doses at more spots within its surface compared to any other treatment.

For instance, the dark areas shown below the penetration depth of 1.52 mm from the surface in Figure 4-14, demonstrate higher doses were absorbed at this orientation. Notice also that the maximum penetration depths at 90 and 270 degree regions were at least above 3mm from the surface ensuring uniform irradiation treatment. The parallel orientation to the electron beam provided uniform irradiation throughout the sample, but it appeared to be overexposed to that at α=45 degrees.

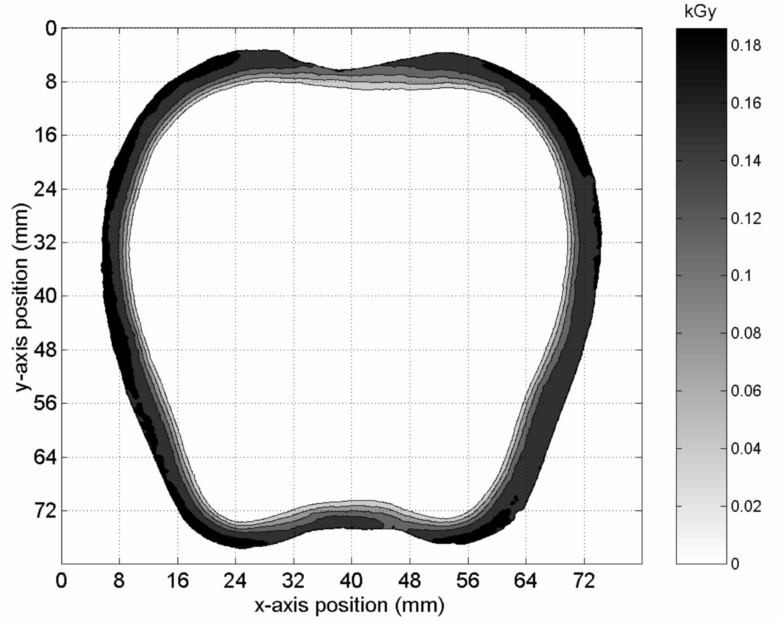

Figure 4-13. HD-810 film dose distribution in the apple-phantom irradiated at 100 Gy with the VDG and $\alpha = 22.5$ degrees towards and against a 1.35 MeV plane source.

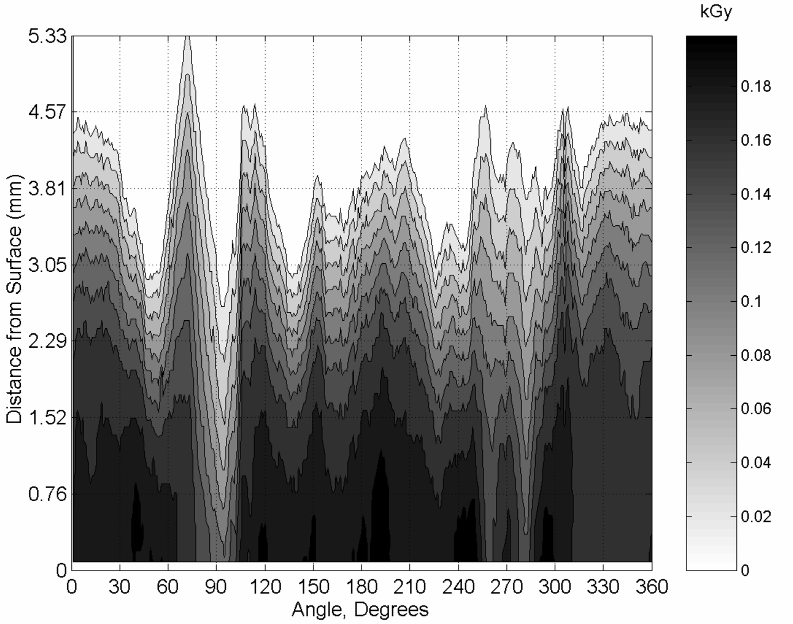

Figure 4-14. HD-810 film dose depth distribution in the apple-phantom irradiated at 100 Gy with the VDG and $\alpha = 22.5$ degrees towards and against a 1.35 MeV plane source.

The evaluation of food positioning strategies in front of the e-beam source demonstrated that tilting the apple-phantom towards the e-beam ensures uniform dose distributions of the entire surface of the phantom, even reaching the critical regions of the apple stem and calyx ends. This is important so the risk associated with bacterial contamination, linked to *Escherichia coli* O157:H7 that may be present in raw apples (CDC, 1996, 1997; Cody et al., 1999), may be reduced on the apple's surface by electron beam irradiation.

4.1.3 Apple-Phantom Contours

The energy deposition profiles and dose depth distributions around the apple-phantom periphery (0-360 degrees), in its vertical plane of symmetry were obtained for the methyl yellow apple-phantom contour slices of 3.175 mm thickness for an absorbed energy of 50 and 100 Gy.

Figure 4-15 and Figure 4-16 show the irradiation treatment energy deposition profile and the dose depth distribution performed at a 90 degree phantom orientation and an absorbed energy of 50 Gy. Similar results are shown in Appendix D (Figure D-25 to Figure D-36).

The dose depth profile shows that the methyl yellow apple-phantom contours did not have a linear response to the dose vs. penetration depth. This behavior can be seen in the energy deposition contour graph that shows higher doses were located between 0 to 45 degrees and 135 to 180 degrees (Figure 4-16) around the phantom periphery, and from the phantom calibration curve shown in Figure 3-10. Unexposed areas were found between 80 to 100 degrees (top) and 240 to 300 degrees (bottom) for the α=90 degree orientation.

The energy deposition was improved with the apple-phantoms exposed at an α=45 degree orientation towards the source (Figure 4-17). The dose depth presented in Figure 4-17 shows an improvement for the unexposed areas (top and bottom) shown in Figure 4-15 at α=90 degrees.

Figure 4-18 shows a more uniform dose distribution compared to Figure 4-16 where high dose regions were present on the left and right sides of the phantom surface. The penetration depth decreased at an orientation of α=45 degrees, but it was more uniform to that of α=90 degree orientation in the regions where the phantom shows treatment.

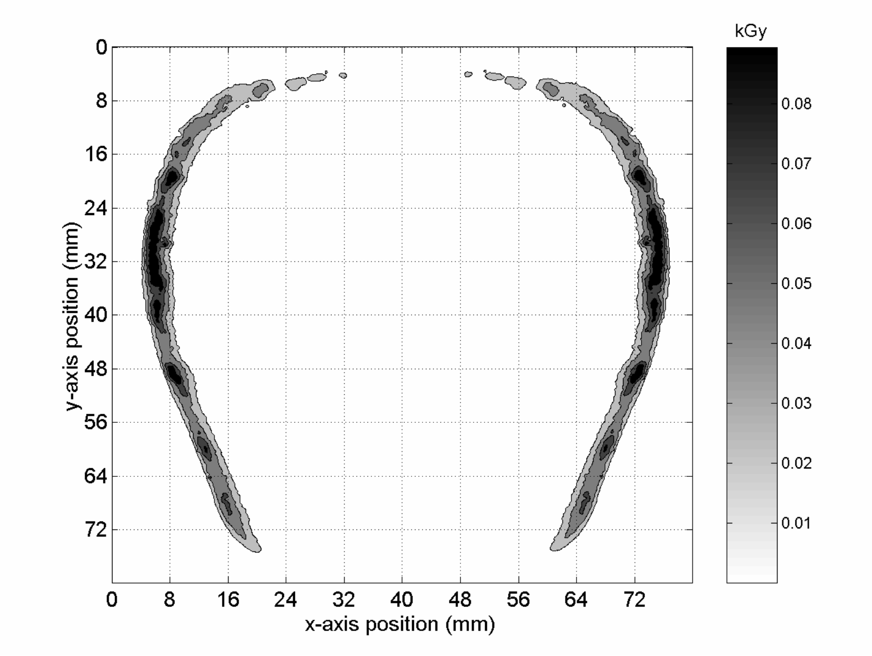

Figure 4-15. Methyl yellow apple contour dose distribution in the apple-phantom irradiated at 50 Gy with the VDG and α = 90 degrees towards and against a 1.35 MeV plane source.

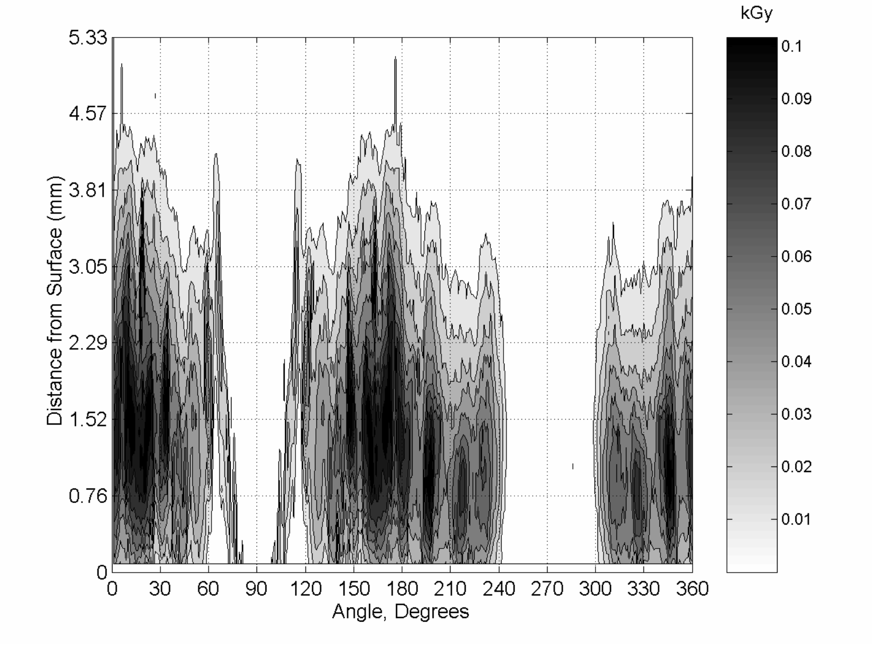

Figure 4-16. Methyl yellow apple contour dose depth distribution in the apple-phantom irradiated at 50 Gy with the VDG and α = 90 degrees towards and against a 1.35 MeV plane source.

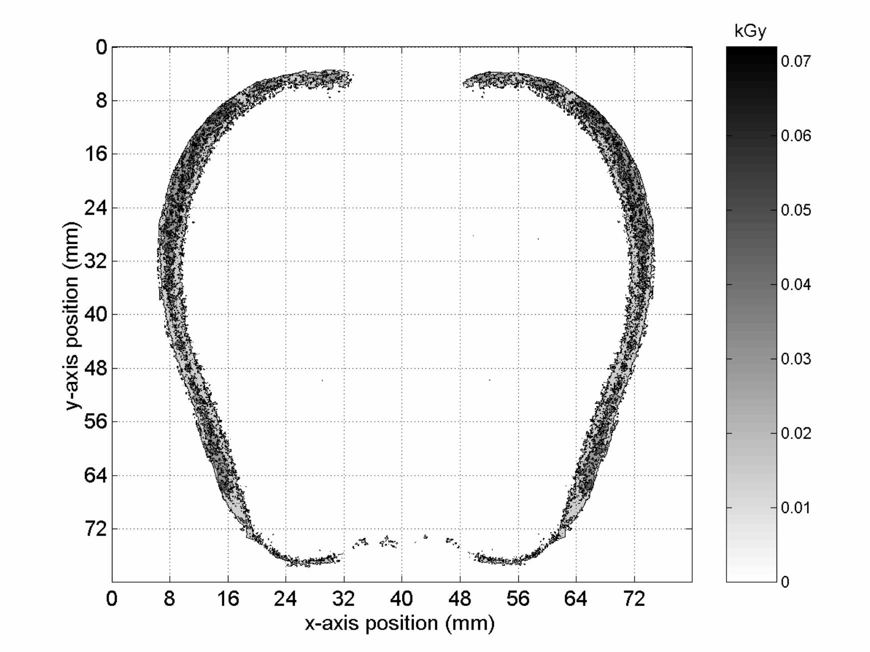

Figure 4-17. Methyl yellow apple contour dose distribution in the apple-phantom irradiated at 50 Gy with the VDG and $\alpha = 45$ degrees towards and against a 1.35 MeV plane source.

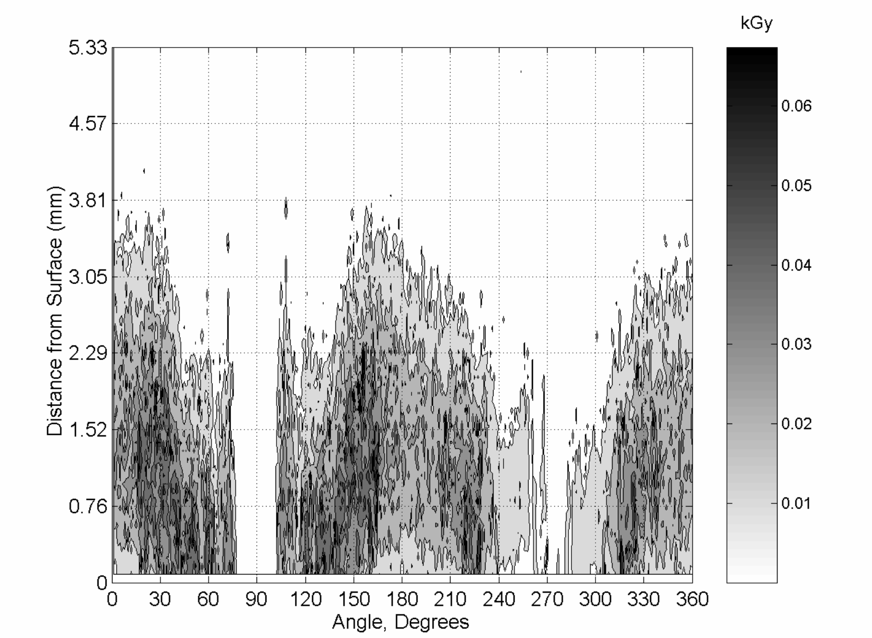

Figure 4-18. Methyl yellow apple contour dose depth distribution in the apple-phantom irradiated at 50 Gy with the VDG and $\alpha = 45$ degrees towards and against a 1.35 MeV plane source.

At an orientation of 22.5 degrees towards the e-beam source (Figure 4-19), the apple-phantom showed little improvement at the bottom and top regions. The regions located between 225 to 250 degrees (bottom left side) and 290 to 315 degrees (bottom right side) showed improvement to the treatment performed at 45 degrees with regard to penetration depth and higher absorbed dose (Figure 4-20). However, both irradiations did not show significant dose deposition between 90 and 270 degrees in spite of their orientation at 50 Gy (Figure 4-20).

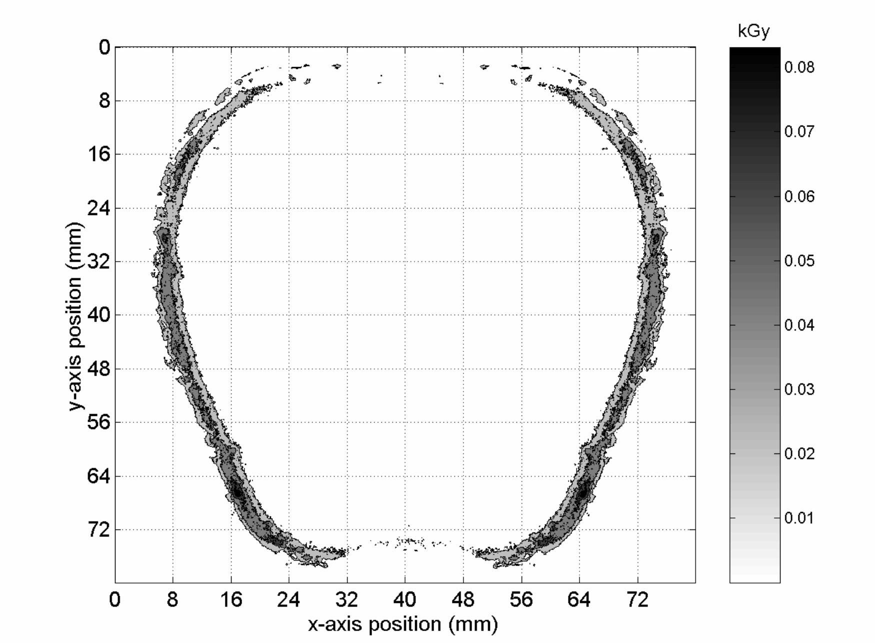

Figure 4-19. Methyl yellow apple contour dose distribution in the apple-phantom irradiated at 50 Gy with the VDG and α = 22.5 degrees towards and against a 1.35 MeV plane source.

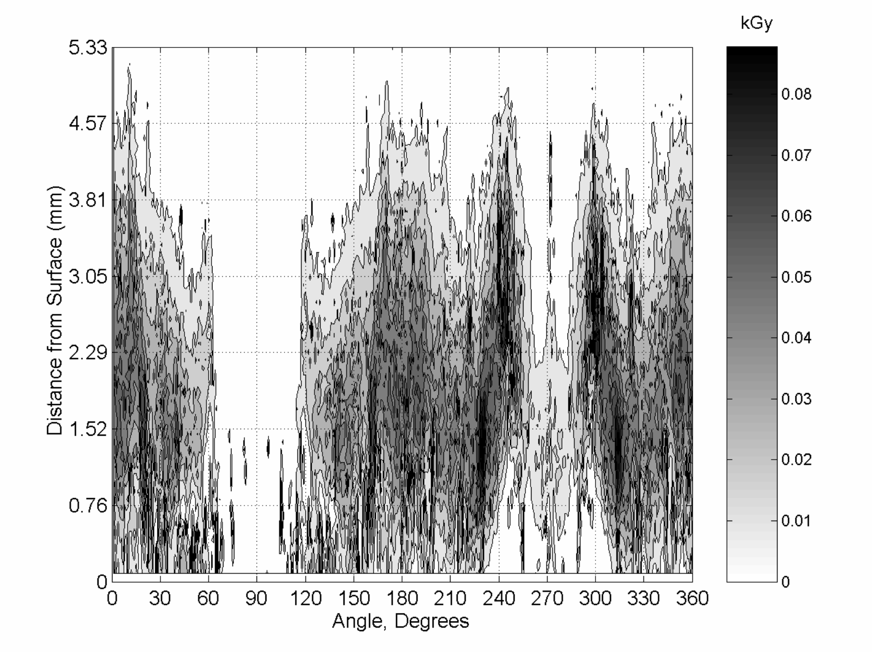

Figure 4-20. Methyl yellow apple contour dose depth distribution in the apple-phantom irradiated at 50 Gy with the VDG and α = 22.5 degrees towards and against a 1.35 MeV plane source.

The influence of a higher dose in the dose deposition, and penetration depth profiles around the phantom periphery were studied also at 100 Gy. The results are discussed next. Similar results are shown in Appendix D (Figure D-37 to Figure D-48)

Figure 4-21 shows no irradiation treatment at the top and bottom regions of the phantom located between 60 to 120 and 250 to 300 degrees, respectively.

Figure 4-22 shows the depth dose distribution for the apple-phantom irradiated at α=90 degree orientation. Most of the radiation treatment can be observed in the left and right sides, but no irradiation was detected at the top and bottom regions, between 60 to 110 degrees and 240 to 310 degrees (Figure 4-22). The highest dose regions were located approximately at 15 and 165 degrees with both occurring at a penetration depth of 1.65 mm from the surface (Figure 4-22).

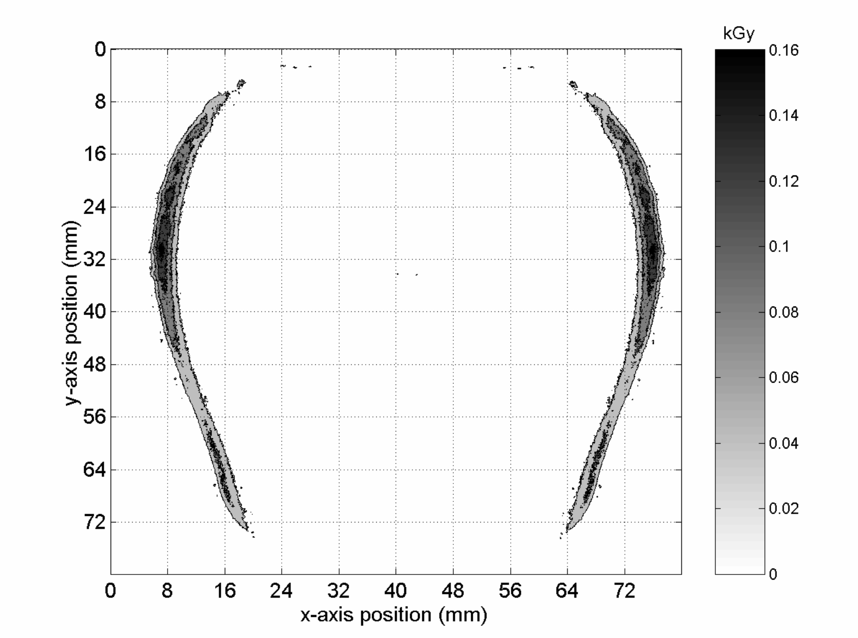

Figure 4-21. Methyl yellow apple contour dose distribution in the apple-phantom irradiated at 100 Gy with the VDG and $\alpha = 90$ degrees towards and against a 1.35 MeV plane source.

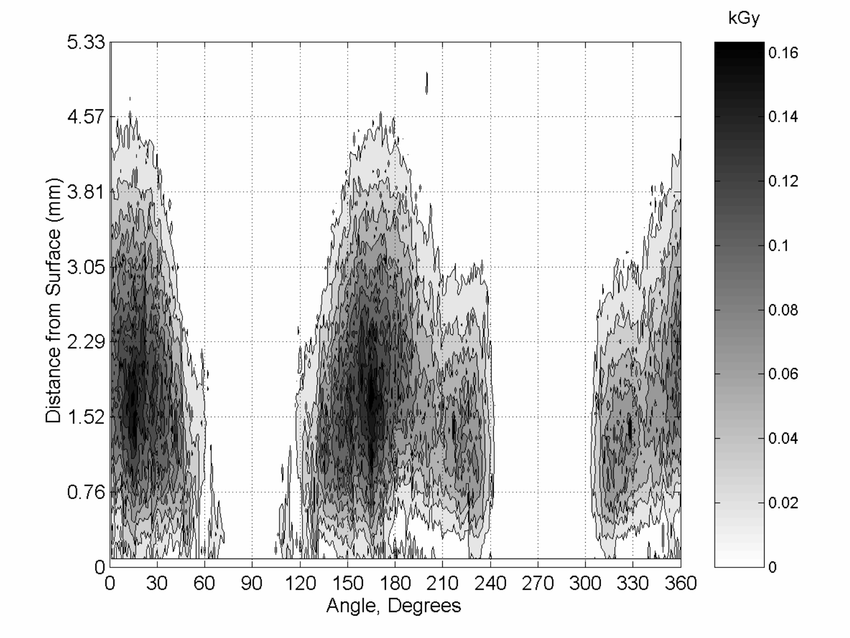

Figure 4-22. Methyl yellow apple contour dose depth distribution in the apple-phantom irradiated at 100 Gy with the VDG and α = 90 degrees towards and against a 1.35 MeV plane source.

Samples irradiated at α=45 degree orientation towards the e-beam (Figure 4-23 and Figure 4-24) showed a better irradiation treatment to those at α=90 degree orientation (Figure 4-21 and Figure 4-22). The penetration depth decreased around the phantom surface; however, the dose distribution profile shows more uniformity based on the dose contour lines. The apple-phantom bottom region between 240 and 300 degrees, (Figure 4-24) at a α=45 degree orientation showed improved results to the radiation exposure at α=90 degree orientation.

At a 45 degree orientation, (Figure 4-23), high dose values were located between 120 and 180 degrees (left side) at penetration depths of 1.52 and 0.76 mm from the surface (Figure 4-24). Also, the bottom right side (~ 300 degrees) showed higher dose values compared to the ninety degree orientation.

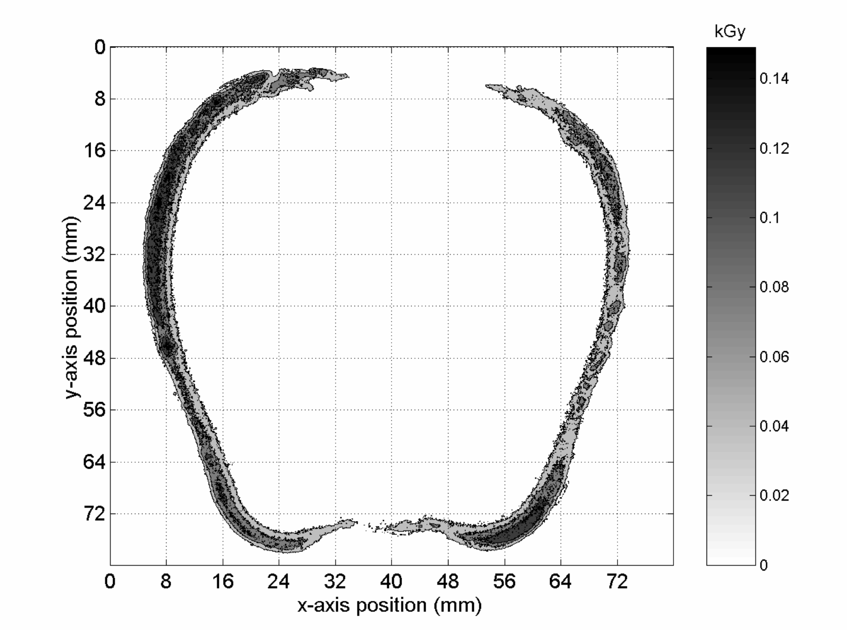

Figure 4-23. Methyl yellow apple contour dose distribution in the apple-phantom irradiated at 100 Gy with the VDG and α = 45 degrees towards and against a 1.35 MeV plane source.

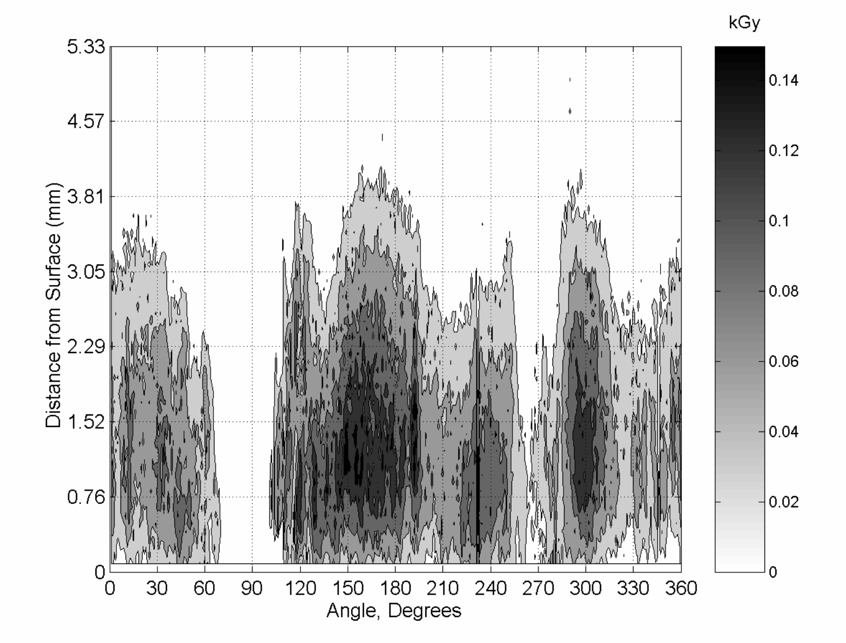

Figure 4-24. Methyl yellow apple contour dose depth distribution in the apple-phantom irradiated at 100 Gy with the VDG and α = 45 degrees towards and against a 1.35 MeV plane source.

The irradiation performed at 22.5 degrees towards the e-beam showed the best results (Figure 4-25). It was observed that the phantom bottom region shows absorbed radiation between 240 and 330 degrees with a minimum penetration depth of 2.3 mm from the surface (Figure 4-26). The highest dose regions lie within 1 mm and 3 mm depth from the surface throughout the phantom periphery. At this orientation, there was a definite improvement at all regions located below 0.76 mm from the surface. The dose distribution (Figure 4-26) showed minor breaks were no radiation was observed compared to the α=90 and α=45 degree orientations.

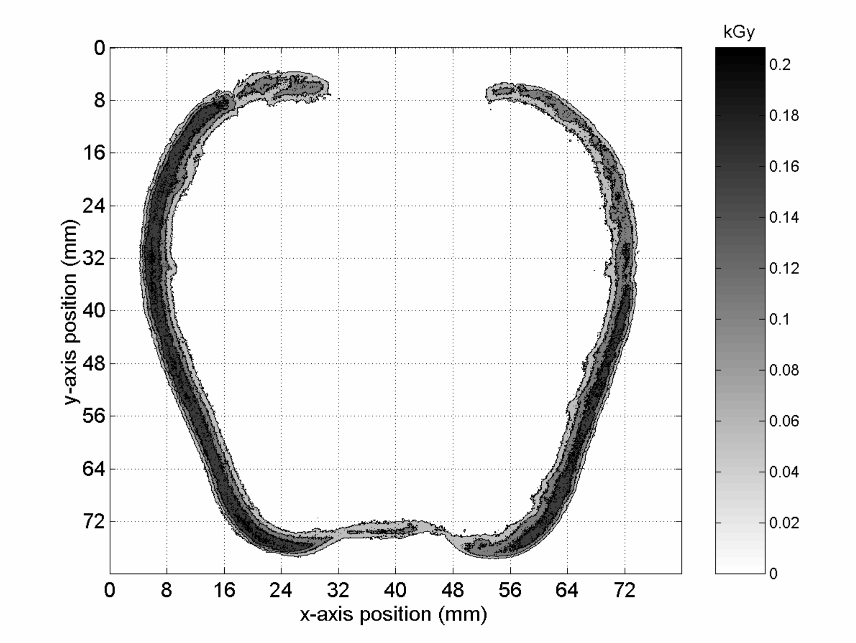

Figure 4-25. Methyl yellow apple contour dose distribution in the apple-phantom irradiated at 100 Gy with the VDG and α = 22.5 degrees towards and against a 1.35 MeV plane source.

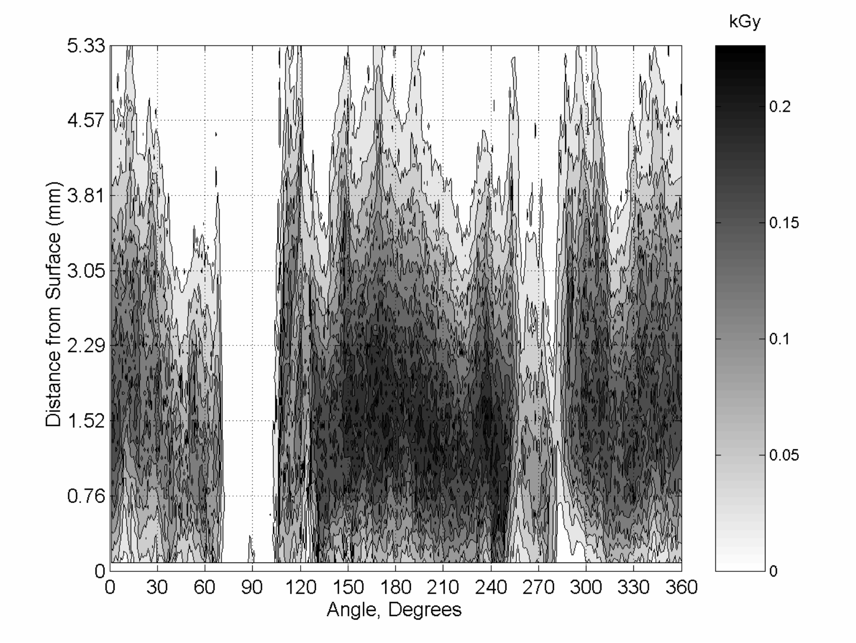

Figure 4-26. Methyl yellow apple contour dose distribution in the apple-phantom irradiated at 100 Gy with the VDG and α = 22.5 degrees towards and against a 1.35 MeV plane source.

4.1.4 Dose Uniformity Ratio Description for E-Beam Irradiation with the VDG

The dose uniformity ratio, D_{max}/D_{min}, defined as the maximum dose, D_{max}, to the minimum dose, D_{min}, at a penetration depth from the surface along the phantom periphery was obtained for both GAFCHROMIC® HD-810 film and methyl yellow apple-phantom contours.

Figure 4-27 shows the dose uniformity ratio for the radiochromic film irradiated at 50 Gy for the different orientation angles. The 22.5 and 45 degrees apple-phantom orientations towards the electron beam provided a better irradiation compared to that at 90 degrees. It can be seen also that the samples irradiated at 22.5 and 45 degrees at a penetration depth of approximately 2.0 mm, become more uniform compared to that of 90 degrees. Figure 4-5 and Figure 4-7 confirmed this behavior as the dose contour lines show to be more uniform with increasing penetration depths.

The higher dose uniformity ratios found at the 90 degree orientation appeared to be at least twice that at 22.5 degrees. Figure 4-4 showed that between the 180 and 240 degree regions higher doses resulted at the bottom left and right sides of the apple while small doses were obtained at the 90 and 270 positions. The 90 degree orientation towards the beam line showed higher D_{max}/D_{min} values due to the small amounts of dose at the top and bottom that increased the ratio significantly compared to the other two orientations.

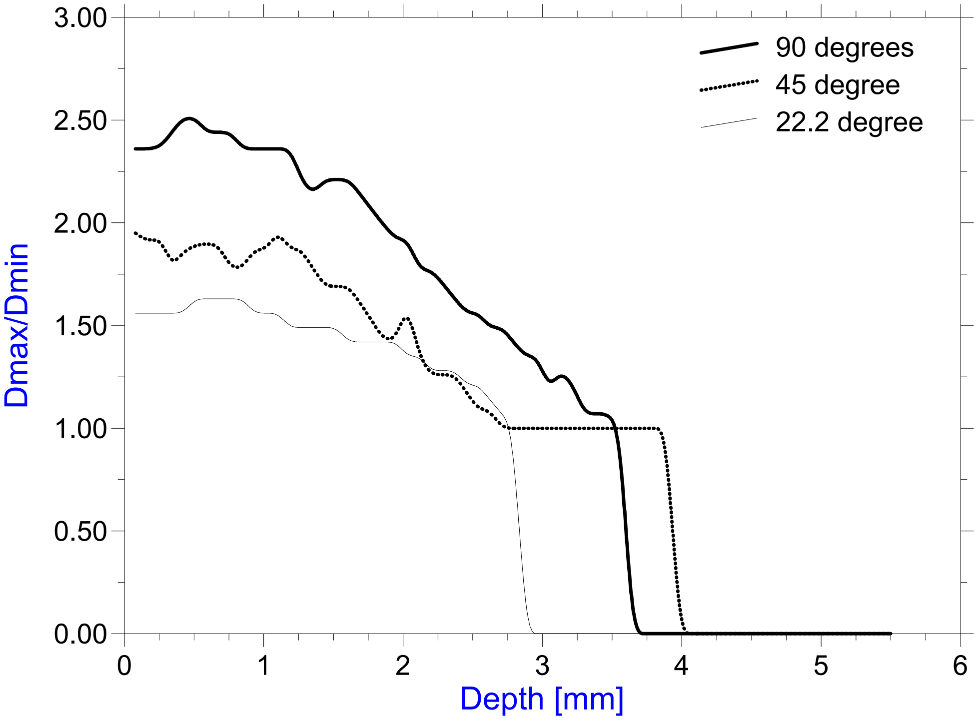

Figure 4-27. HD-810 film dose uniformity ratio in the apple-phantom irradiated at 50 Gy with the VDG and α = 90, 45, and 22.5 degrees towards and against a 1.35 MeV plane source.

Figure 4-28 shows the dose uniformity ratios for the radiochromic film irradiated at 100 Gy. The 45 degree orientation produced a more uniform irradiation treatment compared to the other two. The ratio at 45 degrees was found to be the most uniform as penetration depth increased. The dose uniformity ratio became more constant with increasing penetration depths at 45 and 22.5. Figure 4-14 shows that higher doses resulted in the periphery of the phantom due to the direct alignment with the electron beam. This orientation resulted in more electrons striking the phantom's periphery with less scattering thus over exposing the phantom compared to the 45 degrees orientation.

From Figure 4-27 and Figure 4-28 it can be seen that for both energies, the 90 degree orientation resulted in the least effective irradiation treatment. However, the 22.5 degree orientation was the best irradiation treatment at 50 Gy, while the 45 degree orientation was better at 100 Gy. Also, the uniformity ratios decrease with increasing penetration depth showing that D_{max} values also decrease with increasing penetration depths.

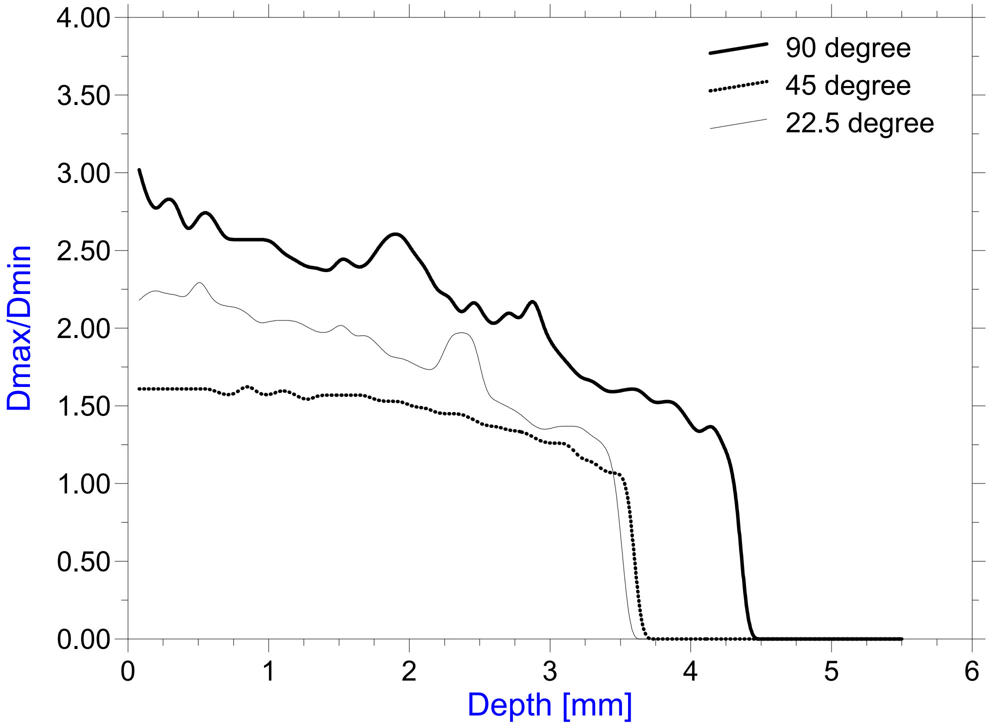

Figure 4-28. HD-810 film dose uniformity ratio in the apple-phantom irradiated at 100 Gy with the VDG and α = 90, 45, and 22.5 degrees towards and against a 1.35 MeV plane source.

Figure 4-29 and Figure 4-30 shows the dose uniformity ratio for the methyl yellow apple-phantom contour of 3.175 mm thickness and for 50 Gy and 100 Gy, respectively. For all phantom orientations towards the beam, the D_{max}/D_{min}, ratio increases up to a maximum value and then decreases until a minimum point showing that the electrons have lost all of their energy. Specifically, the apple-phantom contour slices follow a non-linear trend regarding dose uniformity ratio vs. penetration depth. The uniformity ratio was found to be the highest for the 90 degree orientation followed by the 22.5 degrees, and finally the 45 degrees. To analyze the non-linear behavior of the methyl yellow apple-phantom contour slices, an assumption was made. The GAFCHROMIC® HD-810 film dose distribution data used to calculate the dose uniformity ratios (Figure 4-27 and Figure 4-28) was used as the absolute reference to compare the methyl yellow dose uniformity ratios. The assumption of the results is described next.

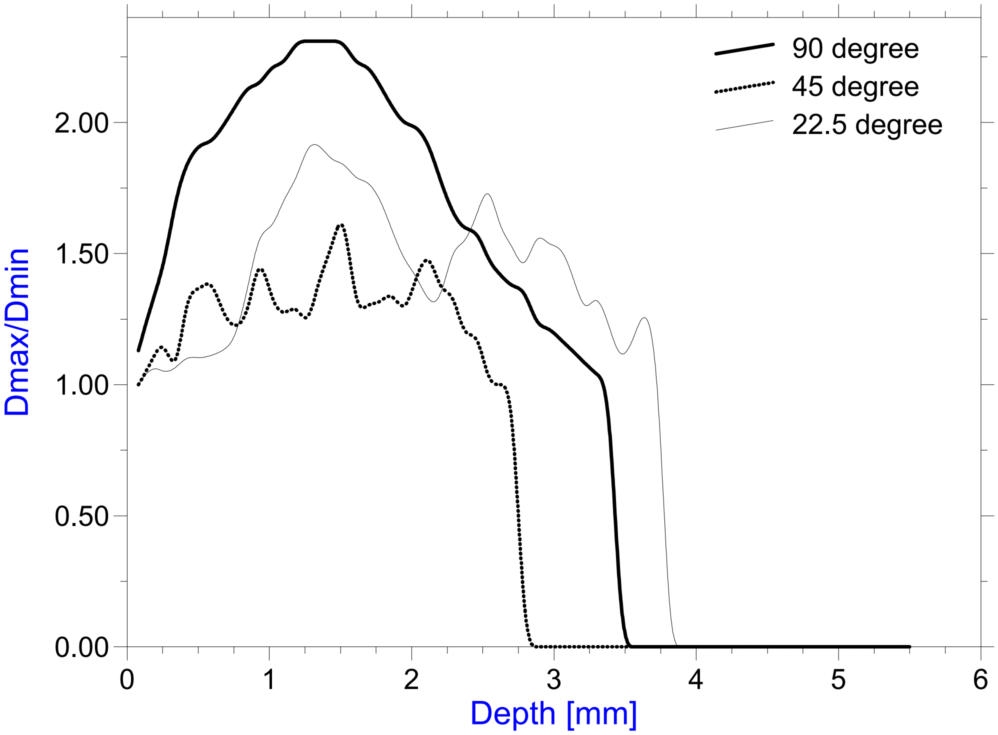

Figure 4-29. Methyl yellow apple-phantom dose uniformity ratio irradiated at 50 Gy with the VDG and α = 90, 45, and 22.5 degrees towards and against a 1.35 MeV plane source.

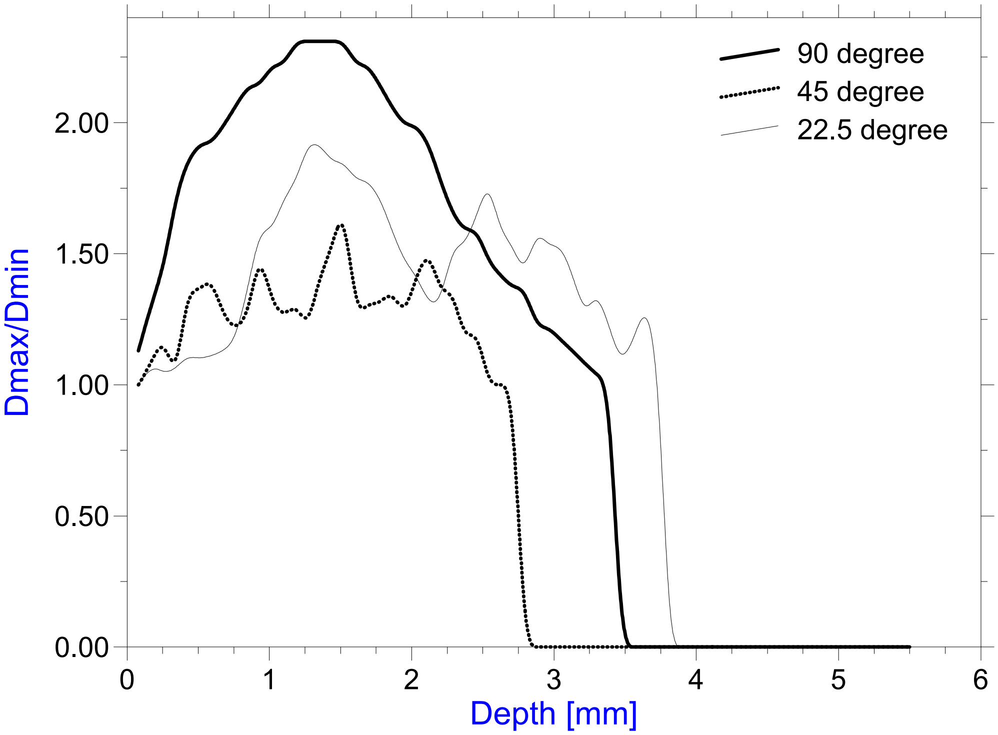

Figure 4-30. Methyl yellow apple-phantom dose uniformity ratio irradiated at 100 Gy with the VDG and α = 90, 45, and 22.5 degrees towards and against a 1.35 MeV plane source.

4.1.5 Comparison Dose Uniformity Ratio Film vs. Apple-Phantoms

This section describes the non-linear response of the dose uniformity ratio in the methyl yellow phantom contour slices versus the HD-810 film used as the reference standard. Figure 4-31 shows the experimental tendencies found by both the methyl yellow apple-phantom slices and the radiochromic film for the different angle arrangements and dose values.

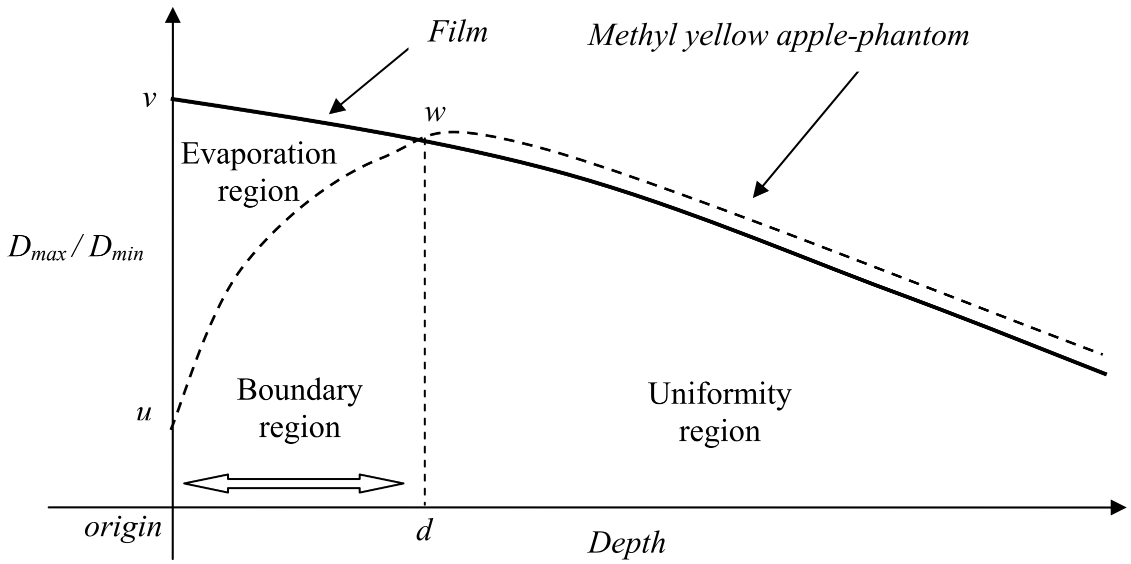

Figure 4-31. HD-810 film contour response vs. methyl yellow apple-phantom contours.

Figure 4-31 shows that the HD-810 film dose uniformity ratio decreases from point, *v*, with increasing penetration depths. The methyl yellow apple-phantom ratio increases initially from point, *u*, up to a maximum point, *w*, where both curves show a decreasing tendency for increasing penetration depths. The non-linear response of the methyl yellow phantom can be explained in terms of (1) chloroform evaporation, and (2) chloroform migration.

Right before the irradiation treatment, each sample (apple-phantom), was cut in half as described in Section 3.2.4 and vacuum packaged in a polyethylene plastic bag. After the exposure to the e-beam was completed, the apple-phantom was stored in an area with no light for 24 hours and then cut in 3.175 mm thick slices. These procedures were used for all samples to achieve consistency and to stabilize any chemical reactions resulting from the irradiations within the phantom.

After the irradiation treatment was completed, and the phantoms were removed from their packages, it was observed that the chloroform migrated to the surfaces of the phantoms and the polyethylene bag, due to the vacuum procedure. Excess chloroform was then carefully cleaned from the phantoms surface using lint-free wipes. After 24 hours later, the samples were cut into a 3.175 mm thick contour slice to be used in the scanning process (Section 3.6.2).

The chloroform started to evaporate from the sample immediately after it was originally cut in half (Figure 3-13). Then, when the right halve was cut into a 3.175 mm thick slice, the outer face of the slice experienced evaporation for a period of 24 hours. Most of the evaporation occurred in the outer and inner faces of the apple-phantom slice; however, all samples followed the same procedure for consistency.

Figure 4-32 shows a 3-D model of an apple-phantom slice with chloroform evaporating from all directions; most of the evaporation may have occurred within the outer surface that was exposed to air for 24 hours before the slice was cut.

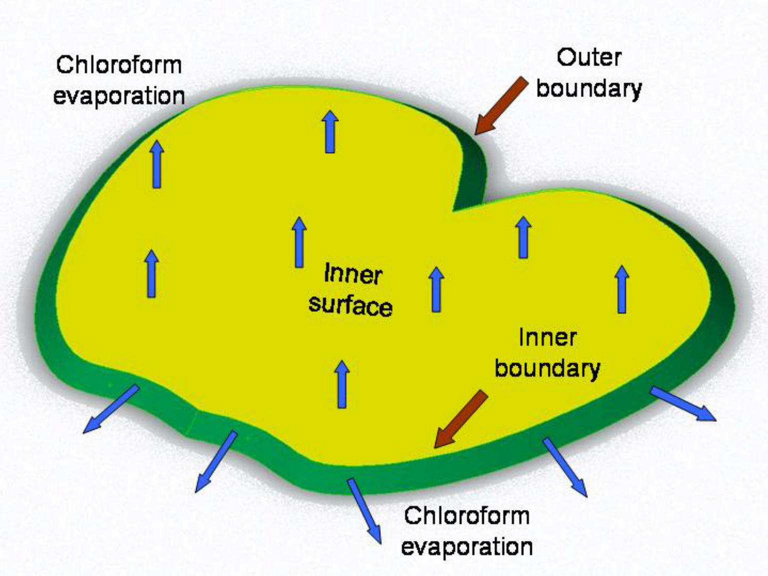

Figure 4-32. Chloroform evaporation in an apple-phantom slice.

Because the inner surface had not been exposed to air as the outer surface, all phantom contours were placed in the transmission scanner with the inner surface oriented to the top so that the scanner measured the intensity of the light transmitted from the inner surface to the outer surface of the samples as shown in Figure 4-33.

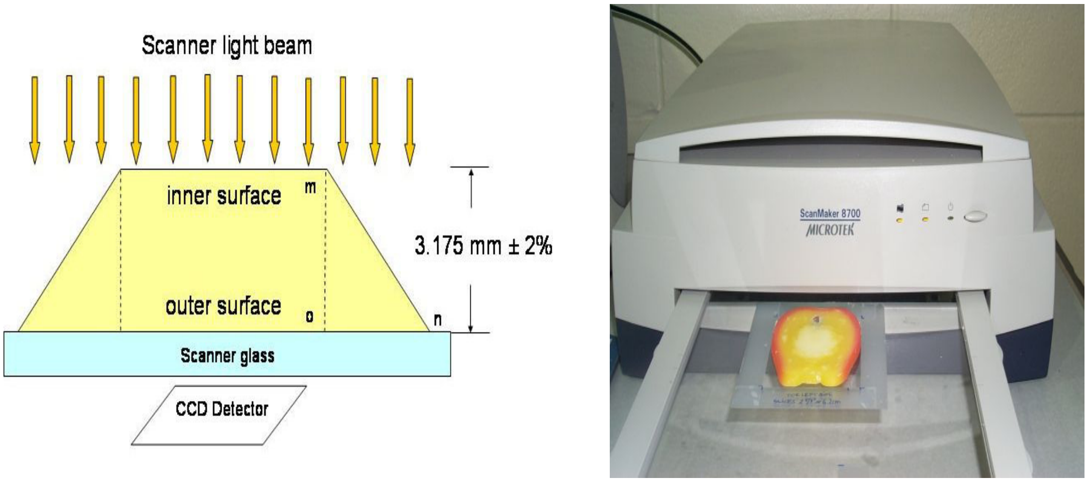

Figure 4-33. Methyl yellow apple-phantom arrangement for transmission scanning (left). Apple-phantom in transmission bed showing inner surface (right).

For illustration purposes, the angle between the scanner glass and the outer surface of the apple-phantom was exaggerated to show the variation in thickness across the inner and outer boundary edges (Figure 4-33 left). The apple-phantom contour shown on the right side of Figure 4-33 shows the actual positioning arrangement used prior to the scanning process. The apple-phantom is oriented with its inner surface to the top and its outer surface touching the transmission scanner glass.

Dose distribution data was indirectly related to the intensity measurement from the scanning signal under the assumption of a fixed thickness. It can be seen that such condition was not true in the region delineated by the points *m, o, n*.(Figure 4-33 left) The distance from point *o* to *n* was too small to be measured. As a result, the image processing analysis was performed on the edge of the phantom contour as described in Section 3.9.

Because the evaporation occurred faster at points located near the surface, it can be observed from Figure 4-31 that the phantom contour ratio starts at a point *u*, and the film at point *v*. However, the difference starts decreasing until point*,* *w*, where both curves meet at a specific penetration depth, *d*, defined as the *boundary region*. The region passed point *d* was defined as the *uniformity region* where both curves followed the same tendency. This behavior explains that evaporation had an effect in the phantom contour edges where the thickness was not completely uniform.

Using all the considerations assumed above and the image processing techniques described in Section 3.9, it was possible to establish the dose uniformity ratios as shown in Figure 4-34 to Figure 4-36.

Figure 4-34 shows the uniformity ratio response at 100 Gy and 90 degrees samples orientation away from the electron beam source. The methyl yellow contours respond closely to the radiochromic film after a penetration depth of 1.5 mm from the surface. As the penetration depth increases it can be seen that the difference in uniformity ratios decreases until both curves intersect each and the difference is almost zero.

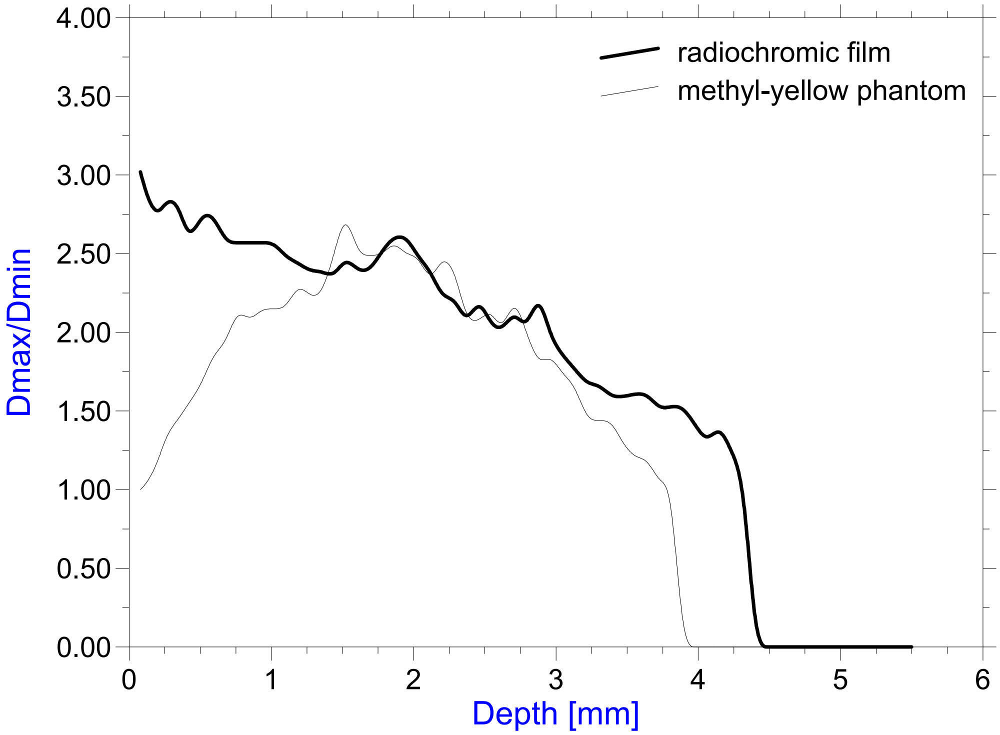

Figure 4-34. HD-810 film vs. apple-phantom contours dose uniformity ratio irradiated at 100 Gy with the VDG and α = 90 degrees towards and against a 1.35 MeV plane source.

Figure 4-35 and Figure 4-36 show the uniformity ratio at α=45 and α=22.5 degrees orientation. The boundary regions for the 45 and 22.5 degree orientations were approximately 0.5 mm and 0.7 mm respectively. The methyl yellow showed the highest ratio for the 90 degree orientation showing that at this configuration the apple-phantom is overexposed compared to those at 45 and 22.5 degree orientations.

The best response was found for the 45 degree orientation where the ratio was the lowest compared to that at 22.5 degree arrangement. Figure 4-35 shows the response for this angle, and also shows the uniformity of the irradiation based on the radiochromic film results.

Figure 4-36, shows that the parallel orientation to the beam at 22.5 degrees shows also a satisfactory result even though the ratio is somewhat higher to that at 45 degrees but less than that at 90 degree. At the 22.5 degree orientation, the uniformity ratio is a little higher because the electron entrance angle is normal to the surface vectors associated with this orientation thus reducing scattering and improving penetration depths.

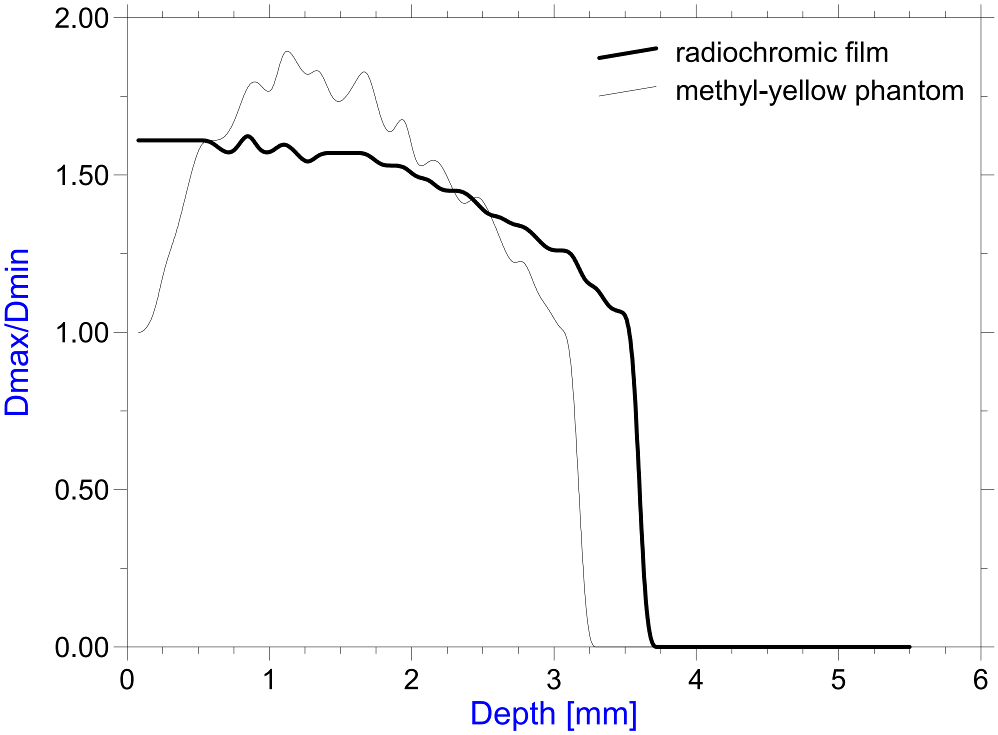

Figure 4-35. HD-810 film vs. apple-phantom contours dose uniformity ratio irradiated at 100 Gy with the VDG and α = 45 degrees towards and against a 1.35 MeV plane source.

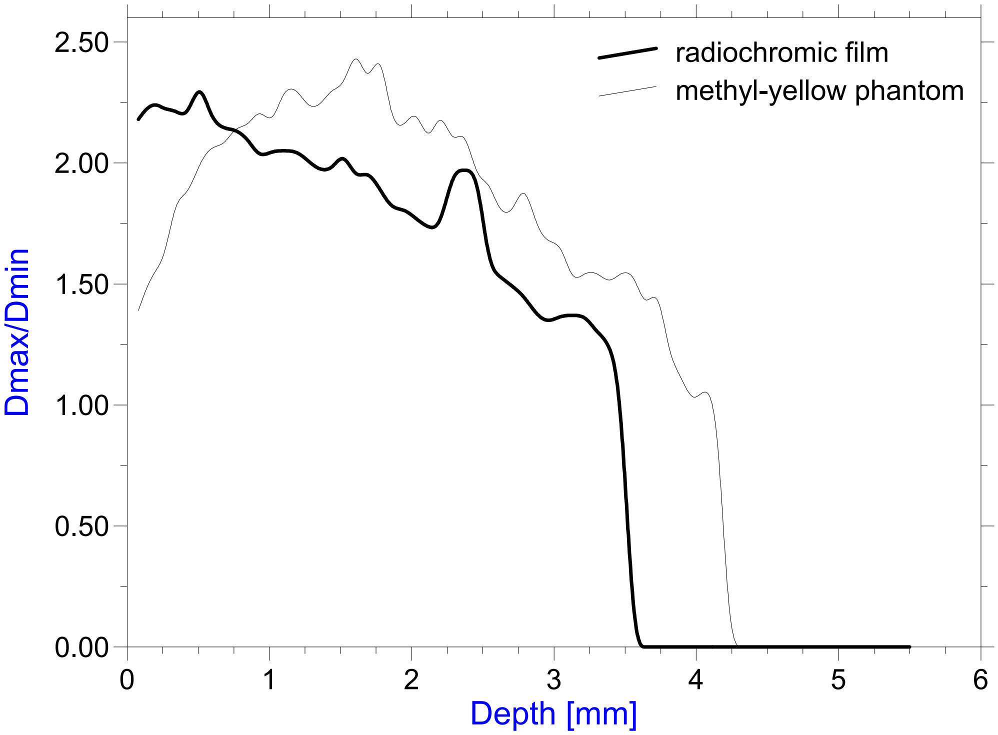

Figure 4-36. HD-810 film vs. apple-phantom contours dose uniformity ratio irradiated at 100 Gy with the VDG and α = 22.5 degrees towards and against a 1.35 MeV plane source.

From Figure 4-25 and Figure 4-26 it can be observed clearly that the 22.5 degree orientation produced higher penetration depths throughout the phantom periphery. Figure 4-13 shows that the deposition data produced with the film contour resembles nicely to the methyl yellow contour shown in Figure 4-25. As a result of chloroform evaporation during the casting method, it was not possible to successfully trace absorbed dose values in the top regions of the methyl yellow apple contours.

Improvements in the casting technique can yield better results. For instance, new phantom molds (Figure 3-12) can be created by placing the pouring hole in a different area that results less critical for the phantom contour analysis.

In general, the methyl yellow phantom contours have shown to detect radiation between 0 and 500 Gy as shown in Figure 3-22. The apple-phantom's main advantage over the HD-810 film consists in its ability to visually show the absorbed dose in any direction. In this study, the apple-phantoms contours were analyzed only in the apple symmetrical plane (top to bottom). The next section shows the potential for the methyl yellow apple-phantoms to produce 3-D reconstructions from intensity data.

4.1.6 Illustration of the Apple-Phantom in 3-D Using Intensity Raw Data

The results presented throughout Sections 4.1.1 to 4.1.5 were obtained in the symmetry plane that divided the apple-phantom in two equal parts as shown in Figure 3-13. This section shows the capability of the methyl yellow apple-phantom to produce three dimensional representations in virtually any plane in any direction. However, for ease of representation standard x, y, and z axis were used. Intensity data of an apple-phantom irradiated at α=45 degrees orientation and 100 Gy absorbed dose with the Van de Graaff accelerator was generated by slicing the phantom left and right sides. A total number of 16 slices, each with 3.175 mm thickness were produced.

Three dimensional representations were produced using the individual data for each phantom slice as shown in Figure 4-37 to Figure 4-40. Figure 4-37 shows the apple-phantom in three dimensions with its left and right sides (located along the z-axis) at the top and bottom of the image, respectively.

A total number of 5 contours were used to represent the phantom. It can be seen that the phantom was irradiated along its periphery as shown with the outside contours. Also notice the apple shows to be irradiated at the top and bottom even though it was oriented 45 degrees away from the source. It can be seen at the center slice that no irradiation treatment resulted either on top or the bottom of the apple-phantom.

Figure 4-38 shows the front of the apple oriented towards the back of the image. It can be seen that the bottom part of the phantom located in the center plane did not receive any irradiation. Notice that the contours located left and right to the center show radiation treatment at the bottom regions.

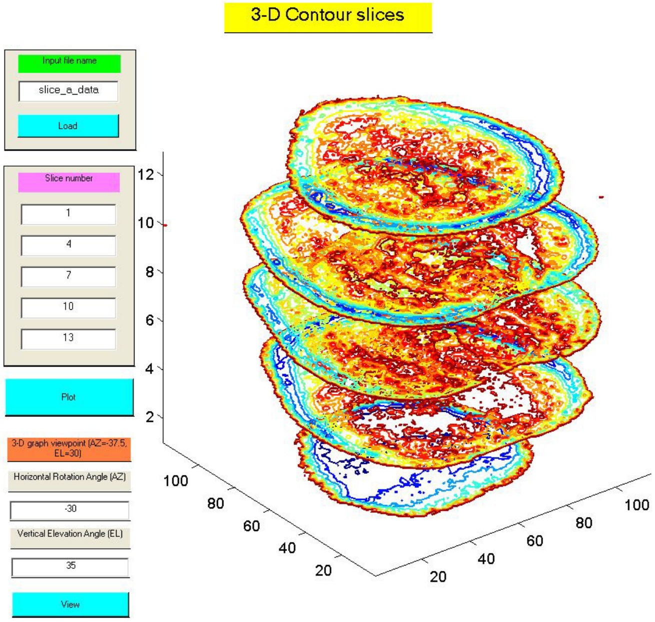

Input file name: slice_a_data

Slice number: 1, 4, 7, 10, 13

Horizontal Rotation Angle (AZ): -30

Vertical Elevation Angle (EL): 35

Figure 4-37. 3-D apple-phantom irradiated at 100 Gy with the VDG and $\alpha = 45$ degrees towards and against a 1.35 MeV plane source (the top region is oriented towards the front).

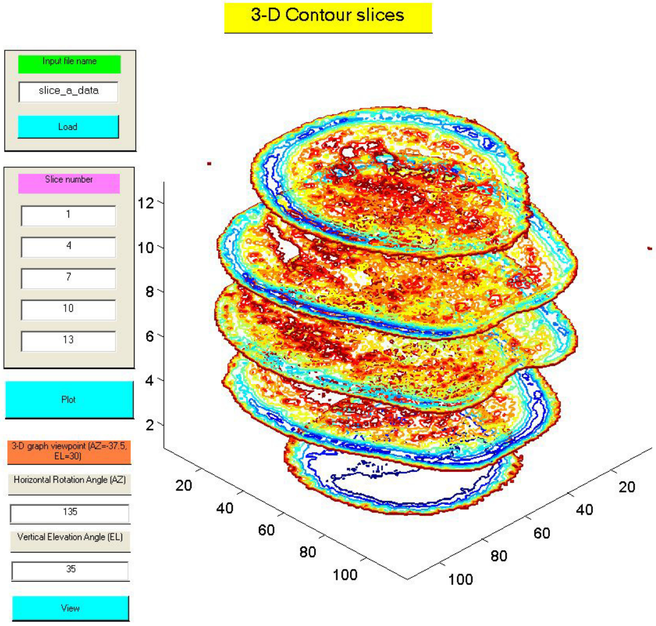

Input file name: slice_a_data

Slice number: 1, 4, 7, 10, 13

Horizontal Rotation Angle (AZ): 135

Vertical Elevation Angle (EL): 35

Figure 4-38. 3-D apple-phantom irradiated at 100 Gy with the VDG and $\alpha = 45$ degrees towards and against a 1.35 MeV plane source (9 slice representation with the top region oriented towards the back).

Figure 4-39 shows the apple-phantom in a different view and with more slices. Again, it was observed that the phantom received radiation treatment on the periphery of the left and right sides. Moving away from the central plane of symmetry shows no signs of radiation exposure on the top and bottom as confirmed with the radiochromic film and phantom contours (Figure 4-9 and Figure 4-21).

Figure 4-40 shows the phantom reconstructed using all the intensity data from the 15 slices produced. Increasing the number of slices provides a better idea of the intensity distribution not only in the symmetry plane as performed in this study but throughout the apple-phantom.

The three dimensional representations of the apple-phantoms help to make clear that the dose distribution and dose depth profiles shown in this research will be different depending on the reference plane chosen for the analysis.

Notice the radiation treatment at the 45 degree orientation shows as blue, green and cyan colors close to the surface of the apple. The yellow, orange and red colors are non-irradiated regions that resulted from the imperfections of the apple-phantom material. The intensity data shown in this section was used exactly as obtained after the scanning procedure. No image processing techniques were applied to remove non-irradiated regions. Even though increasing the number of slices provides a better understanding of the dose distribution throughout the apple, it produces a more difficult three dimensional image to interpret. To overcome this problem, the two dimensional intensity data was visualized as a volume using the procedures shown in the Matlab's Volume Visualization Techniques reference manual.

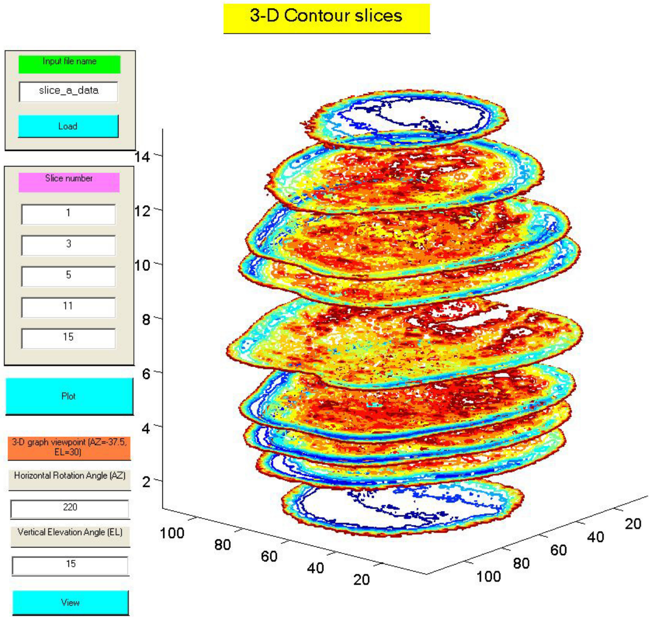

Input file name: slice_a_data

Slice number: 1, 3, 5, 11, 15

3-D graph viewpoint (AZ=-37.5, EL=30)

Horizontal Rotation Angle (AZ): 220

Vertical Elevation Angle (EL): 15

Figure 4-39. 3-D apple-phantom irradiated at 100 Gy with the VDG and α = 45 degrees towards and against a 1.35 MeV plane source (9 slice representation with the top region oriented towards the back).

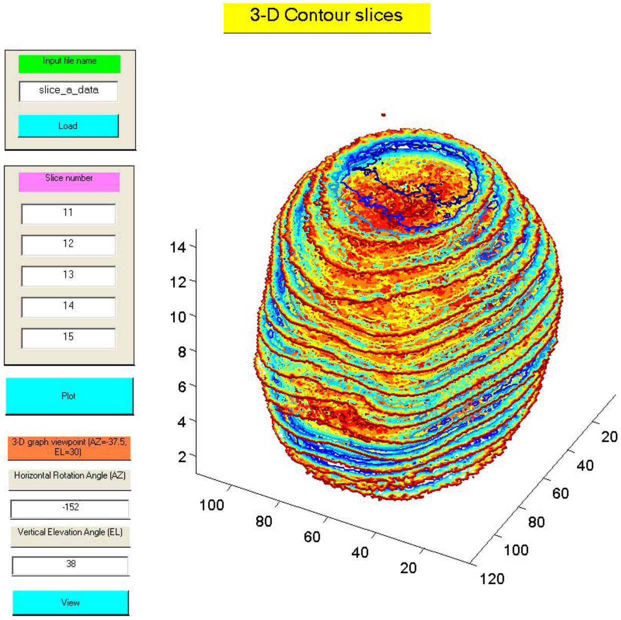

3-D Contour slices

Input file name: slice_a_data

Slice number: 11, 12, 13, 14, 15

3-D graph viewpoint (AZ=-37.5, EL=30)

Horizontal Rotation Angle (AZ): -152

Vertical Elevation Angle (EL): 38

Figure 4-40. 3-D apple-phantom irradiated at 100 Gy with the VDG and α = 45 degrees towards and against a 1.35 MeV plane source (15 slice representation with the top region oriented towards the back).

Figure 4-41 show a 3-D reconstruction from the intensity data from all 16 slices. It may be observed that the apple shape was captured best along the *x*-*y* axis which corresponds to the direction in which the intensity data was obtained.

Figure 4-41 shows the apple-phantom oriented with its top (stem) aligned to the front of the image. In this image, the left and right sides of the phantom are oriented towards the top and the bottom respectively along the *z*-axis.

Notice the depression that exists between 4.32 and 5.40 cm in the *z*-axis corresponding to the phantoms stem. Figure 4-42 shows the apple-phantom bottom region oriented towards the front of the image.

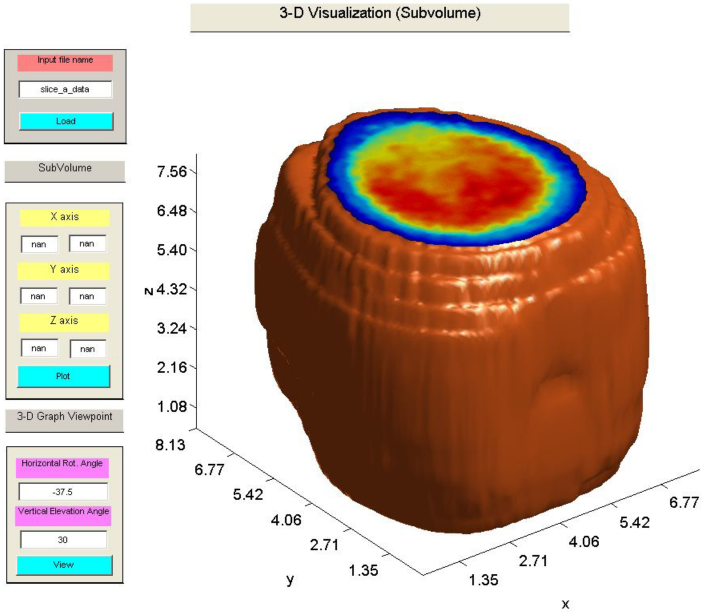

Input file name: slice_a_data

X axis: nan nan

Y axis: nan nan

Z axis: nan nan

Horizontal Rot. Angle: -37.5

Vertical Elevation Angle: 30

Figure 4-41. 3-D apple-phantom irradiated at 100 Gy with the VDG and α = 45 degrees towards and against a 1.35 MeV plane source (the front of the picture is the apple-phantom's top region).

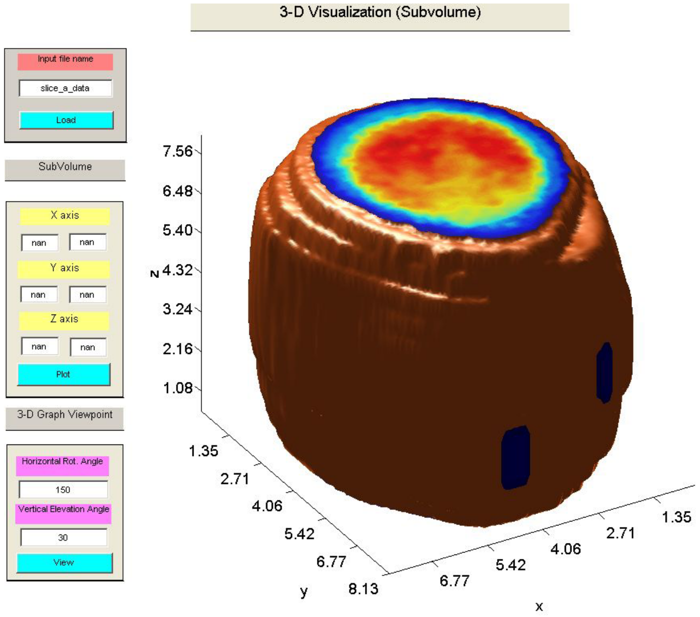

Input file name: slice_a_data

X axis: nan nan

Y axis: nan nan

Z axis: nan nan

Horizontal Rot. Angle: 150

Vertical Elevation Angle: 30

Figure 4-42. 3-D apple-phantom irradiated at 100 Gy with the VDG and α = 45 degrees towards and against a 1.35 MeV plane source (the front of the picture is the apple-phantom's bottom region).

Even though the phantom's shape can be more appreciated in the *x-y* plane, it can be seen that the slices become smaller and smaller along the *z*-plane thus producing the characteristic curvature of the phantom's surface.

Using the volume visualization makes it possible to determine the intensity distribution along any direction in any plane. However, for ease of computations cuts were performed along the *x*, *y*, and *z* planes respectively as shown in Figure 4-43 thru Figure 4-48.

Figure 4-43 shows a 3-D cut at 5.40 cm along the *z*-axis. The phantom followed the same orientation as Figure 4-42. At this particular depth, it can be seen that radiation treatment was most effective on the left and right sides compared to the bottom and top. Figure 4-44 demonstrates the ability to produce a thinner slice compared to Figure 4-43.

Also notice that the intensity distribution changed completely at $z = 4.32$ cm as it got closer to the phantom edge (Figure 4-44). The regions located near the bottom received better treatment to those at the top at this particular depth.

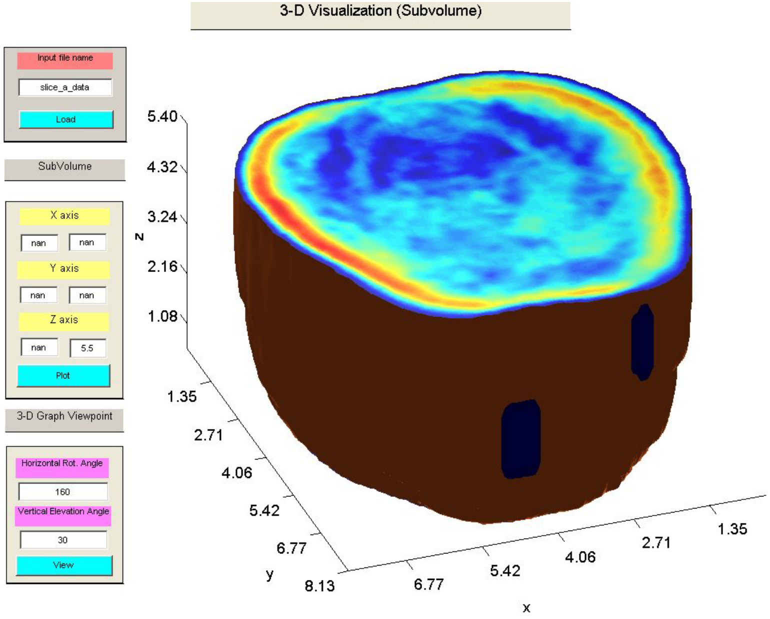

Input file name: slice_a_data

X axis: nan nan

Y axis: nan nan

Z axis: nan 5.5

Horizontal Rot. Angle: 160

Vertical Elevation Angle: 30

Figure 4-43. 3-D half-cut about the z-axis of an apple-phantom irradiated at 100 Gy with the VDG and $\alpha = 45$ degrees towards and against a 1.35 MeV plane source (the front of the picture is the apple-phantom's bottom region).

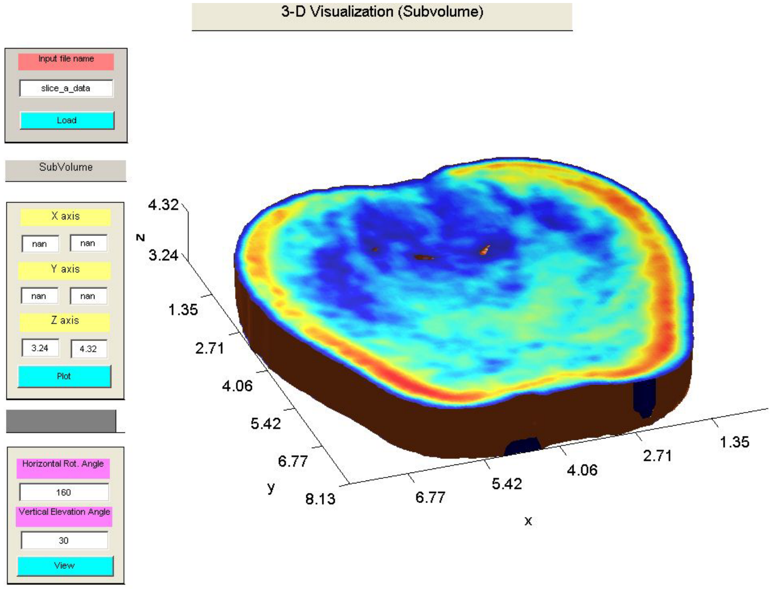

3-D Visualization (Subvolume)

Input file name: slice_a_data

SubVolume

X axis: nan nan

Y axis: nan nan

Z axis: 3.24 4.32

Horizontal Rot. Angle: 160

Vertical Elevation Angle: 30

Figure 4-44. 3-D slice-cut about the z-axis of an apple-phantom irradiated at 100 Gy with the VDG and α = 45 degrees towards and against a 1.35 MeV plane source (the front of the picture is the apple-phantom's bottom region).

Both figures did not show any treatment at the top of the phantom. This problem was produced mainly due to chloroform evaporation during the casting process. The pouring hole location in the mold geometry was exactly at the top. As a result, during the pouring process the top parts of the mold received less chloroform in spite of the constant temperature of 65 °C kept to produce the methyl yellow solution.

Because the solidification process of the methyl yellow – chloroform - paraffin wax solution inside the mold was very slow, less chloroform was present in the solution from its initial 20% concentration at the end of the pouring. For this reason, it can be seen that no irradiation treatment was detected near the top regions of the apple for both energies and all phantom orientations towards the e-beam.

Figure 4-45 shows a vertical cut at $y = 4$ cm. The apple-phantom was oriented with the bottom regions located in front of the image. It can be observed that at this plane most of the regions have been irradiated. The difference in irradiation treatment was observed with two different planes as shown in Figure 4-43 and Figure 4-45.

The y-plane cut resulted in a more uniform irradiation profile compared to the z-plane cut where no radiation exposure could be found near and at the top regions of the apple as shown in Figure 4-43. Figure 4-46 shows a smaller slice cut,($y = 2.5$ cm), of the same apple-phantom oriented 45 degrees towards the e-beam. A comparison of both Figure 4-45 and Figure 4-46 show a difference in the intensity profile. The face of the slice in Figure 4-46 was closer to the top edge of the phantom (i.e., in the y-plane) showing less irradiation treatment along the bottom of the x-axis in contrast with Figure 4-45.

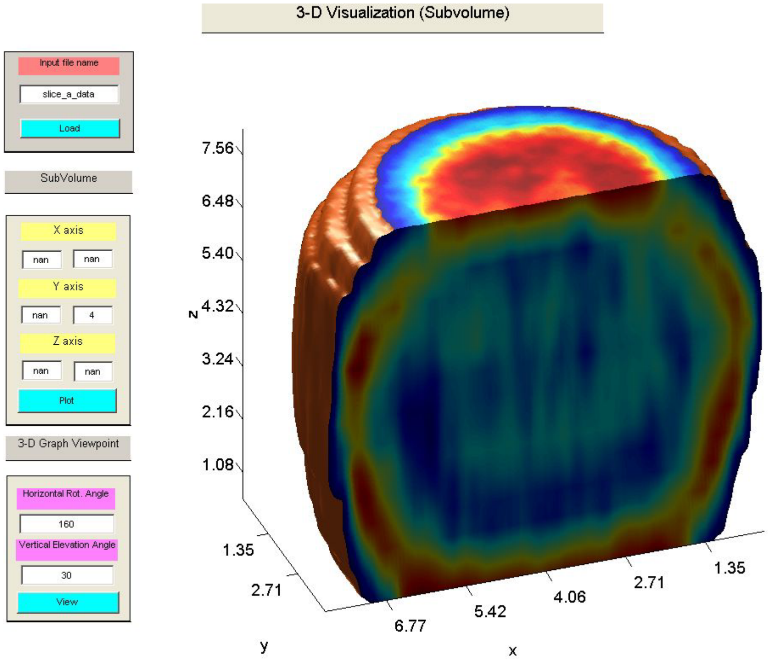

3-D Visualization (Subvolume)

Input file name: slice_a_data

SubVolume

X axis: nan nan

Y axis: nan 4

Z axis: nan nan

3-D Graph Viewpoint

Horizontal Rot. Angle: 160

Vertical Elevation Angle: 30

Figure 4-45. 3-D half-cut about the y-axis of an apple-phantom irradiated at 100 Gy with the VDG and α = 45 degrees towards and against a 1.35 MeV plane source.

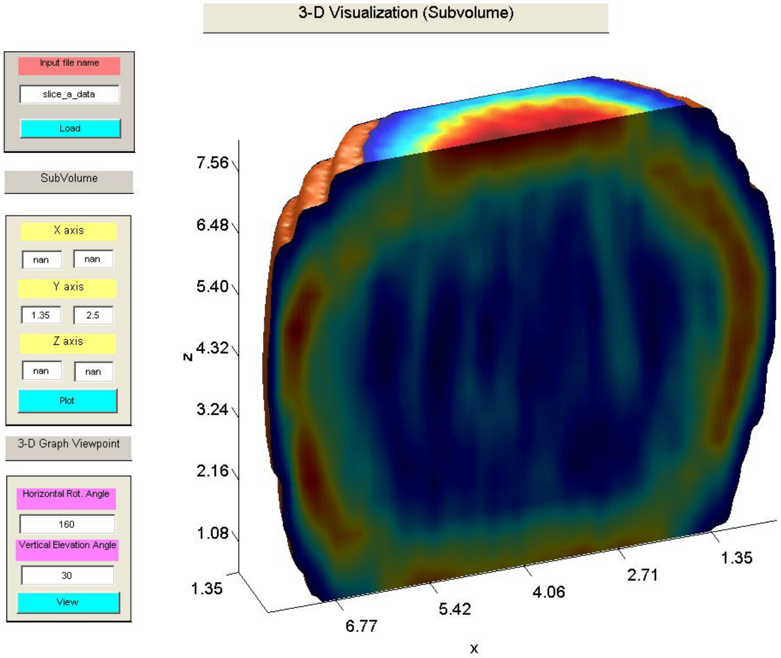

Input file name: slice_a_data

X axis: nan nan

Y axis: 1.35 2.5

Z axis: nan nan

Horizontal Rot. Angle: 160

Vertical Elevation Angle: 30

Figure 4-46. 3-D slice-cut about the y-axis of an apple-phantom irradiated at 100 Gy with the VDG and $\alpha = 45$ degrees towards and against a 1.35 MeV plane source.

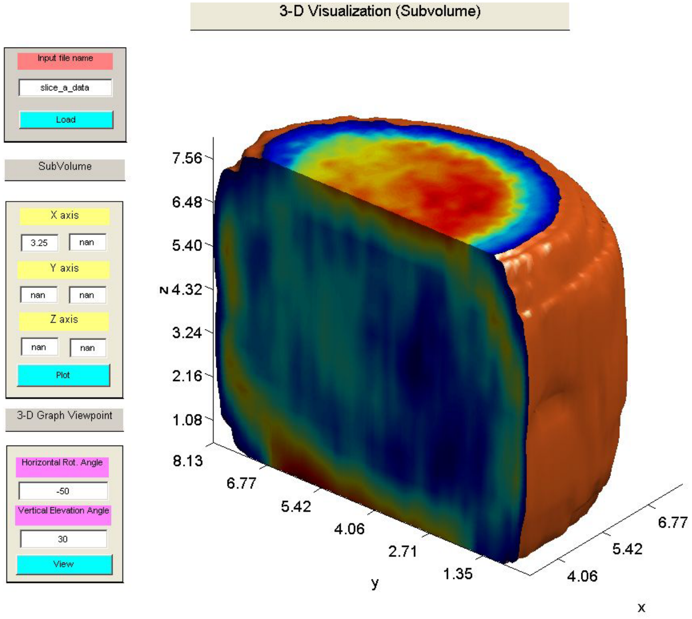

Input file name: slice_a_data

X axis: 3.25 nan

Y axis: nan nan

Z axis: nan nan

Horizontal Rot. Angle: -50

Vertical Elevation Angle: 30

Figure 4-47. 3-D half-cut about the x-axis of an apple-phantom irradiated at 100 Gy with the VDG and α = 45 degrees towards and against a 1.35 MeV plane source (the front of the picture is the apple-phantom's top region).

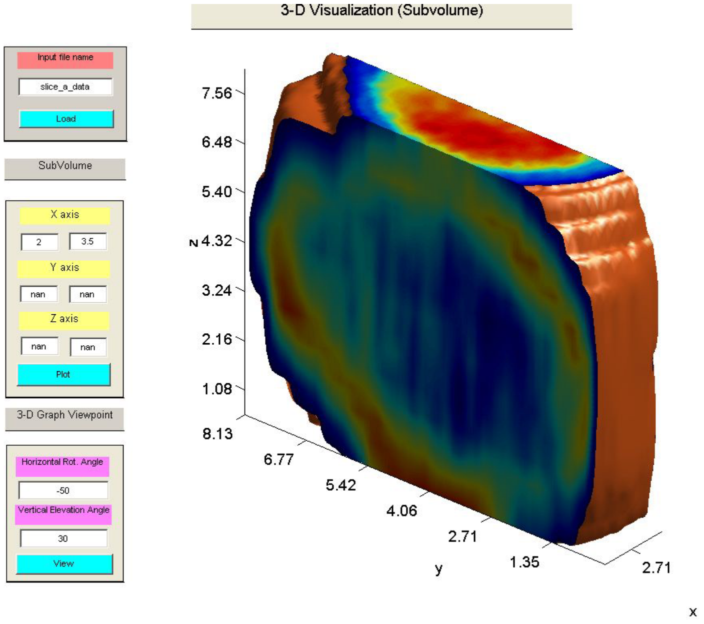

Input file name: slice_a_data

X axis: 2, 3.5

Y axis: nan, nan

Z axis: nan, nan

Horizontal Rot. Angle: -50

Vertical Elevation Angle: 30

Figure 4-48. 3-D slice-cut about the x-axis of an apple-phantom irradiated at 100 Gy with the VDG and α = 45 degrees towards and against a 1.35 MeV plane source (the front of the picture is the apple-phantom's top region).

Figure 4-47 shows a vertical cut at $x = 3.25$ cm using the orientation shown in Figure 4-41. This plane is completely perpendicular to the *z*-plane and it can be observed that the sample was mainly exposed on the left and right sides. Figure 4-46 shows also the difference in intensity profile moving along the same cutting plane. Note that $x = 2$ cm vs. $x = 3.25$ cm shows the latter plane is closer to the apple's center thus received less radiation treatment.

The three dimensional images in this section also show intensity data depicted with the color blue near the surface. All these intensity data values were left in this section to show the complete set of data that resulted from the irradiations. However, the analysis performed in the phantom plane of symmetry in the *z*-axis did not include these data points. The image processing method described in Section 3.9 was used to filter undesired data. In the case of the methyl yellow apple-phantom contours, it was found that a region of 1 mm from the surface could be discarded using image processing methods to prevent incurring into errors due to non-uniform thickness.

In addition, the shape of the 3-D apple-phantom may be improved by using the cutting method proposed in Section 3.5.1 along the *x* and *y* planes. Improving or reducing the thickness of the apple-phantom slice contours in any particular plane will also enhance the 3-D representation of the raw intensity data. The methyl yellow apple-phantom analyzed in this research study shows the possibility to produce three dimensional representations of dose depth distributions. For this study, the possibility was discussed in depth in a particular plane where the analysis was performed.

4.2 E-Beam Irradiation Using the 10 MeV LINAC

Dose deposition profiles were obtained for the HD-810 film and methyl yellow apple contours using the calibration equations described in Sections 3.7 and 3.8. Figure 3-18 shows a group of samples ready for irradiation. Each apple-phantom was positioned face up (stem on top) inside its polystyrene box holder and covered with an identical piece of attenuating material at the top and the bottom. Figure 4-49 shows the layout of the conveyor system of the e-beam facility where the samples were loaded.

Figure 4-49. Conveyor layout of Surebeam Food Research Facility at Texas A&M University.

Figure 4-50 shows the layout of an individual apple-phantom in its packaging for the e-beam irradiation with the 10 MeV electrons and the electron operating range passed the different absorber thicknesses.

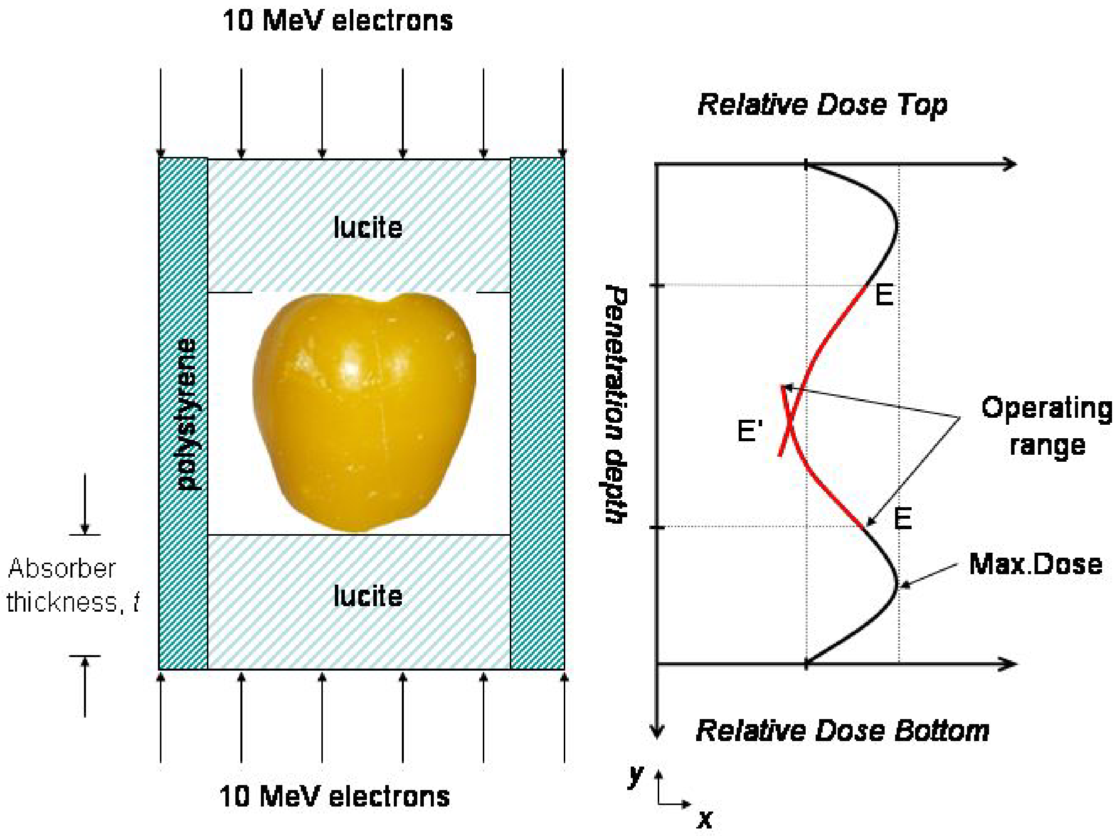

Figure 4-50. Apple-phantom packaging layout for 10 MeV e-beam irradiation.

During the e-beam irradiation the 10 MeV electrons shown in Figure 4-50 penetrate through the Lucite absorber and polystyrene walls before they reach the apple-phantom positioned inside the package. Points E and E' show the operating range for the electrons after a penetration depth, *t* (cm), where the electrons have attenuated their energy from 10 MeV to 1.35 MeV to achieve the desired target doses.

Apple-phantoms were positioned in the conveyor as shown in Figure 3-18. Next, they were irradiated using a 10 MeV dual electron beam. The electron accelerators were located underneath and on top of the conveyor system covering a total width of 60.96 cm from the center of the conveyor width.

For this reason, the apple-phantoms were located exactly at the center of the holder boxes and irradiated in a perpendicular plane to the conveyors direction of motion. Each sample was also set apart a distance of 15 cm to prevent scattering effects from each other.

The dose depth distributions were measured along the y-axis from the phantom top to the bottom using three parallel planes located in the x-axis at 24, 40 and 64 mm defined as *left*, *center*, and *right* planes. The following sections show the dose deposition and dose depth distributions at the HD-810 film and apple-phantom contours for a Lucite thickness of 3, 4, and 4.2 cm.

4.2.1 GAFCHROMIC® HD-810 Film Contour Slices

Figure 4-51 shows the dose deposition data for the radiochromic film with a Lucite thickness of 3 cm (target dose 1 kGy). The electrons penetrated quite uniformly from the bottom and the top until they lost all their energy at the center of the apple. This behavior was observed in Figure 4-52 where the dose depth profile of the electrons was measured from top to bottom at specific locations in the *x*-axis. It can be seen that the top entrance dose at the left and central planes were very close showing the electron beam uniformity (Figure 4-51).The right side (x = 64 mm) showed less irradiation; however, this lower dose may have been a result of the positioning of the apple-phantom inside the bag.

Notice that at the bottom of the apple (Figure 4-51), the film agrees with the target dose (1 kGy). Figure 4-52 shows high dose regions at the top left and right positions of the apple-phantom. These differences resulted due to the positioning of the apple-phantom in the packaging container and apple variations in geometry. The top left side of the apple-phantom that shows the highest absorbed dose is closer to the Lucite absorber compared to its top right side. As a result, the electrons traveled less before reaching the top-left part of the sample hence depositing more energy. Similar results for a Lucite thickness of 4 cm are shown in Appendix E (Figure E-1 to Figure E-4).

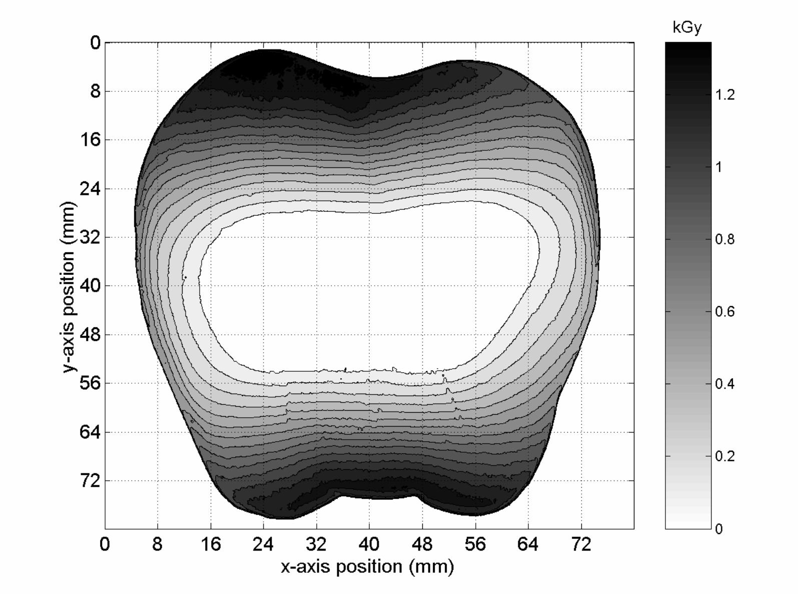

Figure 4-51. HD-810 film dose distribution in kGy using Lucite thickness of 3 cm and a dual beam 10 MeV LINAC accelerator with a conveyor speed of 18.3 m/min (60 ft/min).

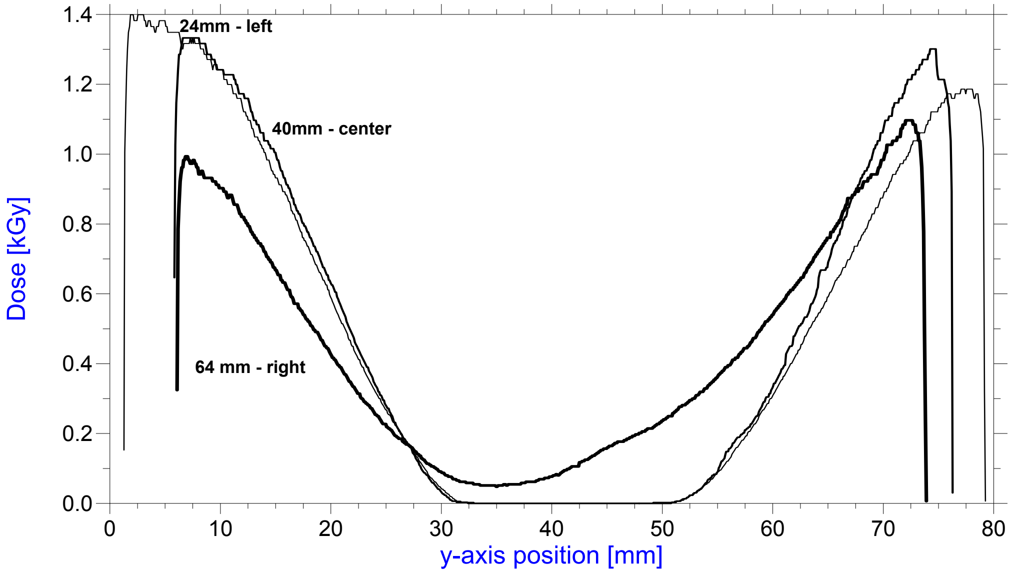

Figure 4-52. HD-810 film depth-dose distribution in kGy using Lucite thickness of 3 cm and a dual beam 10 MeV LINAC accelerator with a conveyor speed of 18.3 m/min (60 ft/min).

Figure 4-53 shows the dose deposition on the film with a Lucite thickness of 4 cm (target dose of 0.4 kGy). It can be observed that the top and bottom regions of film apple contour were uniformly irradiated (Figure 4-54). The left side depth dose curve shows a higher dose than the center and right curves. This high dose was the result of damaged film that produced an incorrect measurement of intensity (thus dose). For the left curve (Figure 4-54), it can be seen that at a depth of approximately 3mm from the top, the dose value decreases to approximately 0.42 kGy, which is closer to the target dose of 0.4 kGy.

The film contour in Figure 4-53 also indicates the apple was over-exposed on its left and right sides. This can be due to the scattering of electrons produced when they hit the walls of polystyrene box holder. The dose at these regions were the highest because the apple-phantom holder walls were not designed with the same thickness as the Lucite attenuating material placed on the top and bottom of the box (Figure 4-50).

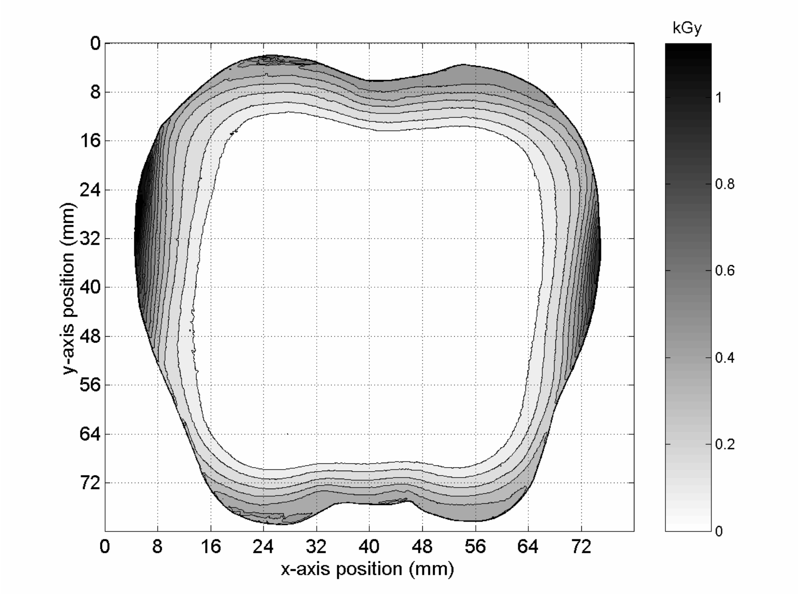

Figure 4-53. HD-810 film dose distribution in kGy using Lucite thickness of 4 cm and a dual beam 10 MeV LINAC accelerator with a conveyor speed of 18.3 m/min (60 ft/min).

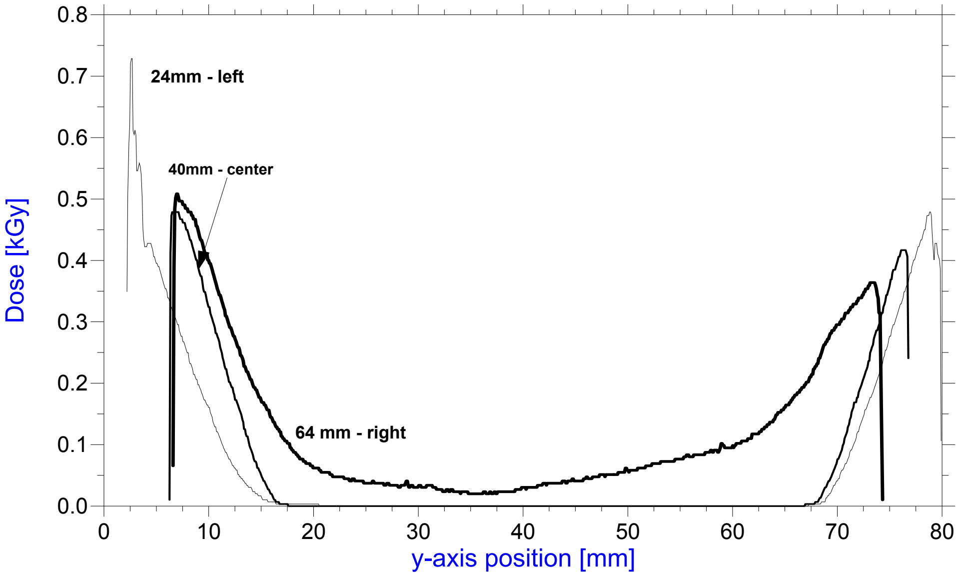

Figure 4-54. HD-810 film dose distribution in kGy using Lucite thickness of 3 cm and a dual beam 10 MeV LINAC accelerator with a conveyor speed of 18.3 m/min (60 ft/min).

Figure 4-55 shows the dose deposition contour on the film in the apple-phantom with a Lucite thickness of 4.2 cm (target dose of 0.2 kGy). The same traits as in both previous cases were observed. First, the left side of the apple (x = 24 mm) shows that a high dose was absorbed near the top of the apple (Figure 4-55). The radiochromic film was damaged at the same region as the one discussed previously. Comparing the left and right sides of the apple film contour at the same position (y = 3 mm) it can be seen that high energy was absorbed on the left side, but not as much as the right side shows. At the bottom right side of the film (y = 80 mm) a high dose was also shown. This dose was also a result of image noise at the periphery of the film.

The center curve shown in Figure 4-56 shows a large peak at y = 60 mm then it levels off to rise again at approximately 75 mm from the top. Again, the large peak was created due to image noise that was not able to be removed from the image thus producing the effect of a higher dose at a point that makes no sense. The center slice can be regarded to have uniformity in the sense that the dose value started decreasing from approximately 0.35 kGy in the top and bottom to zero at the center. The right side curve dropped from approximately 0.25 kGy on each side to zero at the center showing it was very uniform on top and bottom. The right side curve finished earlier than the other two because it was obtained at x = 64 mm compared to the left side obtained at x = 24 mm.

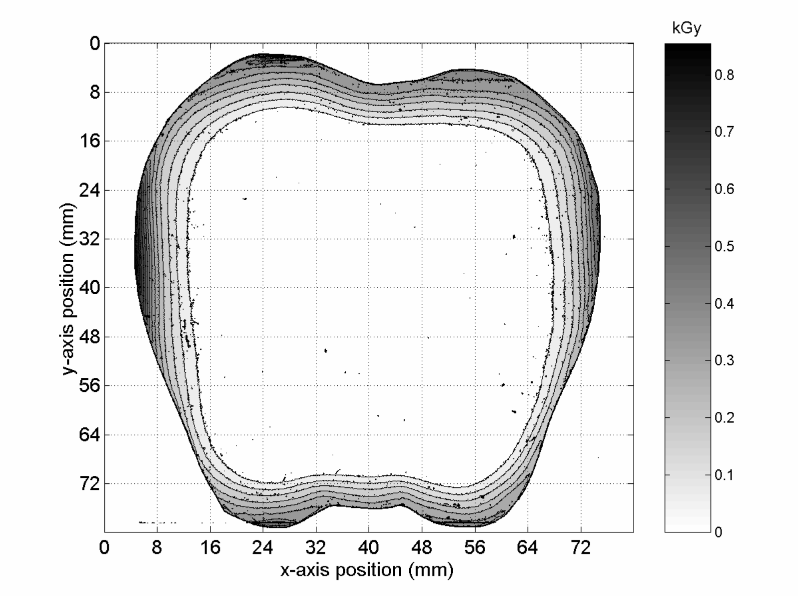

Figure 4-55. HD-810 film dose distribution in kGy using Lucite thickness of 4.2 cm and a dual beam 10 MeV LINAC accelerator with a conveyor speed of 18.3 m/min (60 ft/min).

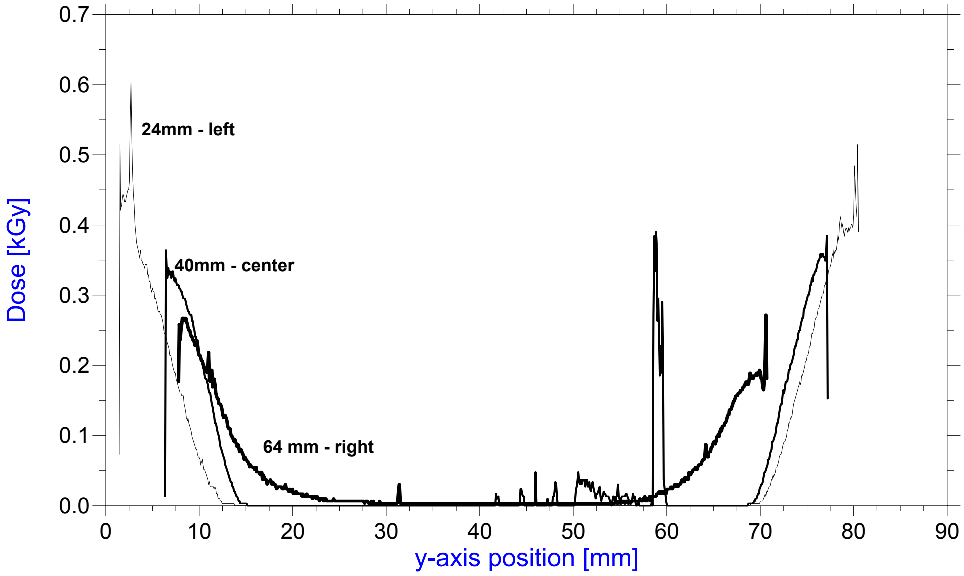

Figure 4-56. HD-810 film dose distribution in kGy using Lucite thickness of 4.2 cm and a dual beam 10 MeV LINAC accelerator with a conveyor speed of 18.3 m/min (60 ft/min).

4.2.2 Dose Uniformity Ratio Description for 10 MeV E-Beam Irradiation

The dose uniformity ratio, D_{max}/D_{min}, as defined in Section 4.1.4 was obtained in HD-810 films for three Lucite absorber thicknesses of 3 (target dose 1.0 kGy), 4 (taget dose 0.4 kGy) and 4.2 (target dose 0.2 kGy) cm, respectively. The results were as follows.

Figure 4-57 shows that the HD-810 film dose uniformity ratio for 3 cm produced the most uniform results compared to that of 4 and 4.2 cm thick Lucite absorbers. The film ratio for the 4 and 4.2 cm absorbers increased past 3.0 mm from the surface. These was the result of the electron scattering and high dose values produced at the left and right sides of the apple-phantoms as shown in Figure 4-53 and Figure 4-55.

Figure 4-54 and Figure 4-56 show that for 4 and 4.2 cm Lucite absorber thicknesses respectively, the absorbed dose decreases linearly from the top to the bottom of the film contour. The regions located near the center (between 30 mm < x 60 mm) show low absorbed dose values. Because of this, the value of the ratio, D_{max}/D_{min}, increased dramatically due to the lower, D_{min}, values located near the center of the film.

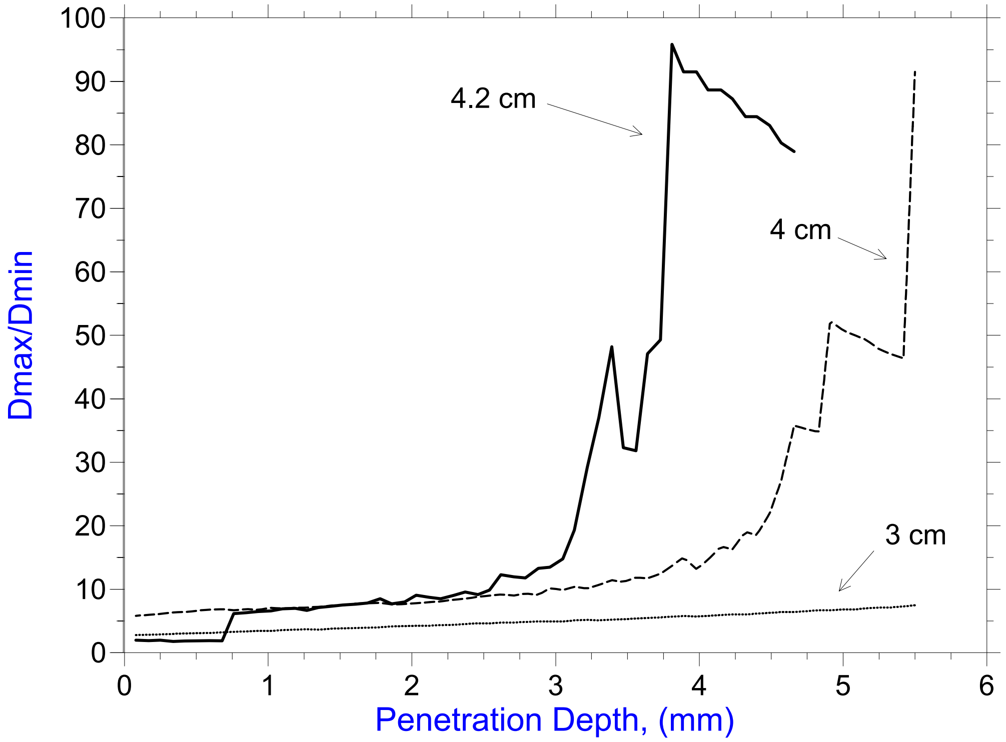

Figure 4-57. Dose uniformity ratio, D_{max}/D_{min}, for 3, 4, and 4.2 cm absorber thicknesses.

4.2.3 Apple-Phantom Contours

Figure 4-58 and Figure 4-59 show the dose deposition contour and dose depth profiles for the methyl yellow apple contours with a Lucite thickness of 3 cm (target dose of 1 kGy). From Figure 4-58 it can be seen clearly that the top left corner and bottom right corner of the phantom contour received a higher doses compared to the rest of the slice. This behavior matches that of the radiochromic film (Figure 4-51). However, the left side curve shown in Figure 4-59 predicts a much lower dose compared to the film. Such a low dose response may be a result of saturation of the dose response of the methyl yellow solution (maximum dose up to 0.5 kGy at saturation), and a reduction of the chloroform concentration due to evaporation during the casting process and waiting period to perform the scanning procedure. Similar results are shown in Appendix E (Figure E-13 to E-24).

The center curve in Figure 4-59 confirms that chloroform evaporated near the top regions of the apple, but not at the bottom. In spite of that, the apple-phantom shows that the dose was uniform in the left and right side of the slice. Both, Figure 4-52 and Figure 4-59 show a decrease in dose from depths 5 mm to 30 mm that seem proportional even though the dose values are different.

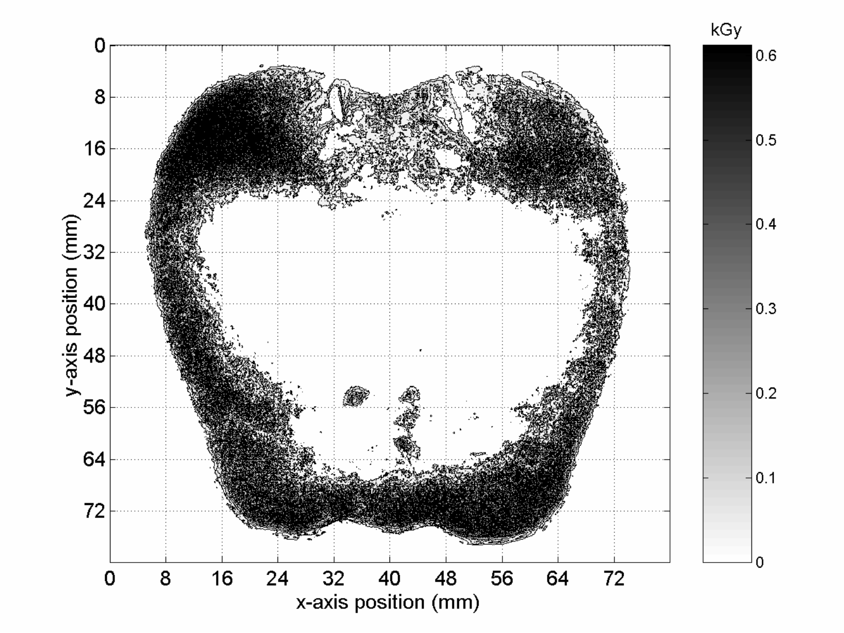

Figure 4-58. Methyl yellow apple-phantom contour dose distribution in kGy using Lucite thickness of 3 cm and a dual beam 10 MeV LINAC accelerator with a conveyor speed of 18.3 m/min (60 ft/min).

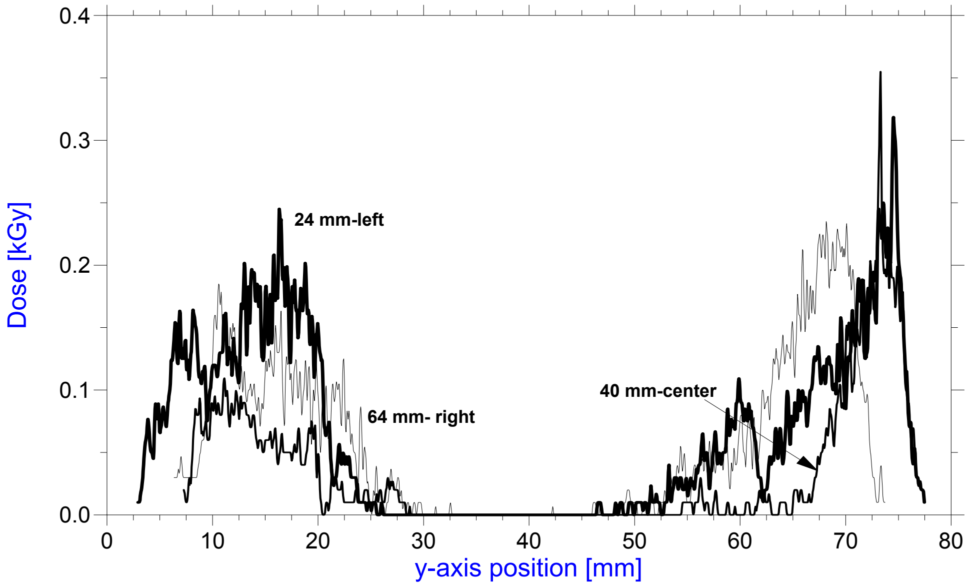

Figure 4-59. Methyl yellow apple-phantom contour depth-dose distribution in kGy using Lucite thickness of 3 cm and a dual beam 10 MeV LINAC accelerator with a conveyor speed of 18.3 m/min (60 ft/min).

Figure 4-60 and Figure 4-61 show the methyl yellow contour response using a Lucite thickness of 4 cm. Notice that the thicker polystyrene sample produced a better dose deposition contour and depth dose profiles. The target dose for 4 cm was approximately 400 Gy. It can be seen that at the top and bottom regions of the phantom the radiation treatment improved over the 3 cm thickness mainly due to the lower dose.

Indeed, Figure 4-61 shows that the top and bottom left sides received approximately 0.3 kGy. This demonstrates the methyl yellow phantom produced uniform results in spite of its lower resolution capability, due to its thickness and grain size, compared to the radiochromic film. The right curve on Figure 4-61 also shows uniformity on both top and bottom at a lower dose compared to the left side. The energy deposition figure shows higher doses were absorbed at the edges of the apple-phantom which confirmed electron scattering occurred due to the polystyrene walls of the box holder.

The center depth dose profile in Figure 4-61 showed a very little dose at the top, but almost an equal response compared to bottom left side. It can be observed in general that the bottom regions of the phantom were uniformly irradiated.

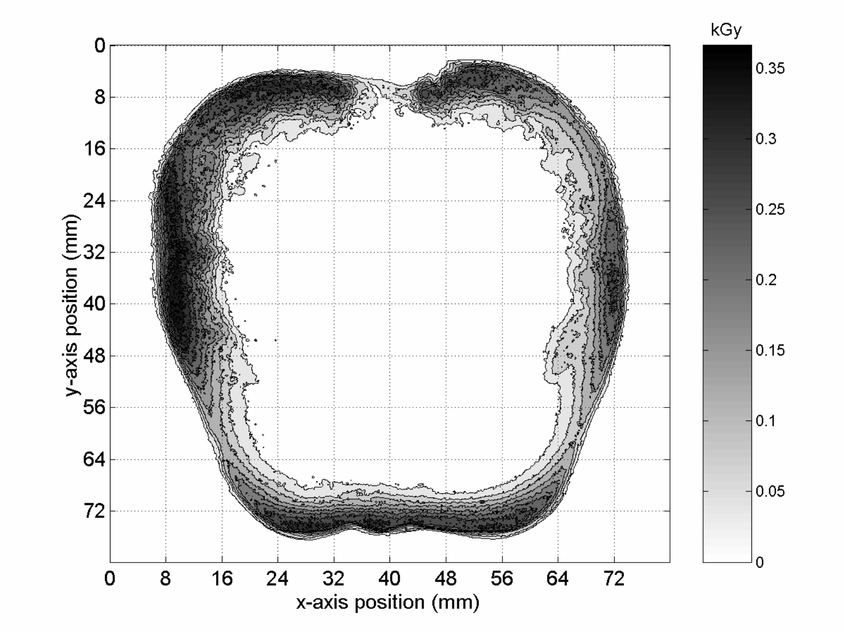

Figure 4-60. Methyl yellow apple-phantom contour dose distribution in kGy using Lucite thickness of 4 cm and a dual beam 10 MeV LINAC accelerator with a conveyor speed of 18.3 m/min (60 ft/min).

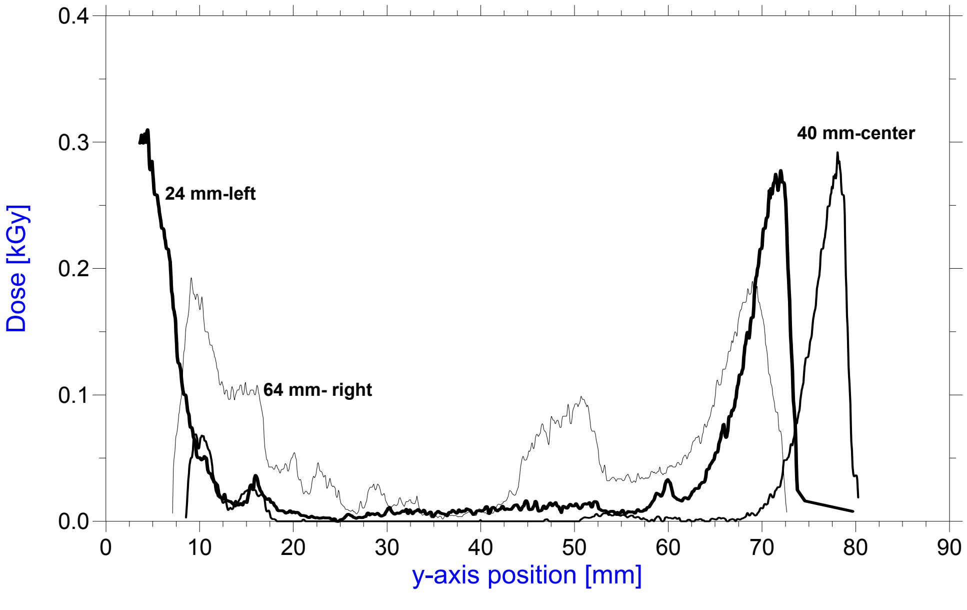

Figure 4-61. Methyl yellow apple-phantom contour depth-dose distribution in kGy using Lucite thickness of 4 cm and a dual beam 10 MeV LINAC accelerator with a conveyor speed of 18.3 m/min (60 ft/min).

Figure 4-62 and Figure 4-63 shows the dose deposition and dose depth profiles for the methyl yellow apple-phantom using a Lucite thickness of 4.2 cm. First, the scale of Figure 4-62 shows that the highest dose was approximately 0.25 kGy. This was remarkable in the sense that the methyl yellow phantom responded best given thicker Lucite absorber that decrease the absorbed dose thus improving the dose response.

Notice the higher dose was found at the left and right sides of the phantom due to electron scattering from the polystyrene holder box. The methyl yellow phantom shows uniform irradiation at the bottom, but it did not completely show the same penetration range as the film in Figure 4-55.

It was very difficult to establish also a result for the center and right curves of Figure 4-63 due to the small data captured within those regions. The top and bottom regions of the left curve (Figure 4-63) show uniformity in the sense that the dose was approximately close at the both sides.

The left side of the apple-phantom shows higher absorbed dose due to the contact between the phantom surface at that point and the polystyrene wall resulting in more electron scattering (thus higher doses and longer penetration depths).

In general it was found that the methyl yellow provided a better response to dose using thicker Lucite absorber samples given the calibration curve in Section 3.7. Due to the natural response found in the calibration curve, lower absorbed doses provide better results.

Several factors that had an effect on the dose measurement were the variations in thickness of the Lucite absorber, the apple-phantom placement inside the box holder, and the cutting and scanning procedure.

Overall, the methyl yellow phantom show an acceptable response to lower doses but it may not be considered for high dose applications due to its low dose response.

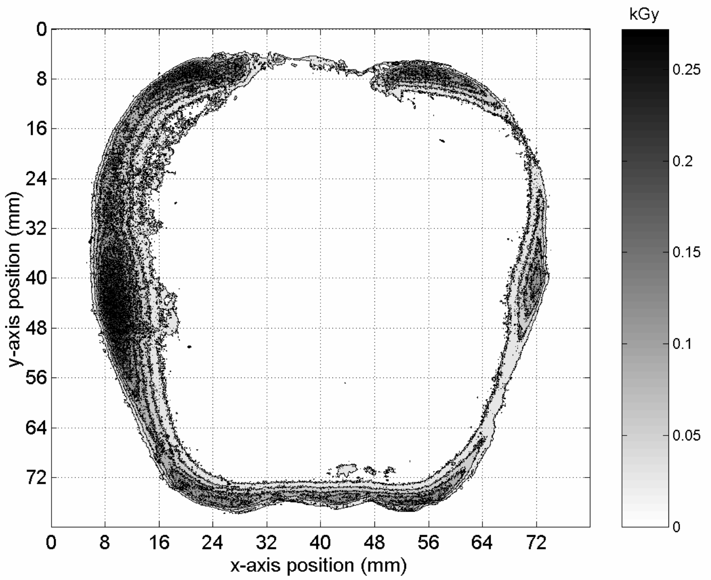

Figure 4-62. Methyl yellow apple-phantom contour dose distribution in kGy using Lucite thickness of 4.2 cm and a dual beam 10 MeV LINAC accelerator with a conveyor speed of 18.3 m/min (60 ft/min).

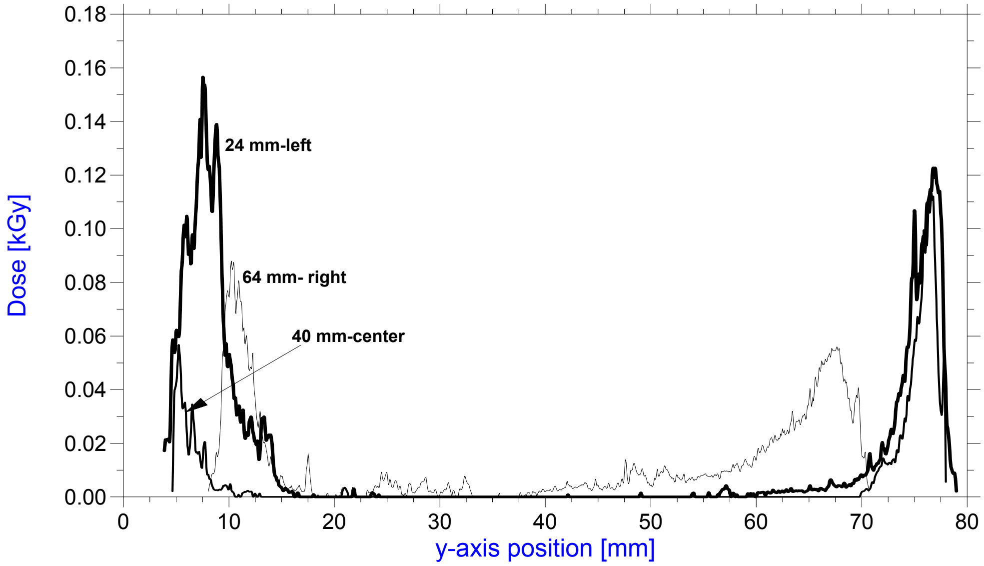

Figure 4-63. Methyl yellow apple-phantom contour depth-dose distribution in kGy using Lucite thickness of 4.2 cm and a dual beam 10 MeV LINAC accelerator with a conveyor speed of 18.3 m/min (60 ft/min).

4.3 X-ray Irradiation Using 5 MeV LINAC

The irradiation experiment on the apple-phantoms was performed with a 5 MeV LINAC using an X-ray converter at the Food Research Facility at Texas A&M University. A target dose of 0.6 kGy was delivered to three methyl yellow apple-phantoms positioned into a custom made holder traveling with a conveyor speed of 0.61 m/min as described and shown in Section 3.4.3 and Figure 3-19. The average energy of the X-ray photons was obtained from the cumulative photon flux distribution as shown in Figure 4-63.

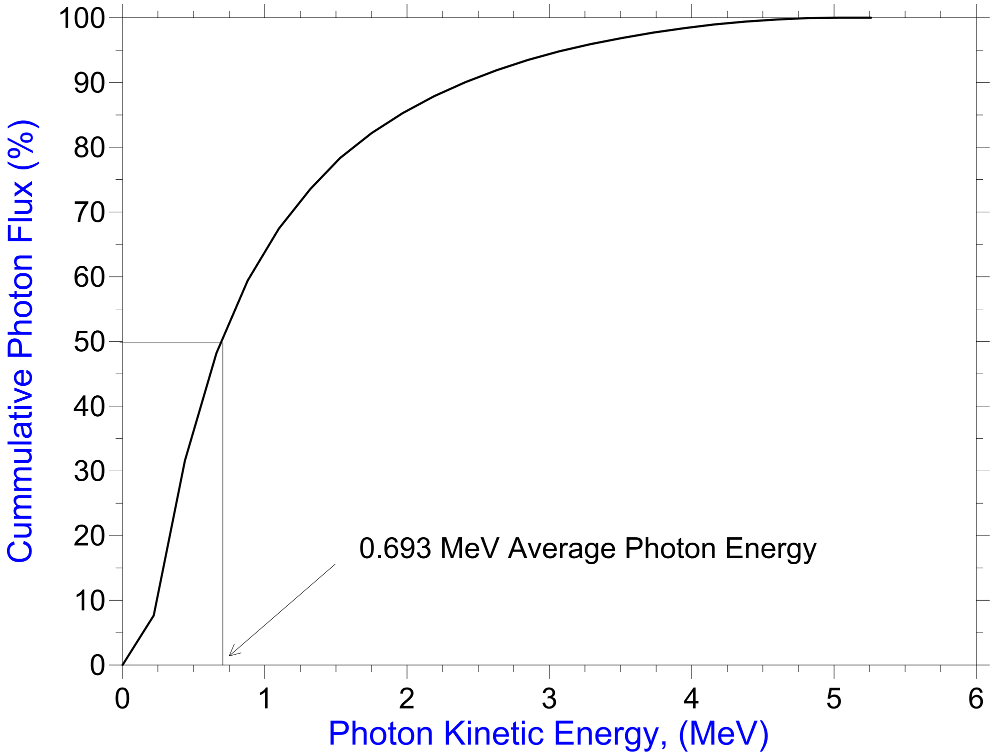

Figure 4-64. Cummulative distribution of X-ray spectra.

Figure 4-64 shows that the average energy of the photons produced was 0.693 MeV. Figure 4-65 shows the actual photon spectrum of X-ray radiation for 5 MeV electrons.

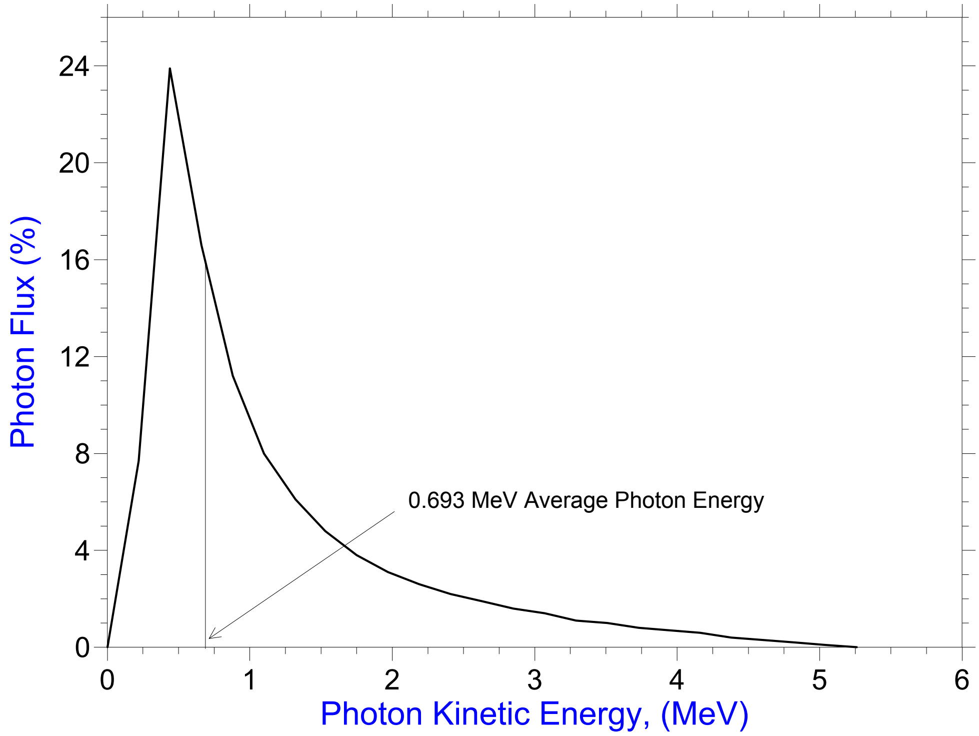

Figure 4-65. Photon spectrum 21 cm away from X-ray converter (IAEA, 2002).

The X-ray beam exit window was located perpendicular to the conveyor's direction of motion and separated a distance of 30.48 cm from the custom made holder. To insure the samples were positioned in the X-ray target area, the custom-made holder was constructed with 3 holes to place the apples. The distance from the bottom of the holder to the center of the apple positioned in each hole was 31 cm. The conveyor was set to travel at a speed of 60.96 cm/min to provide the 0.6 kGy target dose. Each apple-phantom was positioned inside the holder gap resting on its side so that the apple center of symmetry (where the film was located) was perpendicular to the beam. The methyl yellow and HD-810 film contours were produced using the guidelines described in Sections 3.2.4 and 3.2.5 respectively. Intensity data was related to dose using the calibration equations shown in Figure 3-21 and Figure 3-22. The results are shown next.

4.3.1 GAFCHROMIC® HD-810 Film Contours

Figure 4-66 shows the energy deposition contour for the radiochromic film. It can be observed that the phantom received a maximum dose of approximately 0.6 kGy at the top. Figure 4-67 shows several curves at penetration depths of 9, 16, 34, 50, and 68 mm from the surface. Appendix F shows similar results (Figure F-1 to Figure F-4).

Notice the dose decrease as the X-rays traveled through the apple at the different depths. The entrance dose was approximately 0.6 below 9 mm from the surface and the exit dose at the bottom of the phantom was approximately 0.4 kGy at a depth of 68 mm. The dose at each particular penetration depth remained quite uniform across the *x*-axis.

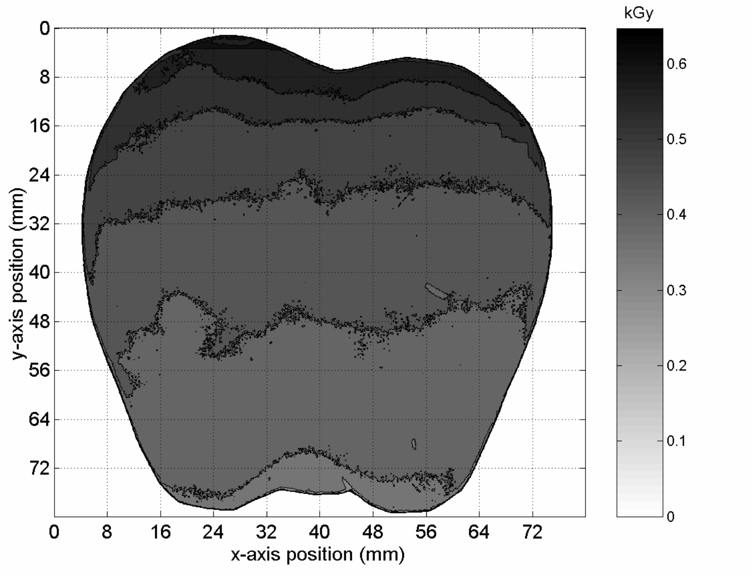

Figure 4-66. HD-810 film dose distribution in kGy using a custom-made polystyrene holder and a 5 MeV LINAC accelerator with a conveyor speed of 0.61m/min (2 ft/min).

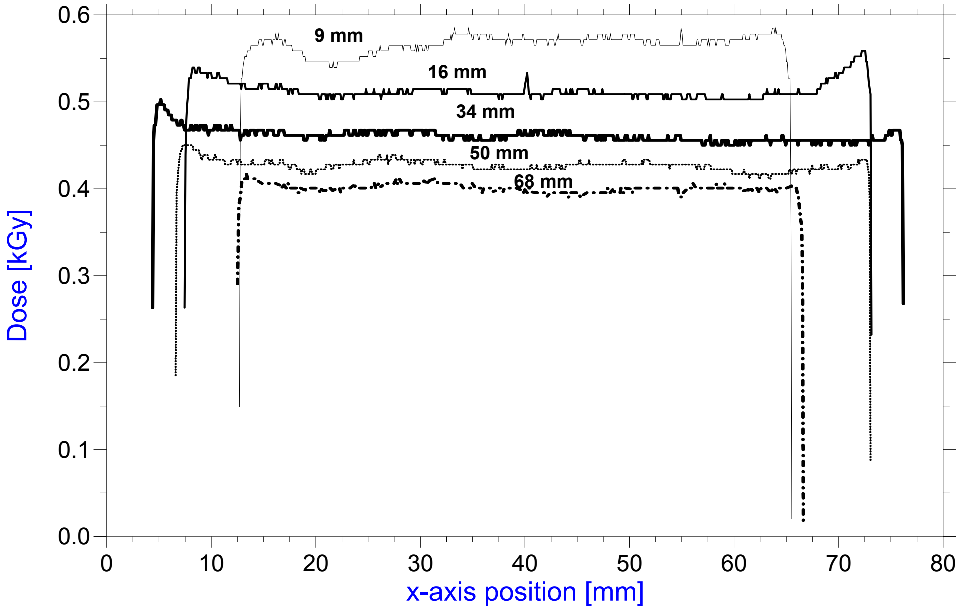

Figure 4-67. HD-810 film dose distribution in kGy using a custom-made polystyrene holder and a 5 MeV LINAC accelerator with a conveyor speed of 0.61 m/min (2 ft/min).

4.3.2 Dose Uniformity Ratio Description for 5 MeV X-ray Irradiation

The dose uniformity ratio, D_{max}/D_{min}, defined in Section 4.1.4 was obtained in HD-810 films for the three apple-phantom samples irradiated at a target dose of 0.6 kGy. The results were as follows.

Figure 4-68 shows that the dose uniformity ratio for all apple-phantom samples was mostly uniform passed 2 mm from the surface. The high values of the uniformity ratio located near the top resulted due to the low absorbed dose values near the bottom regions of the apple-phantom.

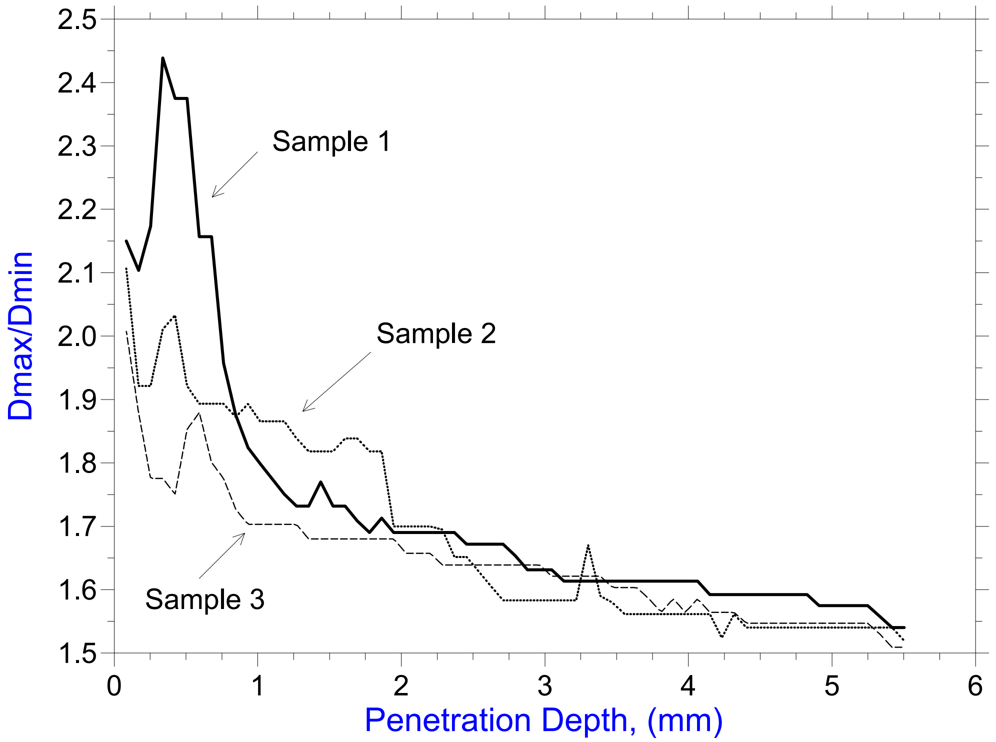

Figure 4-68. Dose uniformity ratio, D_{max}/D_{min}, for 5 MeV X-Ray irradiation.

In spite of this, the ratio decreased almost linearly after 2 mm from the surface of the apple-phantom. The dose uniformity ratio of the X-rays in the apple-phantoms decreased linearly showing the variation in dose from the top to the bottom of the phantom.

This linear decrease resulted due to the X-ray spectrum that shows the average photon energy was 0.693 MeV. The rest of the photons followed the energy distribution shown in Figure 4-65. Because of this, Figure 4-66 shows higher dose values located at the top of the apple-phantom compared to the bottom region. Also, the apple-phantom was oriented with its top (stem) oriented closer to the X-ray exit window resulting in higher dose values in the top regions.

4.3.3 Apple-Phantom Slices

Figure 4-69 shows the methyl yellow energy deposition contour in the methyl yellow apple-phantom. The highest dose found was 0.4 kGy located at the left, right and bottom regions of the contour. The lack of continuity shown in the contour was the result of chloroform evaporation on the top of the apple. Similar results are shown in Appendix F (Figure F-5 to Figure F-8).

Indeed, the bottom region appeared to be uniformly irradiated as shown in Figure 4-70. Remarkably the methyl yellow phantom responded similarly to the radiochromic film in the bottom region with approximately 0.4 kGy as seen in Figure 4-70 and Figure 4-67 at a depth of 68 mm. For regions near the top the methyl yellow showed uniformity in the sense that the dose remained constant up to a certain penetration depth before it became very small due to the lack of continuity in the sample.

In dose terms the regions near the top surface were not able to produce the same results as the film. In fact, the maximum dose found was 0.4 kGy at the top and bottom showing that the methyl yellow contour saturated near the top regions of the sample due to the higher absorbed dose.

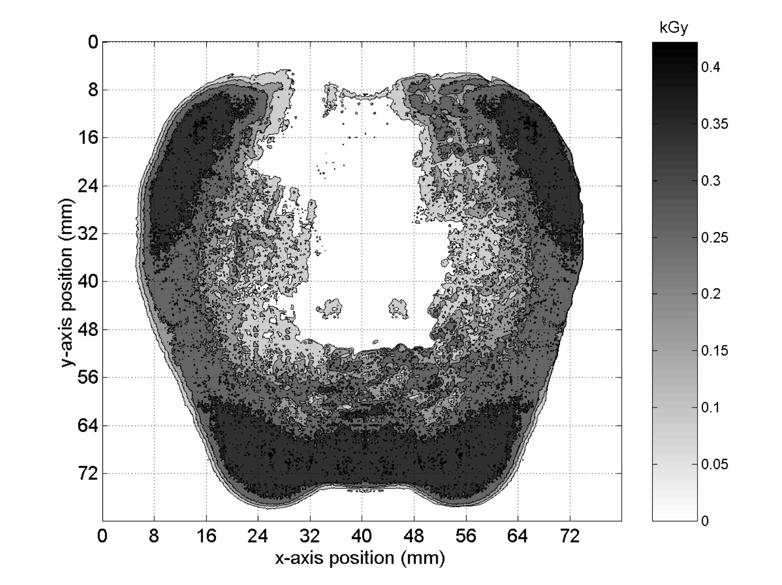

Figure 4-69. Methyl yellow apple-phantom contour dose distribution in kGy using a custom-made polystyrene holder and a 5 MeV LINAC accelerator with a conveyor speed of 0.61 m/min (2 ft/min).

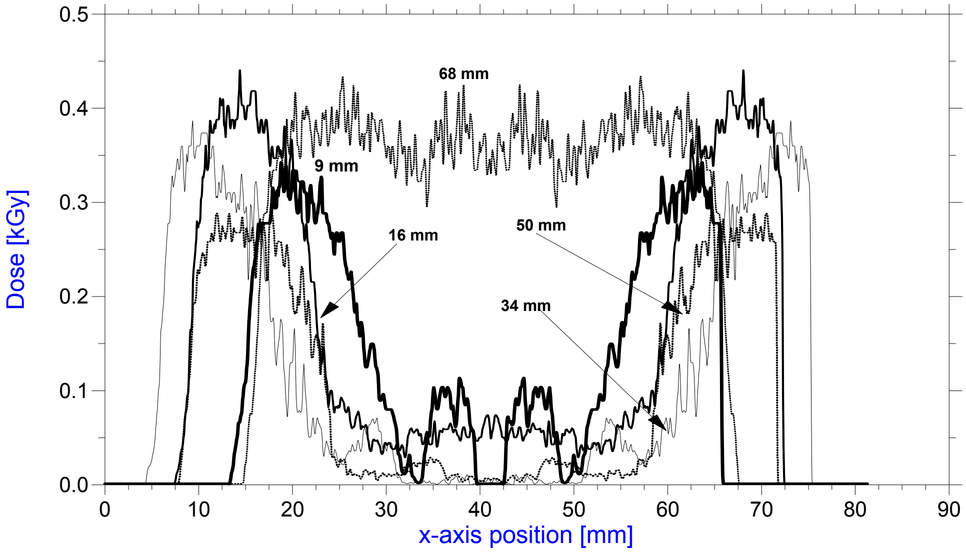

Figure 4-70. Methyl yellow apple-phantom contour dose distribution in kGy using a custom-made polystyrene holder and a 5 MeV LINAC accelerator with a conveyor speed of 0.61 m/min (2 ft/min).

CHAPTER V

CONCLUSIONS AND RECOMMENDATIONS

The conclusions described below were relevant to all the experimental results performed in this research.

1. The use of a phantom (to represent a complex shaped food) composed of paraffin wax, chloroform, and methyl yellow was successful to detect absorbed radiation using 1.35 MeV electrons. A solid state three dimensional “apple” phantom helped to visually determine absorbed dose in the phantom vertical axis of symmetry throughout its periphery.
2. The chemical solution response to absorbed dose was found to be non-linear for 1.35 MeV electrons for doses ranging from 10 Gy to 500 Gy. The optimal operating range for the chemical solution was between 100 and 300 Gy.
3. A transmission flatbed scanner proved to be successful and economical tool to obtain dose deposition and dose depth profiles of apple-phantom slices 3.175 mm thick using Matlab. Image Processing was performed in Red Green Blue (RGB) color space where it was found that the Green channel offered the best response to absorbed doses between 10 and 500 Gy using 1.35 MeV electrons.

4. A cutting band-saw was found also successful to produce uniform cuts of the methyl yellow apple-phantoms. In particular, for this research apple-phantom contours of 3.175 mm ± 5% were obtained
5. Vacuum packaging of apple-phantoms with polyethylene bags also proved to be successful to evacuate the air gap that existed between the methyl yellow apple faces and the HD-810 film.

5.1 E-Beam Irradiation Using Van De Graaff Accelerator

Dose deposition and dose depth profiles in methyl yellow apple-phantoms and HD-810 film showed that:

1. The 90 degree orientation of the y-axis toward the e-beam, for both HD-810 film and the methyl yellow apple contours, showed that high dose were located in areas near the left and right bottom regions for both 50 and 100 Gy target doses. Surface regions near the top and bottom, between 80 to 100 degrees and 240 to 300 degrees, respectively, were not irradiated. The dose depth distribution plots for both film and methyl yellow apple were nearly the same showing no irradiation exposure at the top and bottom areas, however the methyl yellow profile showed more penetration at the sides compared to the film.
2. Increasing the target dose from 50 to 100 Gy showed to improve the distribution along the left and right side of the apple; however, no measurable penetration depths were found at the top and bottom.
3. The apple-phantom showed very close uniformity ratios between 2.5 and 2.0 for penetration depths of 1.5 mm and 3 mm at the 45 and 22.5-degree orientations.

4. The 45 degree orientation improved the treatment in the top and bottom regions of the apple. The HD-810 film provided treatment between 80-100 degrees (top) and 240-300 degrees (bottom). The methyl yellow phantom contour showed the same tendency at the bottom, but not at the top due to chloroform evaporation.
5. The dose uniformity ratio improved significantly showing a more uniform results for both the film and methyl yellow phantom contours. Specifically, the ratio stayed most uniform between 1.5 and 2.0 for penetration depths of 0.5 to 3.5 mm from the phantoms surface. As a result, it was found that the treatment at 45 degrees treatment produced more uniform results for wider penetration depths.
6. The methyl yellow boundary region was reduced at 45 degrees orientations producing penetration depths comparable to those obtained with the film.
7. The 22.5 degree orientation resulted in the largest exposure for both film and methyl yellow phantom contours. The largest penetration depth was in average 3.0 mm throughout the periphery of the phantom as confirmed with the film. The top and bottom regions between 80 to 100 degrees and 240 to 300 degrees were completely exposed showing high dose values.
8. Regions located at the top and bottom left side, top right side, and bottom right side showed also very high doses compared to the rest of the apple periphery. The methyl yellow phantom contour demonstrated the same tendency but it did not show any treatment at the top (~ 75 to 100 degrees) due to chloroform evaporation.

9. The dose uniformity ratio at α=22.5 degrees was surprisingly higher to that at α=45 degrees showing that the apple-phantoms were over-exposed at this orientation. In this case, the apple-phantom was completely parallel to the e-beam thus the electron incidence angle was normal to the surface vectors producing the least scattering and highest penetration depths throughout the apple periphery.
10. In general, tilting the apple-phantom towards the e-beam source resulted in more uniform irradiations. However, it was found that the phantoms could be over-exposed when oriented exactly parallel to the e-beam at α=22.5 degrees. The 45 degree orientation ensured uniformity throughout the phantom periphery for wider penetration depths without overexposing the product. In contrast, the 90 degree orientation was found to be the least effective at the top and bottom regions.
11. The methyl yellow apple-phantom worked fine to detect absorbed radiations at 50 and 100 Gy. Also, it works as an indicator to show visually in any direction where the radiation treatment was performed.

5.2 E-Beam Irradiation Using 10 MeV SureBeam LINAC

Dose distribution and dose depth profiles in the methyl yellow apple-phantoms and HD-810 film showed that:

1. For a Lucite thickness of 3 cm (target dose of 1.0 kGy), the HD-810 film confirmed a very uniform irradiation treatment at the top and bottom regions with a maximum dose of 1.2 kGy located at the top left region of the apple. As expected, the dose decreased in a linear tendency from the surface to the highest penetration depth until the electrons lost all their energy.
2. The methyl yellow apple contour saturated due to the high absorbed dose compared to its maximum response. Nonetheless, the same absorption trend was found with the highest doses located at the top and bottom regions of the apple.
3. For a Lucite thickness of 4 cm (target dose of 0.4 kGy), the irradiation treatment was completely uniform as indicated by the radiochromic film. The highest doses were located at the left and right sides showing the scattering effects due to the phantom positioning inside the box holder. Approximately a maximum dose of 0.5 kGy was found at all the three planes analyzed from top to bottom.
4. The methyl yellow apple-phantom contour responded better using a thickness of 4 cm of attenuating material. The phantom contour indicated the electron response very well at the top and bottom regions of the apple, also showing a decreasing linear response to dose from the surface to the largest penetration depth. However, due to saturation, the methyl yellow phantom showed maximum

doses of 0.35 kGy at the left and right sides of the phantom compared to 0.8 kGy for the film.

5. For a Lucite thickness of 3 cm (target dose of 0.2 kGy), the radiochromic film confirmed showed complete uniformity throughout most of the apple-phantom periphery. Higher dose spots were located at the left side of the samples due to electron scattering. The average dose at the top and bottom in the three planes analyzed was 0.3 kGy.
6. The methyl yellow apple-phantom indicated a maximum dose of 0.25 kGy at the left side of the apple. It was found also that the dose decreased linearly with increasing penetration depth.
7. In general, the methyl yellow apple-phantom contours provided a great visual confirmation as an indicator to detect the absorbed radiation using the 10 MeV LINAC. The methyl yellow phantom responded better to lower doses and its contours resembled closely to those of the film. The high doses located at the left and right sides of the phantom in both film and methyl yellow contours were produced entirely due to electron scattering with the polystyrene walls of the holder box.

5.3 X-Ray Irradiation Using 5 MeV SureBeam LINAC

Dose distribution and dose depth profiles in the methyl yellow apple-phantoms and HD-810 film showed that:

1. The X-ray irradiation completely penetrated the entire apple-phantom from top to bottom. The highest doses observed with the film were located at the top region of the phantom where the X-ray beam hit first the apple. The entrance dose throughout most of the top region was approximately 0.6 kGy while the dose at the bottom region was approximately 0.4 kGy.
2. X-ray irradiation was quite uniform across the apple from its left to right sides at different penetration depths from its top surface. It was found that the dose decreased approximately 25% from the top to the bottom in the radiochromic film.
3. The methyl yellow apple-phantom contour responded very well at depths close to the surface. However, the central region of the phantom contour did not show any irradiation because of the image noise found at the central regions of the contours. Image noise resulted from air bubbles collected at the central part of the phantom slices. In fact, the RGB intensity raw data showed complete penetration scheme just like the radiochromic film. The maximum doses found were 0.4 kGy at the top and bottom. In the bottom region the methyl yellow phantom contour was quite uniform and predicted a dose of 0.4 kGy just like the film. At the top, however, the dose was not the same due to saturation.

5.4 Further Recommendations

The immediate solutions that can improve the efficiency of the methyl yellow apple-phantom include:

1. Producing a new mold where the pouring hole is placed at a side wall of the phantom to avoid chloroform evaporation in critical areas such as the top and bottom regions of the phantom.
2. Reducing the paraffin, chloroform, and methyl yellow solution pouring temperature as low as possible (below 65 ^{o}C) to produce faster cooling and less chloroform evaporation.
3. Pour the paraffin, chloroform, and methyl yellow solution very slowly to avoid producing air bubbles that create image noise.
4. Reducing the thickness of the phantom contour with a different cutting technique that can produce cleaner cuts resulting in less image noise, and most accurate intensity measurements.
5. Develop a new calibration curve using the blue channel to try improving the maximum dose response range.
6. Analyze quantitatively the effect of chloroform evaporation in the solid to determine more accurately the absorbed dose.
7. Increase the mass percentage of microcrystalline wax (above 1%) in the paraffin, chloroform, and methyl yellow solution to improve the strength of the solid.
8. Implement image processing analysis using Fast Fourier Transforms (FFT) as a possible alternative to image noise reduction.

REFERENCES

Alderson S.W., Lanzl L.H., Rollins M., and Spira J. 1962. An instrumented phantom system for analog computation of treatment plans. *Am. J. Roentgenol*. 87: 185-195.

Alpen, E.L. 1998. *Radiation Biophysics*. 2nd ed. New York: Academic Press.

Alva, H., Mercado-Uribe, H., Rodriguez-Villafuerte, M., and Brandan, M.E. 2002. The use of a reflective scanner to study radiochromic film response. *Phys. Med. Bio*. 47(16): 2925-2933.

ASTM. 2002. E51540. Standard practice for use of a radiochromic liquid dosimetry system. In *Annual Book of ASTM Standards.* Section 5. Vol. 12.02: Apparatus, 162-170. West Conshohocken, Pa.: ASTM International

Attix, F.H. 1986. *Introduction to Radiological Physics and Radiation Dosimetry*. New York: John Wiley & Sons.

Aydarous, A.S., Darley, P.J., and Charles, M.W. 2001. A wide dynamic range, high-spatial-resolution scanning system for radiochromic dye films. *Phys. Med. Bio*. 46(5): 1379-1389.

Barakat, M.F., El-Salamawy, K., El-Banna, M., Abdel-Hamid, M., and Taha, A. 2001. Radiation effects on some dyes in non-aqueous solvents and in some polymeric films. *Radiat. Phys. Chem*. 61(2): 129-136.

Bazioglou, M., and Kalef-Ezra, J. 2001. Dosimetry with radiochromic films: A document scanner technique, neutron response, applications. *App. Radiat. Iso*. 55(3): 339-345.

Borsa, J., Chu, R., Sun, J.S., Linton, N., and Hunter, C. 2002. Use of CT scans and treatment planning software for validation of the dose component of food irradiation protocols. *Radiat. Phys. Chem*. 63(3-6): 271-275.

Burdick, H.E. 1997. *Digital Imaging: Theory and Applications*. New York: McGraw Hill.

Butson, M.J., Yu, P. K. N., Cheung, T., and Metcalfe, P. 2003. Radiochromic film for medical radiation dosimetry. *Materials Science & Engineering R-Reports*. 41(3-5): 61-120.

Chao, A., and Tigner, M. 1999. *Handbook of Accelerator Physics and Engineering*. River Edge, N.J.: World Scientific Publishing Co.

Clark, G. L. 1963. *The Encyclopedia of X-rays and Gamma Rays*. New York: Reinhold Publishing Corp.

Clark, G. L., and Bierstedt, P.E. 1955. X-ray dosimetry by radiolysis of some organic solutions: I. Dithizone and methyl yellow solutions. *Radiat. Res*. 2: 199-218.

Eichholz, G.G., and Poston, J.W. 1979. *Principles of Nuclear Radiation Detection*. Ann Arbor, Mich.: Ann Arbor Science Publisher Inc.

Fulton, W. 1996. A few scanning tips. Available from: http://www.guides.sk/scantips2/index.html#menu (accessed Dec 14, 2003)

Gann, R.G. 1999. *Desktop Scanners: Image Quality Evaluation*. Upper Saddle River, N.J.: Prentice-Hall.

Gonzalez, R.C., and Woods, R.E. 1992. *Digital Image Processing*. Reading, Mass.: Addison-Wesley Publishing.

Gore, J.C., Ranade, M., Maryanski, M.J., and Schulz, R.J. 1996. Radiation dose distributions in three dimensions from tomographic optical density scanning of polymer gels: I. Development of an optical scanner. *Phys. Med. Biol*. (41):2695-2704.

Hornak, J.P. 1996. The basics of MRI: Imaging hardware. http://www.cis.rit.edu/htbooks/mri/ (accessed May 12, 2004).

Humphries, S. 1986. *Principles of Charged Particle Acceleration*. New York: John Wiley.

IAEA Technical Reports Series No. 409. 2002. Dosimetry for food irradiation. Vienna, Austria.: IAEA.

ICRU. (1984). Radiation dosimetry: Electron beams with energies between 1 and 50 MeV. Bethesda, MD.: International Commission on Radiation Units and Measurements, Report No. 35.

ICRU. (1989). Tissue substitutes in radiation dosimetry and measurement. Bethesda, MD.: International Commission on Radiation Units and Measurements, Report No. 44.

International Specialty Products Corporation. Gafchromic® HD-810 radiochromic dosimetry film and D-200 pre-formatted dosimeters for high-energy photons: Configuration, specifications, and performance data. Available from: http://www.ispcorp.com/products/dosimetry/content/products/radiochromic/radoback.html (accessed September 20, 2003).

Knoll, G. F. 1999. *Radiation Detection and Measurement*, 3rd ed. Upton, N.Y.: John Wiley & Sons.

Kovacs, A., Baranyai, M., Wojnarovits, L., McLaughlin, W.L., Miller, S.D., Miller, A., Fuochi, P.G., Lavalle, M., and Slezsak, I. 2000. Application of the Sunna dosimeter film in gamma and electron beam radiation processing. *Radiat. Phys. Chem*. 57(3-6): 691-695.

Kovacs, A., Baranyai, M., Wojnarovits, L., Miller, S., Murphy, M., McLaughlin, W.L., Slezsak, I. and Kovacs, A.I. 2002. Applicability of the Sunna dosimeter for food irradiation control.*Radiat. Phys. Chem*. 63(3-6):777-780.

Kovacs, A., Wojnarovits, L., Kurucz, C., Al-Sheikhly, M., and McLaughlin, W.L. 1998. Large-scale dosimetry using dilute methylene blue dye in aqueous solution. *Radiat. Phys. Chem*. 52(1-6):539-542.

Livingston, M.S., and Blewett, J.P. 1962. *Particle Accelerators*. Garden City, N.Y.: McGraw-Hill, Inc.

Loveland, W., Morrissey, D.J., and Seaborg, G.T. 2000. *Modern Nuclear Chemistry*. New York: John Wiley & Sons.

McMurray, C.H., Patterson, M.F., and Stewart, E.M.1998. Food irradiation: A question of preservation. *Chemistry and Industry*. 1: 433-438.

McLaughlin, W.L., Yundong, C., Soares, C.G., Miller, A., Van Dyk, G., and Lewis, D.F. 1991. Sensitometry of the response of a new radiochromic film dosimeter to gamma-radiation and electron-beams. *Nucl. Inst. & Meth A*. 302(1):165-176.

Miyahara, M., Ito, H., Ueno, K., Yamase, Y., and Toyoda, M. 2002a. Evaluation of several dosimeters for identification of irradiated foods using a 5 MeV electron beam. *Journal of Health Science*. 48(1):37-41.

Miyahara, M., Nagasawa, T., Kamimura, T., Ito, H., Toyoda, M., and Saito, Y. 2002b. Identification of irradiation of boned chicken by determination of o-tyrosine and electron spin resonance spectrometry. *Journal of Health Science*. 48(1):79-82.

Murphy, M.K., Miller, S.D., Kovacs, A., McLaughlin, W.L., and Slezsak, I. 2002. Characterization of a new photo-fluorescent film dosimeter for high-radiation dose applications. *Radiat. Phys. Chem*. 63(3-6):751-754.

Olsson, S., and Bergstrand, E.S. 2001. Calibration of Alanine Dosimeters. Report 92. Linkopig, Sweden: ISRN.

Ouattara, B., Sabato, S.F., and Lacroix, M. 2002.Use of gamma-irradiation technology in combination with edible coating to produce shelf-stable foods. *Radiation Physics and Chemistry*. 63(3-6):305-310.

Potsaid, M.S., and Irie, G. 1961. Paraffin base halogenated hydrocarbon chemical dosimeters. *Radiology*. 77:61-65.

Potsaid, M.S., and Irie, G. 1963. An in-phantom radiation detector. *New England J. Med*. (23): 1135-1139.

Regulla, D.F., and Deffner, U. 1982. Dosimetry by electron-spin-resonance spectroscopy of alanine. *Int. J. App. Rad. & Iso*. 33(11):1101-1114.

Schaffer, J.P., Saxena, A., Sanders, T.H., Antolovich, S.D., and Warner, S.B. 2000. *Science and Design of Engineering Materials*. Boston: McGraw-Hill.

Scharf, W.H. 1994. *Biomedical Particle Accelerators*. New York: American Institute of Physics.

Shani, G. 1991. *Radiation Dosimetry: Instrumentation and Methods*. Boca Raton, Fla.: CRC Press.

Shani, G. 2001. *Radiation Dosimetry: Instrumentation and Methods*. 2nd *ed*. Boca Raton, Fla.: CRC Press.

Stevens, M.A., Turner, J.R., Hugtenburg, R.P., and Butler, P.H. 1996. High-resolution dosimetry using radiochromic film and a document scanner. *Physics in Medicine and Biology*. 41(11):2357-2365.

Takács, J. 1997. *Energy Stabilization of Electrostatic Accelerators*. New York: John Wiley & Sons.

Tarte, B.J., Jardine, P.A., VanDoorn, T., Nitschke, K.N., and Poulsen, M.G. 1997. Development of a CCD array imaging system for measurement of dose distributions in doped agarose gels. *Med. Phys*. 24(9):1521-1525.

Turner, J.E. 1996. *Atoms, Radiation, and Radiation Protection*. 2^{nd} ed. New York: John Wiley & Sons.

Wakabayashi, M., Irie, G., Shibata, S., Kawanishi, S., Suzaki, K., Sugawara, T., Yamada, E., Iwasaki, N., Mitsuhashi, H., and Oyama, O. 1963. Studies on radiation dosimetry by a solid color changing substance. *J. Radiat. Res*. 4: 68-79.

Wilson, E. J. 2001. *An Introduction to Particle Accelerators*. New York: Oxford University Press.

Wolodzko, J.G., Marsden, C., and Appleby, A. 1999. CCD imaging for optical tomography of gel radiation dosimeters. *Med. Phys*. 26(11): 2508-2513.

Yoshino, T., Furukawa, I., and Kawamura, F. 1981. Chemical changes in the chloroform-paraffin-dye system irradiated with ^{60}Co gamma-rays. II. Formation of hydrogen chloride and absorption energy in the solid. *J. Radiat. Res*. 22: 395-404.

Yoshino, T., Sakaue, M., and Shimizu, Y. 1979. Chemical changes in the chloroform-paraffin-dye system irradiated with ^{60}Co gamma-rays. I. Examinations on variable factors. *J. Radiat. Res*. 20: 196-208.

Young, H.D., and Freedman, R.A. 1996. *University Physics*. 9th ed. Cambridge, N.Y.: Addison-Wesley.

Zhongli, C., Xiaoning, P., Hunting, D., Cloutier, P., Lemay, R., and Sanchez, L. 2003. Dosimetry of ultrasoft x-rays (1.5 keV Al-K alpha) using radiochromatic films and colour scanners. *Phys. Med. Bio*. 48(24):4111-4124.

APPENDIX A

PRELIMINARY RESULTS: VAN DE GRAAFF ACCELERATOR

A.1.1 VDG Calibration Using Parallel Plate Ionization Chamber and Farmer Dosimeter

The following discussion refers to the calibration of a 2 MeV electrostatic Van de Graaff (VDG) accelerator. The term *calibration* refers explicitly to the measurement of the absorbed dose irradiation at a point in *space* defined as *irradiation point P* positioned in front of the electron beam exit window as shown in Figure A-1.

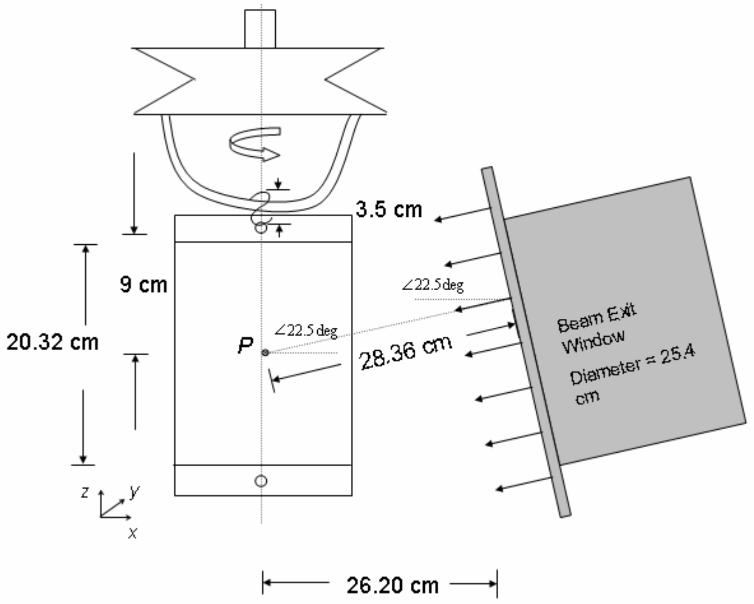

Figure A-1. Lateral view of irradiation point P positioned in front of exit window

Absorbed dose, *D*, measured at point *P* was performed by means of a Farmer absolute ionization chamber containing a volume of 0.03 cm^3 at a distance of 28.36 cm parallel to the exit window. A parallel-plate transmission ion chamber filled with air was used to measure the amount of charge, *C*, resulting from radiation exposure in air between the plates. Next, the VDG accelerator was calibrated in terms of the ratio of charge to absorbed dose (exposure in air[4]), $R_{(C/D)}$, specifically at point *P*.

Multiple experiments were carried out and data measurements over time were categorized and ranked according to modifications made to the transmission ionization chamber until stable charge measurements resulted. Table A-1 shows the modifications classified in two sets A and B as follows:

Table A-1. Lucite Parallel Plate Transmission Ionization Chamber Specifications

	SET A	*SET B*
(1) Parallel plate hole diameter, *D*, (cm)	19.05	21.59
(2) Wall separation or thickness, *t*, (cm)	0.635	0.3175
(3) Chamber air volume , *V*, (cm^3)	180.89	116.17
(4) Washers (3.175 mm thickness) between air volume	Yes	No
(5) Cable type	Bare copper wire	Coaxial cable
(6) Connector insulation	No	Yes
(7) Common brass ground connection	No	Yes

---

[4] Shani , "Radiation Dosimetry: Instrumentation and Methods", 3. Absorbed Dose defined in terms of exposure in air as $D_{air} = 0.877*R$ [rad] when R =1 Roentgen

Part I. Calibration Results for the Parallel Plate Transmission Ion Chamber Set A

$R_{(C/D)}$ vs. Charge at 45 V

The discussion herein describes the development of a calibration curve for the Van de Graaff accelerator in terms of the ratio of charge to absorbed dose at irradiation point *P* for a particular configuration of the transmission ionization chamber. During this test the electron Van de Graaff dose rate was typically 0.01 G/hr (1 rad / hr) decreasing over time, and an electron beam current of 4 μA. Since the startup, the dose rate and the current have been typical during operation.

The following measurements were obtained at 24 °C and 20 % rh for 1.35 MeV electrons at the irradiation point *P*.

Table A-2. Parallel Plate Ionization Chamber Calibration Data at 45 volts

Farmer Ionization Chamber Dose, *D*	Farmer Ionization Chamber Dose, *D*	Transmission Ion Chamber Charge, *C*	$R_{(C/D)}$	Transmission Ion Chamber Voltage
(kRoentgens)	(kGy)	(Cx10^{-8} coulombs)	(Cx10^{-8} coulombs / kGy)	(V)
9.930	0.087	22746	261190	45
8.550	0.075	20004	266779	45
9.030	0.079	21196	267650	45
8.710	0.076	20531	268777	45

Mean $R_{(C/D)}$	266099
Std Dev $R_{(C/D)}$	3373
Std Dev $R_{(C/D)}$ (%)	**1.27%**

The results shown in Table A-2 were obtained at 45 volts as the saturation voltage for the ionization current. The charge to dose ratio variability obtained was 1.27%. Figure A-2 below shows variability of the charge to dose ratio, $R_{(C/D)}$, at 45 volts.

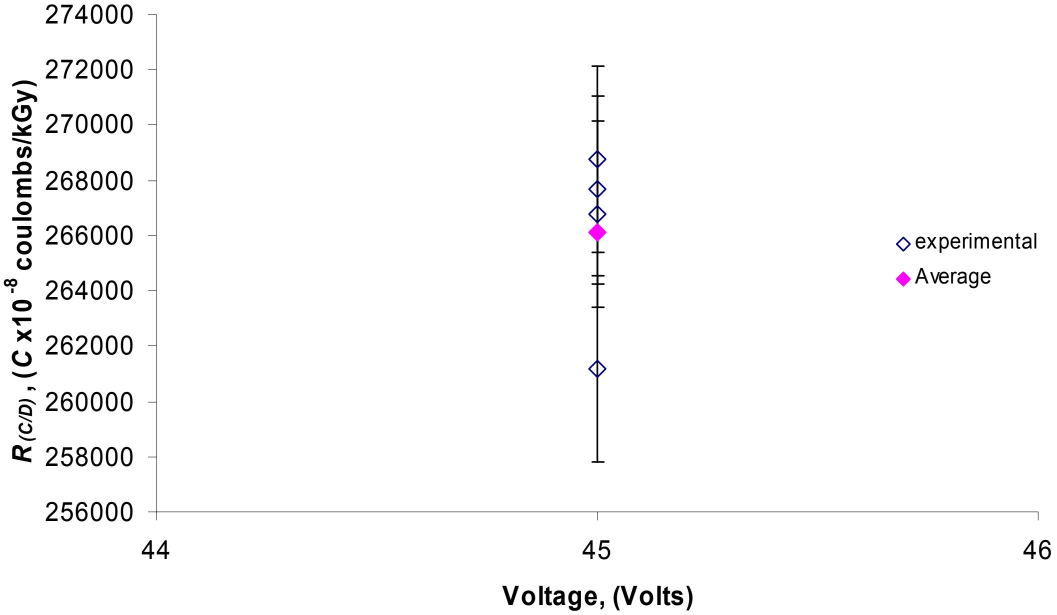

Figure A-2. Van de Graaff Calibration. Ratio of the transmission ion chamber charge to the Farmer absorbed dose.

Next, a plot of the Farmer ionization chamber dose, *D*, vs. the Transmission Ion chamber charge, *C*, shows the average ratio of charge to dose for Table A-2 data.

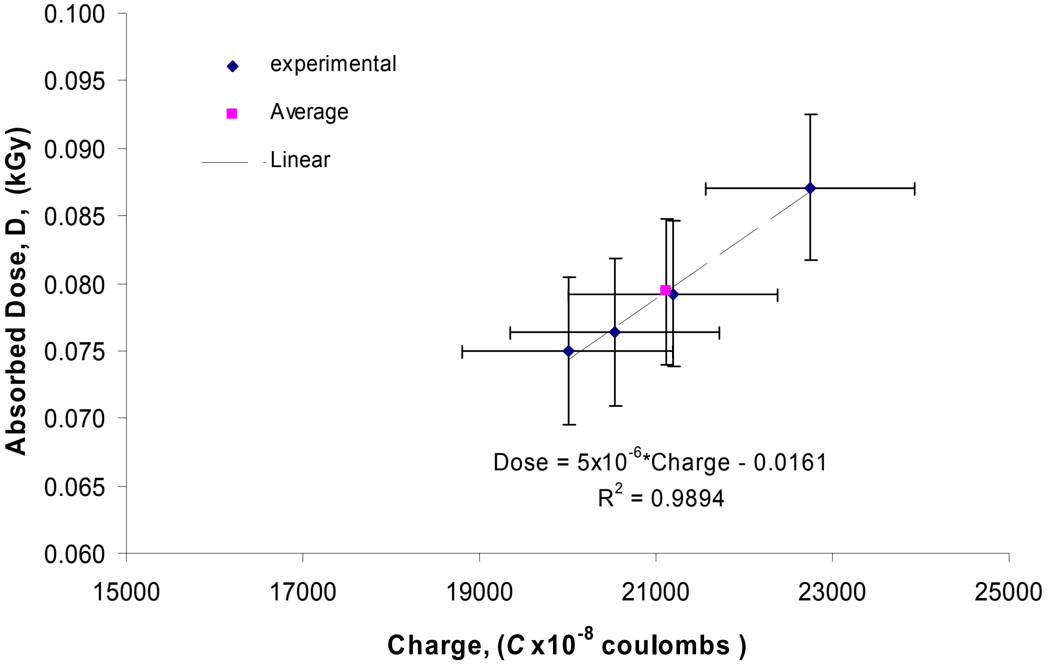

Figure A-3. Absorbed Dose vs. Charge with Transmission Ion Chamber at 45 Volts.

Figure A-2 shows a linear relationship with an $r^2 = 0.9894$ between absorbed dose and charge at 45 volts. The standard deviation resulted in 6.81% and 5.63% for the dose and charge respectively.

Part II. Calibration of the Parallel Plate Transmission Ion Chamber Set B

Voltage vs. $R_{(C/D)}$ Response

The results discussed herein correspond to modifications performed in the Transmission Ion chamber as shown in Table A-1. The reproducibility of the dose measurement, *D*, at point *P* was analyzed in terms of the charge to dose ratio, $R_{(C/D)}$, illustrated previously. The electron Van de Graaff dose rate and beam current were the same as described in Set A.

Results from Set A demonstrated a very small variation of $R_{(C/D)}$; however, at that point in time it was the only test performed using the assumption of 45 volts as the voltage required to produce the charge saturation in the Transmission Ion chamber volume. Several tests were conducted to find the optimal voltage required for the transmission ion chamber operation. Particularly, individual 9 volts (V) batteries were connected in series to provide measurements in the range of 18 V to 135 V.

The modifications described in Table A-1 Set B did not occur at the same time. However, the results that follow are presented providing a brief explanation of which of the modification events occurred in chronological manner. Also, all measurements in each table were taken consecutively after a modification was performed.

Tables A-2.1 through A-2.11 show the experimental data obtained when bare copper wires connecting the high voltage terminal and signal circuits in the Transmission Ion chamber were replaced with coaxial cables. It was suspected that ionized charges may have been collecting in the bare copper wire surfaces which could lead to erroneous measurements. Coaxial cables are coated with an insulator that protect better against any induced ionization which may occur in bare copper wires.

The results in Table A-2.1 through Table A-2.5 showed high variations in $R_{(C/D)}$ ranging from 9 % to 18%. It may be possible that such variation in the charge to dose ratio may be produced due to a time effect. In order to analyze this effect, several data sets were obtained after a time interval. The data in Table A-2.6 was used as a reference, and measurements in Tables A-2.7 and A-2.8 were read with 5 and 10 minutes in between tests resulting in 6% and 4.20% respectively. Further measurements were obtained in the same fashion resulting in 6.45% and 4.32% variation in Tables A-2.10 and A-2.11. The data in Tables A-2.12 and A-2.13 showed outlier values which are of unknown explanation, and were not used for statistic calculations.

Table A-2.1 Parallel Plate Ionization Chamber Calibration Data

Farmer Ionization Chamber Dose, *D*	Farmer Ionization Chamber Dose, *D*	Transmission Ion Chamber Charge, *C*	$R_{(C/D)}$	Transmission Ion Chamber Voltage
(kRoentgens)	(kGy)	(Cx10^{-8} coulombs)	(Cx10^{-8} coulombs / kGy)	(V)
7.160	0.063	11868	189001	45
8.045	0.071	11921	168961	45
6.530	0.057	12018	209855	45
6.550	0.057	12453	216787	45

Mean $R_{(C/D)}$	196151
Std Dev $R_{(C/D)}$	21634
Std Dev $R_{(C/D)}$ (%)	**11.03**

Table A-2.2 Parallel Plate Ionization Chamber Calibration Data

Farmer Ionization Chamber Dose, *D*	Farmer Ionization Chamber Dose, *D*	Transmission Ion Chamber Charge, *C*	$R_{(C/D)}$	Transmission Ion Chamber Voltage
(kRoentgens)	(kGy)	(Cx10^{-8} coulombs)	(Cx10^{-8} coulombs / kGy)	(V)
4.830	0.042	12403	292806	63
4.840	0.042	12686	298868	63
7.390	0.065	20167	311170	63

Mean $R_{(C/D)}$	300948
Std Dev $R_{(C/D)}$	9357
Std Dev $R_{(C/D)}$ (%)	**3.11**

Table A-2.3 Parallel Plate Ionization Chamber Calibration Data

Farmer Ionization Chamber Dose, *D*	Farmer Ionization Chamber Dose, *D*	Transmission Ion Chamber Charge, *C*	$R_{(C/D)}$	Transmission Ion Chamber Voltage
(kRoentgens)	(kGy)	(Cx10^{-8} coulombs)	(Cx10^{-8} coulombs / kGy)	(V)
7.080	0.062	20381	328241	81
6.120	0.054	19915	371047	81
6.170	0.054	20396	376930	81

Mean $R_{(C/D)}$	358739
Std Dev $R_{(C/D)}$	26576
Std Dev $R_{(C/D)}$ (%)	**7.41**

Table A-2.4 Parallel Plate Ionization Chamber Calibration Data

Farmer Ionization Chamber Dose, *D*	Farmer Ionization Chamber Dose, *D*	Transmission Ion Chamber Charge, *C*	$R_{(C/D)}$	Transmission Ion Chamber Voltage
(kRoentgens)	(kGy)	(Cx10^{-8} coulombs)	(Cx10^{-8} coulombs / kGy)	(V)
6.700	0.059	19582	333260	81
5.690	0.050	20038	401553	81
8.290	0.073	20003	275132	81

Mean $R_{(C/D)}$	336648
Std Dev $R_{(C/D)}$	63278
Std Dev $R_{(C/D)}$ (%)	**18.80**

Table A-2.5 Parallel Plate Ionization Chamber Calibration Data

Farmer Ionization Chamber Dose, *D*	Farmer Ionization Chamber Dose, *D*	Transmission Ion Chamber Charge, *C*	$R_{(C/D)}$	Transmission Ion Chamber Voltage
(kRoentgens)	(kGy)	(Cx10^{-8} coulombs)	(Cx10^{-8} coulombs / kGy)	(V)
6.130	0.054	20489	381119	81
6.160	0.054	20210	374099	81
7.500	0.066	20252	307898	81
6.930	0.061	20259	333338	81

Mean $R_{(C/D)}$	349114
Std Dev $R_{(C/D)}$	34623
Std Dev $R_{(C/D)}$ (%)	**9.92**

Table A-2.6 Parallel Plate Ionization Chamber Calibration Data

Farmer Ionization Chamber Dose, *D*	Farmer Ionization Chamber Dose, *D*	Transmission Ion Chamber Charge, *C*	$R_{(C/D)}$	Transmission Ion Chamber Voltage
(kRoentgens)	(kGy)	(Cx10^{-8} coulombs)	(Cx10^{-8} coulombs / kGy)	(V)
6.900	0.061	20485	338522	99
5.590	0.049	20474	417630	99
5.710	0.050	20475	408873	99
5.870	0.051	20078	390016	99
5.730	0.050	20798	413873	99

Mean $R_{(C/D)}$	407598
Std Dev $R_{(C/D)}$	12258
Std Dev $R_{(C/D)}$ (%)	**3.01**

Table A-2.7 Parallel Plate Ionization Chamber Calibration Data

Farmer Ionization Chamber Dose, *D*	Farmer Ionization Chamber Dose, *D*	Transmission Ion Chamber Charge, *C*	$R_{(C/D)}$	Transmission Ion Chamber Voltage
(kRoentgens)	(kGy)	(*C* x10^{-8} coulombs)	(*C* x10^{-8} coulombs / kGy)	(V)
5.590	0.049	20739	423035	117
5.100	0.045	21035	470298	117
5.120	0.045	20979	467213	117
6.010	0.053	22161	420451	117

Mean $R_{(C/D)}$	445249
Std Dev $R_{(C/D)}$	27192
Std Dev $R_{(C/D)}$ (%)	**6.11**

Table A-2.8 Parallel Plate Ionization Chamber Calibration Data

Farmer Ionization Chamber Dose, *D*	Farmer Ionization Chamber Dose, *D*	Transmission Ion Chamber Charge, *C*	$R_{(C/D)}$	Transmission Ion Chamber Voltage
(kRoentgens)	(kGy)	(*C* x10^{-8} coulombs)	(*C* x10^{-8} coulombs / kGy)	(V)
5.400	0.047	20460	432028	135
5.090	0.045	21016	470796	135
5.180	0.045	20828	458478	135
5.480	0.048	20880	434461	135

Mean $R_{(C/D)}$	448941
Std Dev $R_{(C/D)}$	18835
Std Dev $R_{(C/D)}$ (%)	**4.20**

Table A-2.9 Parallel Plate Ionization Chamber Calibration Data

Farmer Ionization Chamber Dose, *D*	Farmer Ionization Chamber Dose, *D*	Transmission Ion Chamber Charge, *C*	$R_{(C/D)}$	Transmission Ion Chamber Voltage
(kRoentgens)	(kGy)	(*C* x10^{-8} coulombs)	(*C* x10^{-8} coulombs / kGy)	(V)
4.650	0.041	21310	522554	135
4.680	0.041	21466	523005	135
4.630	0.041	21026	517817	135

Mean $R_{(C/D)}$	521125
Std Dev $R_{(C/D)}$	2874
Std Dev $R_{(C/D)}$ (%)	**0.55**

Table A-2.10 Parallel Plate Ionization Chamber Calibration Data

Farmer Ionization Chamber Dose, *D*	Farmer Ionization Chamber Dose, *D*	Transmission Ion Chamber Charge, *C*	$R_{(C/D)}$	Transmission Ion Chamber Voltage
(kRoentgens)	(kGy)	(*C* x10^{-8} coulombs)	(*C* x10^{-8} coulombs / kGy)	(V)
4.860	0.043	21445	503142	135
5.250	0.046	21159	459554	135
4.610	0.040	21091	521671	135

Mean $R_{(C/D)}$	494789
Std Dev $R_{(C/D)}$	31890
Std Dev $R_{(C/D)}$ (%)	**6.45**

Table A-2.11 Parallel Plate Ionization Chamber Calibration Data

Farmer Ionization Chamber Dose, *D*	Farmer Ionization Chamber Dose, *D*	Transmission Ion Chamber Charge, *C*	$R_{(C/D)}$	Transmission Ion Chamber Voltage
(kRoentgens)	(kGy)	(Cx10^{-8} coulombs)	(Cx10^{-8} coulombs / kGy)	(V)
5.090	0.045	21271	476508	117
4.710	0.041	21263	514759	117
4.740	0.042	21335	513233	117

Mean $R_{(C/D)}$	501500
Std Dev $R_{(C/D)}$	21657
Std Dev $R_{(C/D)}$ (%)	**4.32**

Table A-2.12 Parallel Plate Ionization Chamber Calibration Data

Farmer Ionization Chamber Dose, *D*	Farmer Ionization Chamber Dose, *D*	Transmission Ion Chamber Charge, *C*	$R_{(C/D)}$	Transmission Ion Chamber Voltage
(kRoentgens)	(kGy)	(Cx10^{-8} coulombs)	(Cx10^{-8} coulombs / kGy)	(V)
8.310	0.073	22112	303408	117
8.090	0.071	20636	290856	117
4.490	0.039	21116	536248	117
4.320	0.038	20224	533806	117
5.030	0.044	20306	460317	117
4.500	0.039	20306	514532	117

** Outliers 1st and 2nd data point*

Mean $R_{(C/D)}$	511226
Std Dev $R_{(C/D)}$	35302
Std Dev $R_{(C/D)}$ (%)	**6.91**

Table A-2.13 Parallel Plate Ionization Chamber Calibration Data

Farmer Ionization Chamber Dose, *D*	Farmer Ionization Chamber Dose, *D*	Transmission Ion Chamber Charge, *C*	$R_{(C/D)}$	Transmission Ion Chamber Voltage
(kRoentgens)	(kGy)	(Cx10^{-8} coulombs)	(Cx10^{-8} coulombs / kGy)	(V)
6.890	0.060	21044	348265	117
4.630	0.041	20480	504370	117
4.350	0.038	20257	530990	117
4.370	0.038	20305	529812	117
4.630	0.041	21047	518334	117

** Outliers 1st and 2nd data point*

Mean $R_{(C/D)}$	520877
Std Dev $R_{(C/D)}$	12397
Std Dev $R_{(C/D)}$ (%)	**2.38**

Table A-2.14 Parallel Plate Ionization Chamber Calibration Data

Farmer Ionization Chamber Dose, *D*	Farmer Ionization Chamber Dose, *D*	Transmission Ion Chamber Charge, *C*	$R_{(C/D)}$	Transmission Ion Chamber Voltage
(kRoentgens)	(kGy)	(Cx10^{-8} coulombs)	(Cx10^{-8} coulombs / kGy)	(V)
5.090	0.045	21024	470975	135
5.140	0.045	22799	505770	135

Mean $R_{(C/D)}$	488373
Std Dev $R_{(C/D)}$	24604
Std Dev $R_{(C/D)}$ (%)	**5.04**

Next, $R_{(C/D)}$ average values were found for all measurements provided in Tables A-2.1 thru Table A-2.14 at each particular voltage as follows:

Table A-3. Average $R_{(C/D)}$ Ratio for Modification Numbers [5] and [6] Set B

Table #	Average $R_{(C/D)}$	Std Dev $R_{(C/D)}$	Trans. Ion Chamber Voltage
	(Cx10^{-8} coulombs / kGy)	(Cx10^{-8} coulombs / kGy)	Volts
2.1	196151	21634	45
2.2	300948	9357	63
2.3 thru 2.5	348167	19292	81
2.6	407598	12258	99
(2.11 thru 2.13) and 2.7	494713	9626	117
(2.8 thru 2.10) and 2.14	488307	12334	135

The graph below shows the response of the charge to dose ratio in terms of increasing voltage for the Transmission Ion chamber.

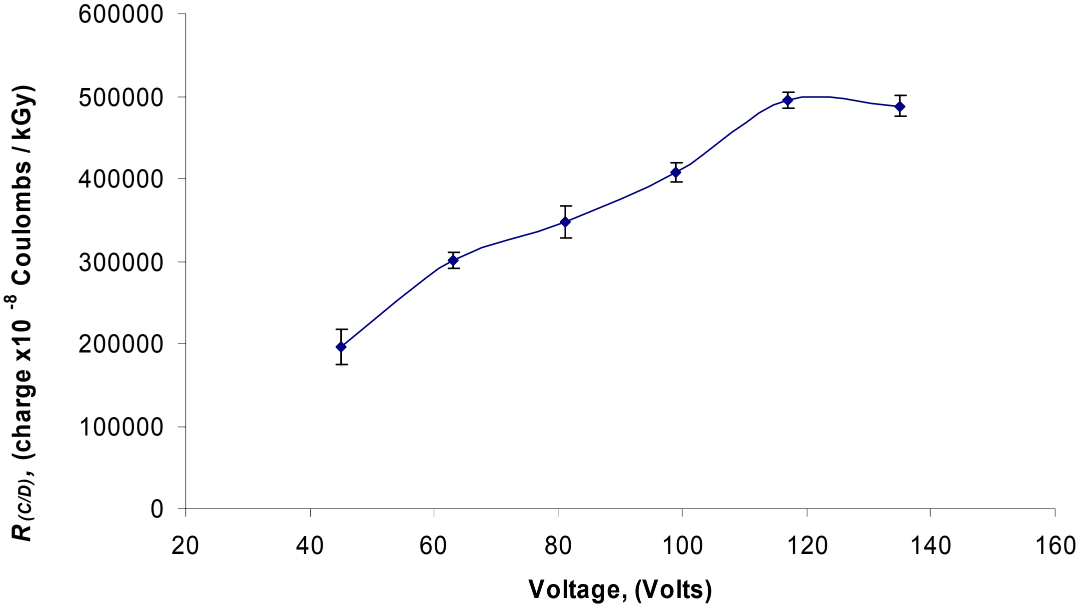

Figure A-4. Experimental Data for Average Ratio of Charge to Dose $R_{(C/D)}$.

From Figure A-4 it can be seen that the data measurements become more stable as voltage increases. At 117 V the curve is at its maximum point decreasing slowly to 135 V. Consequently, it was assumed that the minimum voltage required to operate in the current saturation region was 117 V.

After data measurements were obtained for Table A-2.15 at 135 V, another 9V battery was added to test 144 V. However, the clip leads of the high voltage terminal coaxial cable connecting the batteries were switched resulting in no measurements. Before a solution was found to this problem, the first diagnostic was to check the continuity of the coaxial cable connecting the high voltage terminal leads to the aluminum foil window and the same approach to the signal circuit.

At this point, it was found that washers of 3.175 mm were used to separate the ion chamber parallel plates in each bolt at the end of the vacuum line or electron exit window. The set of washers was removed resulting in a smaller air volume, and reduced thickness between plates. These modifications are listed on Table 1 as numbers two, three, and four and will be referred within Set B as B1. Next, it was also recommended to increase the size of the diameter of the ionization chamber, replace the bare copper wires with coaxial cable with a common ground to a brass plate as described in Table 1. These modifications are listed on Table 1 as numbers one, five, six, and seven, and will be referred within Set B as B2.

Part III. Calibration of the Parallel Plate Transmission Ion Chamber Set B

Voltage vs. $R_{(C/D)}$ Response

After reconstructing the ionization chamber, several tests were performed to determine the variability of $R_{(C/D)}$ with a smaller volume and improved connections. The experimental results are shown in Tables A-4.1 thru A-4.8 as follows.

Table A-4.1 Parallel Plate Ionization Chamber Calibration Data

Farmer Ionization Chamber Dose, *D*	Farmer Ionization Chamber Dose, *D*	Transmission Ion Chamber Charge, *C*	$R_{(C/D)}$	Transmission Ion Chamber Voltage
(kRoentgens)	(kGy)	(Cx10^{-8} coulombs)	(Cx10^{-8} coulombs / kGy)	(V)
6.340	0.056	20269	364539	135
5.630	0.049	20680	418835	135
5.500	0.048	20450	423966	135
5.430	0.048	20290	426072	135
6.130	0.054	20520	381696	135
5.600	0.049	20567	418777	135

** Outliers 1st data point*

Mean $R_{(C/D)}$	413869
Std Dev $R_{(C/D)}$	18267
Std Dev $R_{(C/D)}$ (%)	**4.41**

Table A-4.2 Parallel Plate Ionization Chamber Calibration Data

Farmer Ionization Chamber Dose, *D*	Farmer Ionization Chamber Dose, *D*	Transmission Ion Chamber Charge, *C*	$R_{(C/D)}$	Transmission Ion Chamber Voltage
(kRoentgens)	(kGy)	(Cx10^{-8} coulombs)	(Cx10^{-8} coulombs / kGy)	(V)
5.650	0.050	20503	413780	117
5.940	0.052	20763	398570	117
5.870	0.051	20580	399768	117

Mean $R_{(C/D)}$	404039
Std Dev $R_{(C/D)}$	8457
Std Dev $R_{(C/D)}$ (%)	**2.09**

Table A-4.3 Parallel Plate Ionization Chamber Calibration Data

Farmer Ionization Chamber Dose, *D*	Farmer Ionization Chamber Dose, *D*	Transmission Ion Chamber Charge, *C*	$R_{(C/D)}$	Transmission Ion Chamber Voltage
(kRoentgens)	(kGy)	(Cx10^{-8} coulombs)	(Cx10^{-8} coulombs / kGy)	(V)
5.880	0.052	20358	394783	99
6.080	0.053	19686	369194	99
5.460	0.048	20317	424294	99

Mean $R_{(C/D)}$	396090
Std Dev $R_{(C/D)}$	27574
Std Dev $R_{(C/D)}$ (%)	**6.96**

Table A-4.4 Parallel Plate Ionization Chamber Calibration Data

Farmer Ionization Chamber Dose, *D*	Farmer Ionization Chamber Dose, *D*	Transmission Ion Chamber Charge, *C*	$R_{(C/D)}$	Transmission Ion Chamber Voltage
(kRoentgens)	(kGy)	(C x10^{-8} coulombs)	(C x10^{-8} coulombs / kGy)	(V)
5.510	0.048	20180	417609	81
5.540	0.049	20340	418641	81
8.060	0.071	20231	286209	81
5.390	0.047	20112	425468	81

** Outlier 3rd data point*

Mean $R_{(C/D)}$	420573
Std Dev $R_{(C/D)}$	4271
Std Dev $R_{(C/D)}$ (%)	**1.02**

Table A-4.5 Parallel Plate Ionization Chamber Calibration Data

Farmer Ionization Chamber Dose, *D*	Farmer Ionization Chamber Dose, *D*	Transmission Ion Chamber Charge, *C*	$R_{(C/D)}$	Transmission Ion Chamber Voltage
(kRoentgens)	(kGy)	(C x10^{-8} coulombs)	(C x10^{-8} coulombs / kGy)	(V)
5.510	0.048	19887	411546	63
5.570	0.049	20068	410818	63
5.500	0.048	19978	414181	63

Mean $R_{(C/D)}$	412181
Std Dev $R_{(C/D)}$	1769
Std Dev $R_{(C/D)}$ (%)	**0.43**

Table A-4.6 Parallel Plate Ionization Chamber Calibration Data

Farmer Ionization Chamber Dose, *D*	Farmer Ionization Chamber Dose, *D*	Transmission Ion Chamber Charge, *C*	$R_{(C/D)}$	Transmission Ion Chamber Voltage
(kRoentgens)	(kGy)	(C x10^{-8} coulombs)	(C x10^{-8} coulombs / kGy)	(V)
6.310	0.055	19980	361049	45
11.950	0.105	19846	189368	45
6.060	0.053	20128	378729	45
6.030	0.053	20022	378609	45

** Outlier 2nd data point*

Mean $R_{(C/D)}$	372796
Std Dev $R_{(C/D)}$	10173
Std Dev $R_{(C/D)}$ (%)	**2.73**

Table A-4.7 Parallel Plate Ionization Chamber Calibration Data

Farmer Ionization Chamber Dose, *D*	Farmer Ionization Chamber Dose, *D*	Transmission Ion Chamber Charge, *C*	$R_{(C/D)}$	Transmission Ion Chamber Voltage
(kRoentgens)	(kGy)	(C x10^{-8} coulombs)	(C x10^{-8} coulombs / kGy)	(V)
8.010	0.070	19986	284508	27
14.000	0.123	20021	163064	27
7.290	0.064	20107	314500	27
7.530	0.066	20089	304203	27

** Outlier 2nd data point*

Mean $R_{(C/D)}$	301070
Std Dev $R_{(C/D)}$	70116
Std Dev $R_{(C/D)}$ (%)	**23.29**

Table A-4.8 Parallel Plate Ionization Chamber Calibration Data

Farmer Ionization Chamber Dose, *D*	Farmer Ionization Chamber Dose, *D*	Transmission Ion Chamber Charge, *C*	$R_{(C/D)}$	Transmission Ion Chamber Voltage
(kRoentgens)	(kGy)	(C x10^{-8} coulombs)	(C x10^{-8} coulombs / kGy)	(V)
7.700	0.068	10127	149965	18
4.460	0.039	10085	257835	18
7.880	0.069	10120	146438	18
4.220	0.037	10052	271607	18
4.200	0.037	10077	273579	18

** Outlier 1st and 3rd data points*

Mean $R_{(C/D)}$	267673
Std Dev $R_{(C/D)}$	8577
Std Dev $R_{(C/D)}$ (%)	**3.20**

Next, $R_{(C/D)}$ average values were found for all measurements provided in Tables A-4.1 thru Table A-4.8 at each particular voltage as follows:

Table A-5. Average $R_{(C/D)}$ Ratio for All Modifications on Set B Table A-1

Average $R_{(C/D)}$	Std Dev $R_{(C/D)}$	Trans. Ion Chamber Voltage
(C x10^{-8} coulombs / kGy)	(C x10^{-8} coulombs / kGy)	(V)
413869	18267	135
404039	8457	117
396090	27574	99
420573	4271	81
412181	**1769**	**63**
372796	10173	45
301070	70116	27
267673	8577	18

The graph below shows the response of the charge to dose ratio in terms of increasing voltage for the transmission ion chamber.

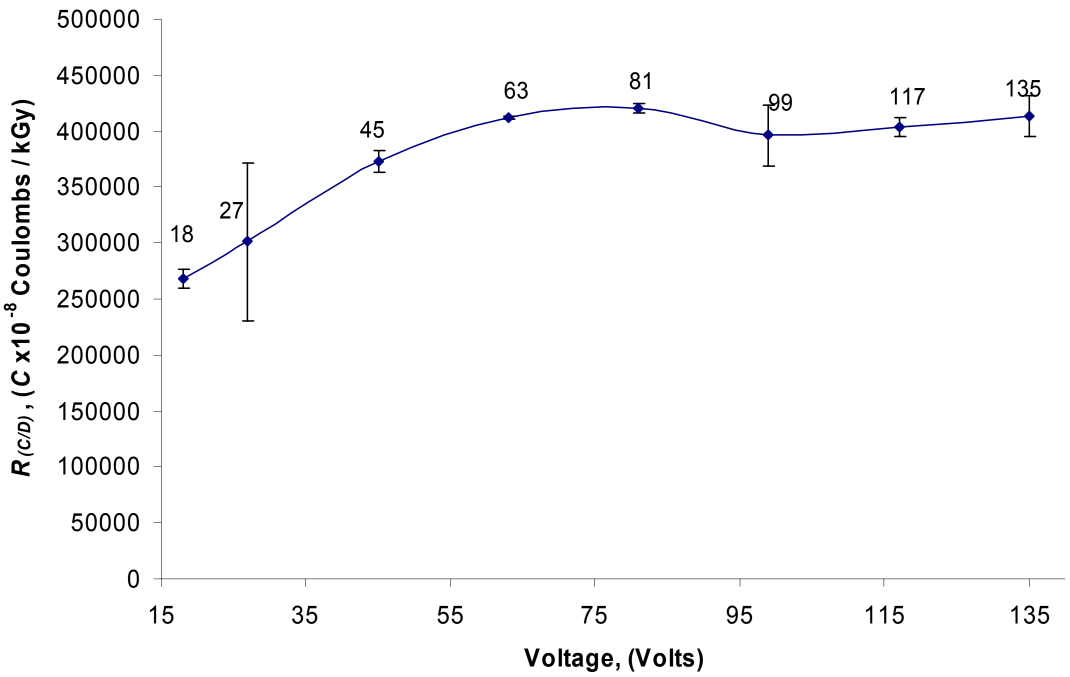

Figure A-5. Experimental Data for Average Ratio of Charge to Dose $R_{(C/D)}$.

A 2% variation was found between 63 V and 81 V. Hence, the operating voltage used for the transmission ion chamber was set at 63 V corresponding to seven 9 V batteries. Also, the standard deviation was the smallest for 63 V as shown in Table A-5.

Part IV. Calibration of the Parallel Plate Transmission Ion Chamber Set B

$R_{(C/D)}$ vs. Charge at 63 V

The results from Part III showed the optimal operating region was 63 V. Further tests were completed using such voltage to predict $R_{(C/D)}$ variability. The status of the Ionization chamber at this point was that described previously in part III.

Table A-6.1 Parallel Plate Ionization Chamber Calibration Data

Farmer Ionization Chamber Dose, *D*	Farmer Ionization Chamber Dose, *D*	Transmission Ion Chamber Charge, *C*	$R_{(C/D)}$	Time, t
(kRoentgens)	(kGy)	(*C*x10^{-8} coulombs)	(Cx10^{-8} coulombs / kGy)	(min)
7.92	0.069	21269	306212	0
6.92	0.061	20721	341433	0
7.20	0.063	20725	328218	0
6.42	0.056	20285	360280	10
5.95	0.052	20276	388567	10
6.01	0.053	20291	384972	15
6.02	0.053	20141	381492	17
5.86	0.051	20089	390896	27
5.67	0.050	20140	405020	27
5.97	0.052	20023	382433	27

Mean $R_{(C/D)}$	366086
Std Dev $R_{(C/D)}$	29706
Std Dev $R_{(C/D)}$ (%)	**8.11**

Table A-6.2 Parallel Plate Ionization Chamber Calibration Data

Farmer Ionization Chamber Dose, *D*	Farmer Ionization Chamber Dose, *D*	Transmission Ion Chamber Charge, *C*	$R_{(C/D)}$	Time, t
(kRoentgens)	(kGy)	(*C*x10^{-8} coulombs)	(Cx10^{-8} coulombs / kGy)	(min)
6.64	0.058	20135	345767	0
6.12	0.054	20274	377736	0

Mean values on Table 6.1

The results above show that there is a 8% variation when operating at 63 V. Note that statistical figures for Table A-6.2 were computed with Table A-6.1. The last column in Table V-6.1 shows the amount of time between measurements, which was included to analyze the possibility of a charging effect. Each data point was obtained right after switching to 63 from previous measurements at lower voltages.

The measurements shown below were obtained after a period of 5 hours of inactivity in which it is assumed that charging effects, if any, should have disappeared.

Table A-6.3 Parallel Plate Ionization Chamber Calibration Data

Farmer Ionization Chamber Dose, *D*	Farmer Ionization Chamber Dose, *D*	Transmission Ion Chamber Charge, *C*	*R* $_{(C/D)}$	Time, t
(kRoentgens)	(kGy)	(*C* x10^{-8} coulombs)	(Cx10^{-8} coulombs / kGy)	(min)
6.77	0.059	20000	336854	0
2.71	0.024	10000	420757	0
5.56	0.049	20031	410798	0

Mean *R* $_{(C/D)}$	389470
Std Dev *R* $_{(C/D)}$	45838
Std Dev *R* $_{(C/D)}$ (%)	**11.77**

The last measurement above was taken after the Van de Graaff tank was filled with compressed nitrogen to a pressure of 2000 kPa to prevent sparks inside the VDG tank.

The results using 63 V showed that there was a variation of approximately 8% for $R_{(C/D)}$. Figure A-6 shows the variability of all measurements shown in Tables A-6.1 thru Table A-6.3.

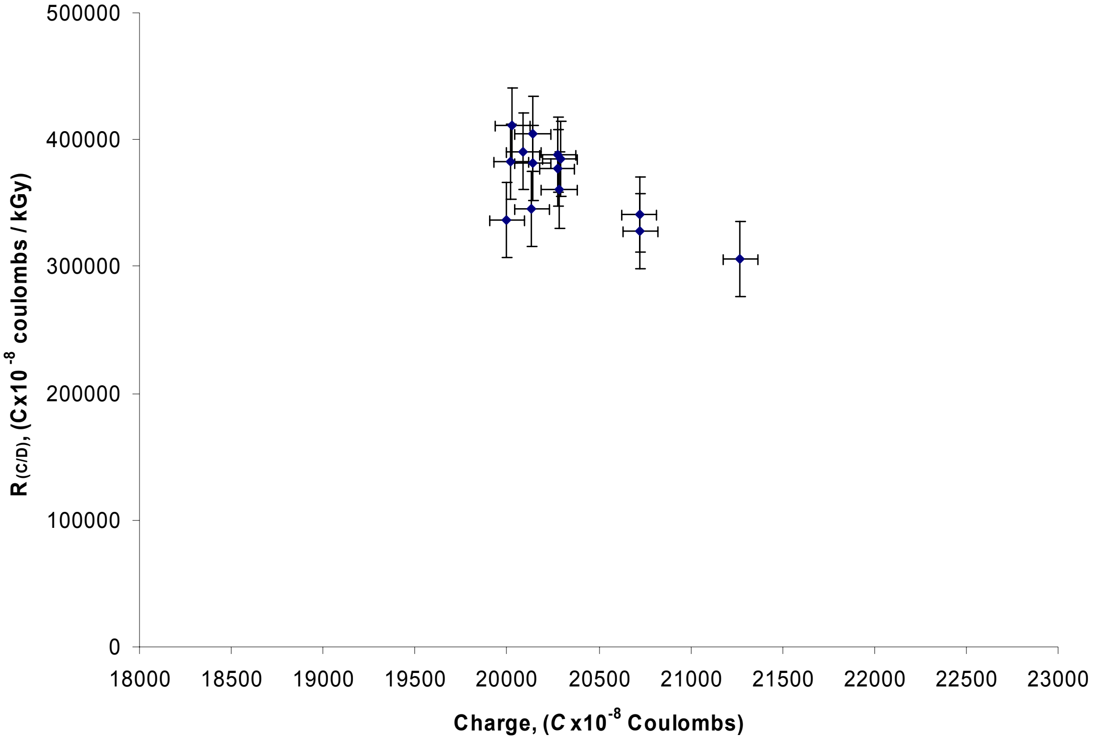

Figure A-6. Analysis of Variability of $R_{(C/D)}$ at 63 Volts using 1.35 MeV electrons.

Experimental results show a variation of approximately 8% to 11% percent for $R_{(C/D)}$ at 63 V.

Part V. Calibration of the Parallel Plate Transmission Ion Chamber Set B

Comparison of Ratios $R_{(C/D)}$ vs Charge

Experimental results for $R_{(C/D)}$ at the saturation voltage described in sections I, II, and IV were compared and calibration curves produced for each specific ratio. Tables A-7 and A-8 show these results.

Table A-7. Average Ratio of Charge to Dose Variation at Saturation Voltage

Set	$R_{(C/D)}$	Volts	Std Dev $R_{(C/D)}$
	(Cx10^{-8} coulombs / kGy)	(V)	(Cx10^{-8} coulombs / kGy)
A	266099	45	3373
B_1	494713	117	9626
B_2	412181	63	1769

Table A-8. Charge Vs. Dose Calibration Curves Using Average $R_{(C/D)}$ Ratio

Dose	*Charge*		
	A	B_1	B_2
[kGy]	(Cx10^{-8} coulombs)	(Cx10^{-8} coulombs)	(Cx10^{-8} coulombs)
0.01	2661	4947	4122
0.02	5322	9894	8244
0.03	7983	14841	12365
0.04	10644	19789	16487
0.05	13305	24736	20609
0.06	15966	29683	24731
0.07	18627	34630	28853
0.08	21288	39577	32975
0.09	23949	44524	37096
0.1	26610	49471	41218
0.2	53220	98943	82436
0.3	79830	148414	123654
0.4	106440	197885	164873
0.5	133049	247356	206091
0.6	159659	296828	247309
0.7	186269	346299	288527
0.8	212879	395770	329745
0.9	239489	445242	370963
1	266099	494713	412181
1.1	292709	544184	453400
1.2	319319	593656	494618
1.3	345928	643127	535836
1.4	372538	692598	577054
1.5	399148	742069	618272

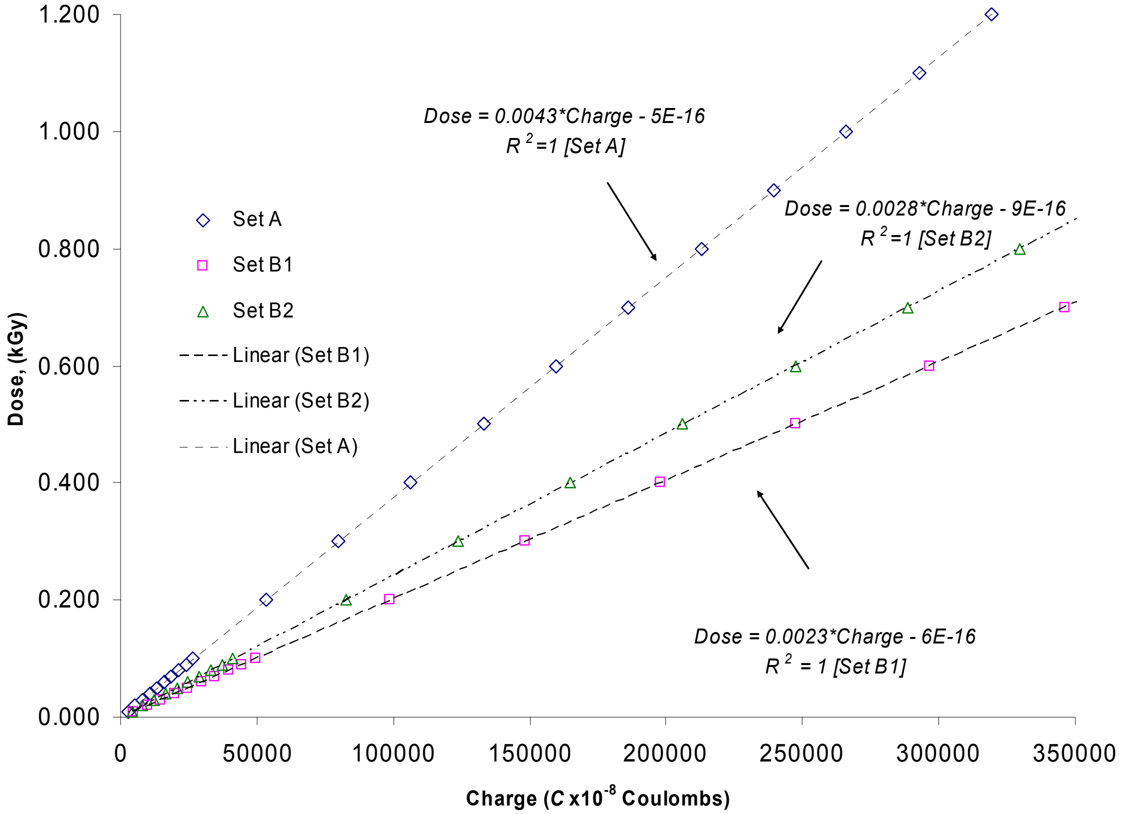

Figure A-7. Van de Graaff Calibration Curves using average experimental $R_{(C/D)}$

Figure A-7 shown above represents all the changes performed to the ionization chamber with the objective to better collect charge since its initial construction. The data measurements with Set A show a higher dose for a given charge amount as expected due to the larger amount of air volume in the chamber. As the air volume was reduced, the charge to dose ratio was also reduced as shown in Set B1. Replacing the copper wire with coaxial cable properly grounded resulted in the curve shown as Set B2. Both curves are very close to each other, however the coaxial cable insulation can protect the inside coaxial cable from picking up any charge ionization close to the cables surface resulting in a more stable measurement.

A.1.2 VDG Electron Beam Alignment

This section refers to the alignment of the electronic beam by means of a bending magnet current setting. In particular, the alignment was performed visually by exposing circular slabs of methyl yellow with a diameter of 21 cm and 1 cm thick. Each circular phantom slab was placed exactly at the exit beam window parallel to the beam prior to exposure. Table A-9 shows the results obtained to align the electronic beam using 1.35 MeV electrons (dose values were obtained using the ratio listed in Set A in Table A-7).

Table A-9. Electron Beam Alignment at the Exit Window Using 1.35 MeV Electrons

Sample Number	Ion Chamber Counts	Dose	Bending Magnet Current	Beam Position w/respect to center
	C $x10^{-8}$ coulombs	Gy	Amps	
A	0	0	0	
B	30,000	128	0.50	High
C	30,000	128	0.65	Low
D	30,000	128	0.60	Center

Figure A-8 below shows the electron beam distribution for the Green channel in the circular slabs at the exit window for the bending magnet currents listed above.

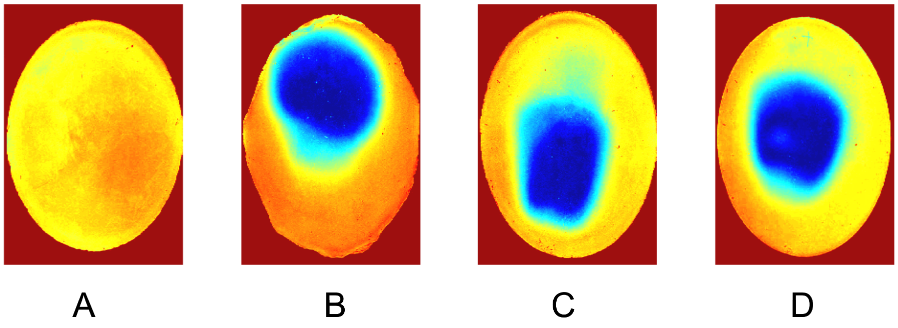

Figure A-8. Van de Graaff electron beam distribution at the exit window for the Green Channel using 1.35 MeV electrons

It was found that the electron beam was centered at a bending magnet current of 0.6 A

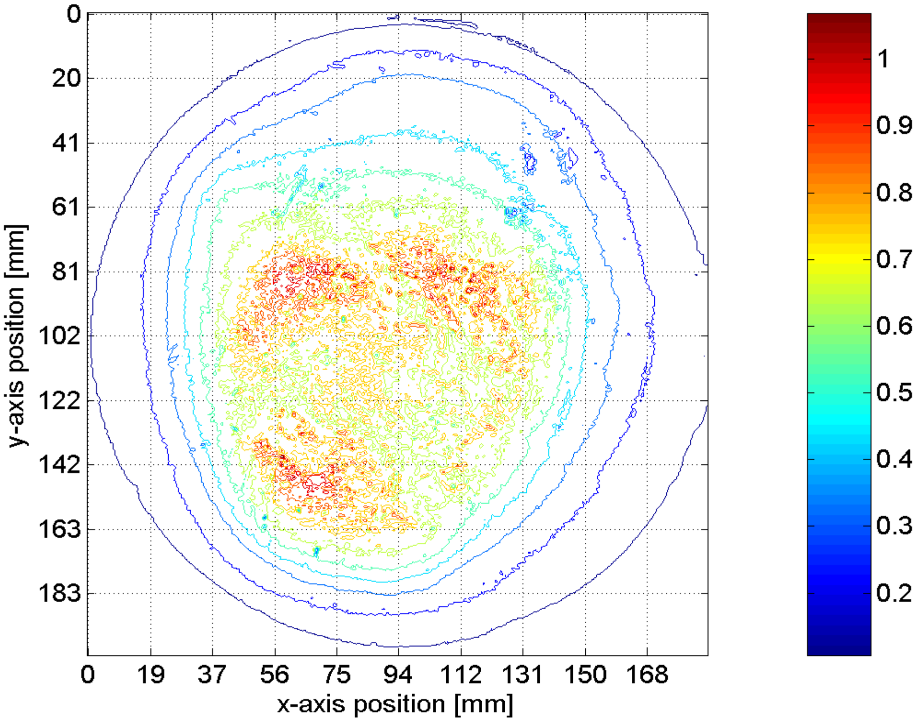

Figure A-9. Electron Beam Distribution using 1.35 MeV electrons at exit window. Optical density Scale, OD = Log(255/I)

Next, the electron beam distribution was found at 25.4 cm away from the exit window where the irradiation point was located at the center of the circular slab. The circular slab was held parallel to the exit window by means of a 38 cm bolt connected to the exit window flange. A distance of 25.4 cm was set by moving two adjustable knots holding the slab in a hollow Plexiglas sheet away from window. The following distribution resulted.

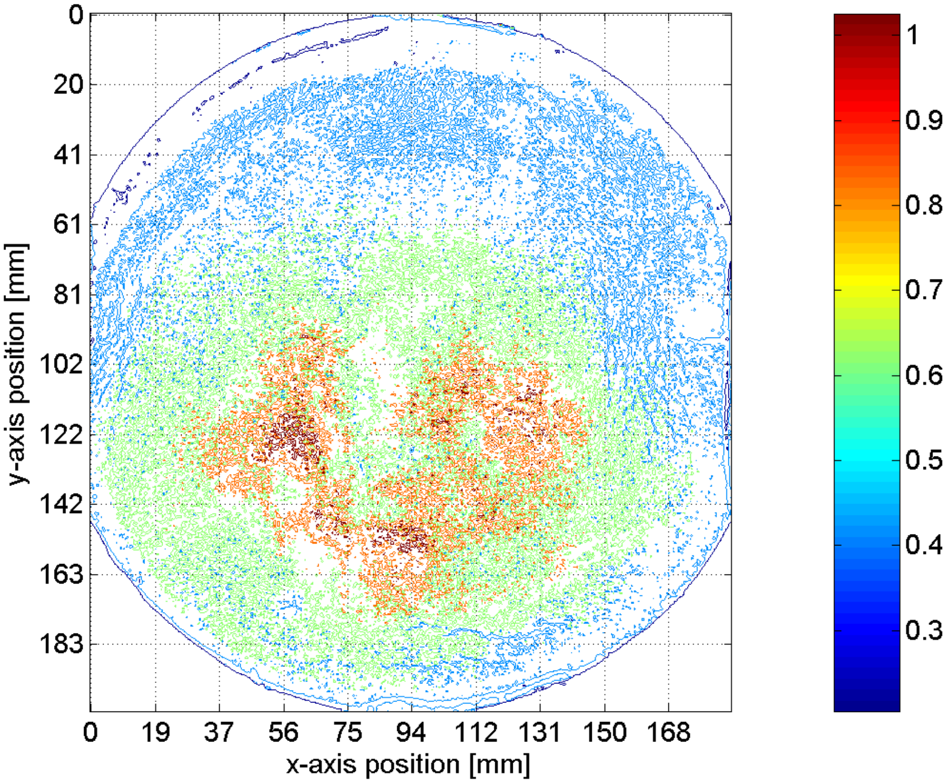

Figure A-10. Electron Beam Distribution using 1.35 MeV electrons 25.4 cm away from exit window.

Figure A-9 shows that the electron beam is aligned at 0.6A spreading outward uniformly from the center. However, at a distance of 25.4 cm away from the exit window the distribution appeared to be offset approximately by 2 cm below the center as shown in Figure A-10. The uniformity of the electron beam was verified for both cases, i.e., at the exit window and 25.4 cm away in the horizontal and vertical directions. For the horizontal direction (x-axis), a segment of data corresponding to ± 2.5 cm from the centerline was plotted from left to right of Figure A-9. Like wise, for the vertical direction, a segment of ± 2.5 cm data from the slab centerline was plotted from the top to the bottom of Figure A-10. The results were as follows:

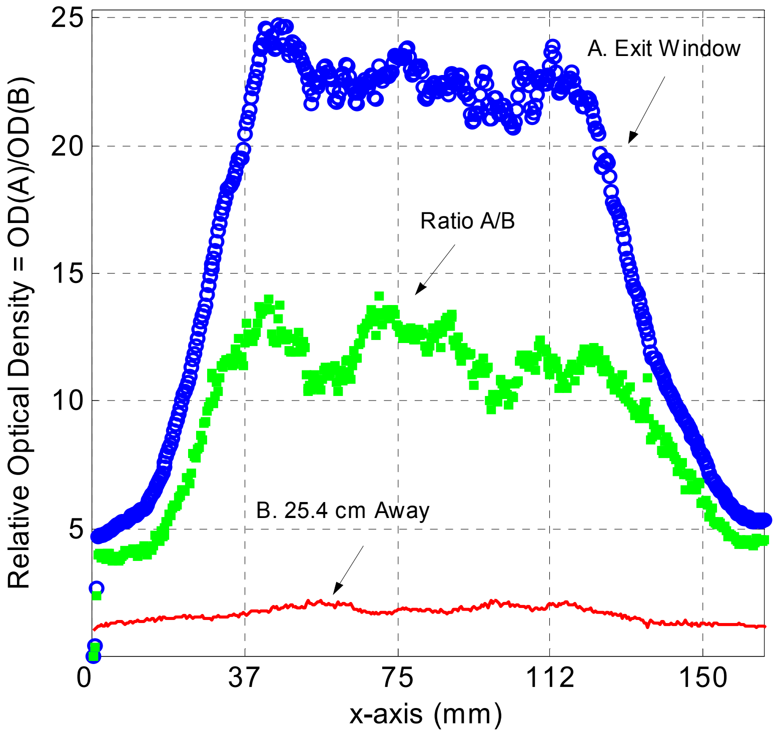

Figure A-11. Horizontal Electron Beam Distribution at Exit Window and 25.4 cm away using 1.35 MeV electrons.

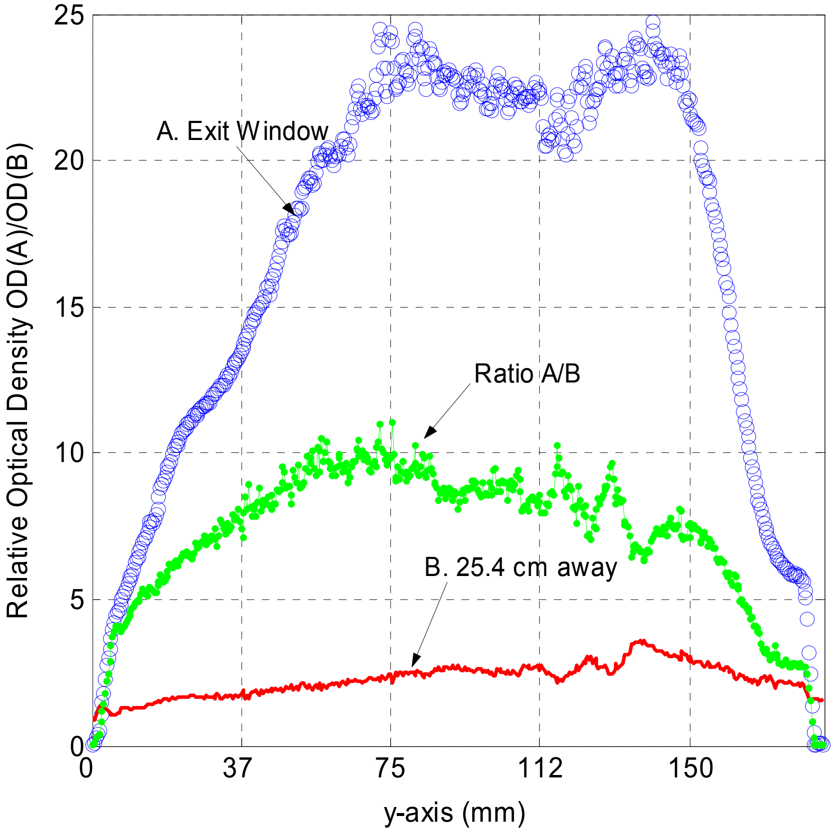

Figure A-12. Vertical Electron Beam Distribution at the Exit Window and 25.4 cm away using 1.35 MeV electrons.

Figures A-11 and A-12 show the uniformity of the beam based on a relative optical density scale. The magnitudes of the optical density values at the exit window were larger to those at 25.4 cm away as expected. Also, the horizontal distribution showed more uniformity at the exit window and 25.4 cm away compared to the vertical distribution were the higher values were located below the center as can be seen in Figure V-11.

APPENDIX B

PRELIMINARY RESULTS: APPLE PHANTOM DEVELOPMENT

B.1 Paraffin Wax – Chloroform – Methyl Yellow Solution

B.1.1 Development of Paraffin Wax – Chloroform – Methyl Yellow Chemical Solution

This preliminary study was performed to develop a chemical solution based on paraffin wax, chloroform, and methyl yellow dye in the form of ice-cube phantoms using an ice-cube tray dispenser. Next, ice-cube dosimeters were irradiated using cumulative gamma ray doses of 100 Gy/hr (10 kRad/hr) at the nuclear reactor (Nuclear Science Center at Texas A&M University). The target doses used were in the range of 100 Gy to 1000 Gy using the above dose rate. It was expected to find a radiation dose that had an effect on the chemical dosimeter, i.e., find the chemical radiation dosimeter color sensitivity for a specific component chemistry which is closest to tissue equivalent material or water.

The following section explains in detail the development of a paraffin, chloroform and microcrystalline wax matrix phantom. Chloroform plays a key role in the chemical dosimeter, thus it was of interest to understand the effect of concentration within the polymeric matrix. Concentrations of chloroform (by wt) ranging from 4-40% were produced. For this analysis paraffin wax, chloroform, and microcrystalline wax were considered the solvent, and methyl yellow dye the solute. Next, the effect of methyl yellow was also tested in two specific concentrations, $1x10^{-4}$ *molal (m)* and $4x10^{-4}$ *m* solutions respectively. The next section explains the process of casting the phantom chemical dosimeter samples using an ice-cube dispenser.

The chemical dosimeter samples were produced using an ice-cube tray dispenser to assure sample geometrical uniformity. The ice-cube tray dispenser had a capacity of 16 cubes. The dimensions for each cube were 3.2 *cm* width x 4.8 *cm* length x 3 *cm* height. The amount of paraffin wax required for each cube was determined from the amount of water in each cube, i.e., 19 mL/cube. The ratio of paraffin to water was 3:3.5 (by wt.). Thus, using a water density of 1 g/cm^3, each cube had a capacity of 19 g of water or 16.3 g of paraffin wax. The total paraffin wax mass for one tray only was obtained as 260.8 grams. Nonetheless, mass balance calculations were obtained using the mass corresponding to 6 out of 16 cubes, i.e., 97.8 grams of paraffin wax. Three samples per concentration of methyl yellow per chloroform mass resulted. For instance, from two concentrations of methyl yellow proposed, 6 samples resulted at a specific chloroform concentration. Table B-1 below shows the number of samples produced for the two concentrations of methyl yellow.

Table B-1. Proposed Sample Number Distribution for Gamma Irradiation

	Chloroform Concentration					
Methyl Yellow Concentration	5%	10%	20%	30%	40%	**Total**
$1*10^{-4}$ *m*	3	3	3	3	3	15
$4*10^{-4}$ *m*	3	3	3	3	3	15
Total	6	6	6	6	6	30

A mass balance was performed to obtain the specific concentrations of chloroform at a fixed 1% microcrystalline wax concentration. Usually, the microcrystalline wax concentration lies between 0.2% and 1% in order to have a uniform non-flaky paraffin wax phantom.

For instance, Figure B-2 shows the development of a 5% chloroform solution in the paraffin wax matrix with a fixed 1% microcrystalline wax content.

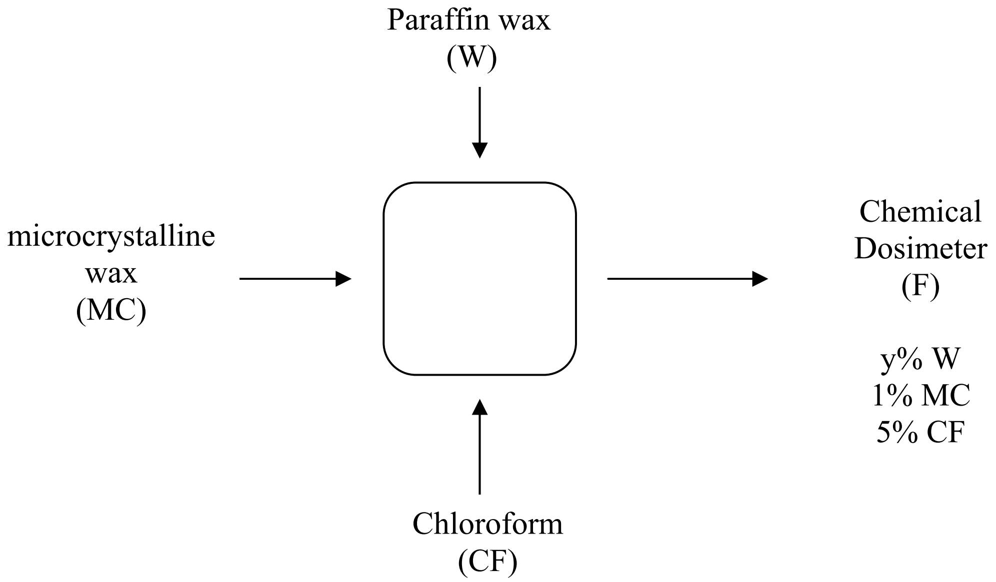

Figure B-2. Paraffin-chloroform-microcrystalline wax chemical system for ice-cube samples.

Mass Balance for System

A. MC Wax

$$MC = 0.01 * F \tag{B-1}$$

$$MC = 0.01 * F = 0.01 * 97.8\,g = 0.978\,g$$

B. Chloroform

$$CF = 0.05 * F \tag{B-2}$$

$$CF = 0.05 * F = 0.05 * 97.8\,g = 4.89\,g$$

C. Paraffin Wax

$$MC + W + CF = F \tag{B-3}$$

$$W = F - MC - CF$$

$$W = 97.8\,g - (0.978 + 4.89)\,g = 91.93\,g$$

Chloroform mass was converted to volume via its density ($\rho = 1.52$ g/cm^3).

$$CF = \frac{4.89\,g}{1.52\,\frac{g}{cm^3}} = 3.22\ cm^3\ = 3.22\ mL \tag{B-4}$$

Next, from two desired concentrations of methyl yellow, $c_1 = 1*10^{-4}\ m$ and $c_2 = 4*10^{-4}\ m$ the required dye masses were obtained as:

$$Molal\,Concentration = \frac{moles\ of\ \ methyl\ \ yellow}{1\ kg\ of\ \left(paraffin\,wax + mc\,wax + chloroform\right)} \tag{B-5}$$

Thus,

$$1*10^{-4}\,m = \frac{n\ moles\,methyl\,yellow}{0.0978\,kg\ solvent} \tag{B-6}$$

$$Methyl\ yellow\,molecular\ weight = \left(12.001*14 + 1.00794*15 + 14.00674*3\right) = 225.29\,g$$

$$n\ moles\,methyl\ yellow = 0.0978\,kg * \left(1*10^{-4}\right)\frac{mol}{kg} = 9.78*10^{-6}\,mol$$

$$mass(c_1 = 1*10^{-4}m) = 9.78*10^{-6}mol*\frac{225.29\,g}{1\,mol} = 2.20*10^{-3}g = 2.20\,mg \qquad \text{(B-7)}$$

$$4*10^{-4}m = \frac{n\ moles\ methyl\ yellow}{0.0978\,kg\ solvent}$$

$$n\ moles\ methyl\ yellow = 0.0978\,kg*\left(4*10^{-4}\right)\frac{mol}{kg} = 3.912*10^{-5}mol$$

$$mass(c_2 = 4*10^{-4}m) = 3.912*10^{-5}mol*\frac{225.29\,g}{1\,mol} = 8.81*10^{-3}g = 8.81\,mg \qquad \text{(B-8)}$$

Tables B-2 shows the results obtained for two desired methyl yellow concentrations, and based on a total mass of 97.8 grams of paraffin wax, chloroform, and microcrystalline wax. Table B-3 shows the amount of paraffin wax, and chloroform required for different chloroform concentrations in the chemical system.

Table B-2. Methyl Yellow Solute Required Using Two Concentrations

Concentration	*Mass*
molal (m)	*mg*
$1*10^{-4}$	2.20
$4*10^{-4}$	8.81

Table B-3. Chloroform-Paraffin Wax-Microcrystalline Wax Solvent Composition

Chloroform mass Concentration	*Chloroform Mass*	*Chloroform Volume ρ =1.52g/cm^3*	*Paraffin wax ρ = 0.93g/cm^3*	*Microcrystalline wax*
%	*grams*	*mL*	*g*	*G*
5	4.89	3.22	91.932	0.978
10	9.78	6.43	87.042	0.978
20	19.56	12.87	77.262	0.978
30	29.34	19.36	67.482	0.978
40	39.12	25.74	57.702	0.978

B.2 Color Response and Mass Stopping Power Characteristics for Paraffin Wax – Chloroform – Methyl Yellow Dye Chemical Solution

Two factors were considered for analysis: 1) linear collision mass stopping power, and 2) dosimeter sensitivity, i.e., color response to absorbed dose. Results were obtained for the concentrations of methyl yellow, and chloroform described in Tables B-2, and B-3 respectively.

B.2.1 Linear Collision Mass Stopping Power

The linear collision mass stopping power of the paraffin, chloroform, microcrystalline wax, methyl yellow solution was obtained and compared to the linear collision stopping power of water. Linear collision stopping power calculations were obtained using the electron stopping power database, *E-Star* (http://physics.nist.gov/PhysRefData/Star/Text/ESTAR.html), from the Physical Reference Database at the National Institute of Standards and Technology.

The *E-Star* database computes the stopping powers and the range for electrons under the guidelines proposed by the International Commission on Radiation Units and Measurements, ICRU, Report 37: *Stopping Powers for Electrons and Positrons*, and Report 49: *Stopping Powers and Ranges for Protons and Alpha Particles*.

E-Star has the capability of computing stopping powers of any particular material, based on the mass fraction composition of each element present in the material. In this study, mass fractions for each component of the chemical dosimeter were found as described next.

The parameters used to sort the different mass fractions were the changing chloroform concentrations (5% to 40%) and the two proposed methyl yellow solute concentrations in the dosimeter of $1*10^{-4}$ *m* and $4*10^{-4}$ *m* respectively.

Because the mass fraction of microcrystalline wax was very small (1%) compared to the paraffin wax, the latter mass was added to that of paraffin for each concentration. Therefore, the density for each component was found as follows:

$$\text{dosimeter density} = \rho = \frac{\sum \text{mass components}}{\sum \text{volume components}} \qquad \text{(B-9)}$$

The following sample calculations were based on 5% chloroform (See Section B.2.1 – Table B-3) concentration at $1*10^{-4}$ *m* solution. It was assumed that the mass of microcrystalline wax had the same density as the paraffin wax, thus both masses were added. Then:

$$\rho = \frac{(4.89 + 92.91)g}{(3.217 + 99.903)cm^3} = 0.9484 \frac{g}{cm^3}$$

Next, using equation B-9 the dosimeter density was approximated from the mass and volume values at each particular concentration of chloroform and dye. Table B-4 and B-5 shows the mass and volume components respectively for varying chloroform and methyl yellow concentrations. The chemical dosimeter density values are presented in Table B-6.

Table B-4. Dosimeter Matrix Total Mass Composition

Chloroform Concentration	*Chloroform*	Paraffin & microcrystalline wax	*Total mass*
%	g.		
5	4.89	92.91	97.80
10	9.78	88.02	97.80
20	19.56	78.24	97.80
30	29.34	68.46	97.80
40	39.12	58.68	97.80

Table B-5. Dosimeter Matrix Total Volume Composition

Chloroform Concentration	*Chloroform*	Paraffin & mc wax	*Total volume*
%	cm^3		
5	3.22	99.903	103.123
10	6.43	94.645	101.075
20	12.87	84.129	96.999
30	19.36	73.613	92.973
40	25.74	63.097	88.837

Table B-6. Estimated Dosimeter Density

Chloroform Concentration	*Total Mass, m*	*Total Volume, v*	*Density, ρ*
%	*g*	*cm^3*	*g/cm^3*
5	97.80	103.123	0.948
10	97.80	101.075	0.968
20	97.80	96.999	1.008
30	97.80	92.973	1.052
40	97.80	88.837	1.101

Using the dosimeter density data from Table B-6, the mass fractions for each component (i.e., chloroform, paraffin wax, and methyl yellow) were obtained for the two methyl yellow concentrations. Tables B-7 and B-8 show their respective mass fractions.

Table B-7. Mass Fraction Components of Dosimeter at $1*10^{-4}$ *m* Methyl Yellow

Chloroform	$CHCl_3$	$C_{25}H_{52}$	$C_{14}H_{52}N_3$
5	0.049999	0.949979	0.000022
10	0.099998	0.899980	0.000022
20	0.199996	0.799982	0.000022
30	0.299994	0.699984	0.000022
40	0.399991	0.599987	0.000022

Table B-8. Mass Fraction Components of Dosimeter at 4*10^{-4} *m* Methyl Yellow

Chloroform	$CHCl_3$	$C_{25}H_{52}$	$C_{14}H_{52}N_3$
5	0.049995	0.949915	0.000090
10	0.099991	0.899919	0.000090
20	0.199982	0.799928	0.000090
30	0.299973	0.699937	0.000090
40	0.399964	0.599946	0.000090

Using the *E-Star* database and the information on Tables B-7 and B-8, the linear collision stopping power was obtained for both the chloroform and methyl yellow concentrations. Results were compared statistically to those of water at the 99% level of confidence. The results are shown in Figures B-3 and B-4.

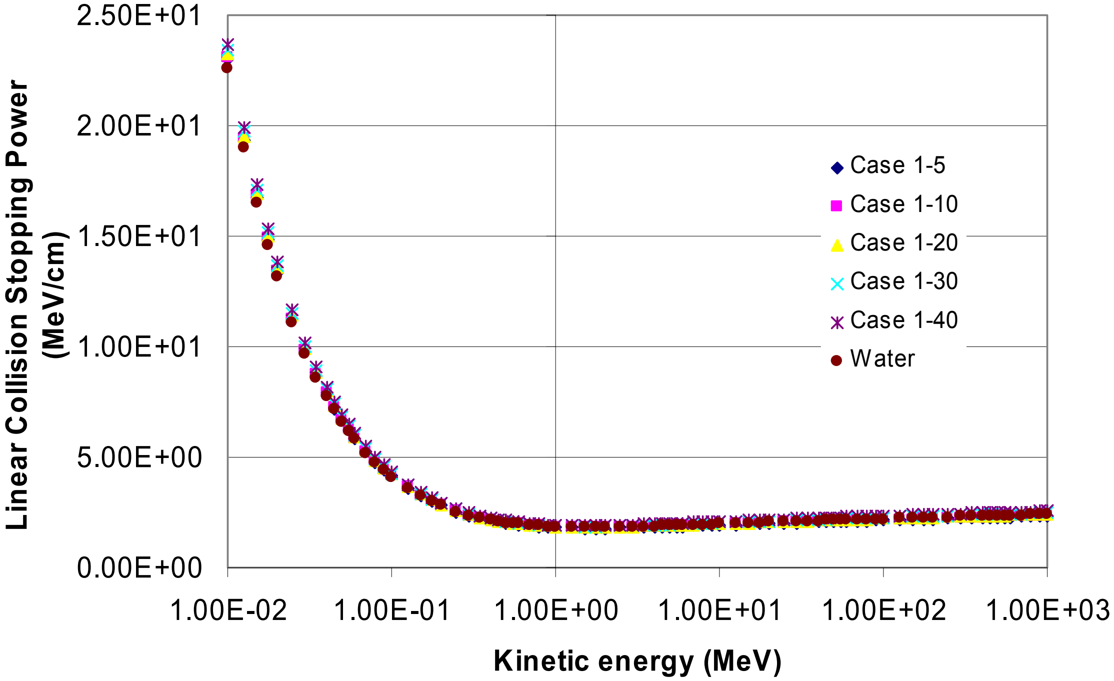

Figure B-3. Linear Collisional Stopping Power at 1x10^{-4} *m* Methyl Yellow for varying chloroform concentrations vs. Water

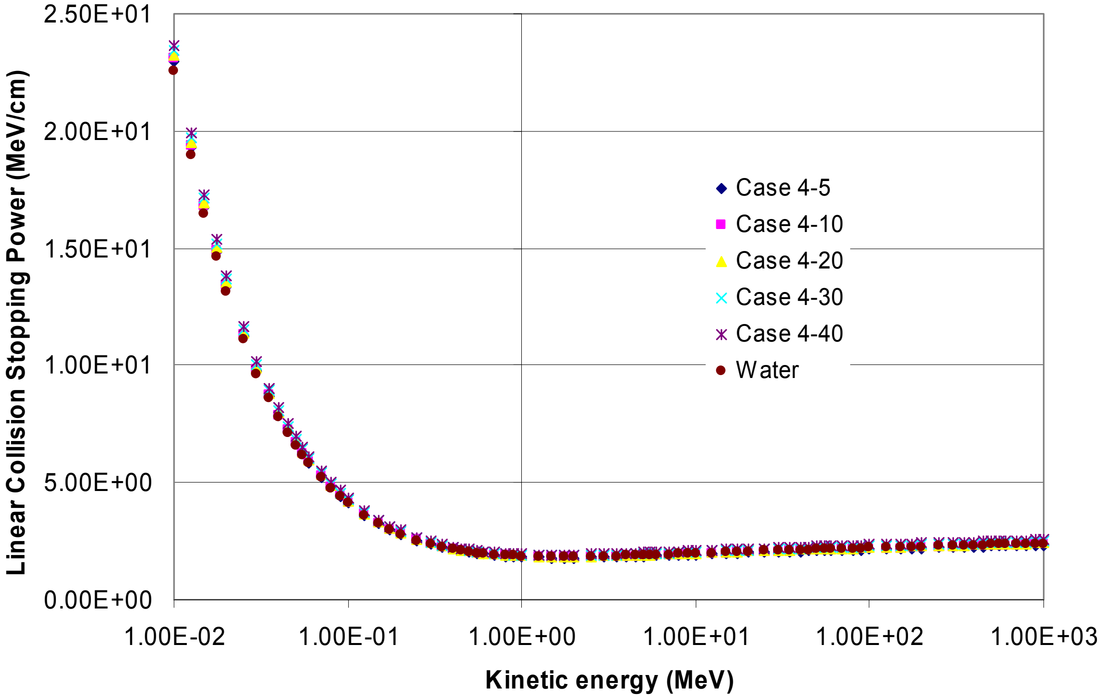

Figure B-4. Linear Collisional Stopping Power at 4x10^{-4} *m* Methyl Yellow for varying chloroform concentrations vs. Water.

From Figures B-3 and B-4, it can be seen that the linear collision stopping power was very close to that of water. For both cases, it was observed that mass stopping power started shifting away to that of water for increasing chloroform mixtures. Analysis of Variance (ANOVA) test at a 99% confidence level showed that there are no significant differences for increasing chloroform within each methyl yellow concentration.

The two dye concentrations were compared to each other resulting in no significant differences at the 99% confidence level. A Fisher's LSD test showed that the least significant difference occurred between 5% and 20% chloroform for both dye concentrations. From the results shown on both statistical tests, it was assumed that the linear mass stopping of the chemical dosimeter can be considered to that of water for the chloroform and dye concentrations studied.

B.2.2 Chemical Dosimeter Color Response Analysis

Standard Red Green Blue (sRGB) and grayscale color spaces were used to determine the color intensity values resulting from the gamma irradiations. Each tray was photographed, with a Sony Mavica digital camera set at a resolution of 640 pixels x 480 pixels, immediately after receiving an irradiation dose. Several sets of pictures containing the color response with varying chloroform and dye concentrations were stored in the computer for analysis.

Using Adobe Photoshop 6.0 (Adobe Systems Incorporated, San Jose, California) all images were cropped and standardized to (144 x 144) pixels selecting the same region in each sample to normalize color measurements. Next, average color values were used to find the color response to dose in sRGB and Grayscale color spaces. Tables B-9 thru B-11 show the Red, Green, Blue, and Grayscale intensity values found for the changing chloroform and methyl yellow concentrations

Table B-9. Red Channel Intensity Data

Dose	1x10^{-4} *m* Low Methyl Yellow					4x10^{-4} *m* High Methyl Yellow				
(Gy)	5%	10%	20%	30%	40%	5%	10%	20%	30%	40%
100	142	229	245	219	214	78	170	231	193	189
200	79	193	205	204	202	50	88	210	176	169
500	47	128	97	174	210	16	21	148	117	123
800	77	131	128	183	185	24	45	81	114	133
1100	22	42	92	103	127	22	42	92	103	127
1500	95	146	119	188	179	21	31	65	76	99
2160	96	148	126	181	172	31	54	90	84	133

Table B-10. Green Channel Intensity Data

Dose	1x10^{-4} *m* Low Methyl Yellow					4x10^{-4} *m* High Methyl Yellow				
(Gy)	5%	10%	20%	30%	40%	5%	10%	20%	30%	40%
100	90	75	105	111	88	25	41	100	52	48
200	34	38	65	41	43	31	43	66	37	43
500	22	61	29	34	47	11	12	17	17	29
800	39	68	53	62	47	16	24	11	14	35
1100	17	22	10	12	30	17	22	10	12	30
1500	50	76	59	42	56	15	18	8	11	27
2160	50	91	66	82	81	22	29	15	16	52

Table B-11. Blue Channel Intensity Data

Dose	1x10^{-4} *m* Low Methyl Yellow					4x10^{-4} *m* High Methyl Yellow				
(Gy)	5%	10%	20%	30%	40%	5%	10%	20%	30%	40%
100	25	45	51	60	53	23	25	19	29	30
200	25	54	48	46	44	26	27	28	33	39
500	28	95	26	93	94	15	18	23	24	34
800	46	100	83	128	108	20	24	11	22	35
1100	21	22	14	22	34	21	22	14	22	34
1500	51	96	89	99	100	20	19	23	29	37
2160	51	100	88	109	106	32	44	44	42	72

Table B-12. Grayscale Channel Intensity Data

Dose	1x10^{-4} *m* Low Methyl Yellow					4x10^{-4} *m* High Methyl Yellow				
(Gy)	5%	10%	20%	30%	40%	5%	10%	20%	30%	40%
100	102	130	149	142	129	48	92	141	107	104
200	52	103	116	109	108	40	59	118	94	93
500	35	85	56	95	115	15	18	77	62	68
800	54	87	81	109	104	22	35	45	60	75
1100	79	101	85	117	109	22	32	49	55	72
1500	66	99	80	104	104	20	26	37	43	59
2160	66	108	111	86	115	29	41	50	48	82

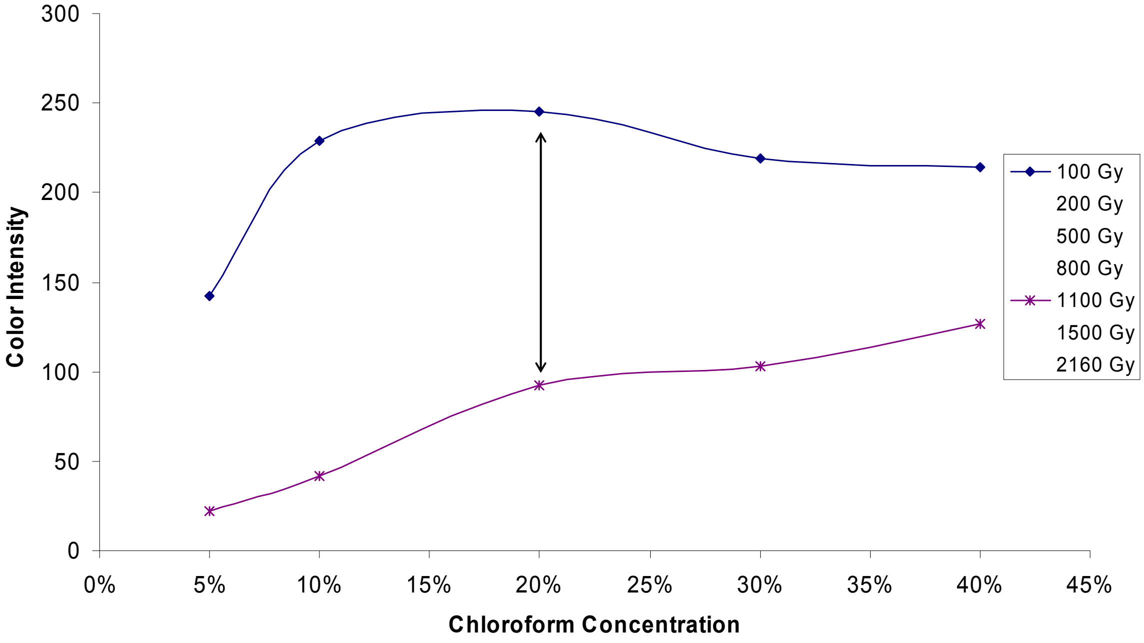

Figure B-5. Red Channel Color vs. Chloroform %. Methyl Yellow Concentration of 1×10^{-4} *m*.

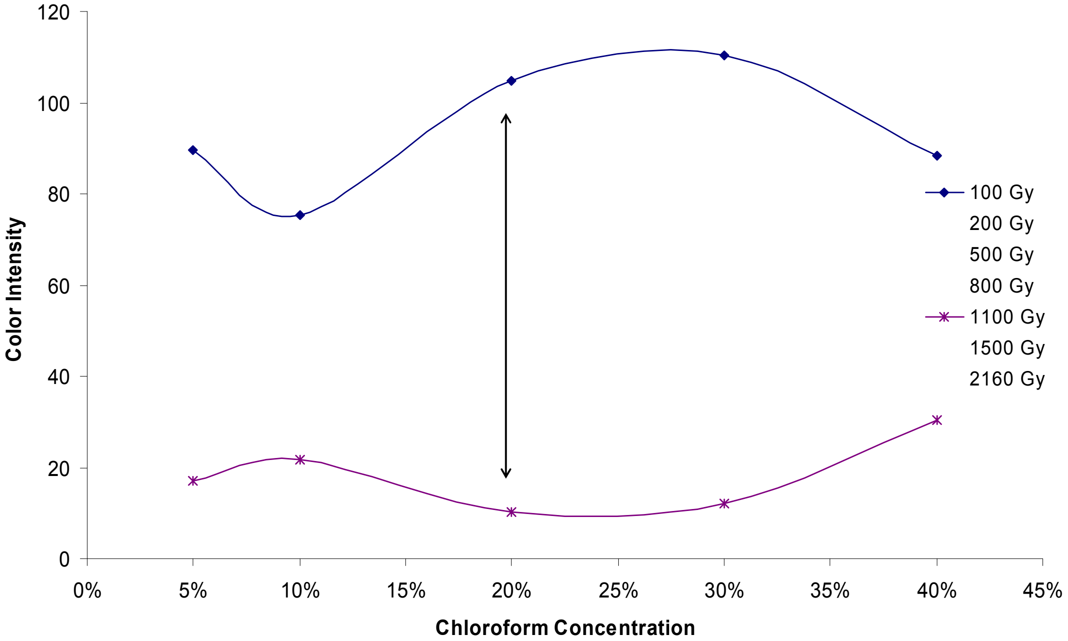

Figure B-6. Green Channel Color vs. Chloroform %. Methyl Yellow Concentration of 1×10^{-4} *m*.

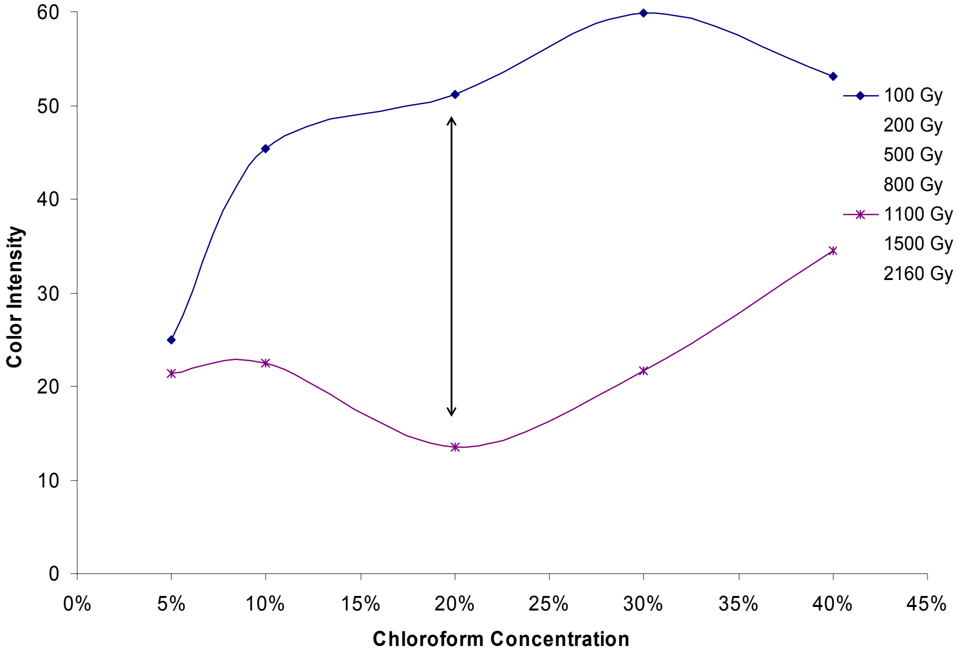

Figure B-7. Blue Channel Color vs. Chloroform %. Methyl Yellow Concentration of $1x10^{-4}$ *m*.

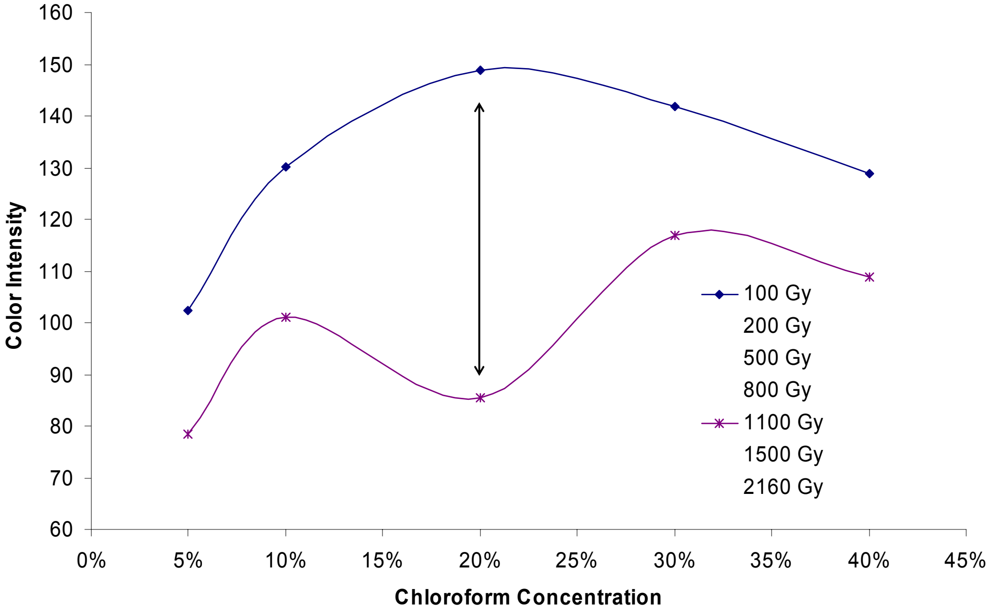

Figure B-8. Grayscale Channel Color vs. Chloroform %. Methyl Yellow Concentration of $1x10^{-4}$ *m*.

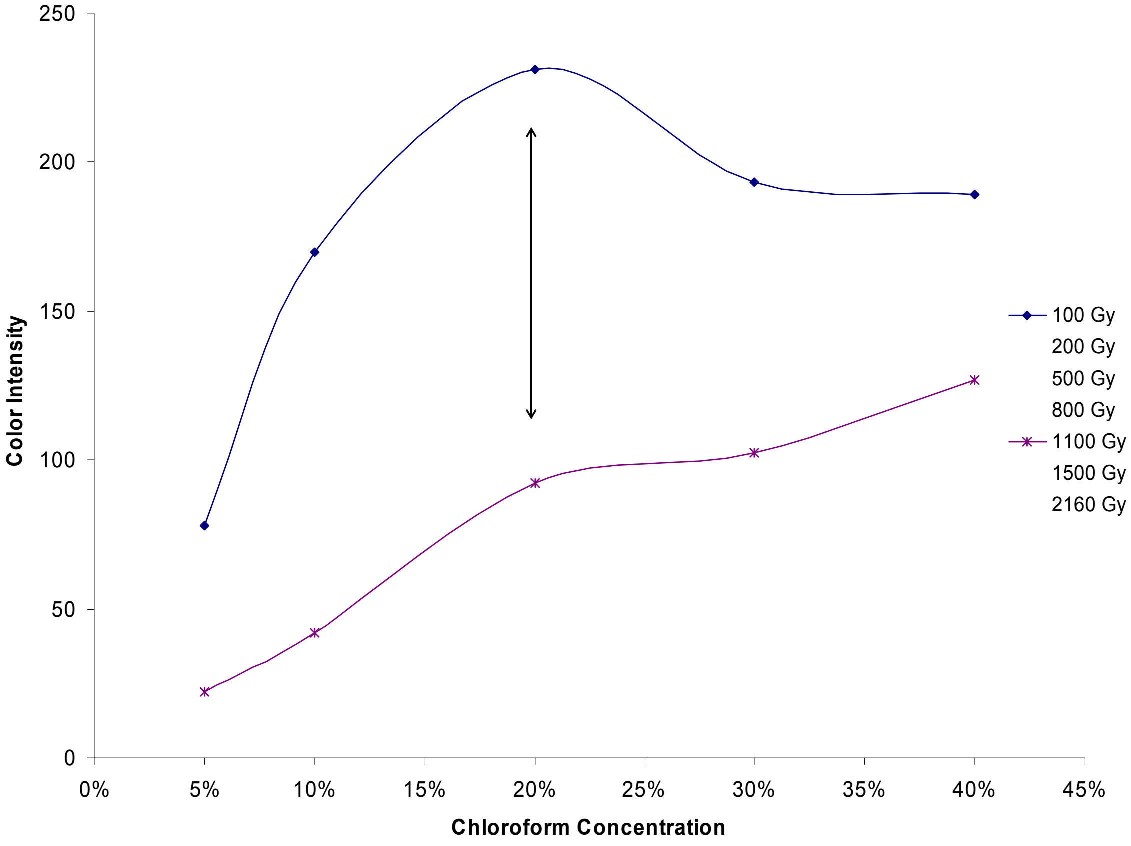

Figure B-9. Red Channel Color vs. Chloroform %. Methyl Yellow Concentration of $4x10^{-4}$ *m*.

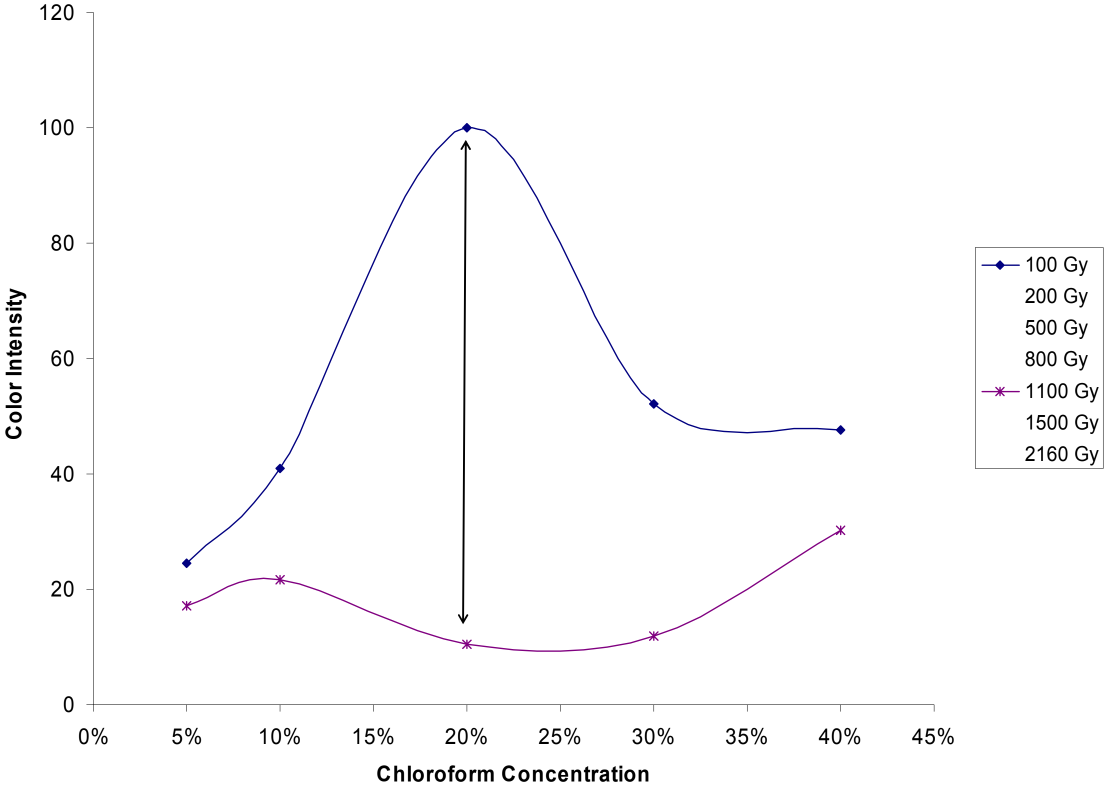

Figure B-10. Green Channel Color vs. Chloroform %. Methyl Yellow Concentration of 4×10^{-4} *m*.

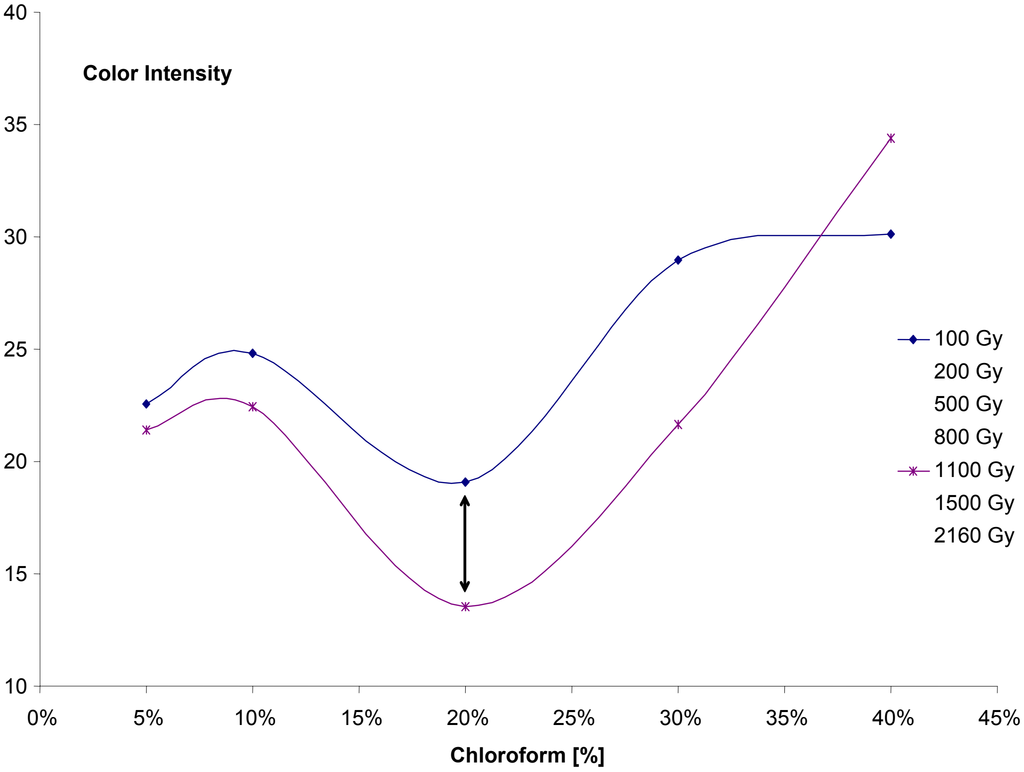

Figure B-11. Blue Channel Color vs. Chloroform %. Methyl Yellow Concentration of $4x10^{-4}$ *m*.

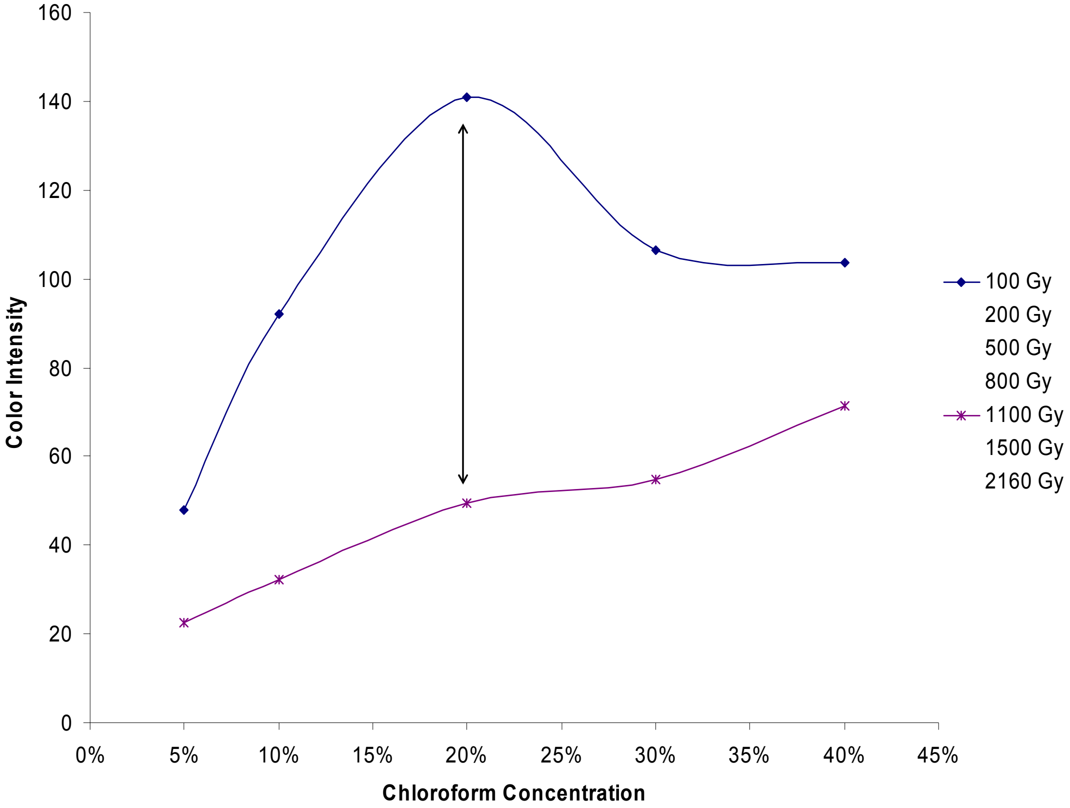

Figure B-12. Grayscale Channel Color vs. Chloroform %. Methyl Yellow Concentration of $4x10^{-4}$ *m*.

Table B-13. Methyl Yellow Color Response at 1×10^{-4} *m*

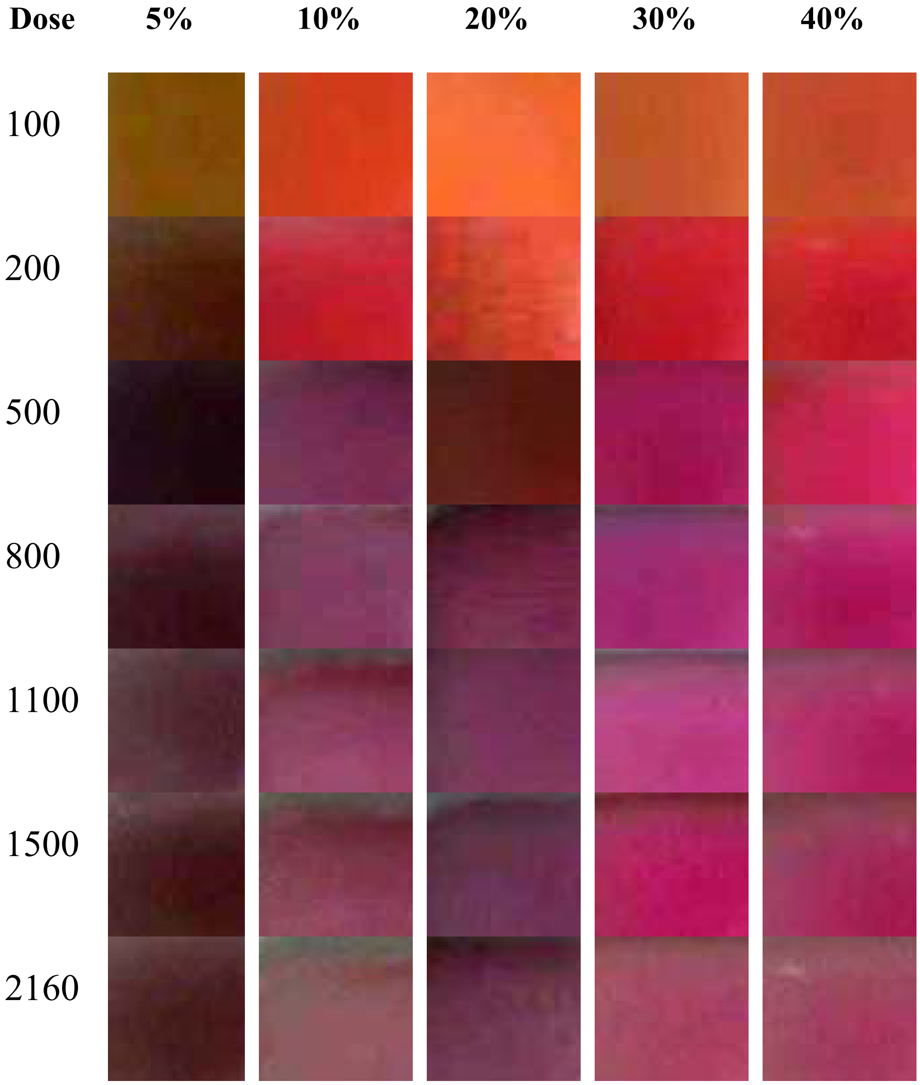

Table B-14. Methyl Yellow Color Response at 4x10^{-4} *m*

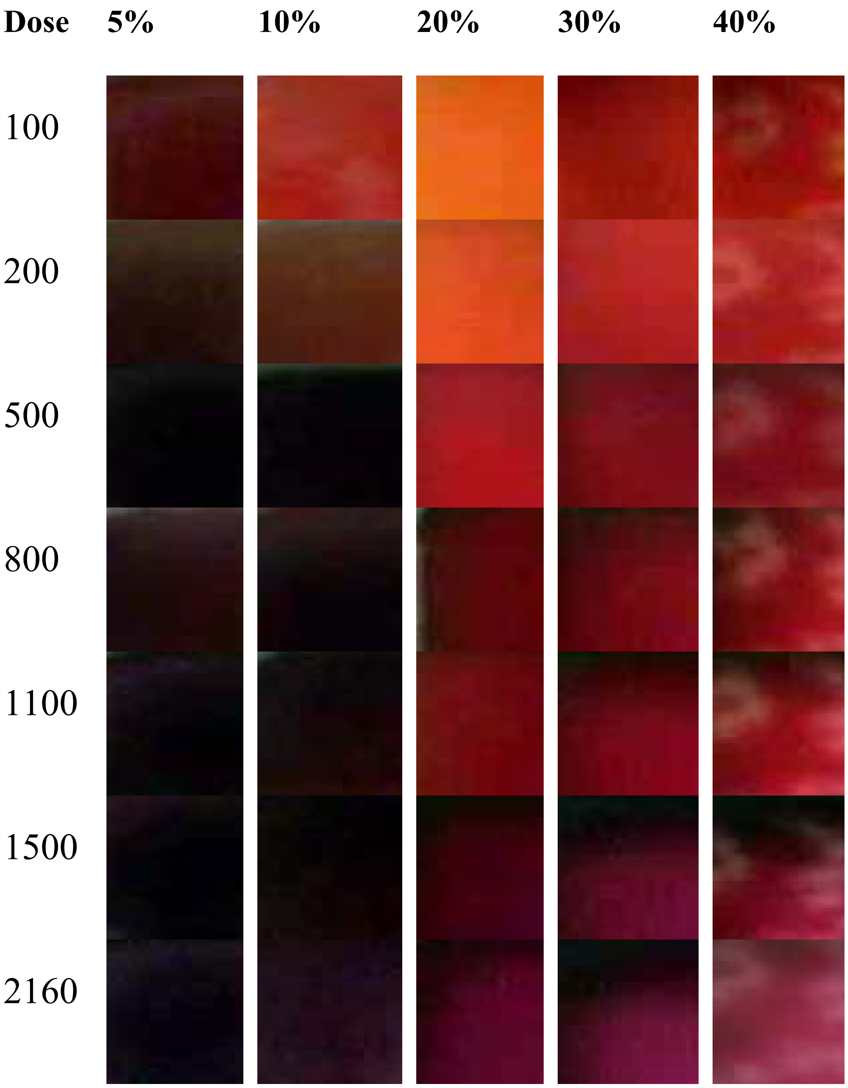

Figures B-9 and B-10 show that the RED and GREEN channels produced the biggest difference between 100 Gy and 1100 Gy at both methyl yellow concentrations. However, at a concentration of 1x10^{-4} *m* it was found that the GREEN channel (Figure B-6) showed a greater difference between 20% and 30% chloroform concentrations compared to the RED (Figure B-5) and BLUE (Figure B-7) channels. At the highest dye concentration, the GREEN (Figure B-10) channel also produced the highest difference between 100 Gy and 1100 Gy at 20% chloroform concentration. Grayscale intensity data showed best results only at the higher concentrations of dye (Figure B-12); however, the intensity difference between 100 and 1100 Gy were smaller to that of the GREEN channel.

Tables B-13 and B-14 show a graphical description of the color sensitivity between 100 and 2160 Gy for different chloroform and dye concentrations. Table B-13 shows that at 20% chloroform there was saturation for both, the high and the low concentrations of methyl yellow.

However, at the lower chloroform concentrations (for both dye concentrations) it was found that the chemical solution saturated faster, resulting in darker shades for increasing doses. Tables B-13 and B-14 show there was an effect between the lower and higher dye concentrations. For the lower concentrations, the color intensity is more representative than at higher concentrations. Despite of the higher color intensity for the lower dye concentrations (Table B-13), it was observed that chemical solution saturates faster at higher doses compared to the higher methyl yellow concentration (Table B-14).

In conclusion, it was found that a chemical composition of 20% chloroform and a concentration of $4\text{x}10^{-4}$ *m* methyl yellow provided the best color response when exposed to gamma rays in the range of 100 to 1160 Gy. Such chemical composition showed to be equivalent to that of water at the 99% confidence level. It is then assumed that that the paraffin, chloroform, methyl yellow solution shall be regarded as tissue equivalent material. The findings of this preliminary study were used as the basis for the chemistry and color response for the paraffin wax, chloroform, methyl yellow solution throughout this research.

APPENDIX C

PRELIMINARY RESULTS: SCANNING TECHNIQUE

C.1 Microtek ScanMaker 8700C Desktop Scanner

A Microtek ScanMaker 8700 Pro Series (Microtek USA, Carson, California) scanner was used to capture the apple phantom slices of 3.175 mm thickness after experimental irradiations. The scanner control software Scan Wizard Pro v 5.0 was used to obtain Intensity data measurements for each scanned image. The behavior of the intensity data measurements with several scanner parameters such as dynamic range, signal response vs. time, reflection vs. transmission modes, and intensity vs. slice thickness were analyzed.

C.2 Scanner Dynamic Range Analysis

The scanner dynamic range was analyzed to understand the variability in intensity data. Specifically, a set of three 3.175 mm thick methyl yellow samples were irradiated with 1.35 MeV electrons and scanned along the beam direction using different dynamic range values. The analysis was performed in the range of 4.0 corresponding to “full range” up to a value of 2.8. These range covered all the scanner dynamic range scale where the image could be seen. Figure C-1 shows the variation of intensity in terms of optical density for the irradiated samples as a function of dynamic range.

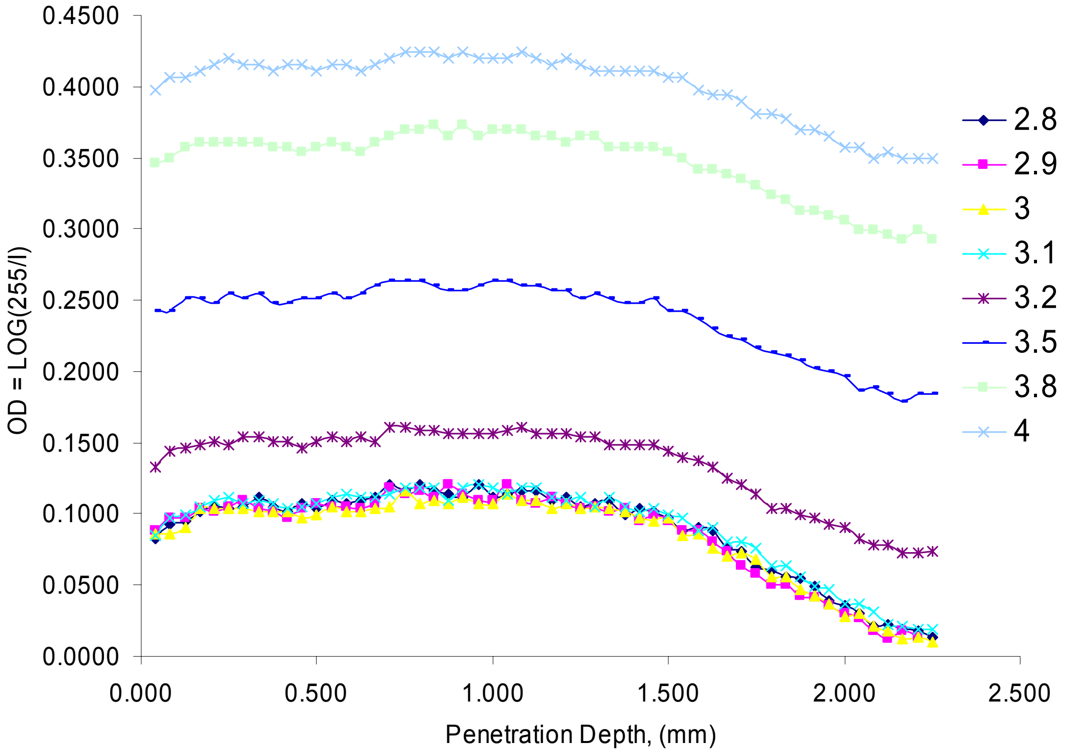

Figure C-1. Dynamic Range Analysis for Microtek Scan Maker 8700 Scanner

Figure C-1 shows a definite variation in optical density data, and thus intensity values for different values of dynamic range. It can be seen that higher dynamic range values yield higher optical density values. However, it was found that intensity data at the "full dynamic range" scale, i.e., a value of 4.0, showed extreme dark areas making it difficult to visualize the images. This effect was related to the thickness of the methyl yellow material that attenuates the light intensity coming from the lamp thus showing dark areas.

To avoid showing dark images, dynamic range values were decreased resulting in the reduction of dark edges and areas that made it difficult to analyze an image. For instance, the following figures show the effect of decreasing the dynamic range from full scale to a value of 3.2 in a 3.175mm sample irradiated under x-rays.

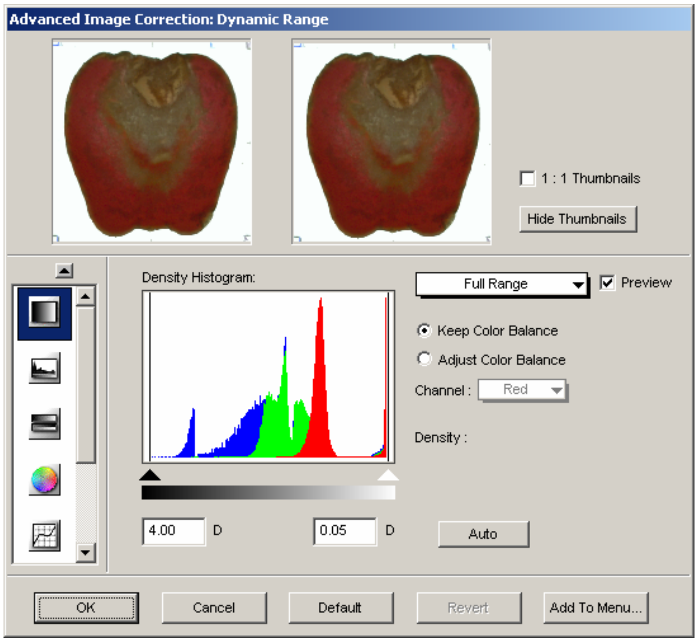

Advanced Image Correction: Dynamic Range

☐ 1 : 1 Thumbnails

Full Range ☑ Preview

● Keep Color Balance

○ Adjust Color Balance

Channel : Red

Density :

4.00 D

0.05 D

Figure C-2. Dynamic Range using Full Range for 3.175 mm thick methyl yellow slice

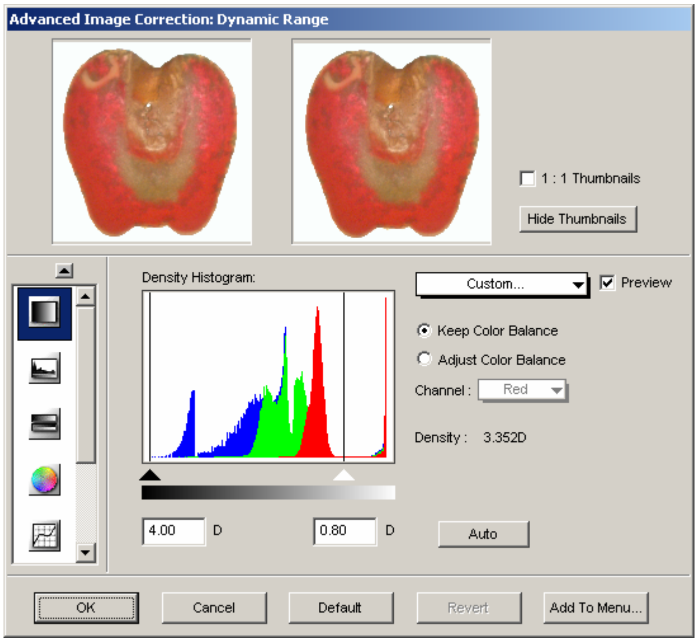

Advanced Image Correction: Dynamic Range

☐ 1 : 1 Thumbnails

☑ Preview

● Keep Color Balance

○ Adjust Color Balance

Channel : Red

Density : 3.352D

4.00 D

0.80 D

Figure C-3. Dynamic Range of 3.2 for 3.175 mm thick methyl yellow slice

It was found that a dynamic range value of 3.2 was the best to analyze intensity data for the proposed methyl yellow thickness (Figure C-3). Dynamic range values below 3.2 showed that intensity data could not be separated in individual curves (Figure C-1) resulting in images that were too bright for analysis. Hence, all scans for the methyl yellow paraffin slices were performed using a fixed dynamic range of 3.2.

C.3 Scanner Signal Intensity vs. Time

The intensity of the scanner signal was analyzed for different scanning times to understand intensity changes due to the lamp warm up. A dynamic range value of 3.2 was fixed as described in Section C-2. Scanning tests were performed on a group of three 3.175 mm thick methyl yellow samples irradiated with 1.35 MeV electrons corresponding to a dose of 320 Gy. After the scanner was turned on, each of the samples were scanned consecutively for 15 times for each scan time with resting periods of 1, 7, 17, 30, and 45 minutes between scan times. Then, intensity data for each scan time was averaged and optical density values calculated. Figure C-4 shows the average OD results found.

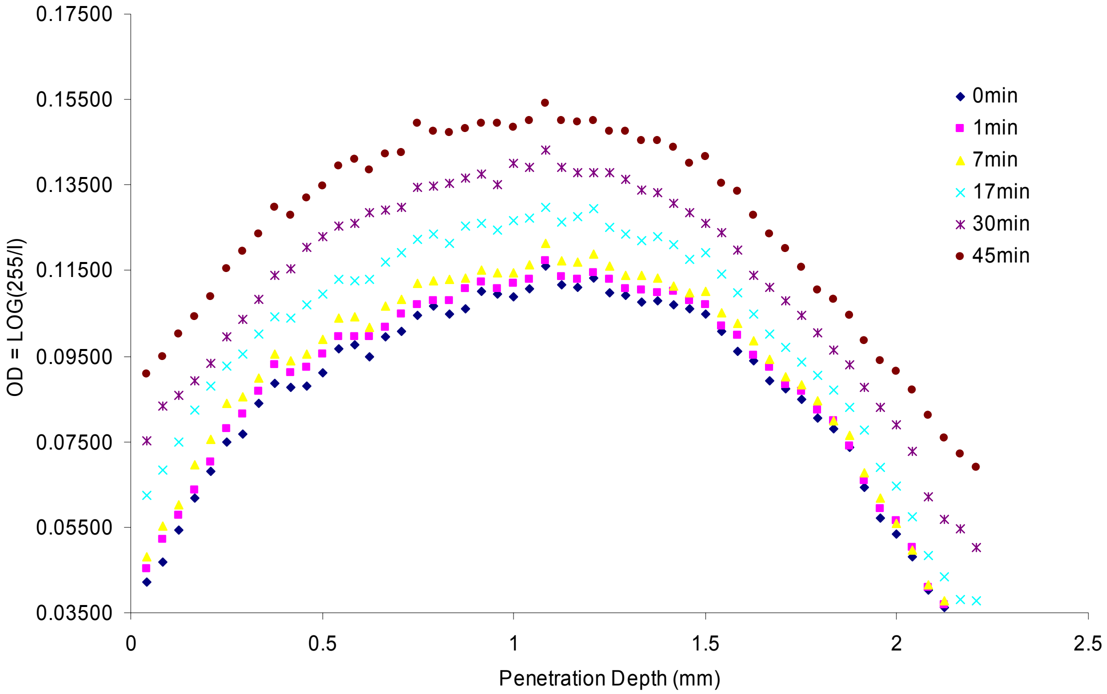

Figure C-4. Intensity variation due to lamp warm up with Microtek 8700 Pro Scanner

Due to the apparent change in intensity data for different scan times, statistical analyses were performed to establish such differences. At the 99% level of significance, it was found that intensity data was not significantly different for 0, 1, and 7 minutes of rest time between scans. In addition, intensity data was not significantly different within each batch produced within each scan time. However, Figure C-4 shows that after 17 minutes of inactivity the intensity data becomes significantly different due to the lamp cooling off. As a result, the scanner was warmed up performing 5 blank scans before any experimental scan was performed. Also, all scanning material was previously sorted before scans to avoid the lamp cooling off.

C.4 Scanning Mode: Reflection vs. Transmission

The scanner offered two scan settings, reflection or transmission modes, and each one with an independent scanning tray. Due to the apple phantom slice thickness both scanning modes were analyzed to determine which method produced the best scan for analysis with MatLab. Results previously found in Sections C-2 and C-3 were implemented for these tests. Three methyl yellow samples of 3.175 mm thick were irradiated with 1.35 MeV electrons and scanned in both modes. Contour plots of the top left side of the apple were produced using Matlab. Figure C-5 shows the results as follows:

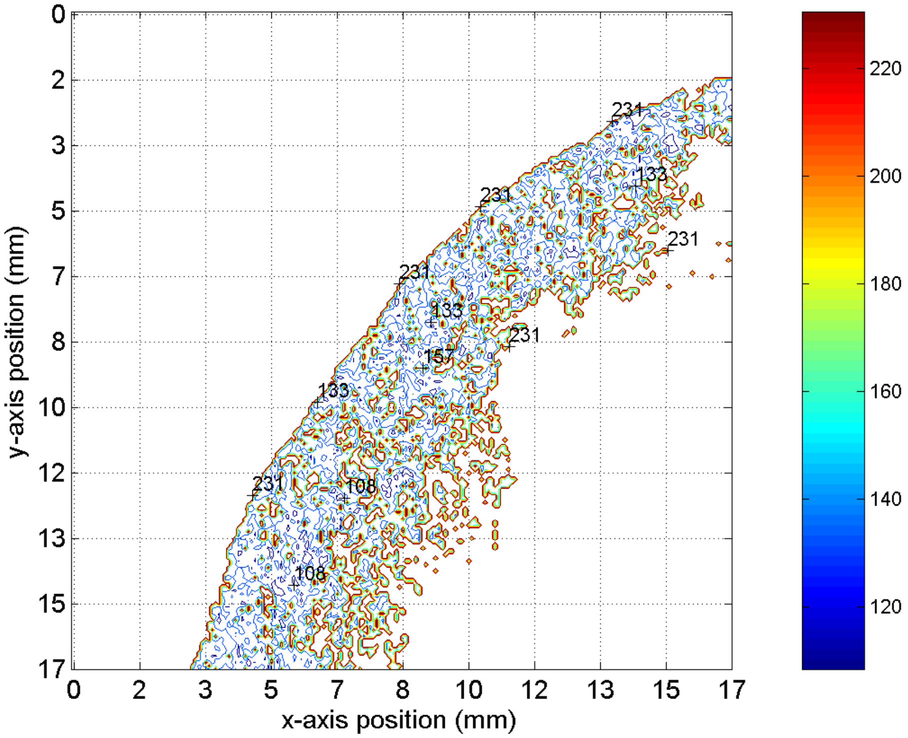

Figure C-5. Intensity Reflection Contour Plot for Top left half of a 3.175 mm thick Methyl Yellow Apple Slice irradiated at 220 Gy.

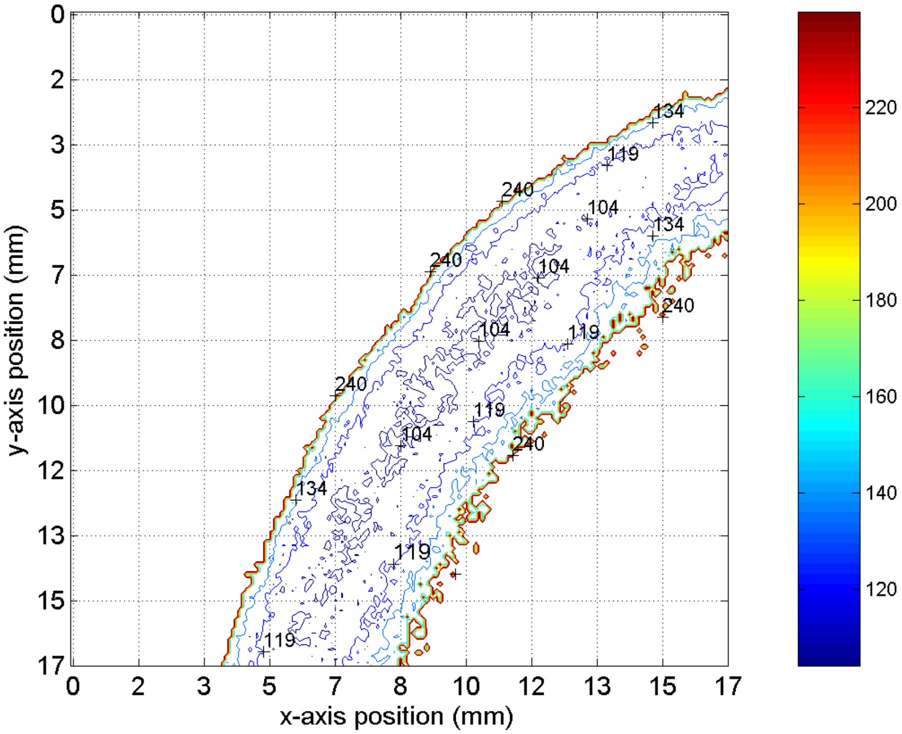

Figure C-6. Intensity Transmission Contour Plot for Top left half of a 3.175 mm thick Methyl Yellow Apple Slice irradiated at 220 Gy.

The intensity distribution produced from the reflection scan shown in Figure C-6 did not produce the expected results for a typical electron distribution. This result was believed to be produced due to the methyl yellow thickness. In the reflection mode, all the light shined into the methyl yellow slice did not reflect back to the Charged Couple Device (CCD) as a result signal was lost and the contour produced was not the optimum.

Figure C-6 shows that for the same 3.175 mm thickness of a methyl yellow slice, the intensity distribution produced by the electrons appeared just fine. Indeed, notice how the intensity decreases to a minimum point where dose is the highest (highest optical density) to later increase again showing the typical trace of an electron distribution. This results show clearly the superior advantage of transmission vs. reflection mode due to the slice thickness. As a result, all experimental scans must be performed under transmission mode using the results previously found in Sections C-2 and C-3.

C.5 Transmission Scanning and Methyl Yellow Slice Thickness Analysis

The influence of the slice thickness parameter was analyzed in two parts. First, the thickness parameter in methyl yellow apple slices was studied in transmission scans using triplicates of irradiated apples at 250 Gy. Each sample was cut 24 hours after the irradiation experiment as described in Chapter 3 Sections 3.5.1, and scanned as described previously in Sections C.2 and C.3. Average data values were obtained and plotted for each thickness analyzed. Figure C-7 shows the results found:

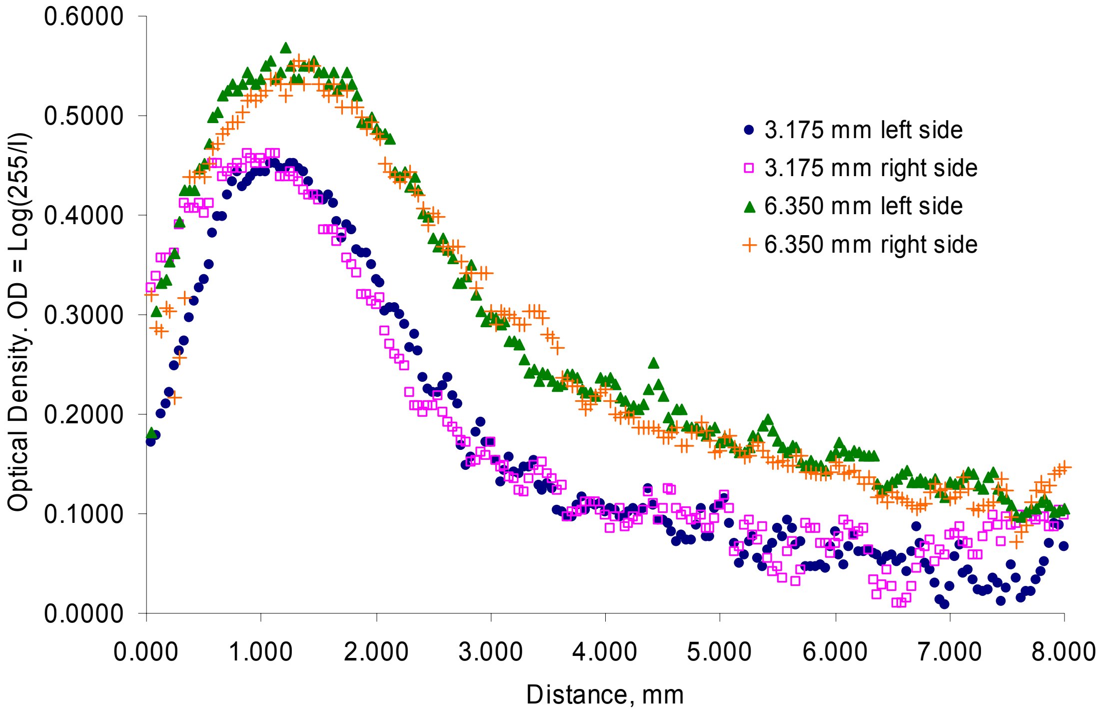

Figure C-7. Methyl Yellow Slice Thickness Analysis for irradiated apple under full rotation at 220 Gy and 0 degrees from its vertical axis.

The slice thicknesses studied were 3.175 mm and 6.350 mm which were able to fit in the transmission scan bay in the scanner. The results showed that the optical density values increased as sample thickness increased by an order of magnitude of 0.1.

Both curves may be used for analysis of relative dose distributions, however, the thinner sample offers the advantage of transmitting most if not all of the light shined through the irradiated sample. As a result, all scans for this research shall be performed for samples of 3.175 mm thick.

C.6 Uniformity of Intensity in Paraffin, Chloroform, Methyl Mellow Slices of Different Thickness

The uniformity of intensity data was tested in triplicates for unirradiated samples. Each control sample thickness was of 3.175, 6.350, and 12.7 mm respectively. Within each control sample, ten randomly selected intensity measurements were read using the histogram function tool in Adobe Photoshop 6. Each region selected at each random location contained an area of 50 x 50 pixels. Tables C-1, C-2, and C-3 show the results for the individual color components of the Red, Green, and Blue channels respectively, and Table C-4 contains their average values.

Table C-1. RGB Color Values for 3.175 mm Slices

Sample1			Sample2			Sample 3		
R	G	B	R	G	B	R	G	B
220.90	205.85	6.44	227.09	215.09	67.69	227.67	206.64	25.74
225.45	206.83	15.32	215.28	200.28	8.89	220.89	203.06	13.85
225.87	209.83	28.70	222.41	209.68	53.69	218.50	200.43	6.89
221.59	203.77	11.76	223.40	207.63	51.77	218.05	197.42	4.41
223.70	208.53	23.17	214.56	200.02	10.64	217.16	197.94	9.60
223.99	209.58	35.61	215.46	199.83	9.22	216.27	196.87	3.65
227.16	208.47	10.70	220.24	206.48	38.42	220.50	201.85	15.03
216.88	190.06	4.72	223.40	207.63	51.77	219.26	203.30	21.52
221.12	203.40	7.79	224.47	207.79	50.05	218.08	201.24	14.55
221.93	207.32	17.71	215.36	201.40	3.34	221.40	205.02	20.11
222.86	**205.36**	**16.19**	**220.17**	**205.58**	**34.55**	**219.78**	**201.38**	**13.54**

Table C-2. RGB Color Values for 6.350 mm Slices

Sample1			Sample2			Sample 3		
R	G	B	R	G	B	R	G	B
213.85	193.71	0.04	212.21	194.84	26.37	223.17	191.97	3.96
207.26	184.31	2.48	216.46	198.74	35.04	227.22	195.67	11.08
220.24	196.28	4.35	218.91	200.81	27.32	204.14	174.67	0.85
210.44	188.50	6.73	219.17	200.52	26.63	207.65	182.50	2.53
220.23	196.50	0.46	218.56	200.98	45.36	203.51	182.04	1.40
223.40	200.25	1.78	217.99	199.34	25.39	223.47	200.81	5.53
217.62	195.78	2.12	217.27	198.21	16.84	200.43	177.21	3.65
218.03	186.01	0.99	208.34	191.09	20.56	200.01	177.99	0.46
218.89	188.17	1.33	211.75	193.97	26.60	218.41	195.02	0.76
221.03	188.78	0.97	208.83	189.64	25.86	210.35	188.32	0.93
217.10	**191.83**	**2.13**	**214.95**	**196.81**	**27.60**	**211.84**	**186.62**	**3.12**

Table C-3. RGB Color Values for 12.7 mm Slices

Sample1			Sample2			Sample 3		
R	G	B	R	G	B	R	G	B
234.78	202.23	0.21	242.63	214.22	0.99	234.29	210.01	0.20
241.50	207.70	0.12	241.44	210.46	0.92	235.66	210.00	0.03
242.62	212.46	2.03	245.02	212.20	0.45	237.39	207.39	0.21
245.57	214.79	0.38	245.04	214.03	2.42	237.90	211.10	0.78
243.85	213.60	0.01	239.01	210.22	0.94	236.62	206.63	0.39
244.22	214.05	0.02	239.67	210.51	0.46	234.89	208.45	0.30
242.90	214.13	0.06	238.61	210.16	0.24	238.25	208.50	0.38
238.86	212.25	0.09	241.18	213.78	0.47	243.33	212.88	0.14
238.58	209.09	0.77	235.04	209.39	1.46	237.77	208.38	0.96
238.38	211.43	0.12	240.49	214.28	0.75	245.17	216.17	0.66
241.13	**211.17**	**0.38**	**240.81**	**211.93**	**0.91**	**238.13**	**209.95**	**0.41**

Table C-4. Average RGB Intensity Data for Control Samples

Thickness	Red			Green			Blue		
(mm)	Sample 1	Sample 2	Sample 3	Sample 1	Sample 2	Sample 3	Sample 1	Sample 2	Sample 3
3.175	223	220	220	205	206	201	16	35	14
6.350	217	215	212	192	197	187	2	28	3
12.700	241	241	238	211	212	210	0	1	0

ANOVA statistical test was used to check for variability between data *within* each thickness. First, the Red channel data was analyzed for variability, second the Green channel and last the Blue channeld data. Results were interpreted for each thickness on the assumption that the null hypothesis (Ho: $\mu_1 = \mu_2 = \mu_3$) is true (Type I error) using a 95% confidence level ($\alpha = 0.05$). Statistical results showed that the average intensity data *within* each thickness for each channel were not significantly different at the selected locations. ANOVA tests were performed to check for variability of intensity measurements *among* the three different thicknesses using a 95% confidence level ($\alpha = 0.05$). Statistical results showed that the average intensity values for each channel were significantly different among thicknesses.

The statistical results found were used as the baseline to establish a specific apple slice thickness. Particularly, apple slices of 3.175 mm thickness were selected to perform the irradiation experiments discussed in Chapter 3 Sections 3.4.1 and 3.4.2.

APPENDIX D

RESULTS FROM E-BEAM IRRADIATION WITH VAN DE GRAAFF ACCELERATOR

D.1 Dose Energy Deposition and Dose Depth Distribution GAFCHROMIC® HD-810 Film

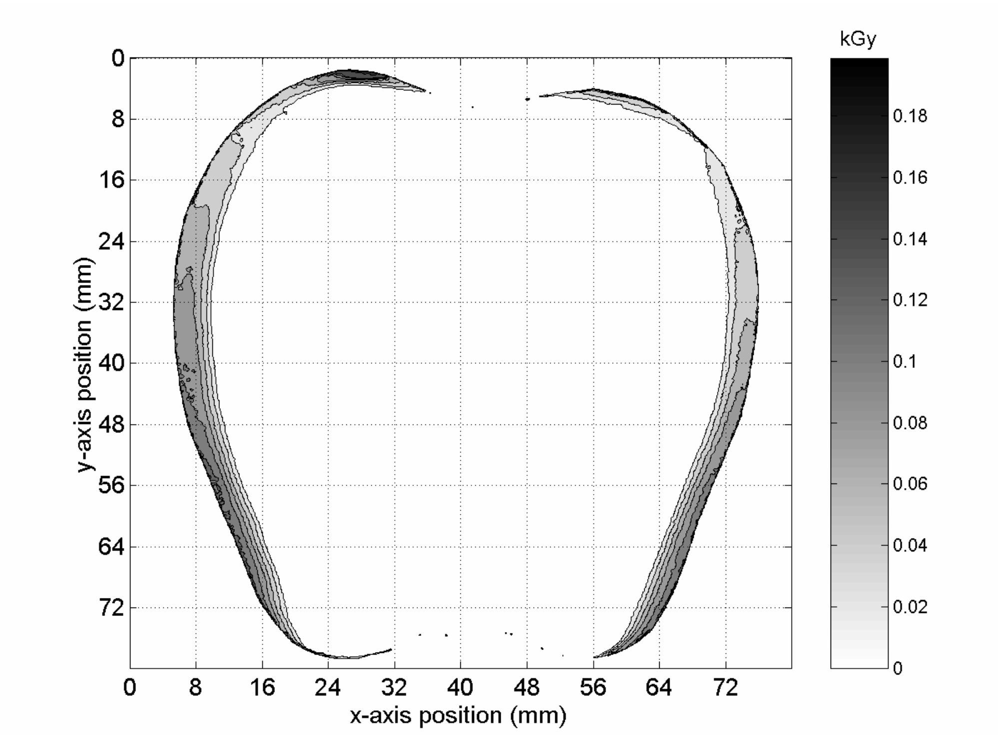

Figure D-1. Film dose distribution in apple phantom irradiated with 50 Gy and 90 degrees.

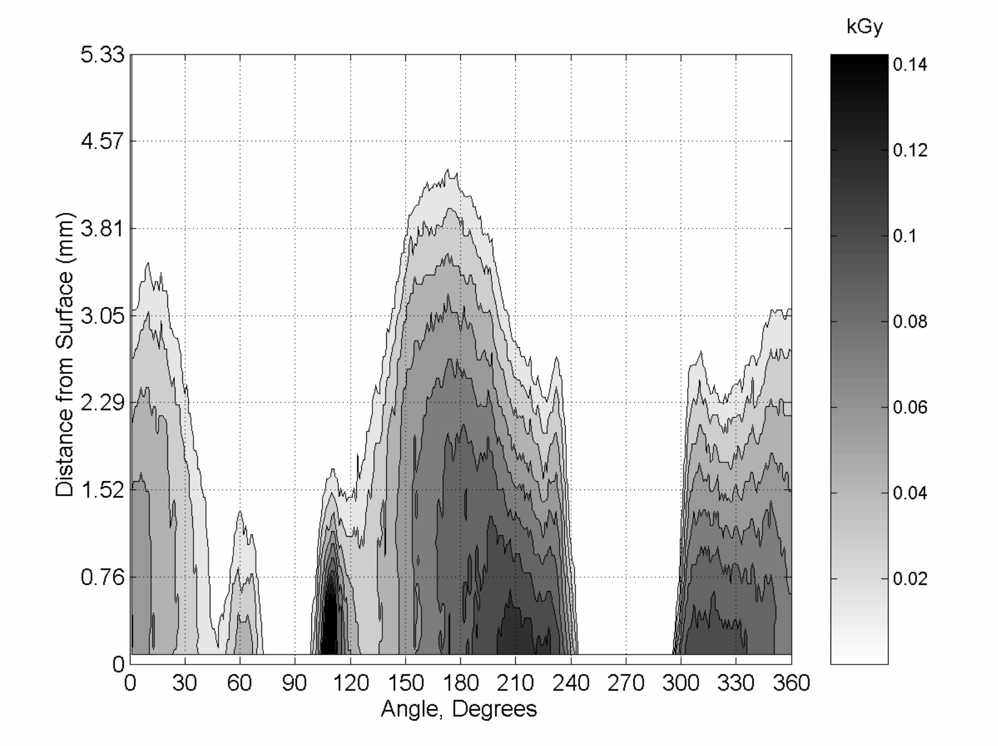

Figure D-2. Film dose-depth distribution in apple phantom irradiated with 50 Gy and 90 degrees.

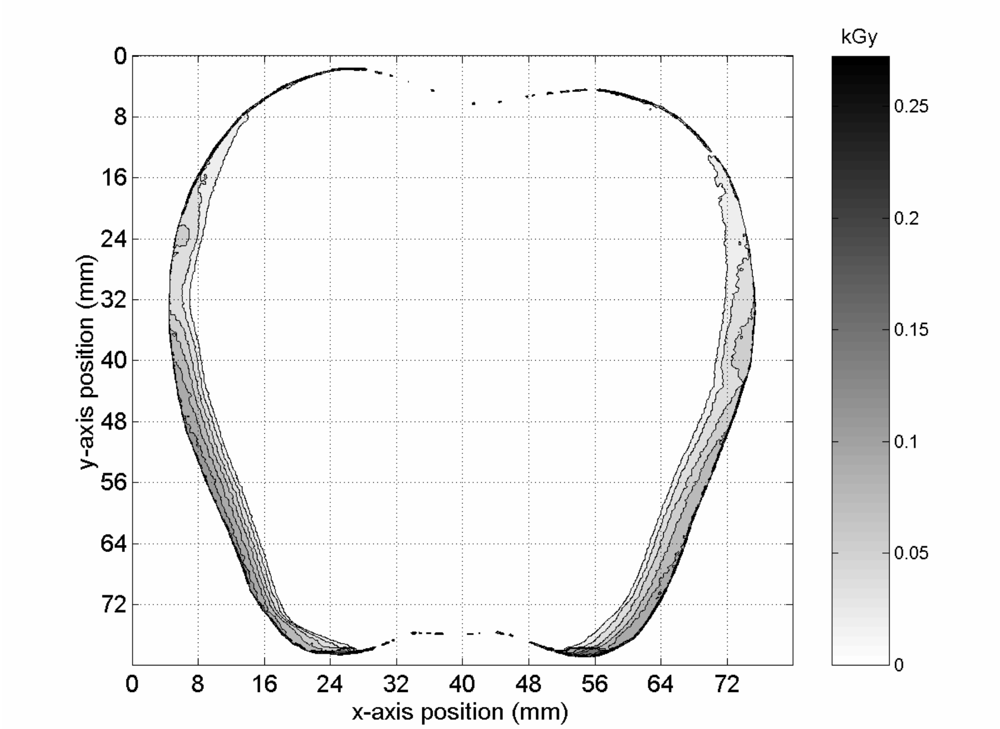

Figure D-3. Film dose distribution in apple phantom irradiated with 50 Gy and 90 degrees.

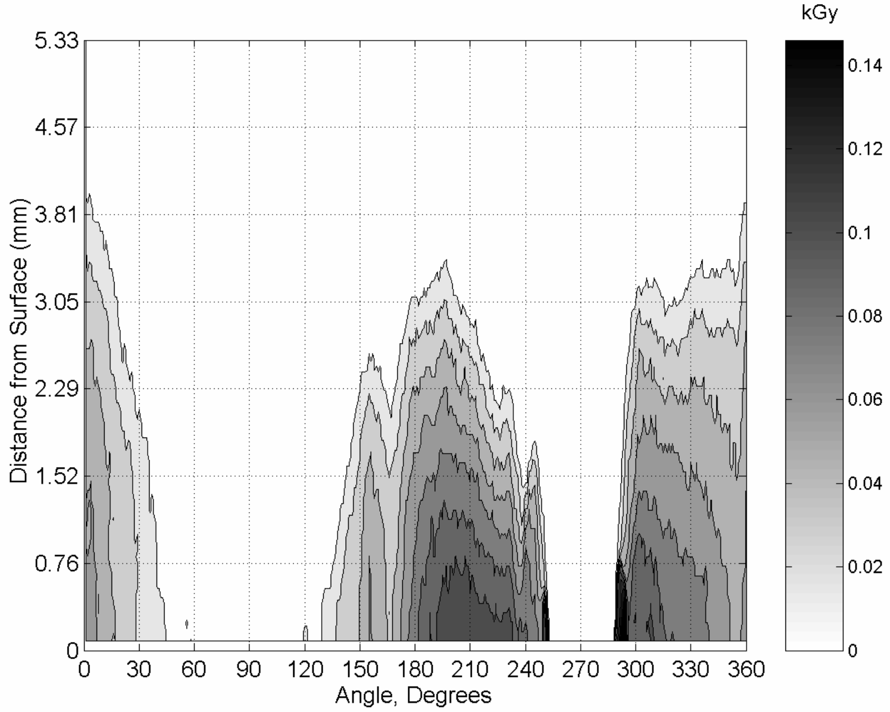

Figure D-4. Film dose-depth distribution in apple phantom irradiated with 50 Gy and 90 degrees.

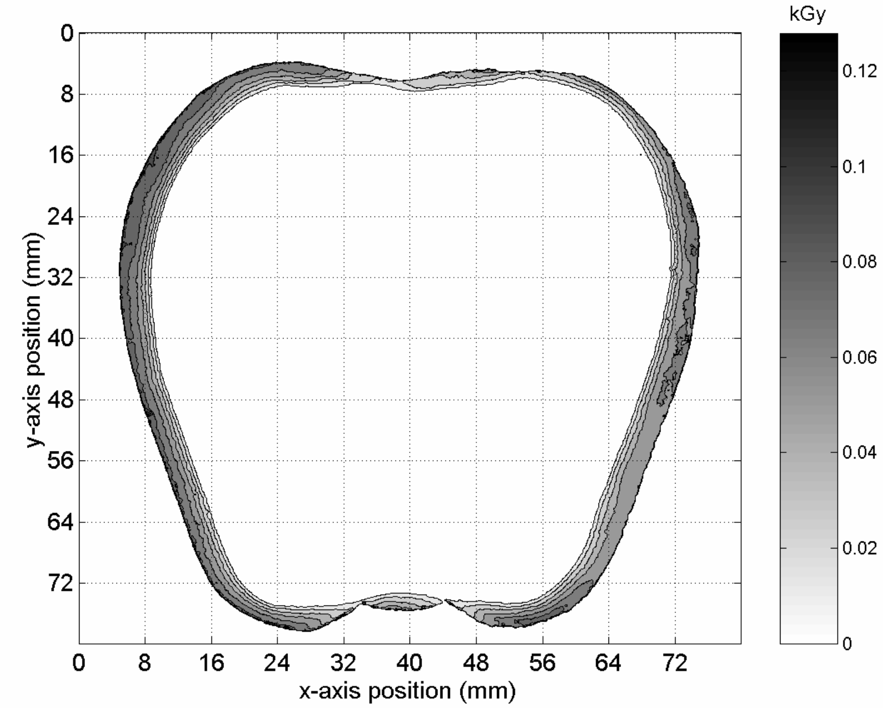

Figure D-5. Film dose distribution in apple phantom irradiated with 50 Gy and 22.5 degrees.

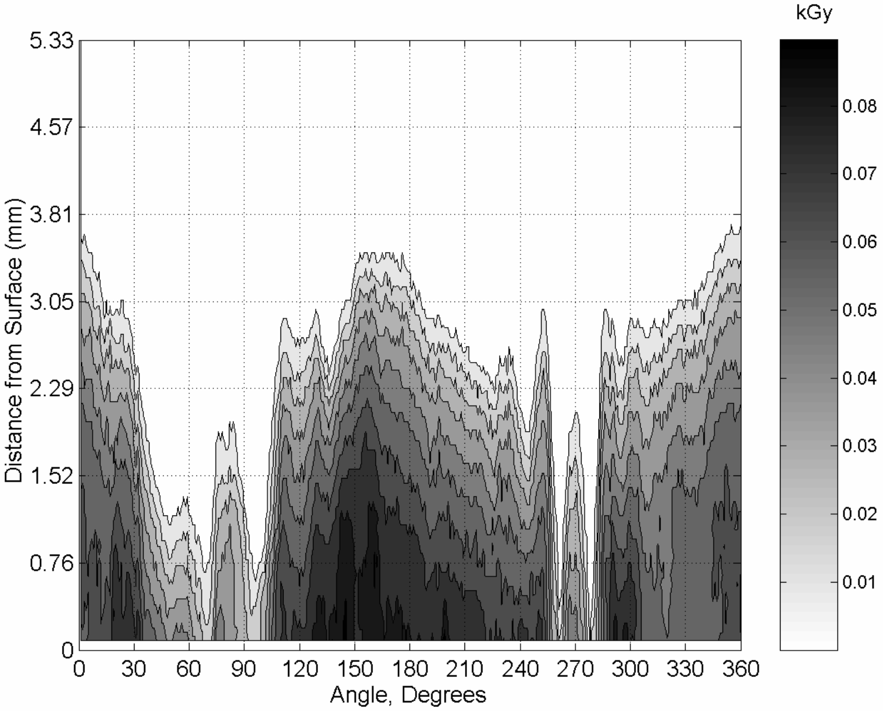

Figure D-6. Film dose-depth distribution in apple phantom irradiated with 50 Gy and 22.5 degrees.

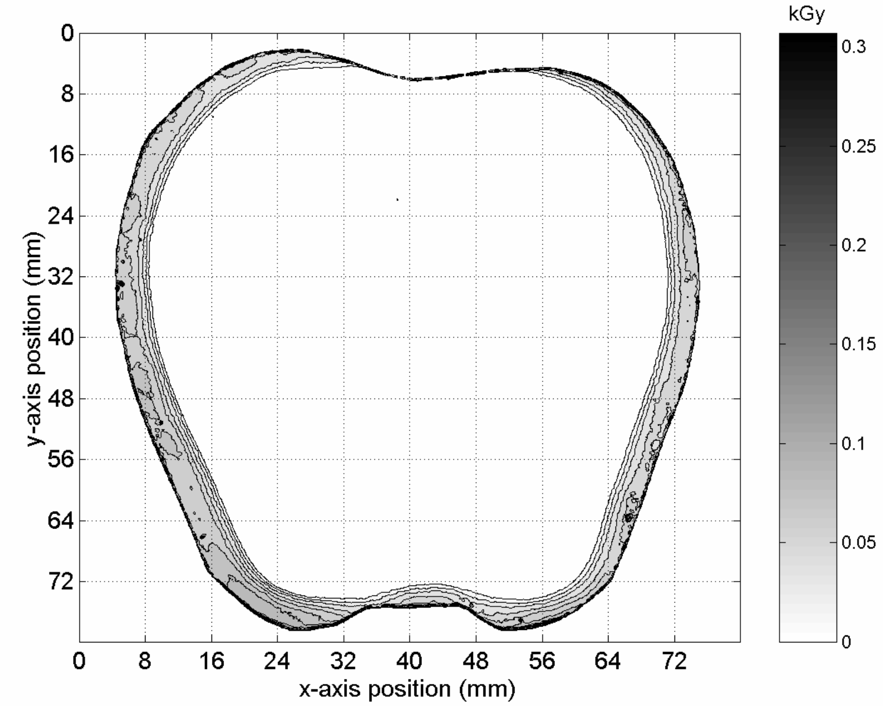

Figure D-7. Film dose distribution in apple phantom irradiated with 50 Gy and 22.5 degrees.

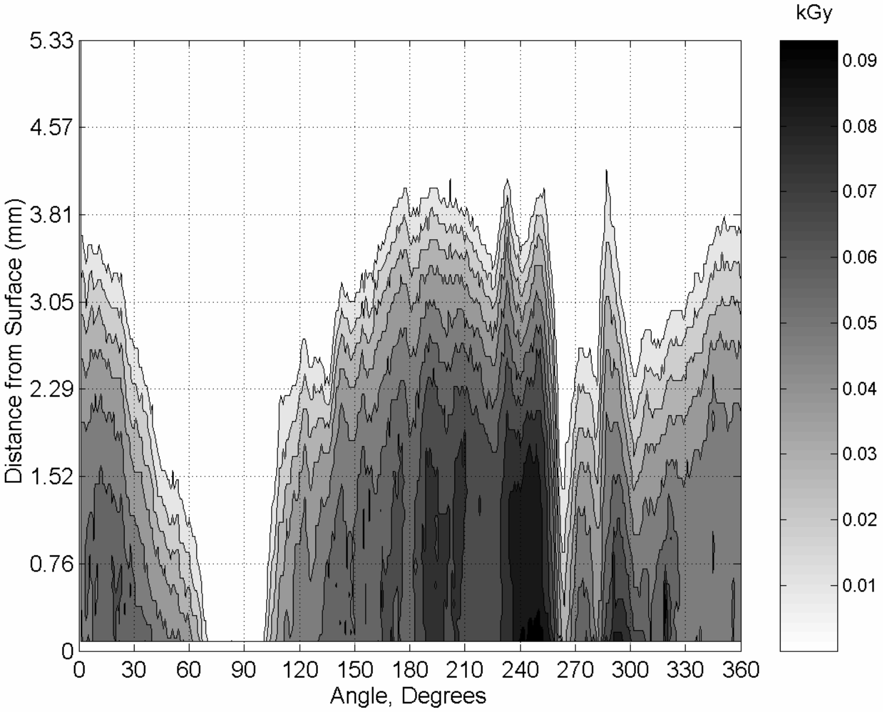

Figure D-8. Film dose-depth distribution in apple phantom irradiated with 50 Gy and 22.5 degrees.

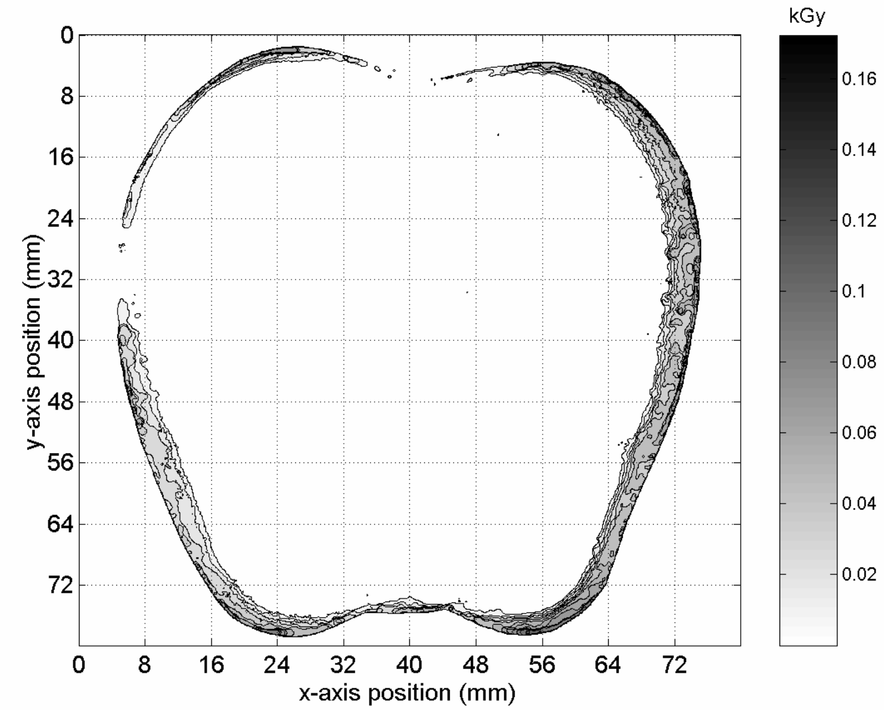

Figure D-9. Film dose distribution in apple phantom irradiated with 50 Gy and 45 degrees.

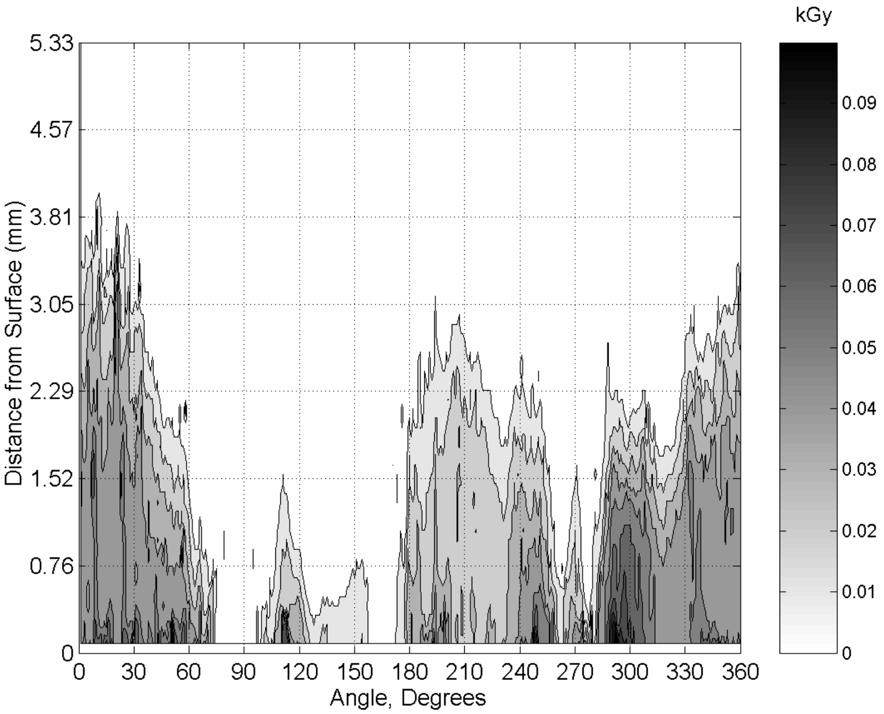

Figure D-10. Film dose-depth distribution in apple phantom irradiated with 50 Gy and 45 degrees.

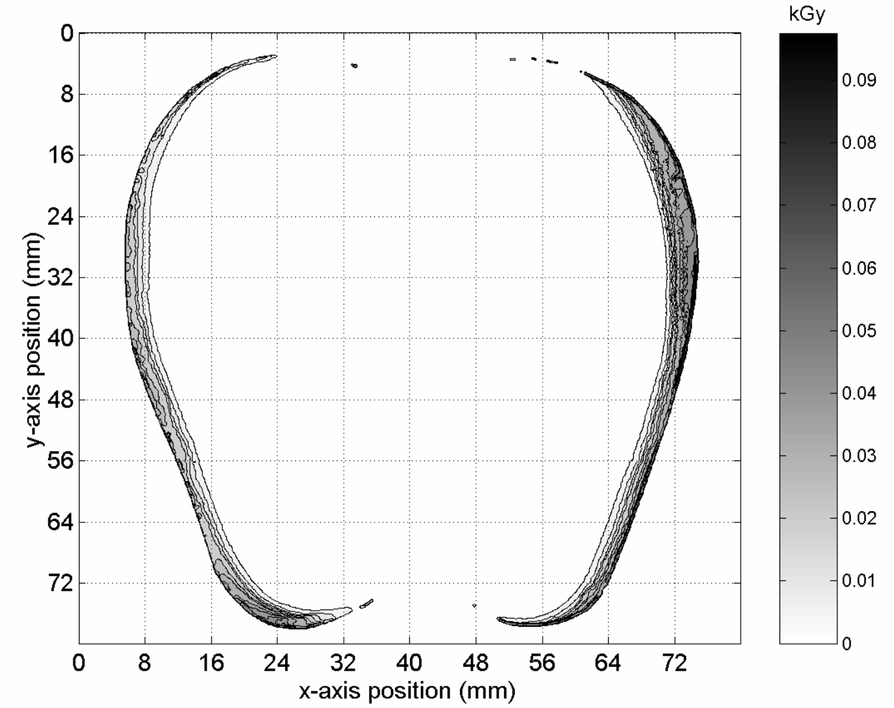

Figure D-11. Film dose distribution in apple phantom irradiated with 50 Gy and 45 degrees.

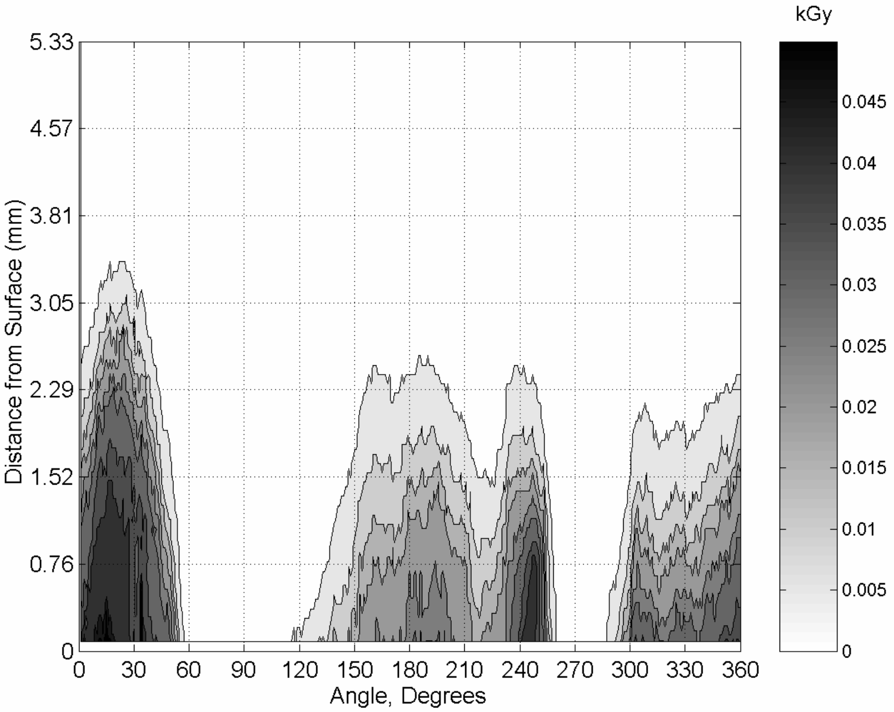

Figure D-12. Film dose-depth distribution in apple phantom irradiated with 50 Gy and 45 degrees.

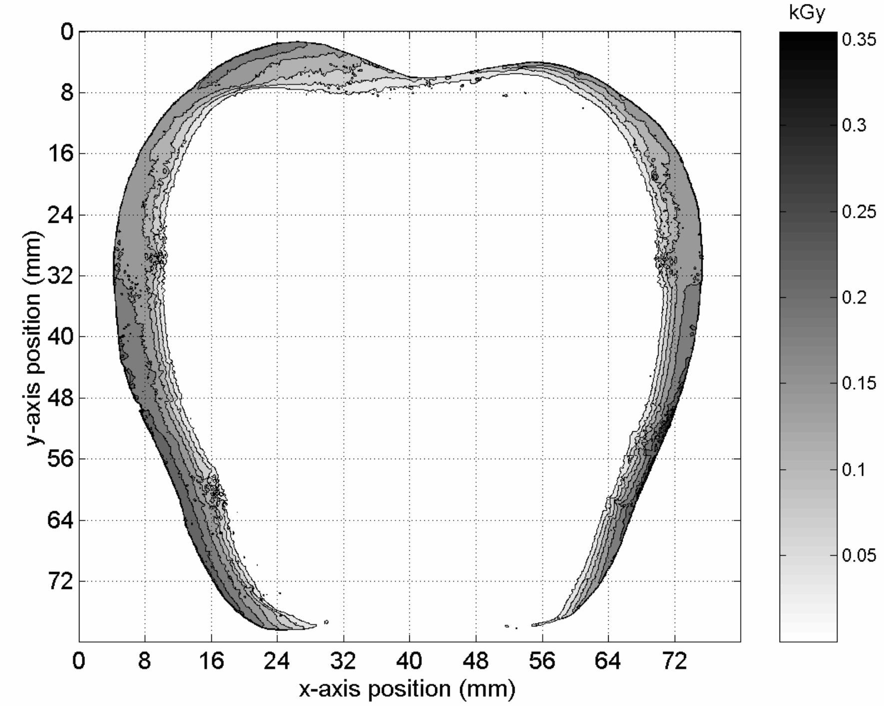

Figure D-13. Film dose distribution in apple phantom irradiated with 100 Gy and 90 degrees.

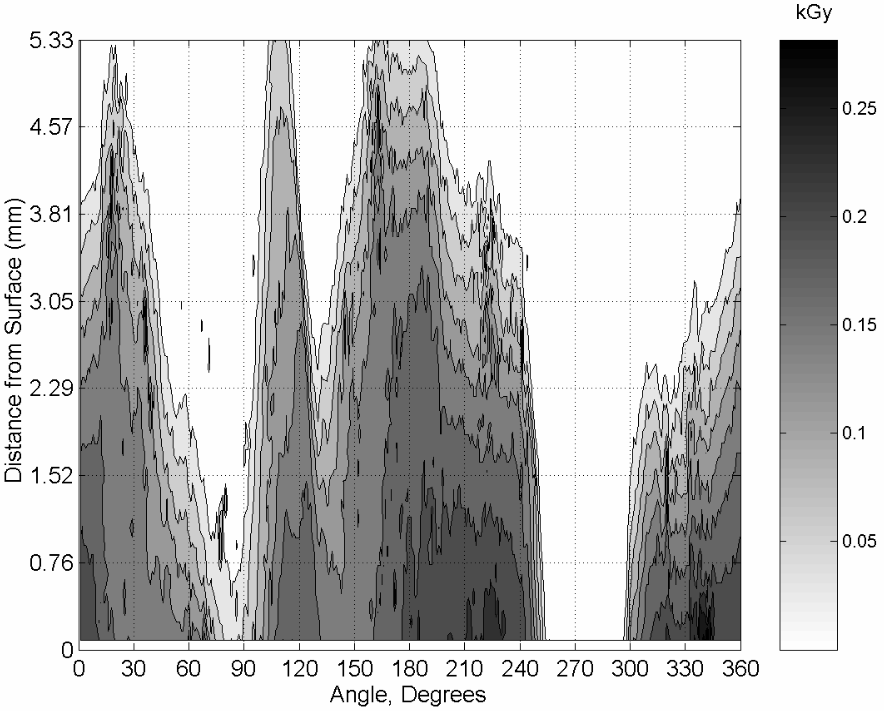

Figure D-14. Film dose-depth distribution in apple phantom irradiated with 100 Gy and 90 degrees.

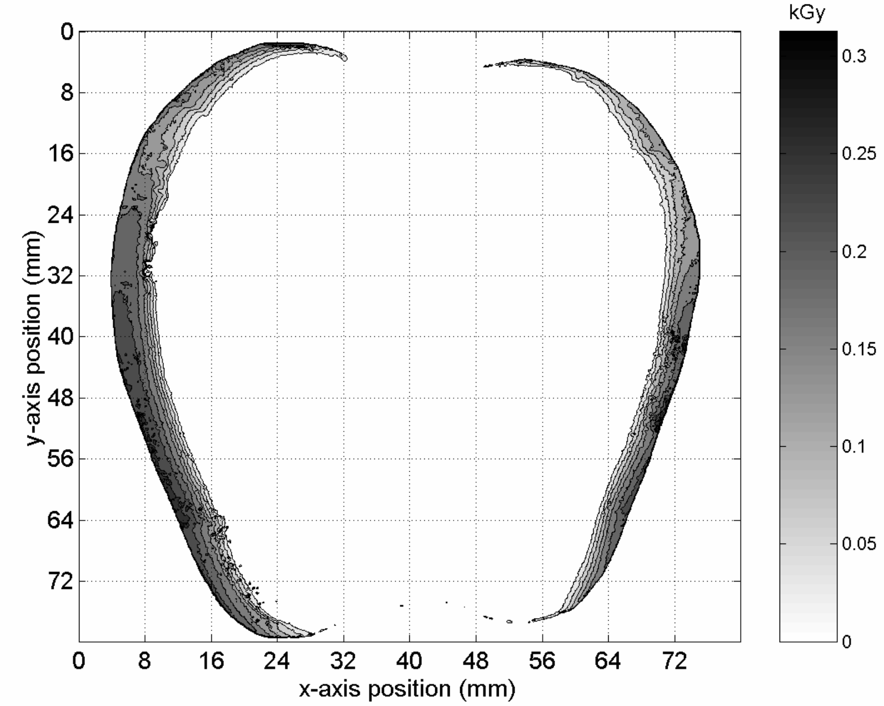

Figure D-15. Film dose distribution in apple phantom irradiated with 100 Gy and 90 degrees.

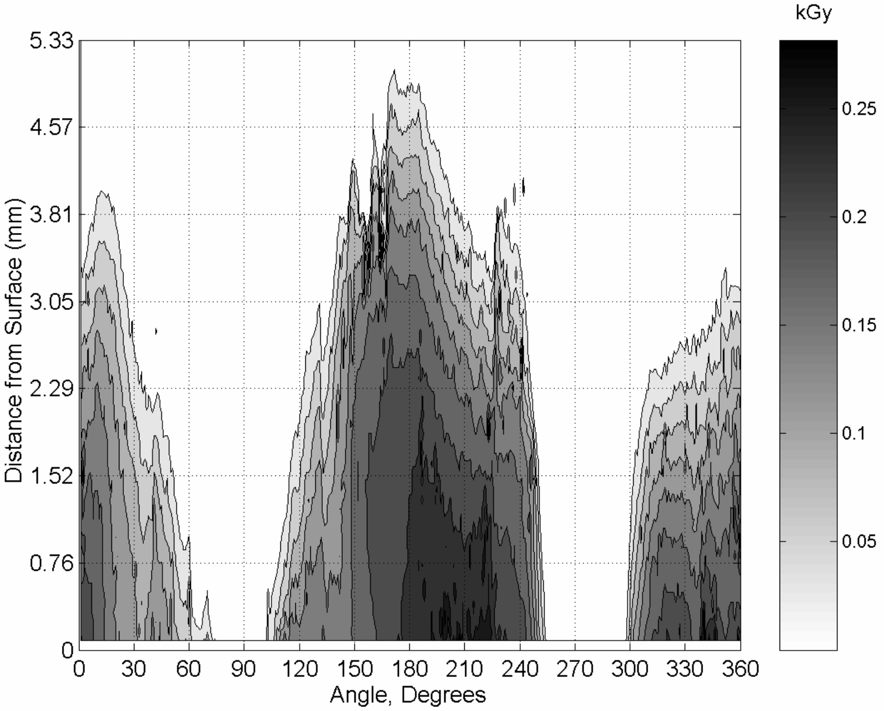

Figure D-16. Film dose-depth distribution in apple phantom irradiated with 100 Gy and 90 degrees.

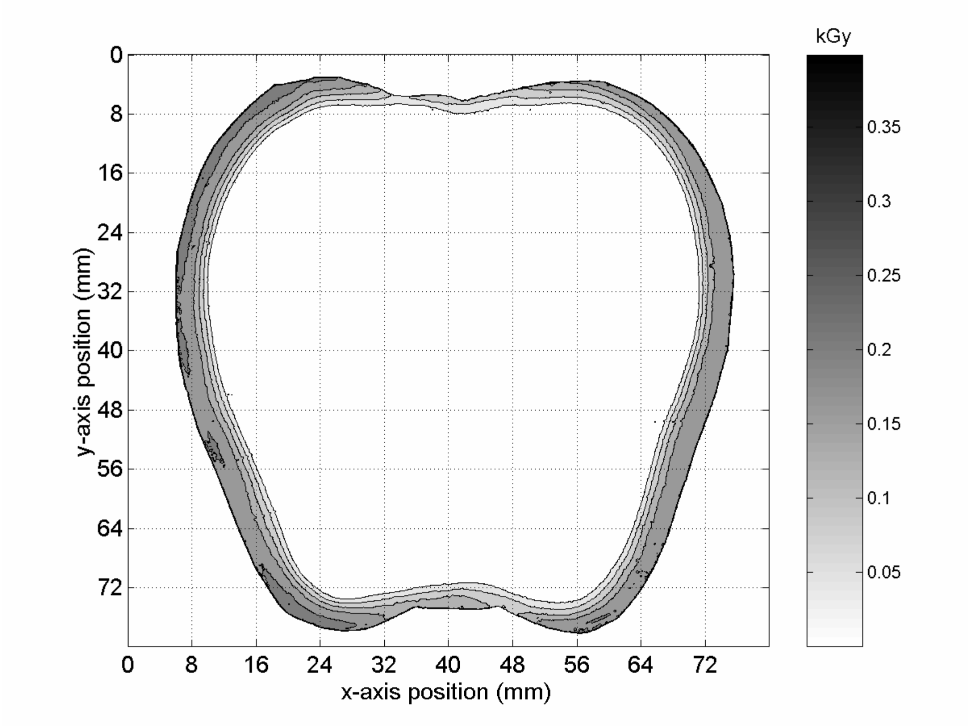

Figure D-17. Film dose distribution in apple phantom irradiated with 100 Gy and 22.5 degrees.

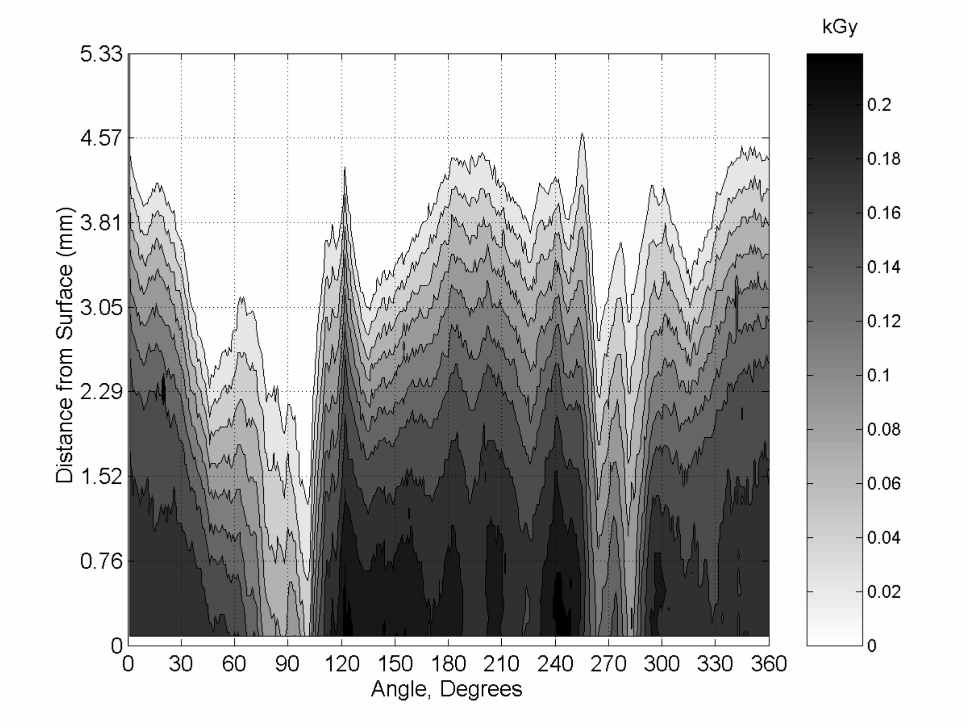

Figure D-18. Film dose-depth distribution in apple phantom irradiated with 100 Gy and 22.5 degrees.

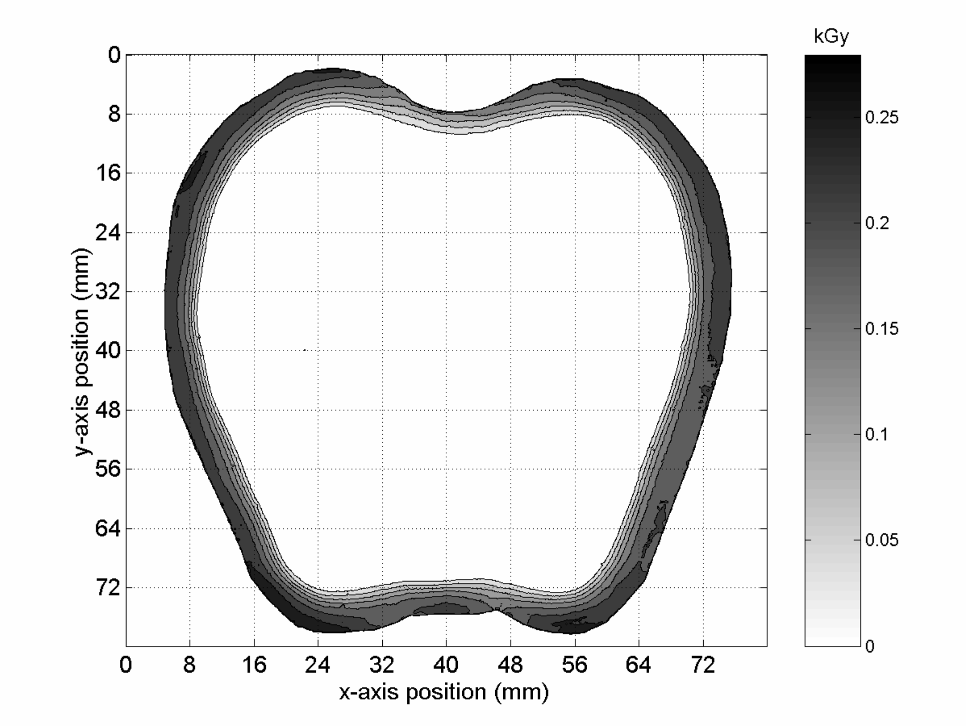

Figure D-19. Film dose distribution in apple phantom irradiated with 100 Gy and 22.5 degrees.

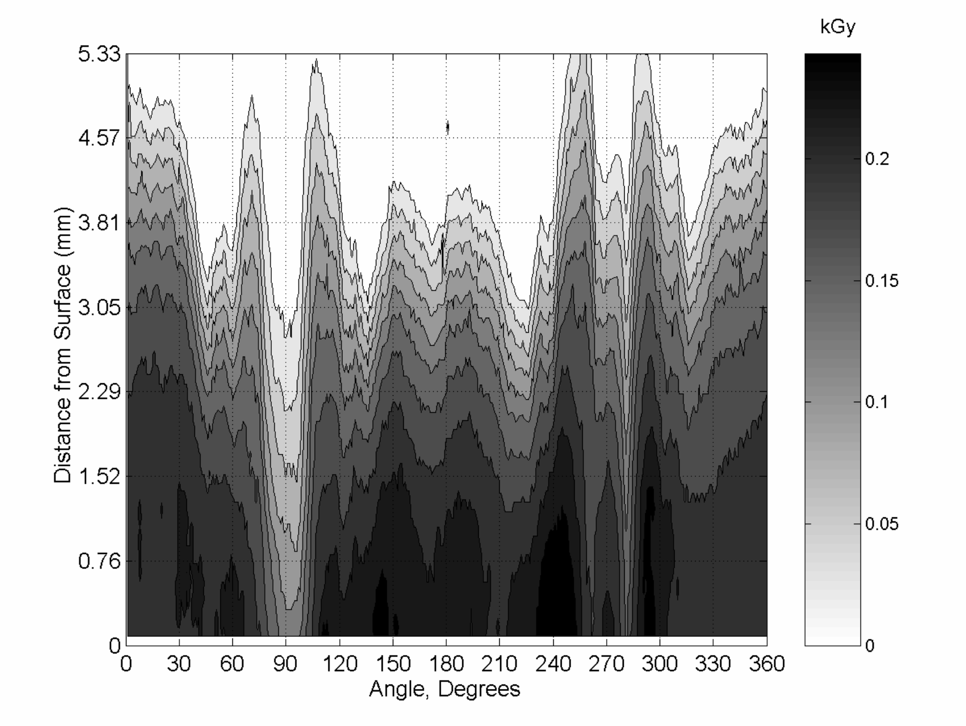

Figure D-20. Film dose-depth distribution in apple phantom irradiated with 100 Gy and 22.5 degrees.

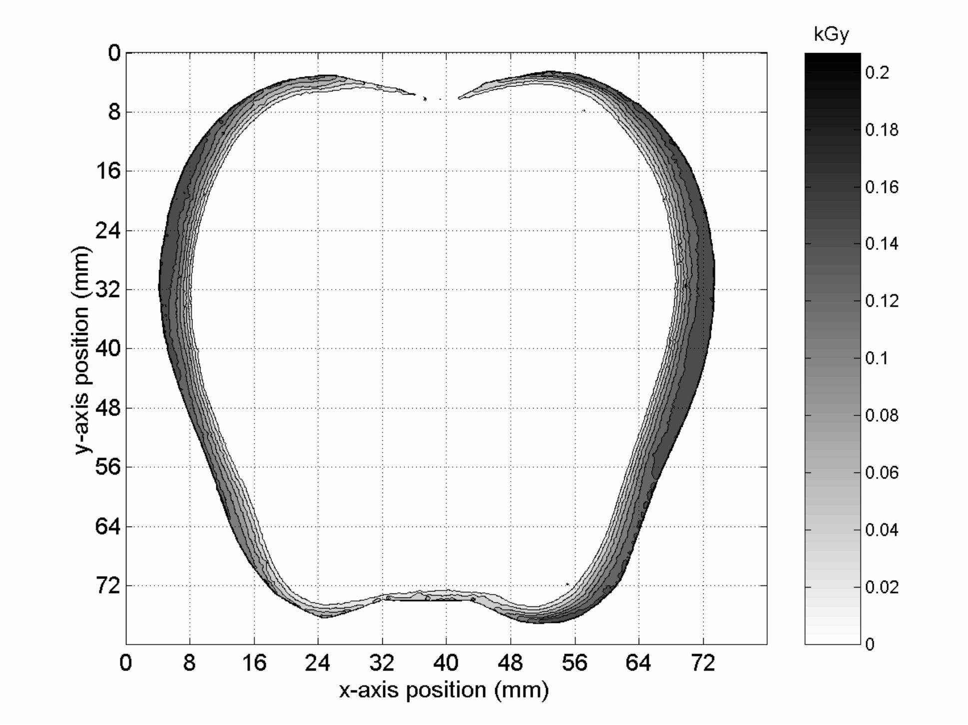

Figure D-21. Film dose distribution in apple phantom irradiated with 100 Gy and 45 degrees.

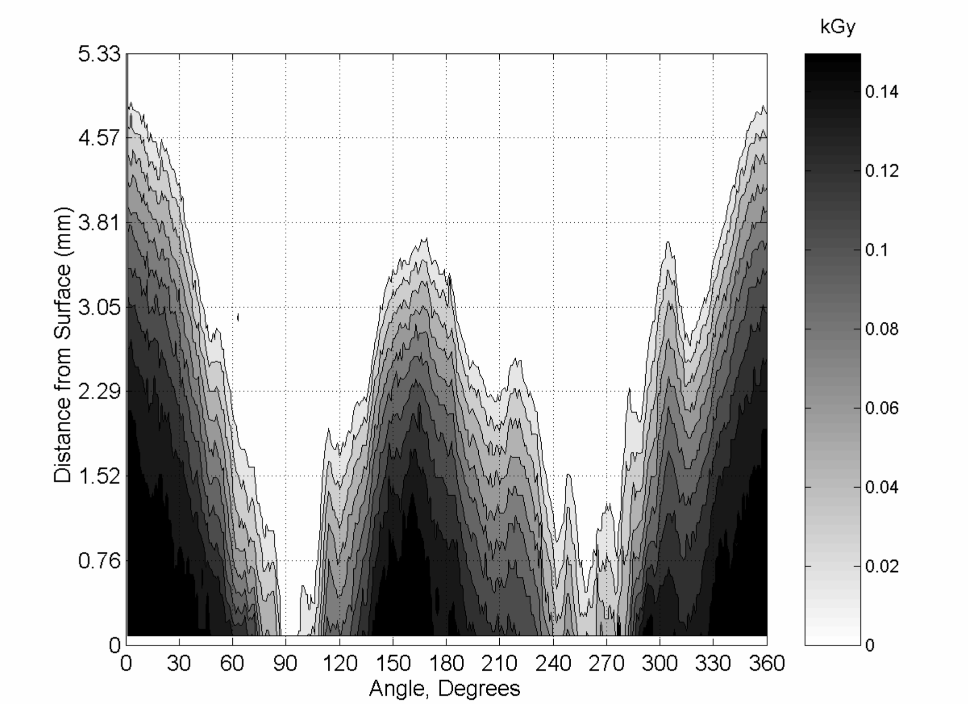

Figure D-22. Film dose-depth distribution in apple phantom irradiated with 100 Gy and 22.5 degrees.

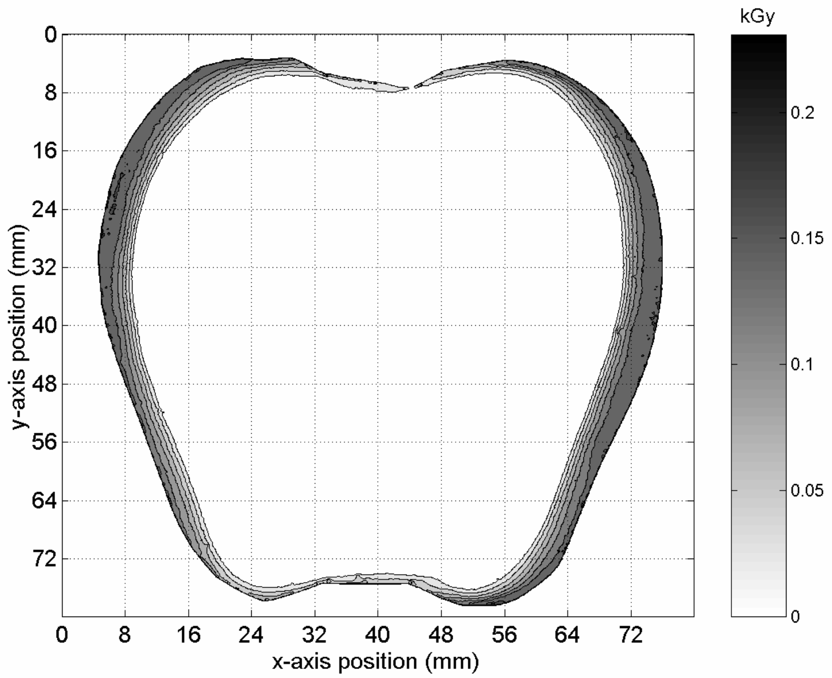

Figure D-23. Film dose distribution in apple phantom irradiated with 100 Gy and 45 degrees.

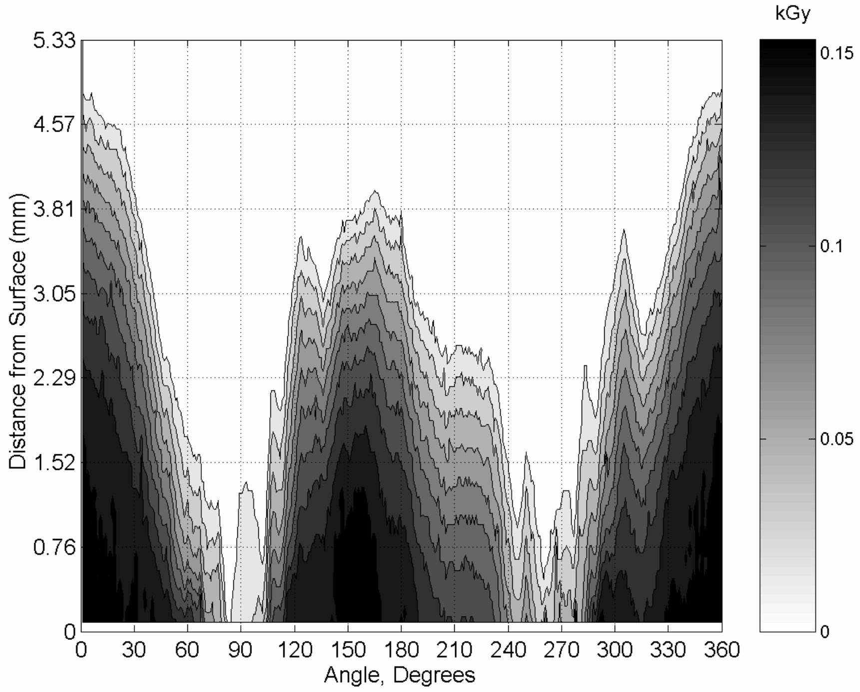

Figure D-24. Film dose-depth distribution in apple phantom irradiated with 100 Gy and 22.5 degrees.

D.2 Dose Energy Deposition and Dose Depth Distribution Methyl Yellow Apple Phantom

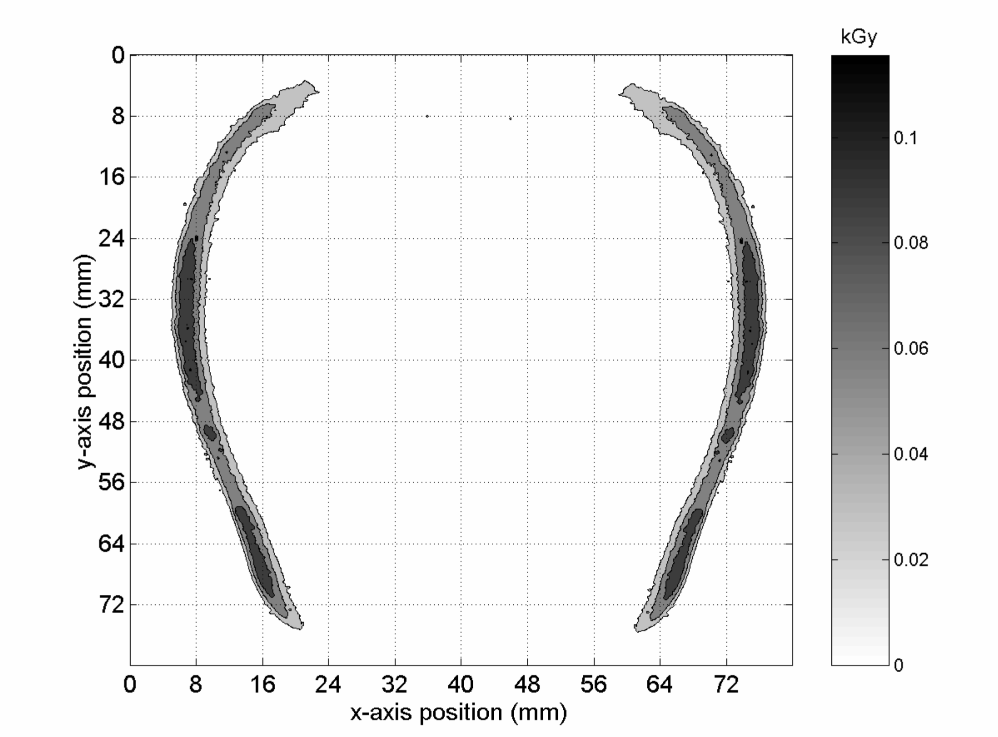

Figure D-25. Methyl Yellow Apple Contour dose distribution irradiated with 50 Gy and 90 degrees.

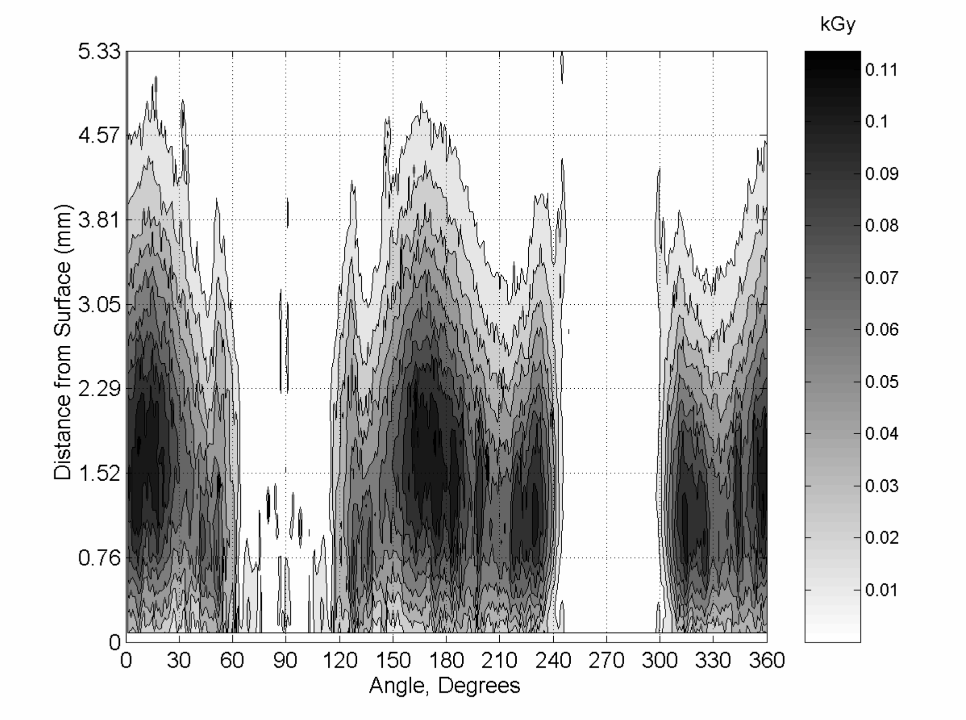

Figure D-26. Methyl Yellow Apple Contour dose-depth distribution irradiated with 50 Gy and 90 degrees.

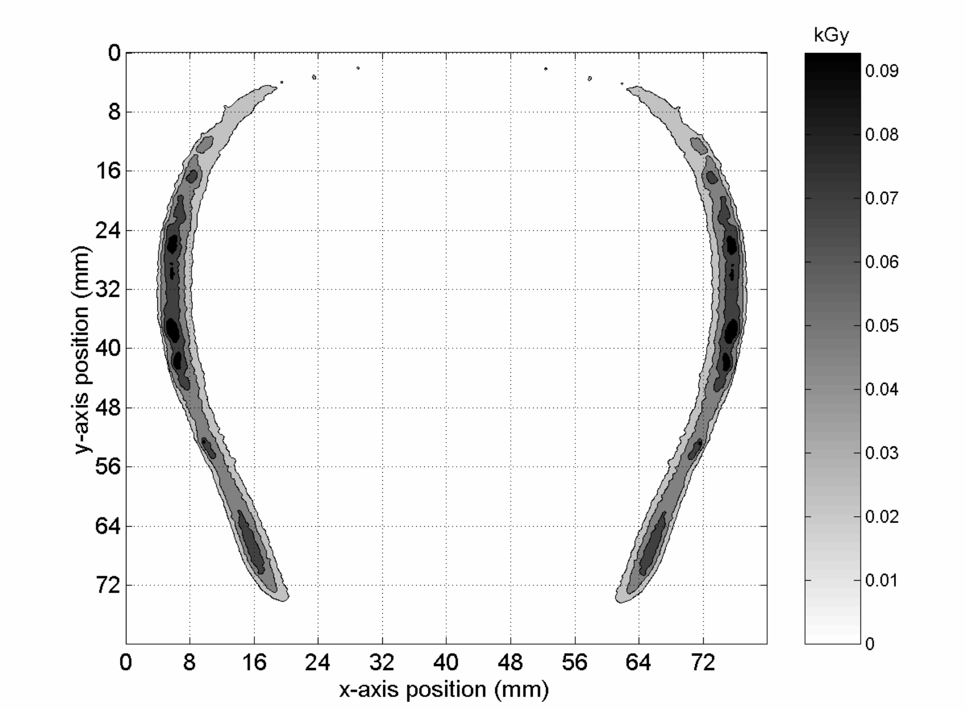

Figure D-27. Methyl Yellow Apple Contour dose distribution irradiated with 50 Gy and 90 degrees.

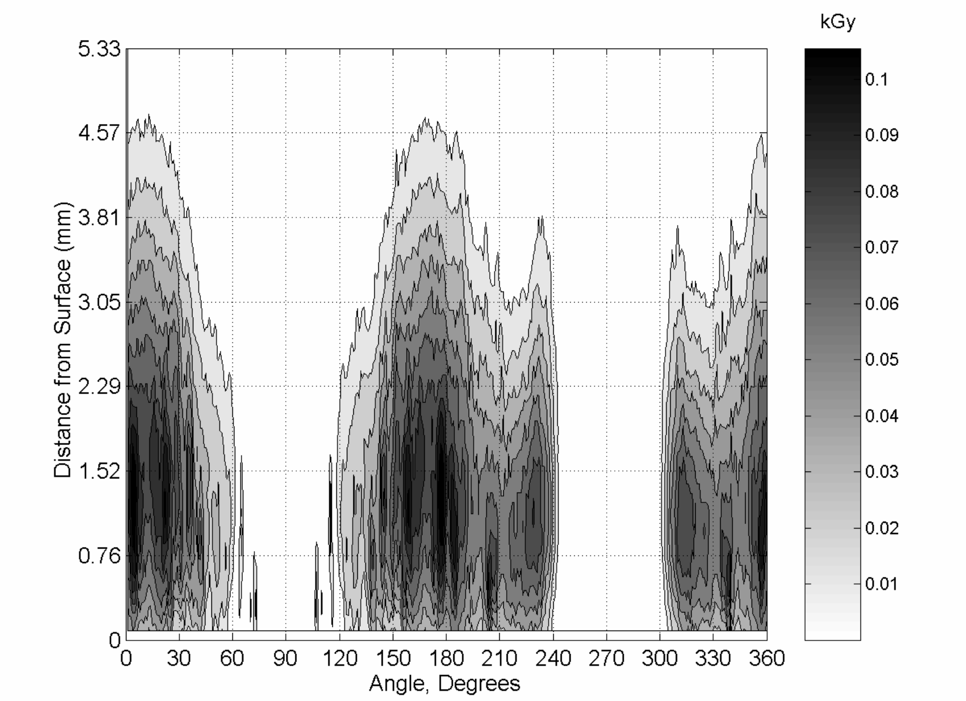

Figure D-28. Methyl Yellow Apple Contour dose-depth distribution irradiated with 50 Gy and 90 degrees.

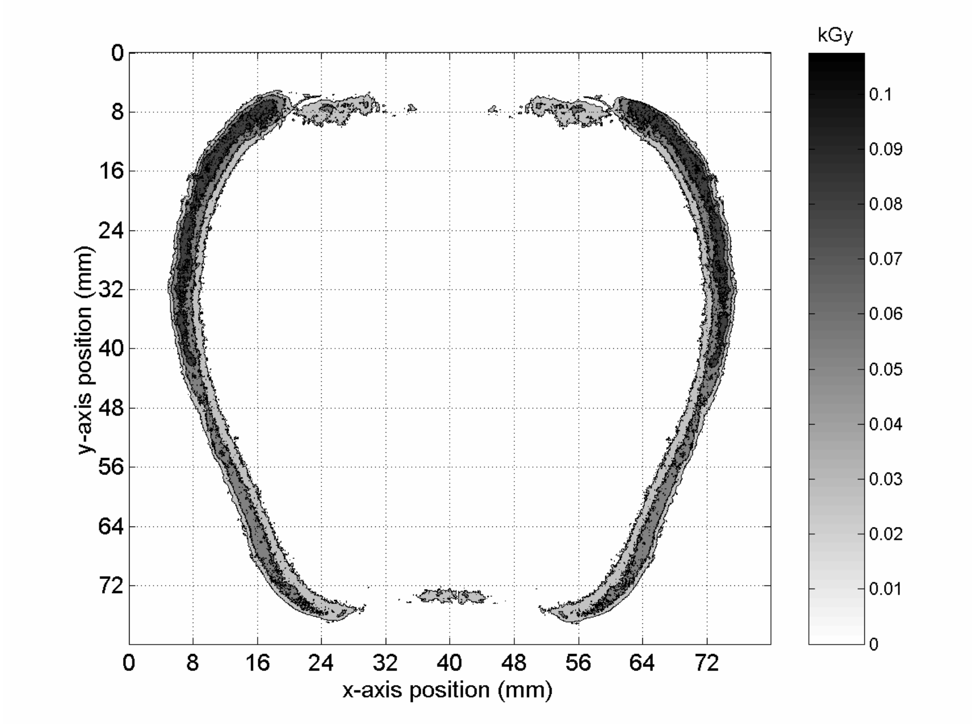

Figure D-29. Methyl Yellow Apple Contour dose distribution irradiated with 50 Gy and 22.5 degrees.

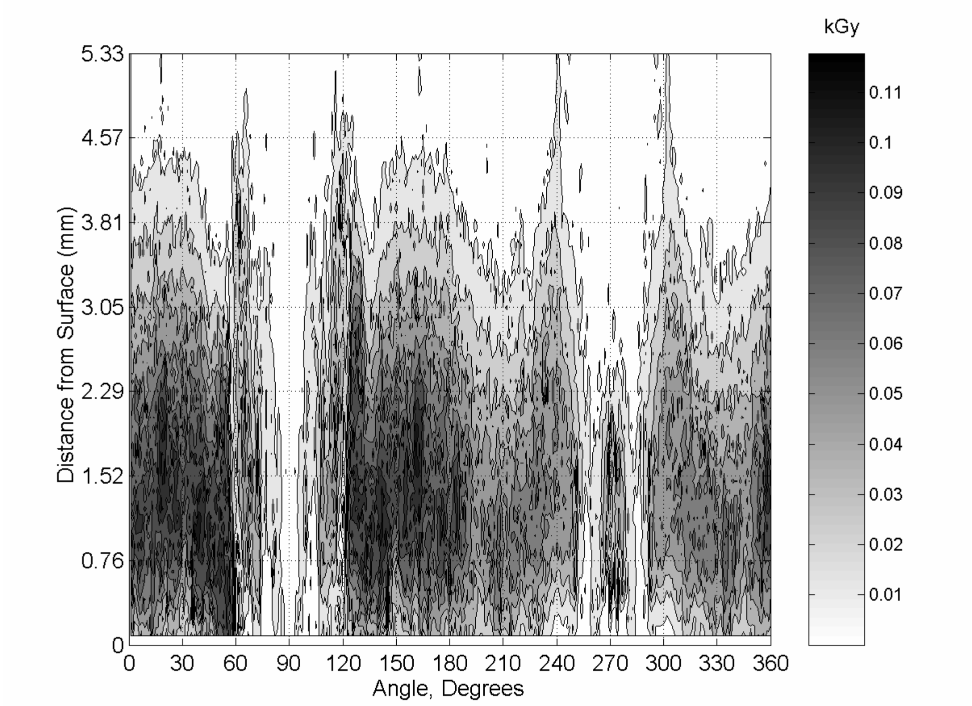

Figure D-30. Methyl Yellow Apple Contour dose-depth distribution irradiated with 50 Gy and 22.5 degrees.

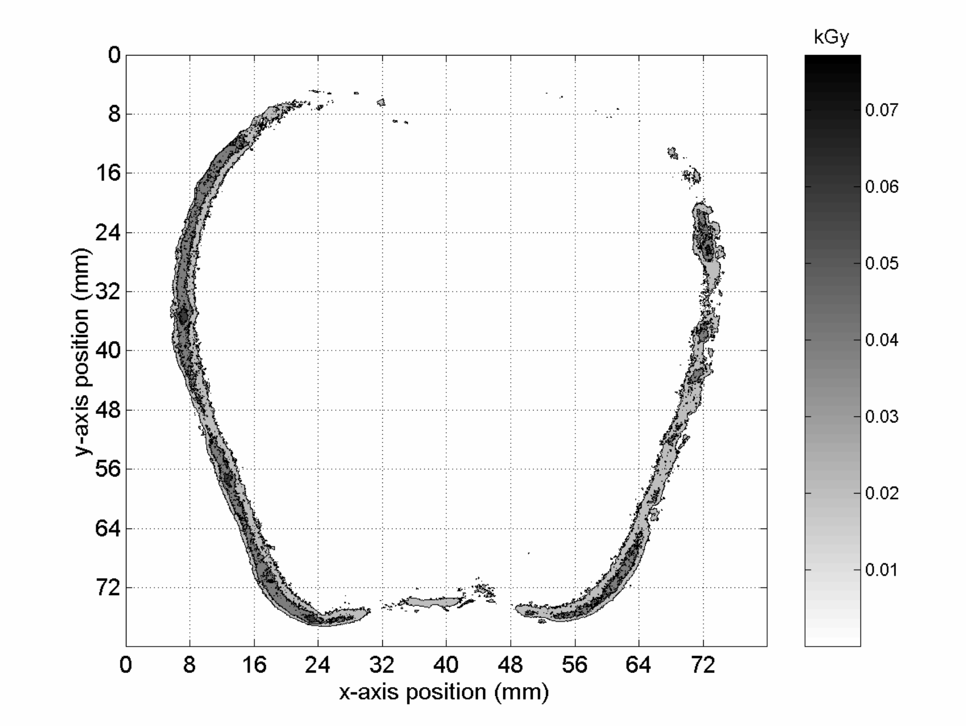

Figure D-31 Methyl Yellow Apple Contour dose distribution irradiated with 50 Gy and 22.5 degrees.

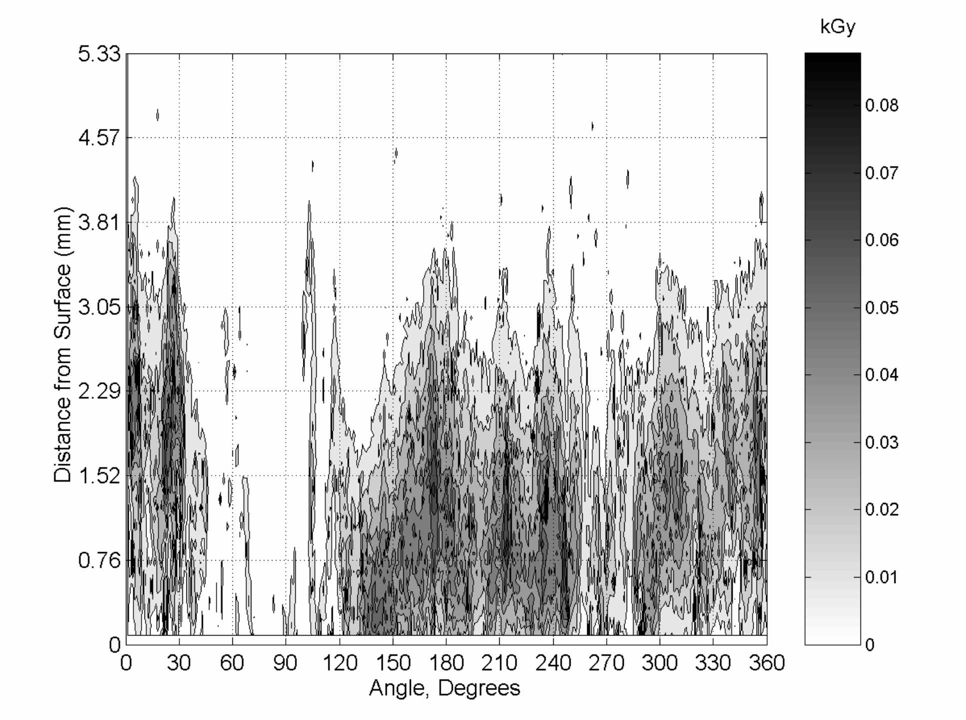

Figure D-32. Methyl Yellow Apple Contour dose-depth distribution irradiated with 50 Gy and 22.5 degrees.

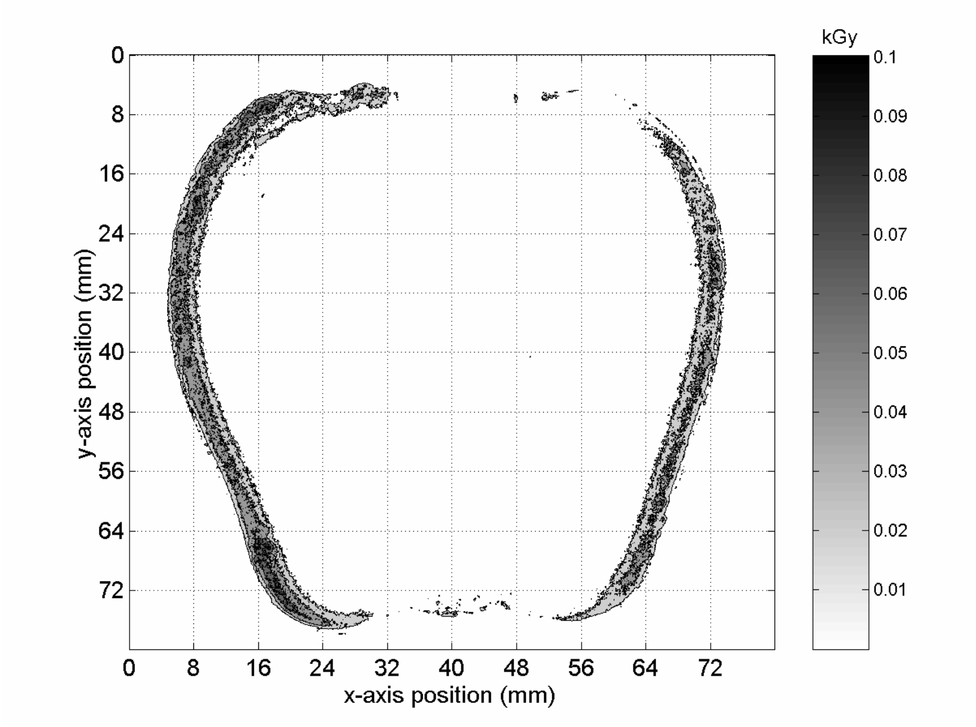

Figure D-33 Methyl Yellow Apple Contour dose distribution irradiated with 50 Gy and 45 degrees.

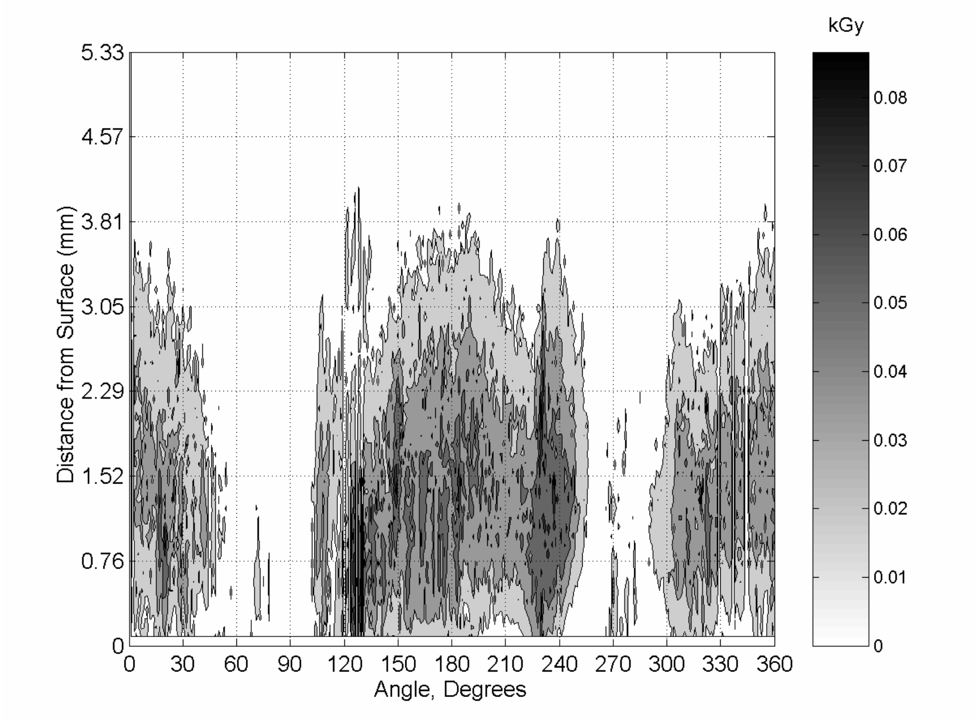

Figure D-34. Methyl Yellow Apple Contour dose-depth distribution irradiated with 50 Gy and 45 degrees.

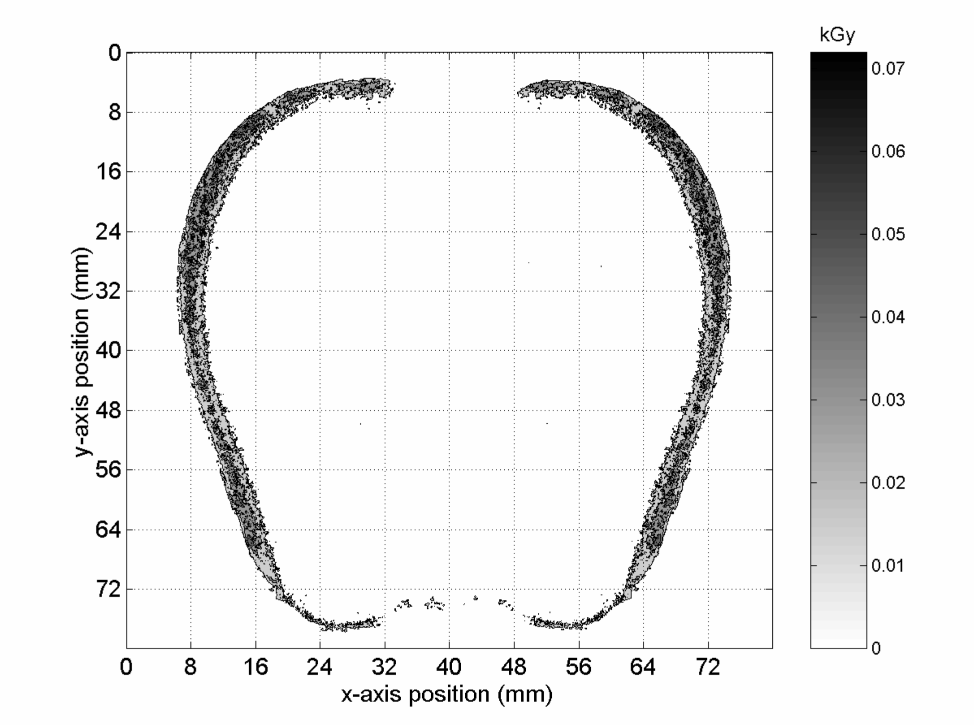

Figure D-35 Methyl Yellow Apple Contour dose distribution irradiated with 50 Gy and 45 degrees.

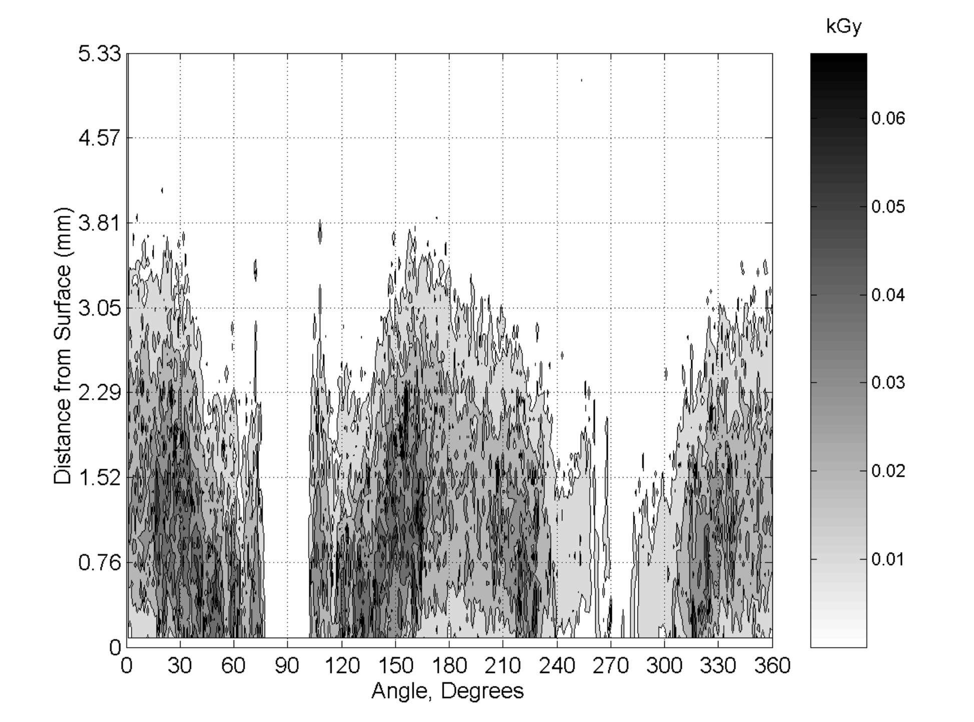

Figure D-36. Methyl Yellow Apple Contour dose-depth distribution irradiated with 50 Gy and 45 degrees.

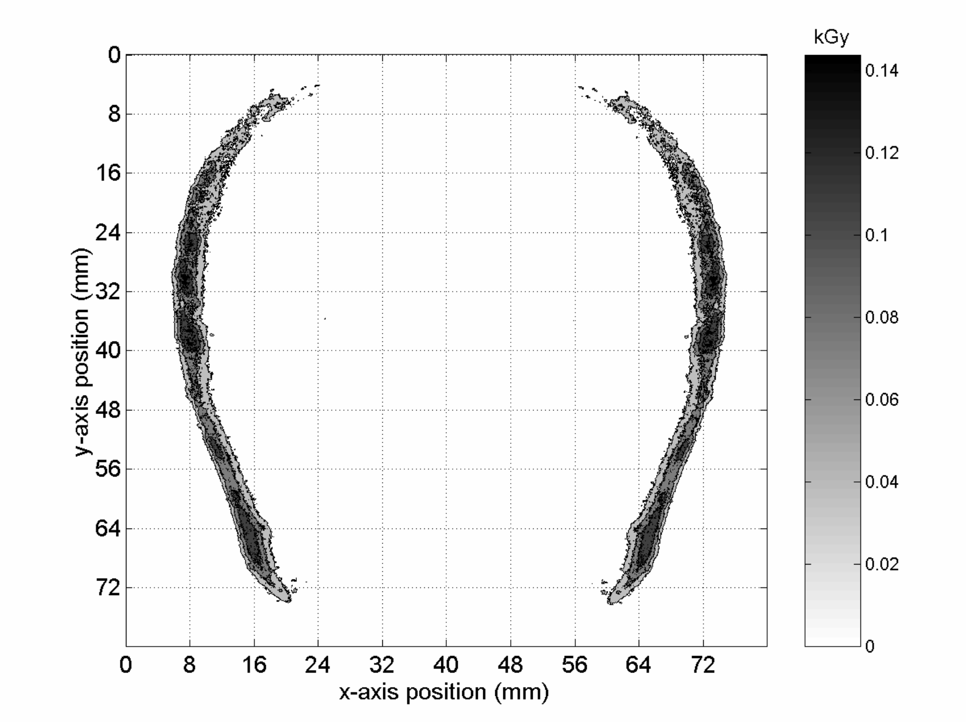

Figure D-37. Methyl Yellow Apple Contour dose distribution irradiated with 100 Gy and 90 degrees.

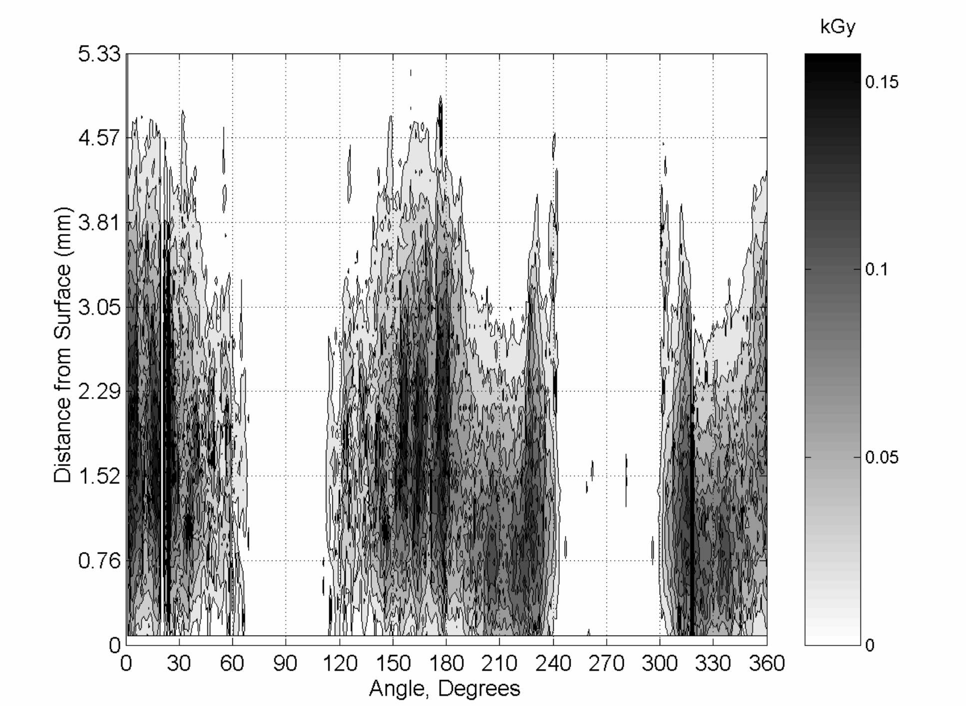

Figure D-38. Methyl Yellow Apple Contour dose-depth distribution irradiated with 100 Gy and 90 degrees.

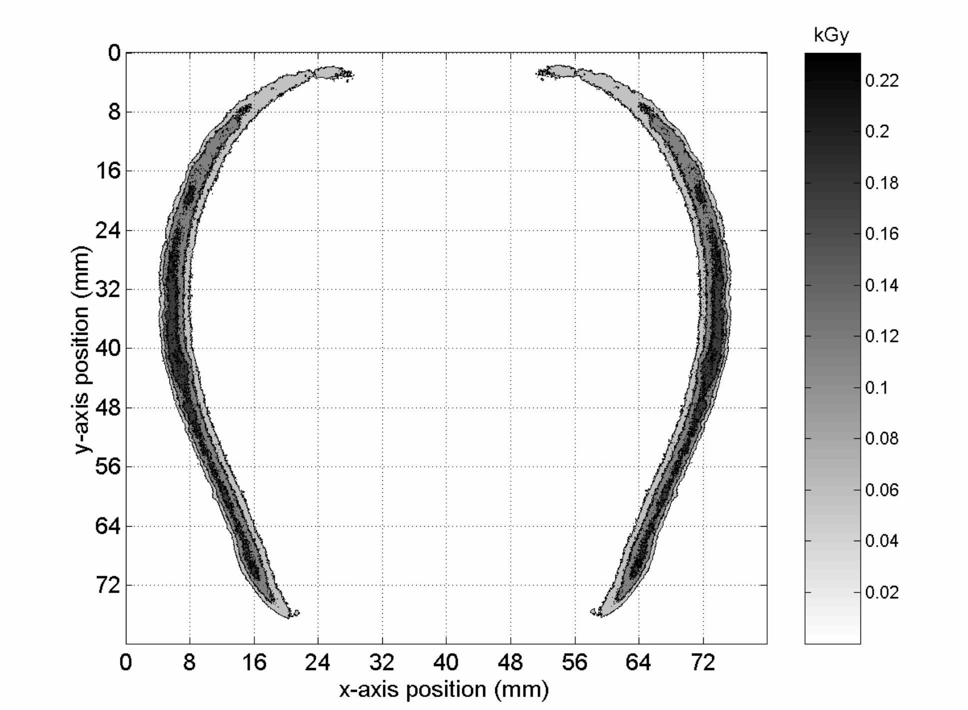

Figure D-39. Methyl Yellow Apple Contour dose distribution irradiated with 100 Gy and 90 degrees.

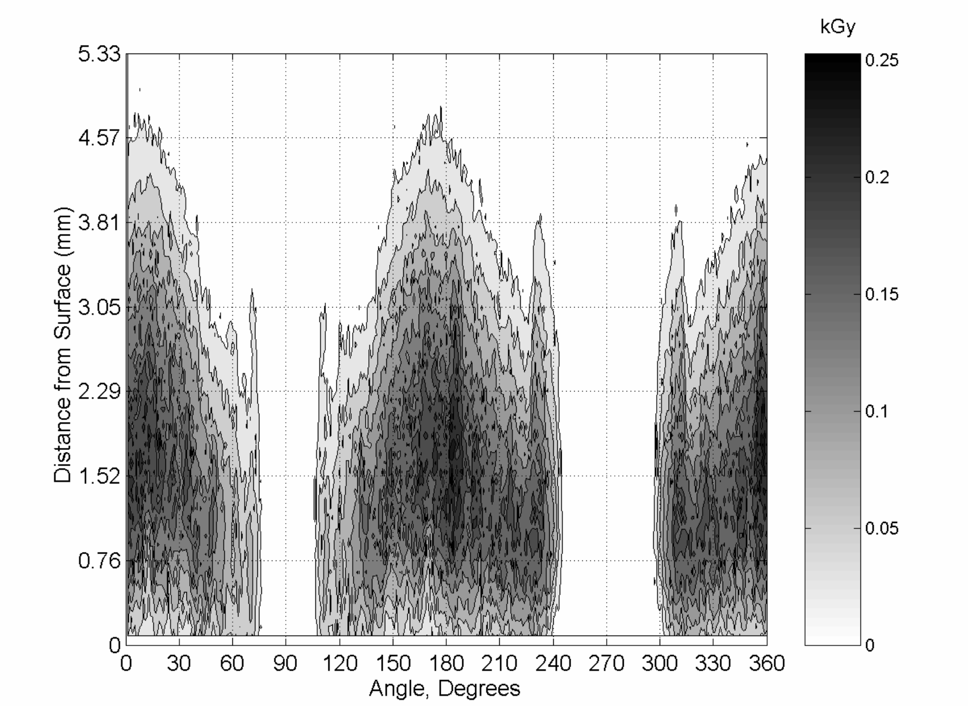

Figure D-40. Methyl Yellow Apple Contour dose-depth distribution irradiated with 100 Gy and 90 degrees.

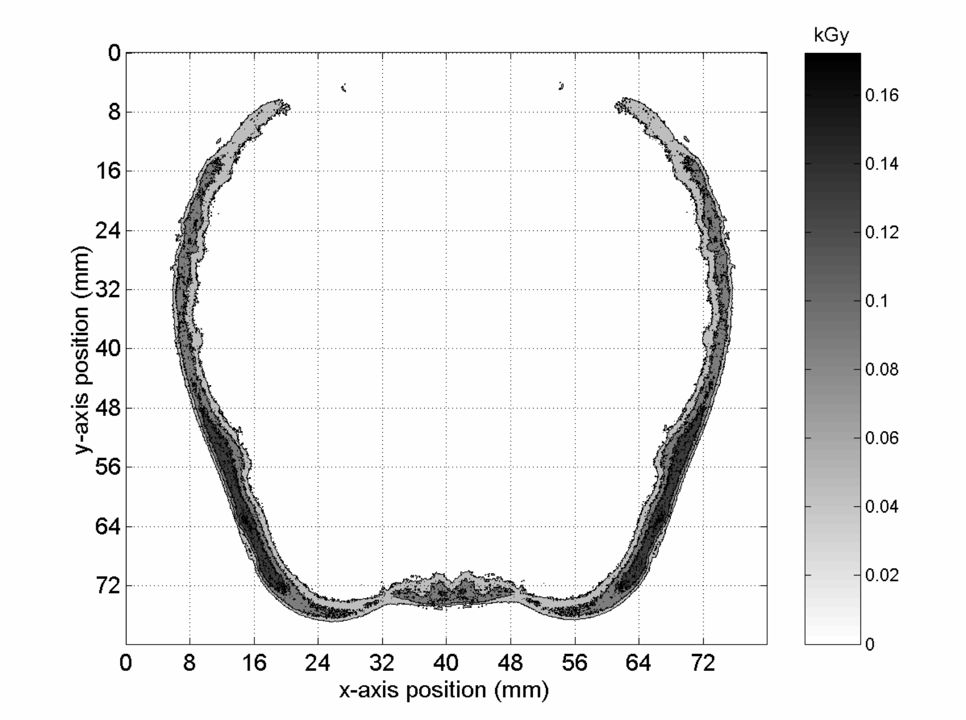

Figure D-41. Methyl Yellow Apple Contour dose distribution irradiated with 100 Gy and 22.5 degrees.

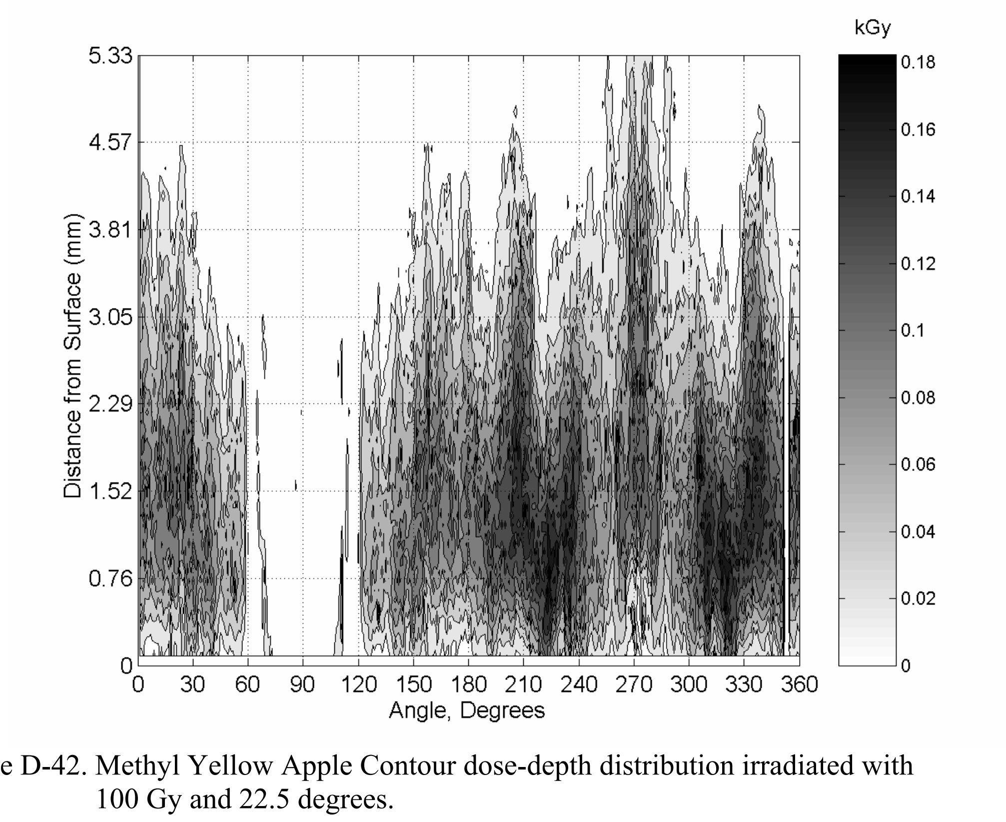

Figure D-42. Methyl Yellow Apple Contour dose-depth distribution irradiated with 100 Gy and 22.5 degrees.

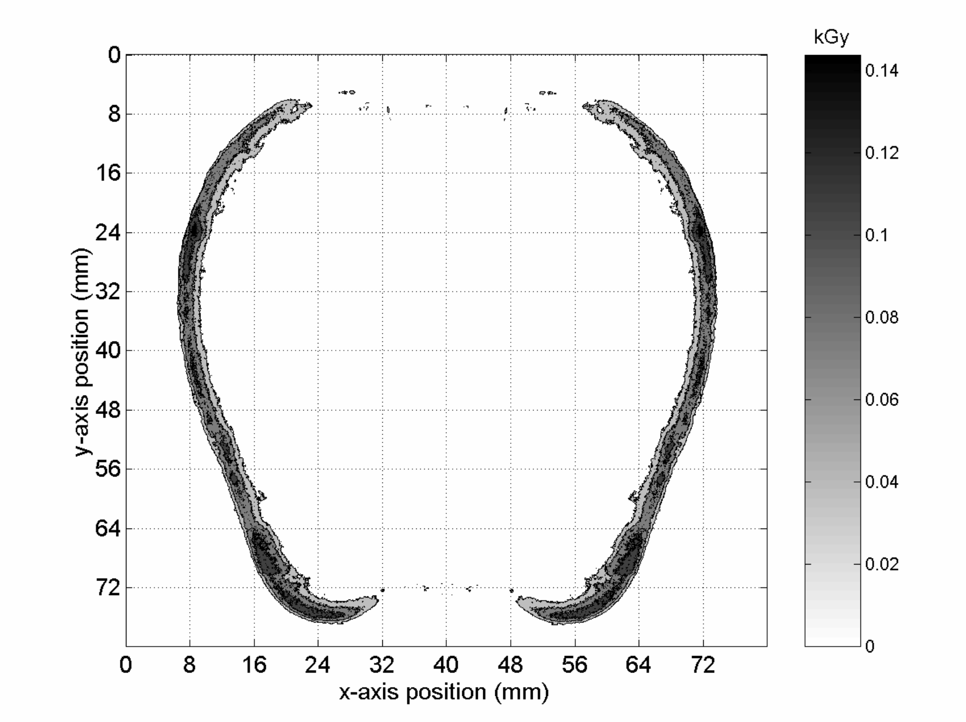

Figure D-43. Methyl Yellow Apple Contour dose distribution irradiated with 100 Gy and 22.5 degrees.

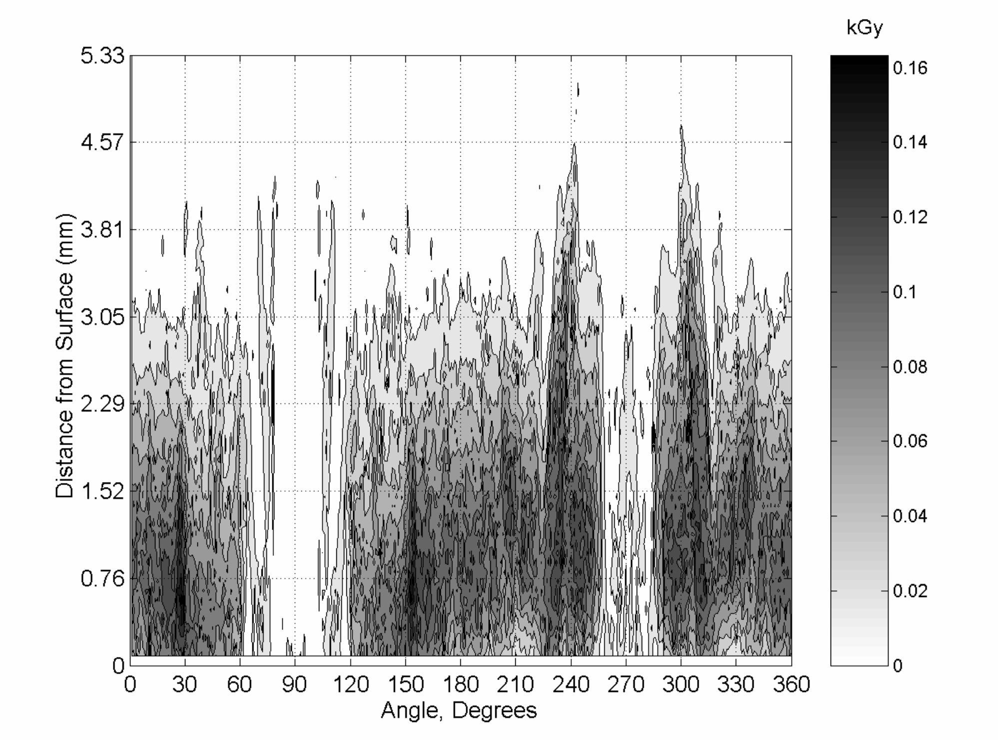

Figure D-44. Methyl Yellow Apple Contour dose-depth distribution irradiated with 100 Gy and 22.5 degrees.

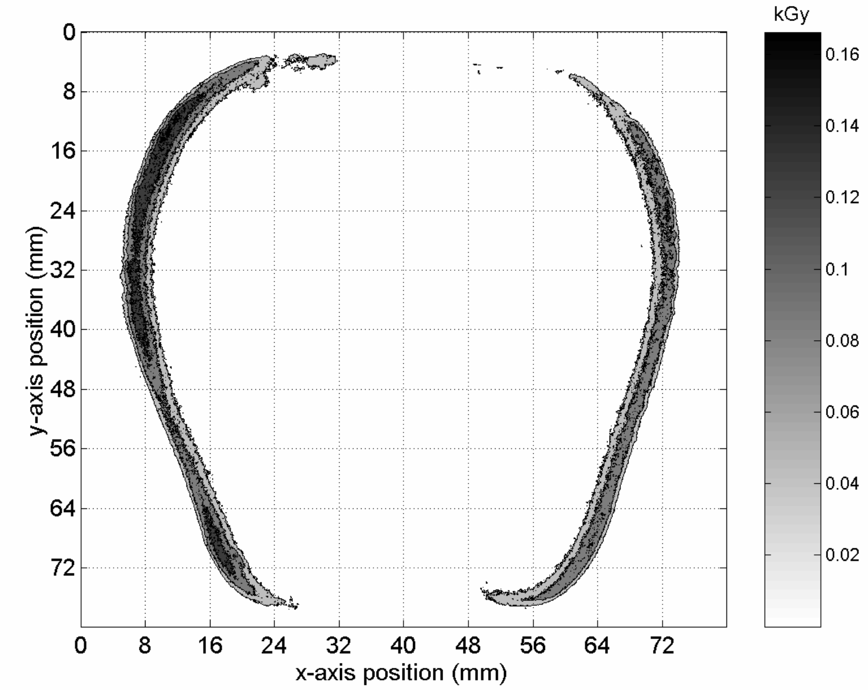

Figure D-45 Methyl Yellow Apple Contour dose distribution irradiated with 100 Gy and 45 degrees.

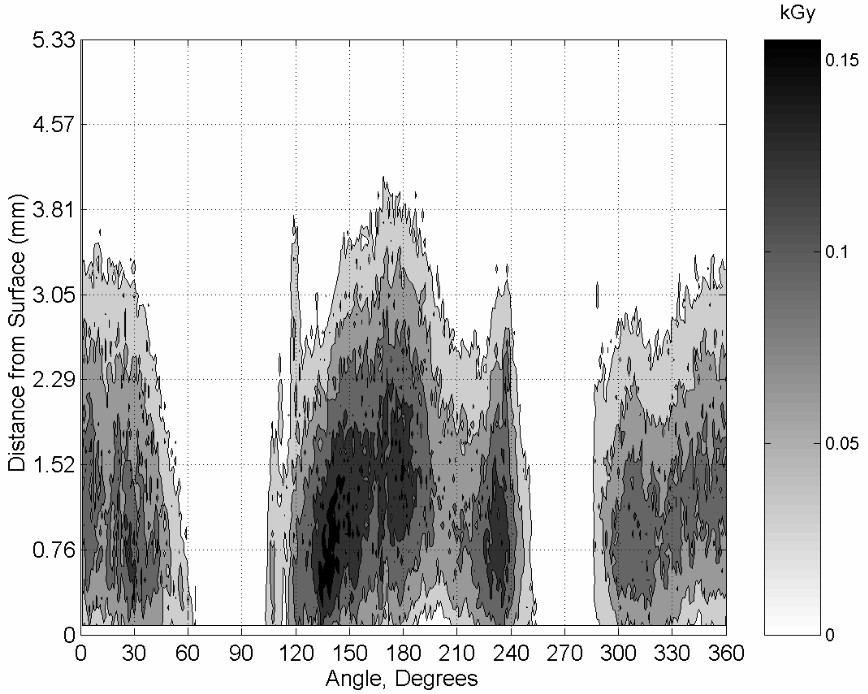

Figure D-46. Methyl Yellow Apple Contour dose-depth distribution irradiated with 100 Gy and 45 degrees.

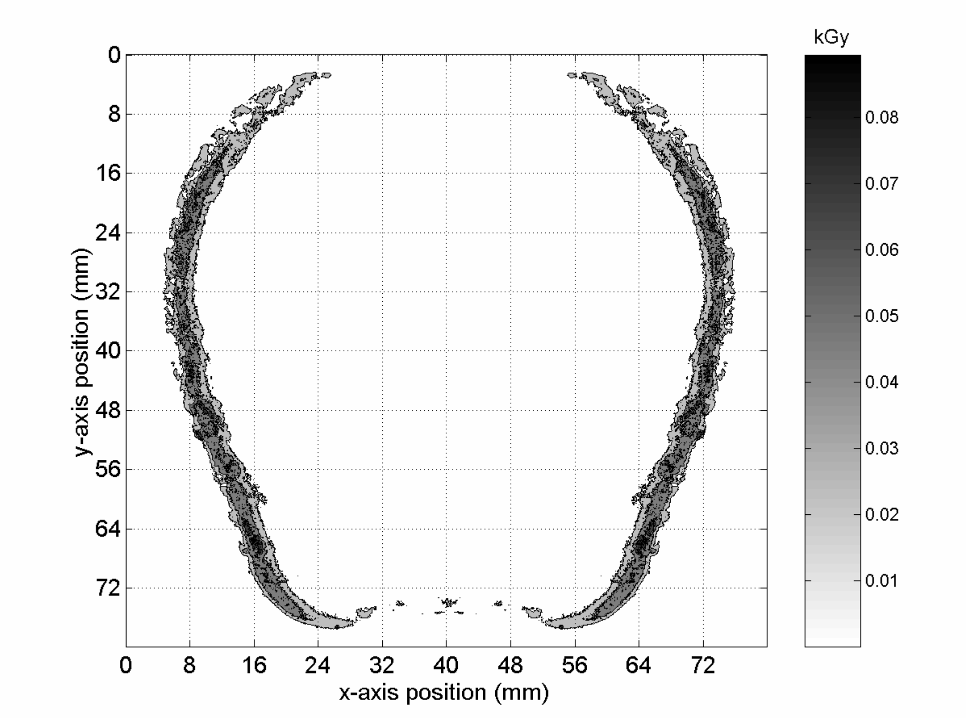

Figure D-47 Methyl Yellow Apple Contour dose distribution irradiated with 100 Gy and 45 degrees.

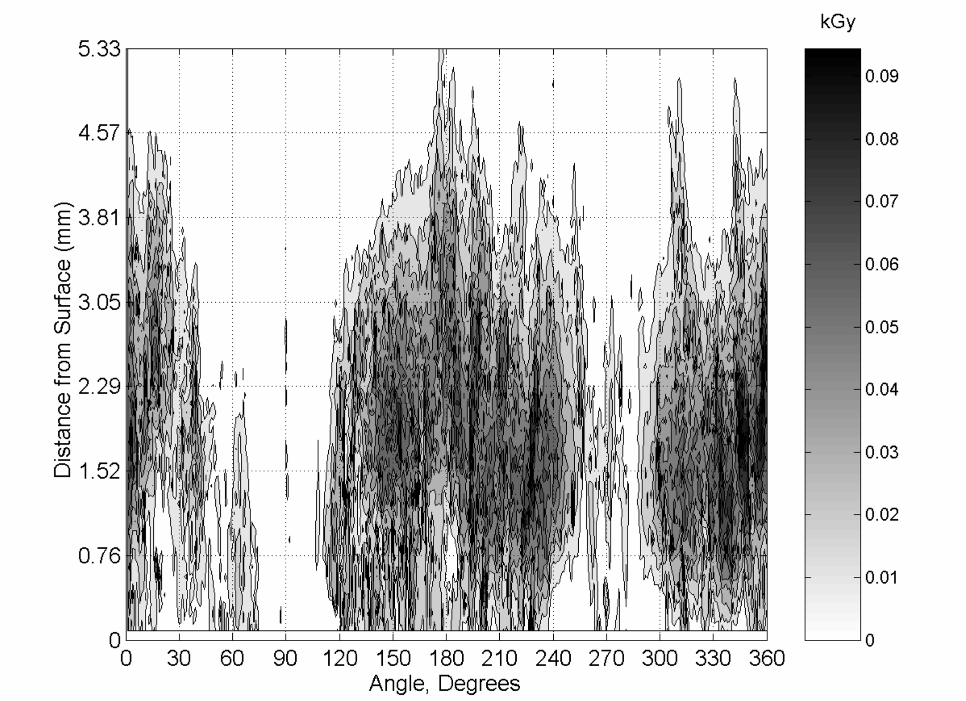

Figure D-48. Methyl Yellow Apple Contour dose-depth distribution irradiated with 100 Gy and 45 degrees.

APPENDIX E

RESULTS FROM E-BEAM IRRADIATION WITH A 10 MEV LINAC

E.1 Dose Energy Deposition and Dose Depth Distribution GAFCHROMIC® HD-810 Film

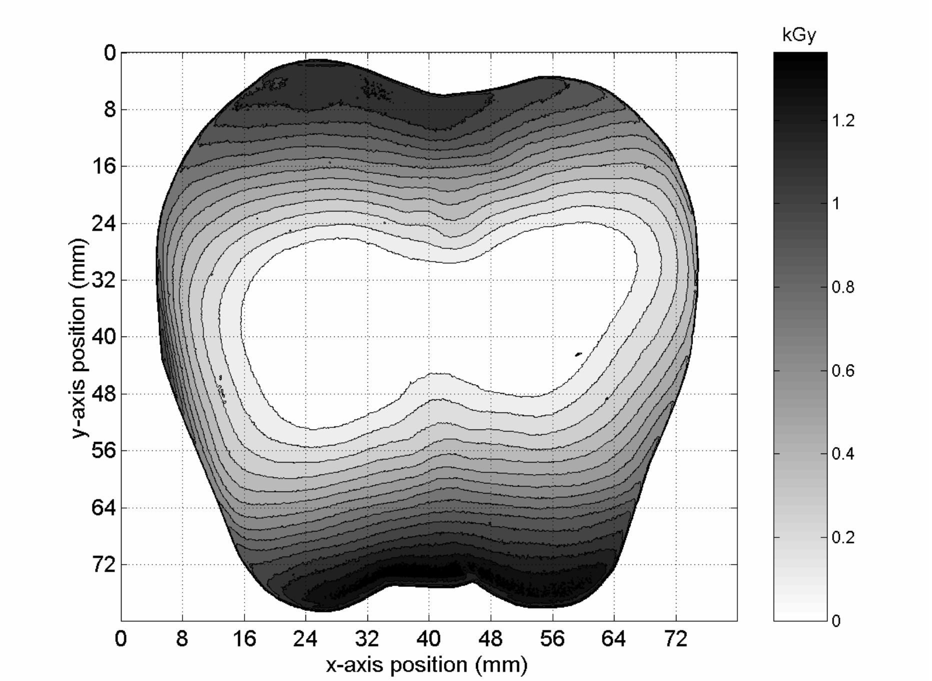

Figure E-1 HD-810 film dose distribution in kGy using Lucite thickness of 3 cm and a dual beam 10 MeV LINAC accelerator with a conveyor speed of 18.3 m/min (60 ft/min).

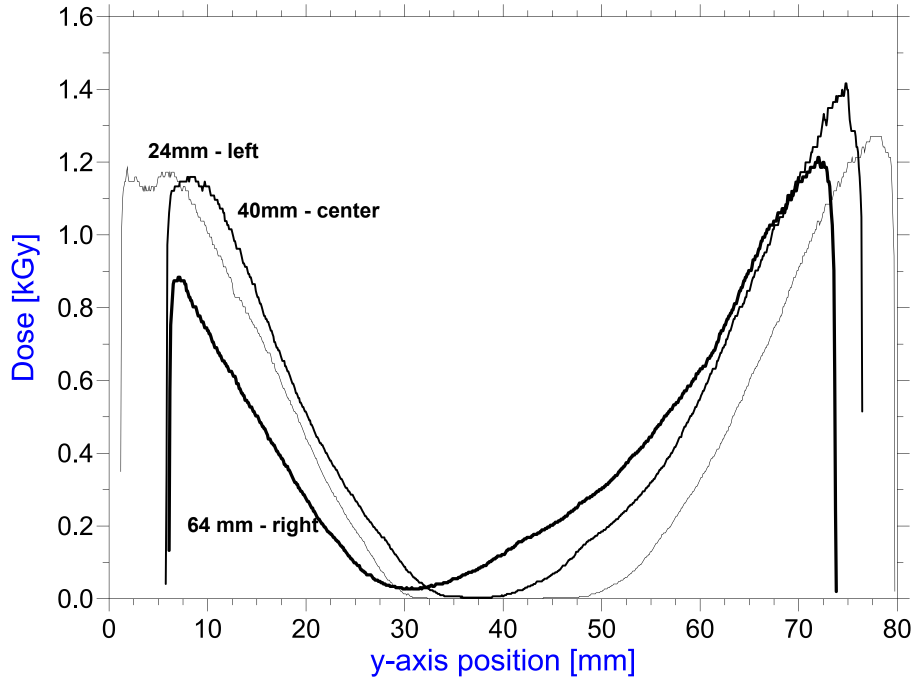

Figure E-2. HD-810 film dose distribution in kGy using Lucite thickness of 3 cm and a dual beam 10 MeV LINAC accelerator with a conveyor speed of 18.3 m/min (60 ft/min).

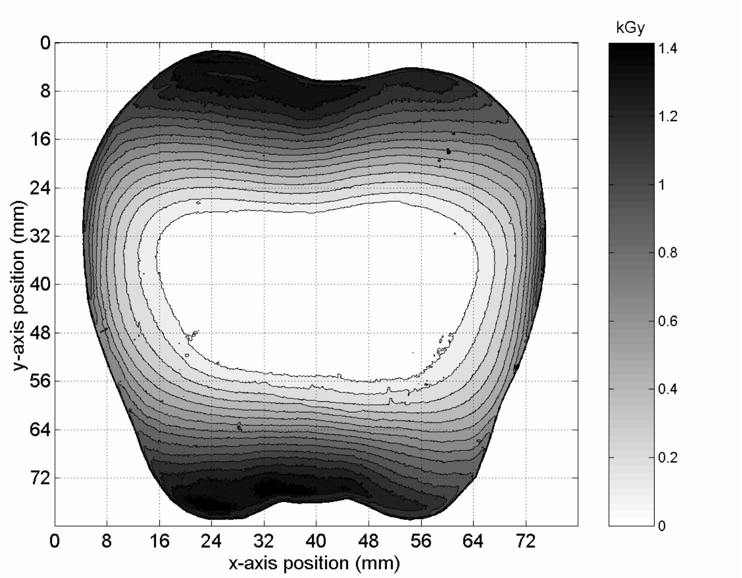

Figure E-3. HD-810 film dose distribution in kGy using Lucite thickness of 3 cm and a dual beam 10 MeV LINAC accelerator with a conveyor speed of 18.3 m/min (60 ft/min).

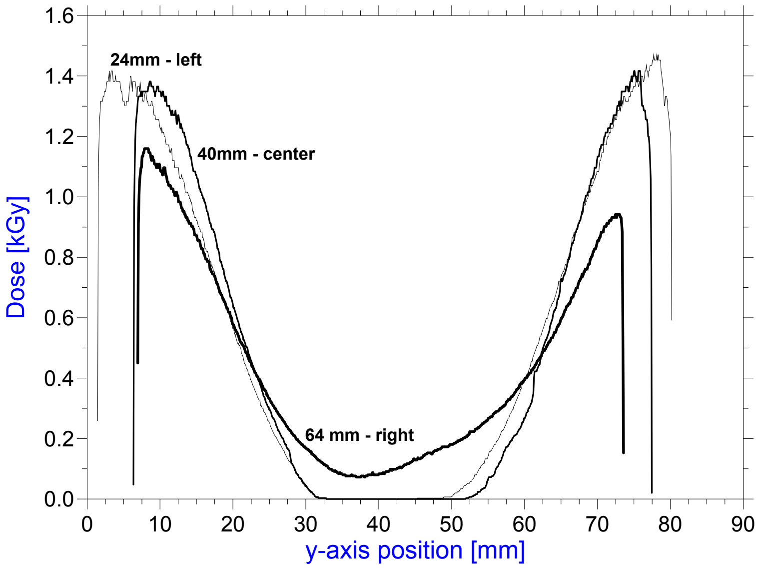

Figure E-4. HD-810 film dose-depth distribution in kGy using Lucite thickness of 3 cm and a dual beam 10 MeV LINAC accelerator with a conveyor speed of 18.3 m/min (60 ft/min).

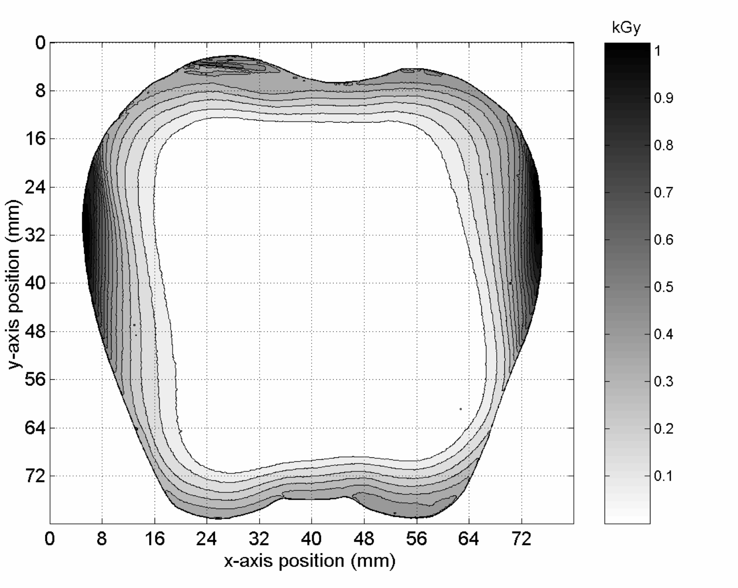

Figure E-5. HD-810 film dose distribution in kGy using Lucite thickness of 4 cm and a dual beam 10 MeV LINAC accelerator with a conveyor speed of 18.3 m/min (60 ft/min).

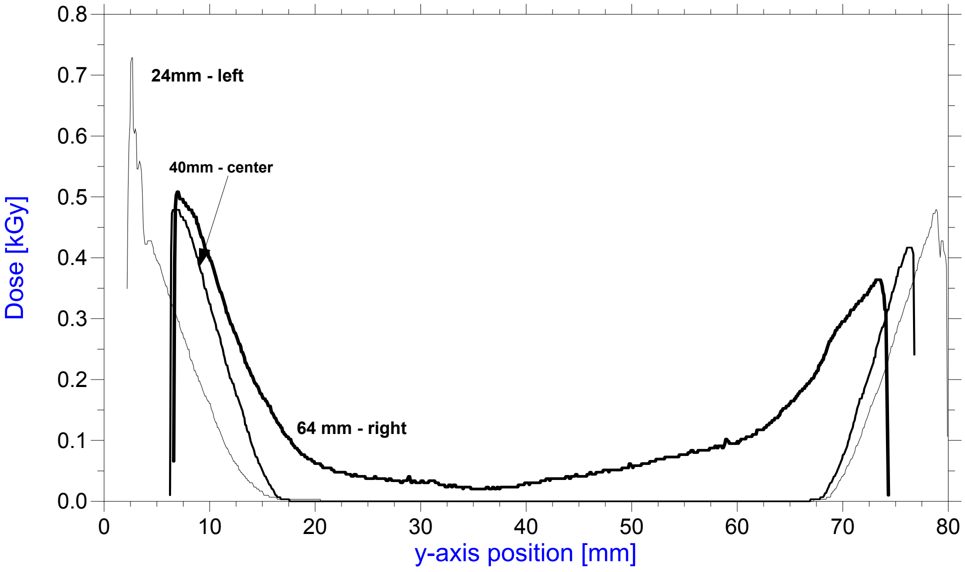

Figure E-6. HD-810 film dose-depth distribution in kGy using Lucite thickness of 4 cm and a dual beam 10 MeV LINAC accelerator with a conveyor speed of 18.3 m/min (60 ft/min).

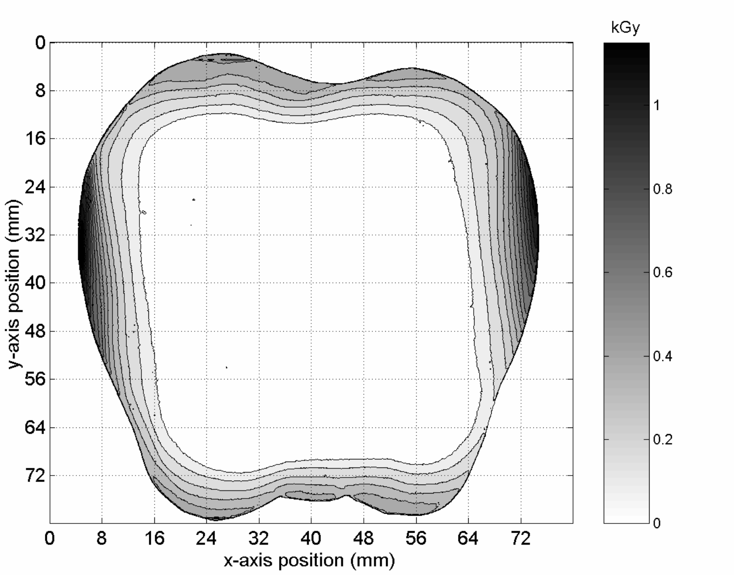

Figure E-7. HD-810 film dose distribution in kGy using Lucite thickness of 4 cm and a dual beam 10 MeV LINAC accelerator with a conveyor speed of 18.3 m/min (60 ft/min)

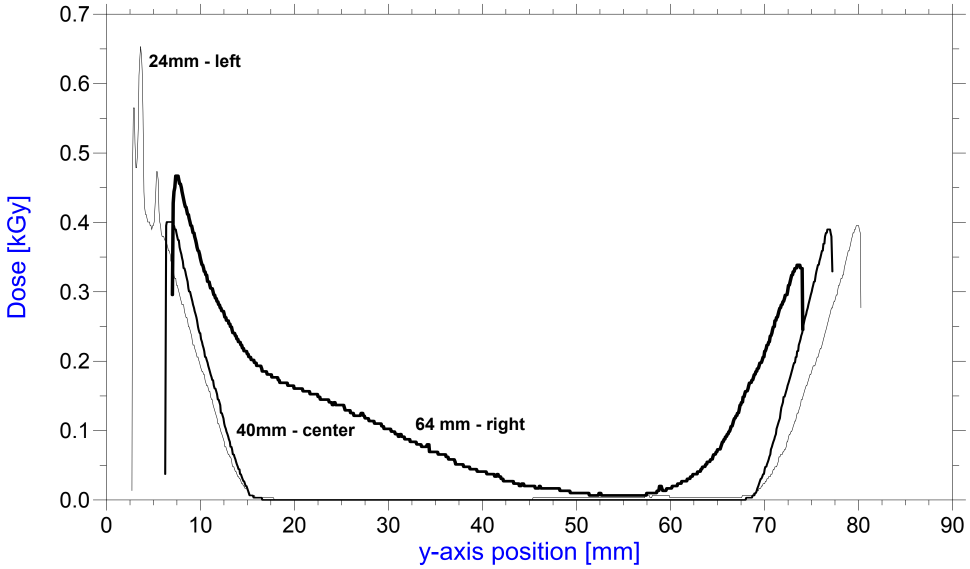

Figure E-8. HD-810 film dose-depth distribution in kGy using Lucite thickness of 4 cm and a dual beam 10 MeV LINAC accelerator with a conveyor speed of 18.3 m/min (60 ft/min).

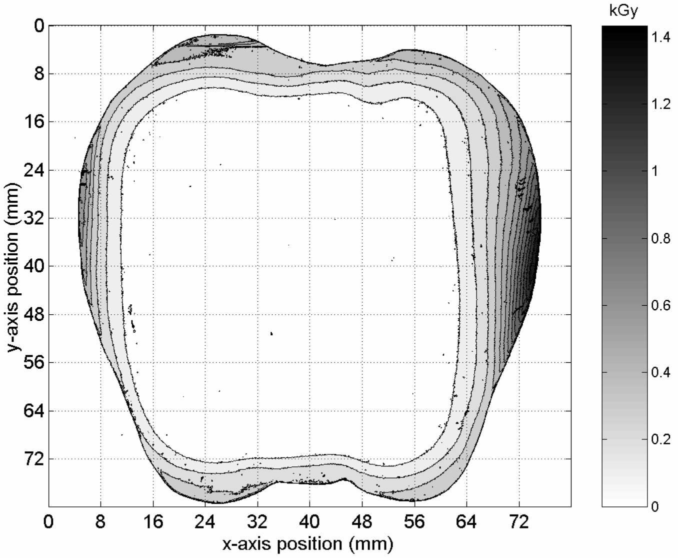

Figure E-9. HD-810 film dose distribution in kGy using Lucite thickness of 4.2 cm and a dual beam 10 MeV LINAC accelerator with a conveyor speed of 18.3 m/min (60 ft/min).

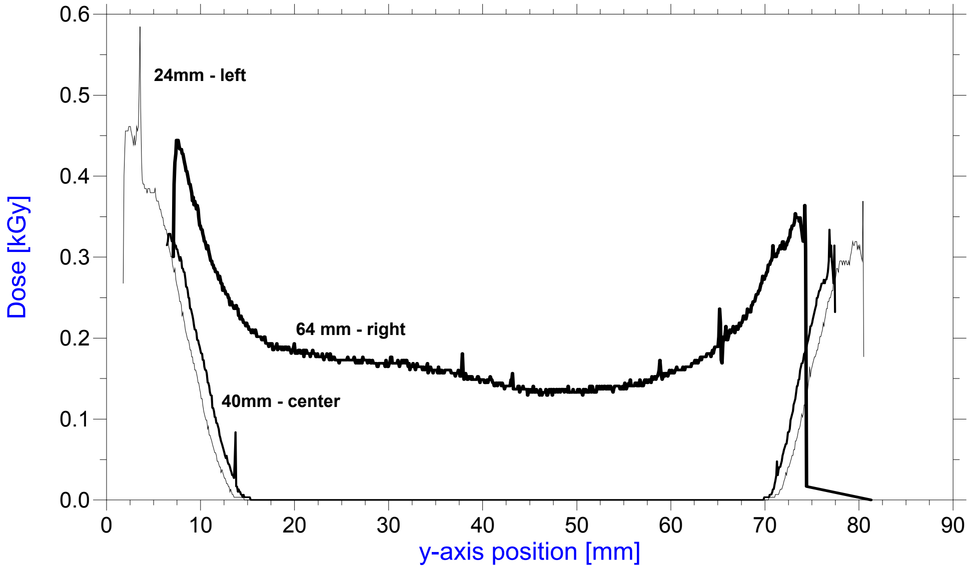

Figure E-10. HD-810 film dose distribution in kGy using Lucite thickness of 4.2 cm and a dual beam 10 MeV LINAC accelerator with a conveyor speed of 18.3 m/min (60 ft/min).

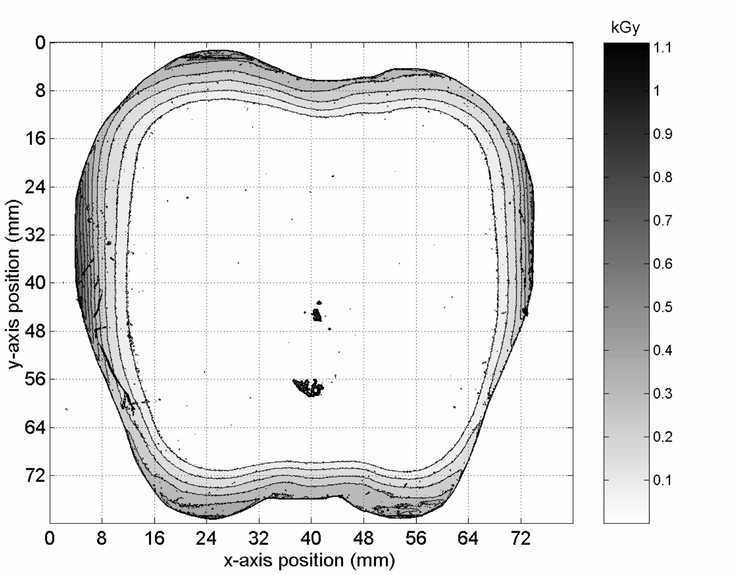

Figure E-11. HD-810 film dose distribution in kGy using Lucite thickness of 4.2 cm and a dual beam 10 MeV LINAC accelerator with a conveyor speed of 18.3 m/min (60 ft/min).

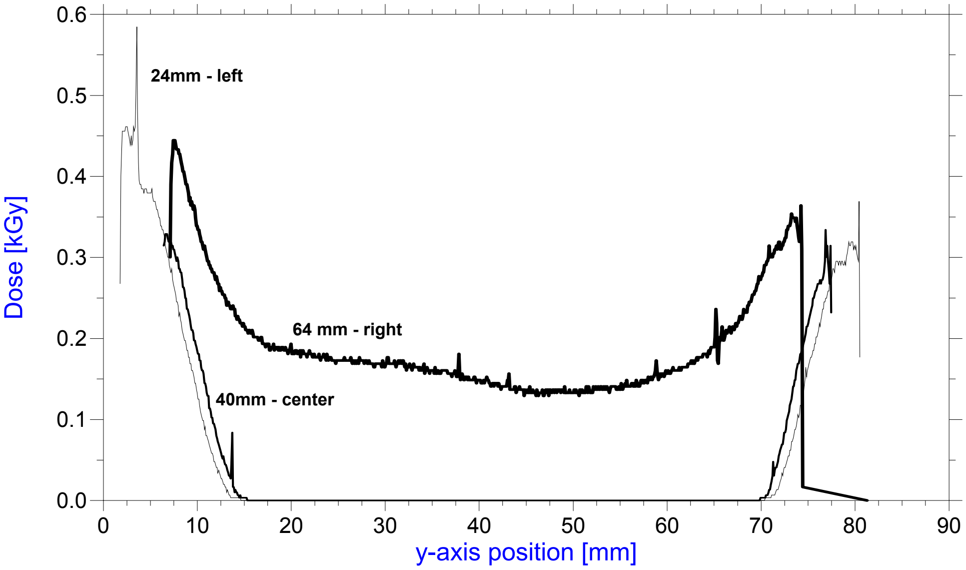

Figure E-12. HD-810 film dose distribution in kGy using Lucite thickness of 4.2 cm and a dual beam 10 MeV LINAC accelerator with a conveyor speed of 18.3 m/min (60 ft/min).

E.2 Dose Energy Deposition and Dose Depth Distribution Apple Phantom Contours

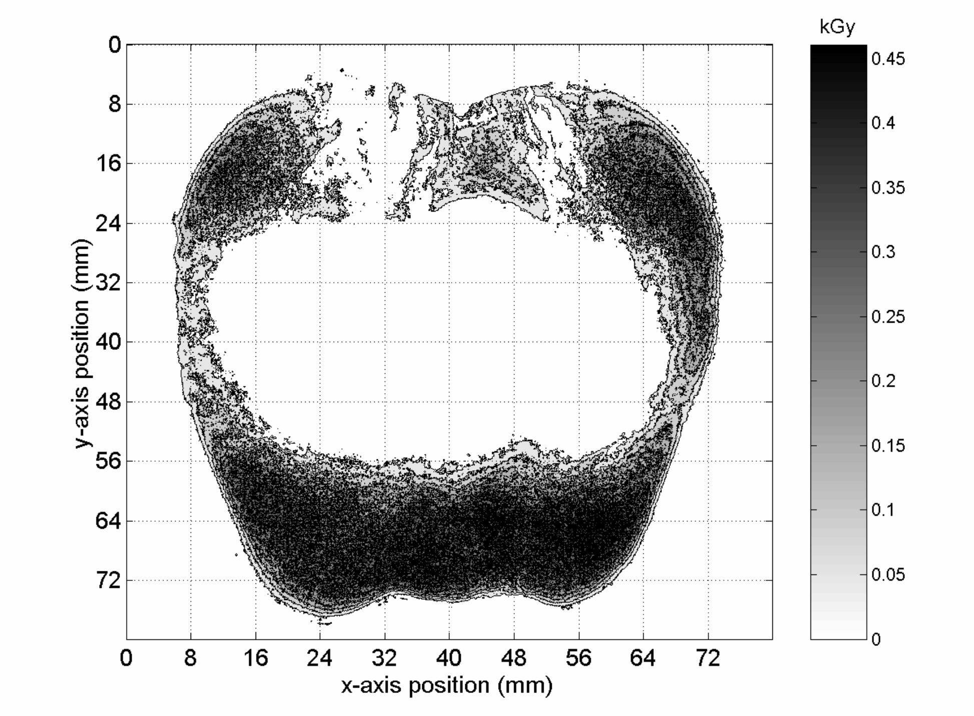

Figure E-13. Methyl yellow apple contour dose response in kGy using Lucite t = 3 cm

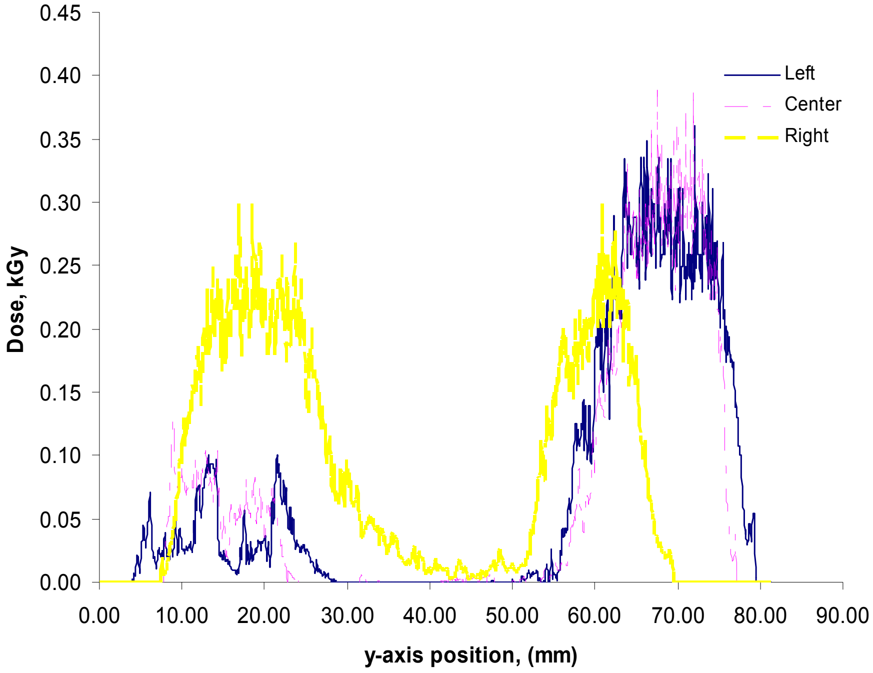

Figure E-14. Methyl yellow depth dose profile in kGy using Lucite t = 3 cm

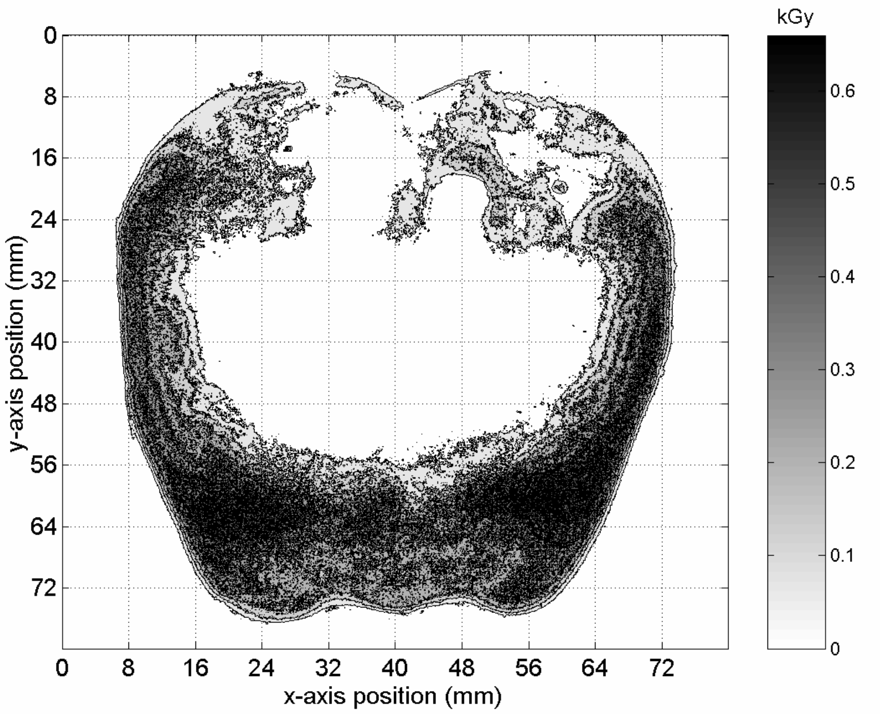

Figure E-15. Methyl yellow apple contour dose response in kGy using Lucite t = 3 cm

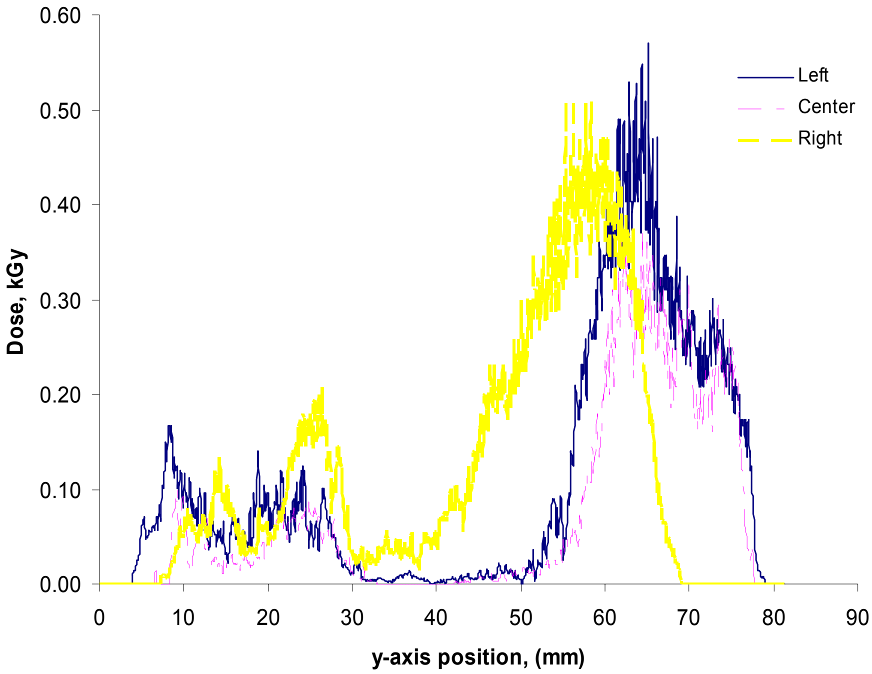

Figure E-16. Methyl yellow depth dose profile in kGy using Lucite t = 3 cm

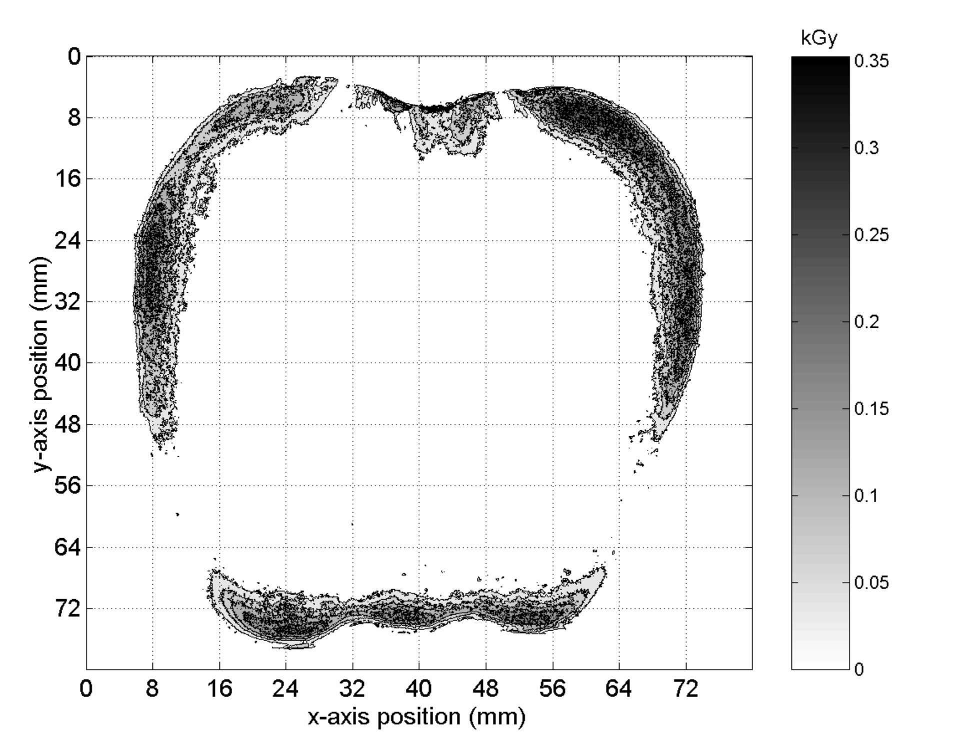

Figure E-17. Methyl yellow apple contour dose response in kGy using Lucite t = 4 cm

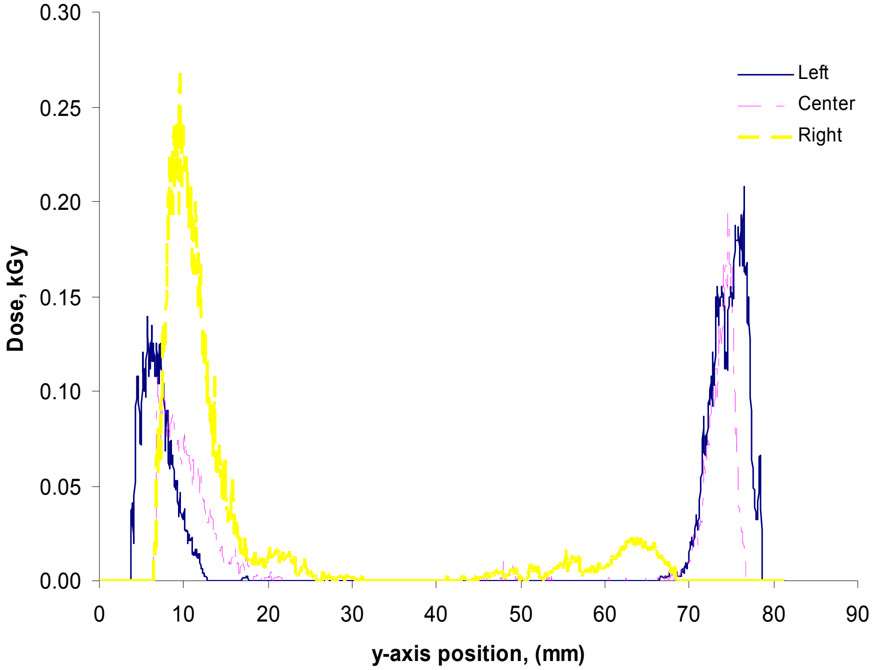

Figure E-18. Methyl yellow depth dose profile in kGy using Lucite t = 4 cm

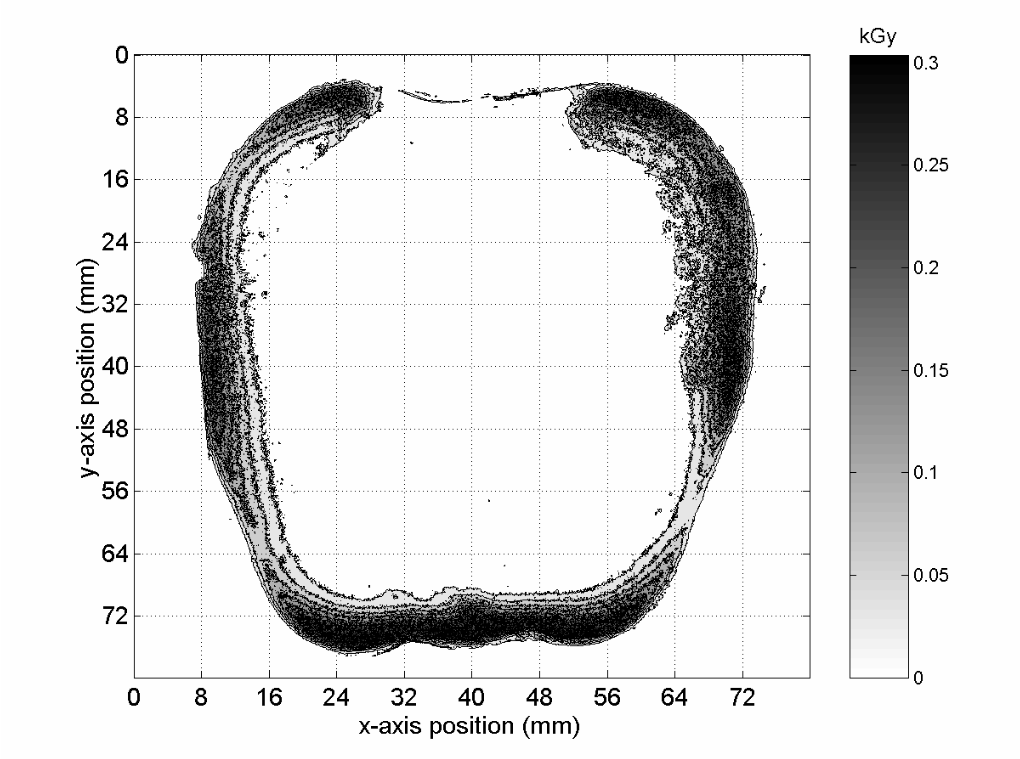

Figure E-19. Methyl yellow apple contour dose response in kGy using Lucite t = 4 cm

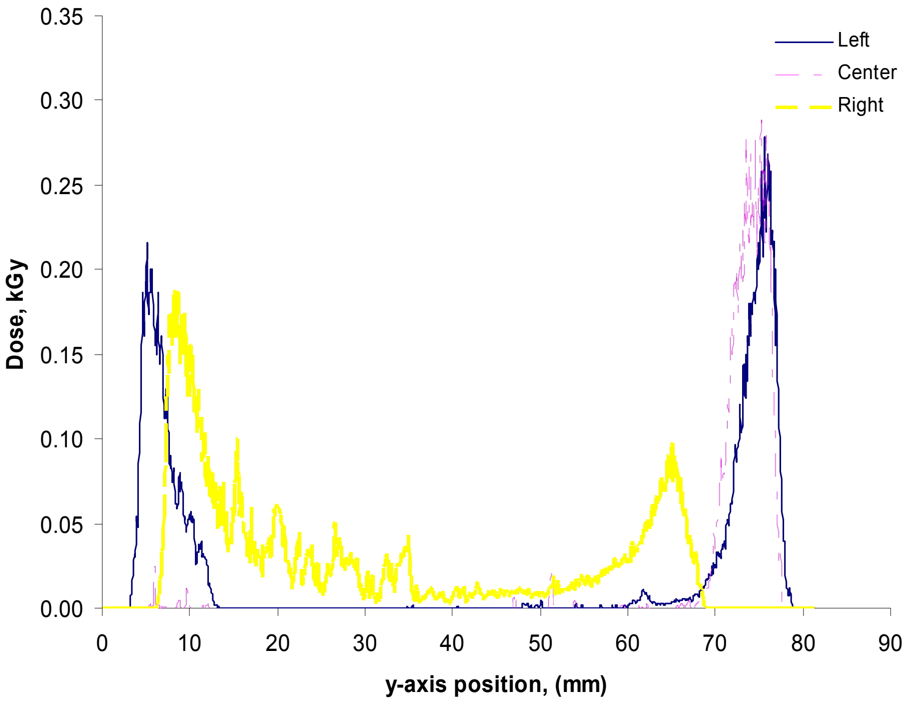

Figure E-20. Methyl yellow depth dose profile in kGy using Lucite t = 4 cm

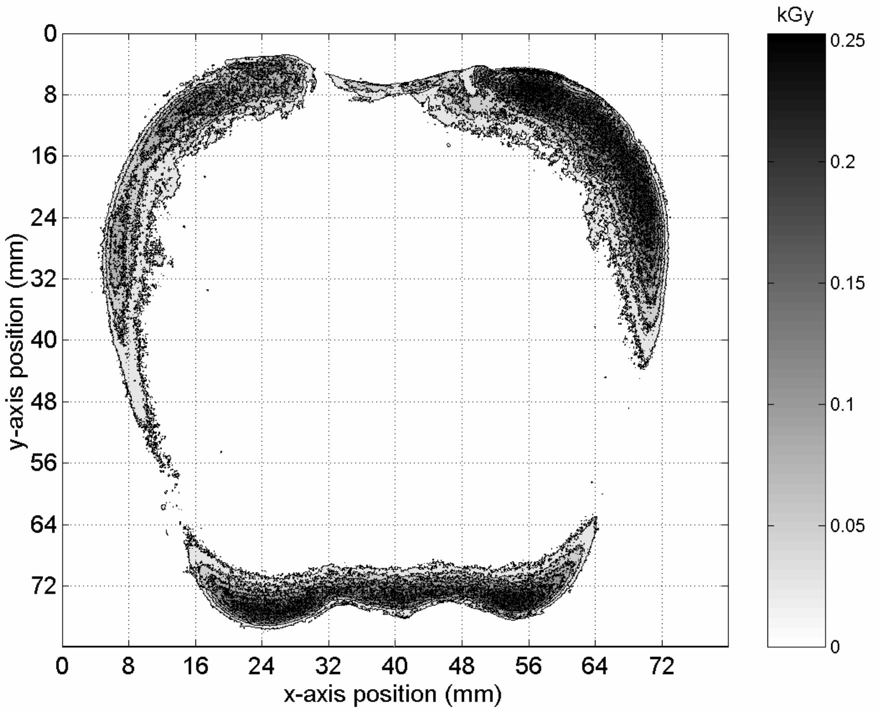

Figure E-21. Methyl yellow apple contour dose response in kGy using Lucite t = 4.2 cm

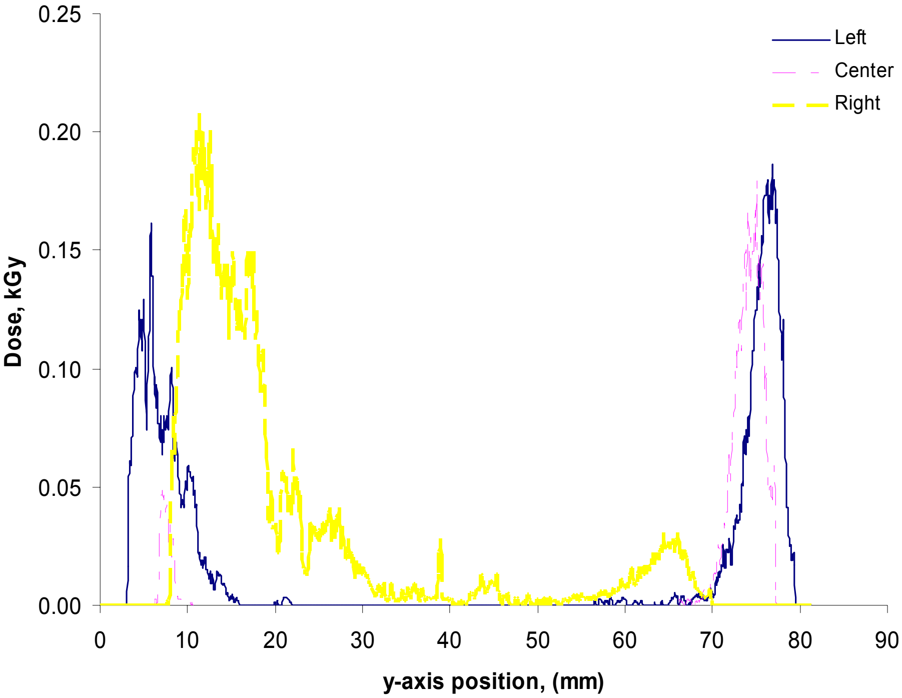

Figure E-22. Methyl yellow depth dose profile in kGy using Lucite t = 4.2 cm

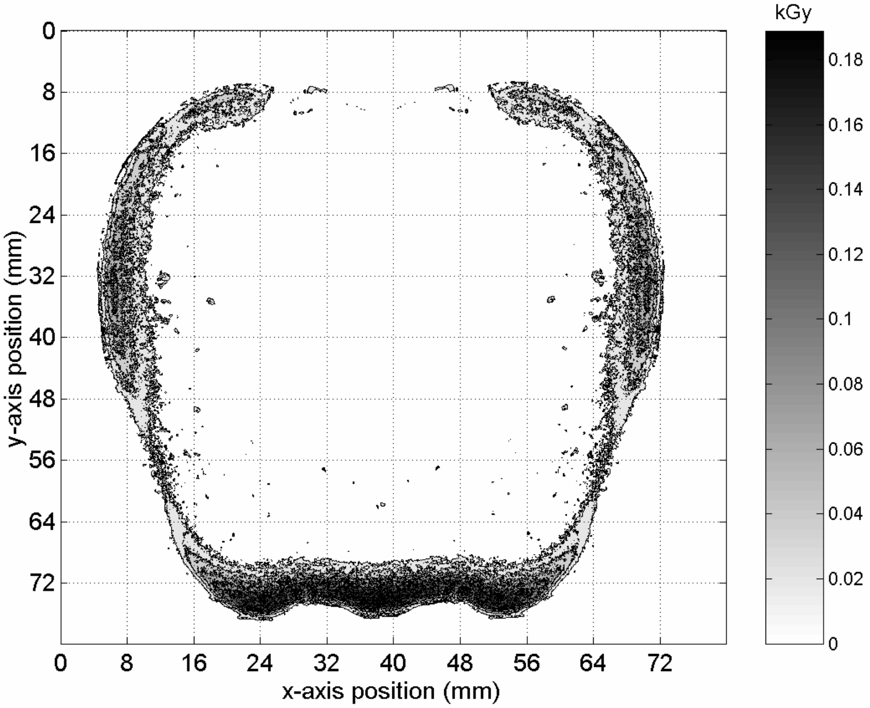

Figure E-23. Methyl yellow apple contour dose response in kGy using Lucite t = 4.2 cm

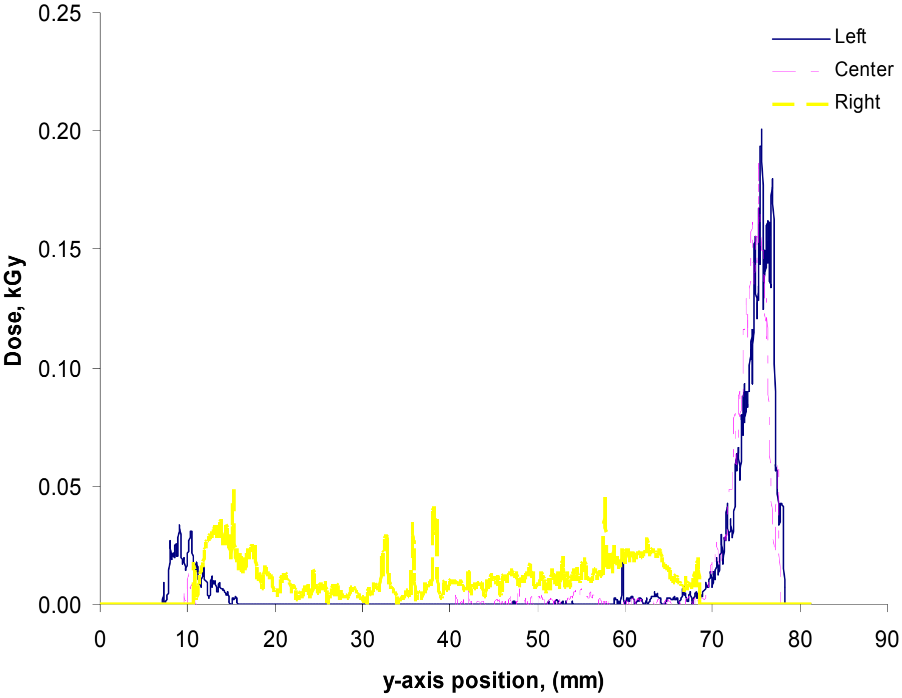

Figure E-24. Methyl yellow depth dose profile in kGy using Lucite t = 4.2 cm

APPENDIX F

RESULTS FROM X-RAY IRRADIATION WITH A 5 MEV LINAC

F.1 Dose Energy Deposition and Dose Depth Distribution GAFCHROMIC® HD-810 Film

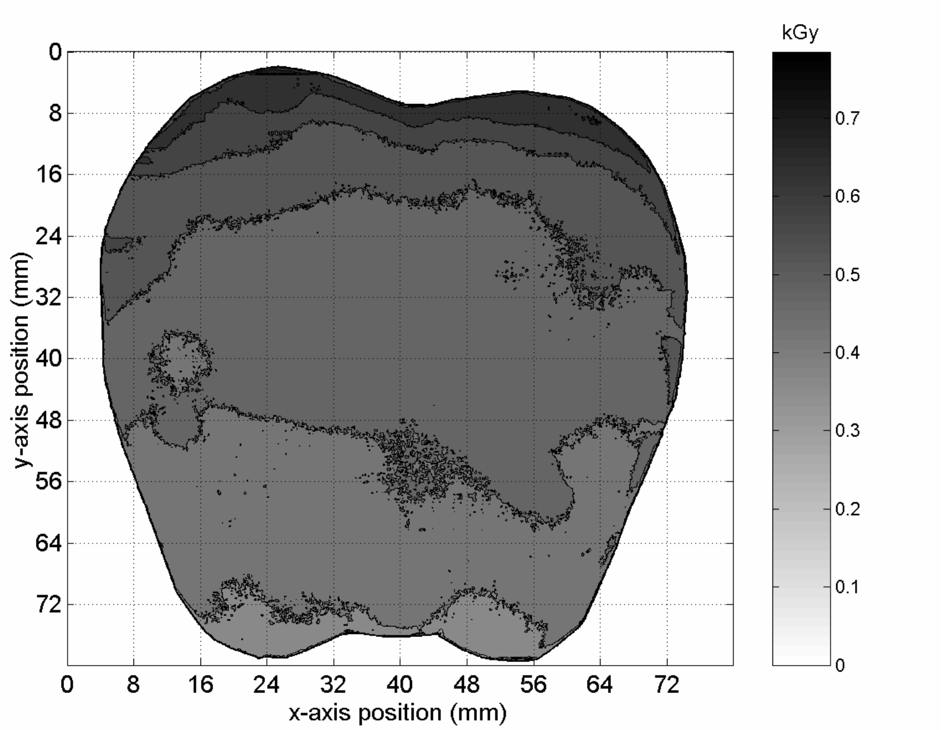

Figure F-1. HD-810 film dose distribution in kGy using a custom-made polystyrene holder and a 5 MeV LINAC accelerator with a conveyor speed of 18.3 m/min (60 ft/min).

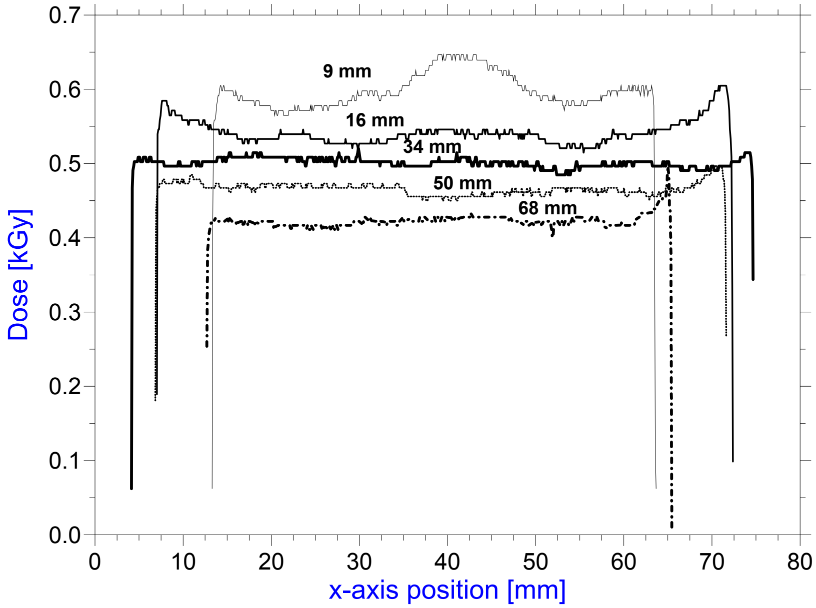

Figure F-2. HD-810 film depth-dose distribution in kGy using a custom-made polystyrene holder and a 5 MeV LINAC accelerator with a conveyor speed of 18.3 m/min (60 ft/min).

.

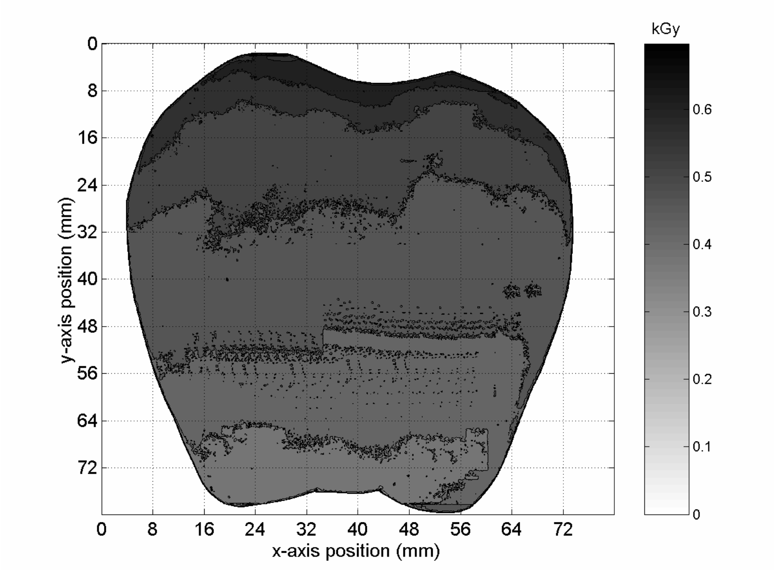

Figure F-3. HD-810 film dose distribution in kGy using a custom-made polystyrene holder and a 5 MeV LINAC accelerator with a conveyor speed of 18.3 m/min (60 ft/min).

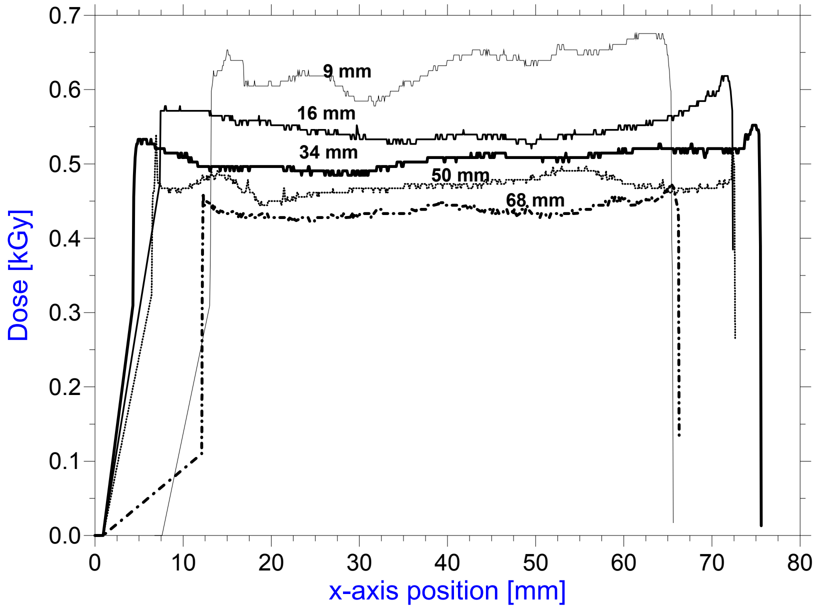

Figure F-4. HD-810 film depth-dose distribution in kGy using a custom-made polystyrene holder and a 5 MeV LINAC accelerator with a conveyor speed of 18.3 m/min (60 ft/min).

F.2 Dose Energy Deposition and Dose Depth Distribution Methyl Yellow Apple phantom contours.

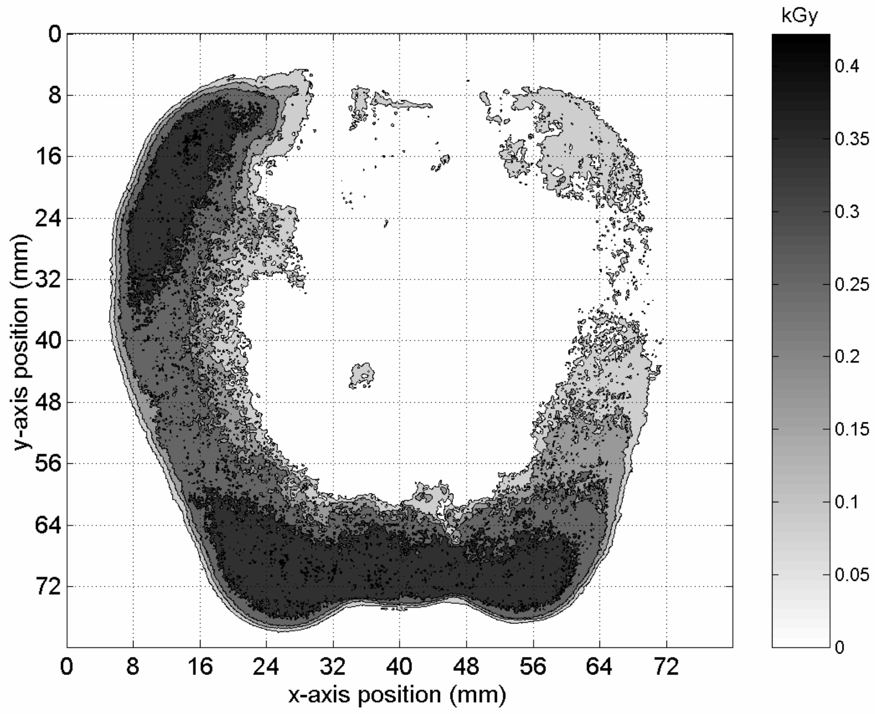

Figure F-5. Methyl yellow apple-phantom contour dose distribution in kGy using a custom-made polystyrene holder and a 5 MeV LINAC accelerator with a conveyor speed of 18.3 m/min (60 ft/min).

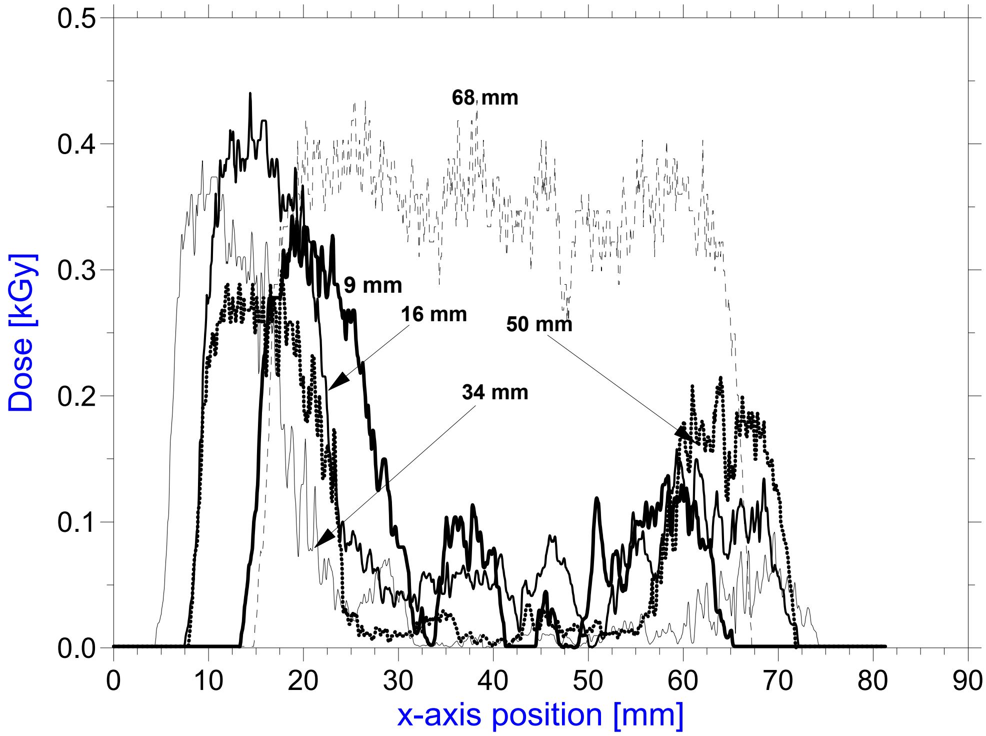

Figure F-6. Methyl yellow apple-phantom contour dose-depth distribution in kGy using a custom-made polystyrene holder and a 5 MeV LINAC accelerator with a conveyor speed of 18.3 m/min (60 ft/min).

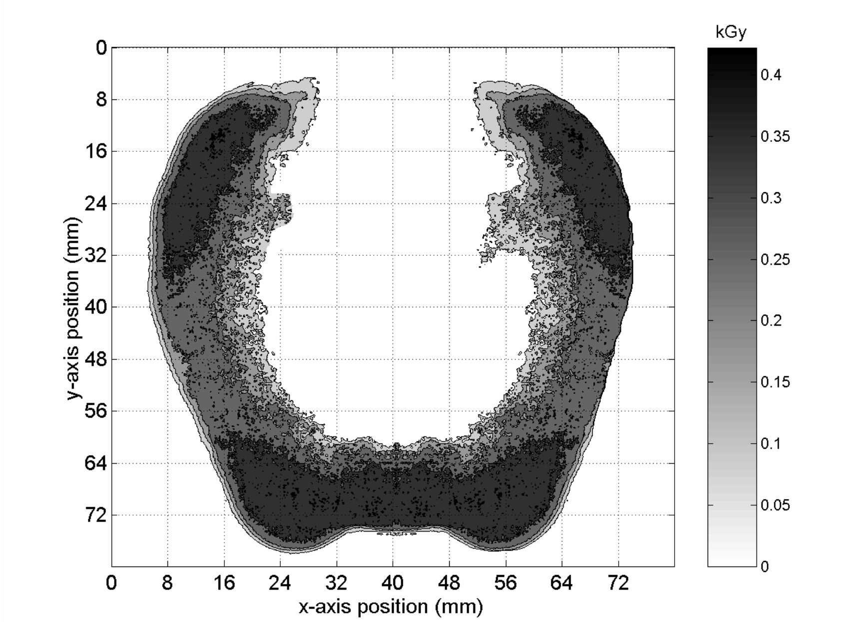

Figure F-7. Methyl yellow apple-phantom contour dose distribution in kGy using a custom-made polystyrene holder and a 5 MeV LINAC accelerator with a conveyor speed of 18.3 m/min (60 ft/min).

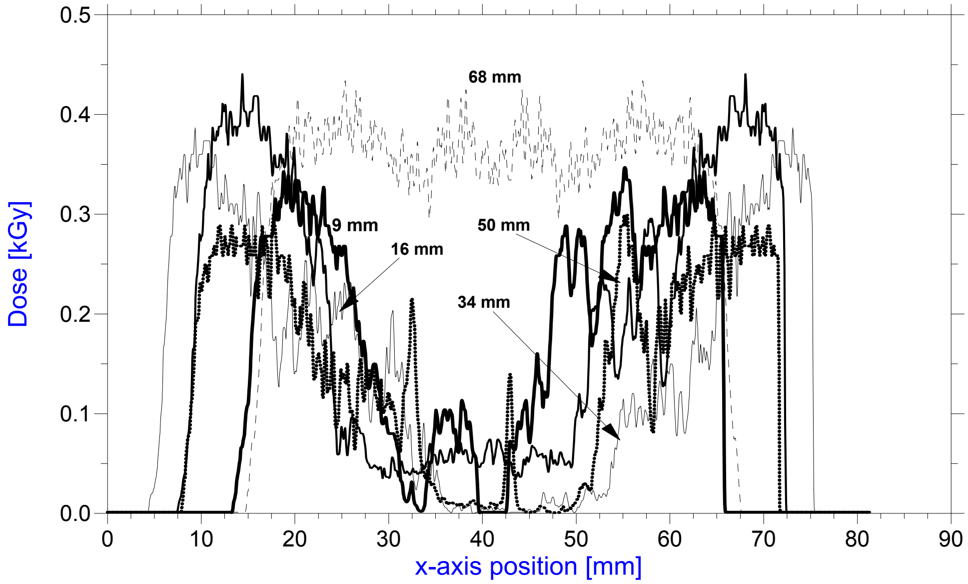

Figure F-8. Methyl yellow apple-phantom contour dose-depth distribution in kGy using a custom-made polystyrene holder and a 5 MeV LINAC accelerator with a conveyor speed of 18.3 m/min (60 ft/min).

VITA

Ramiro Giovanny Rivadeneira was born in Quito, Ecuador. He is the second child of Ramiro Rafael Rivadeneira, and Luz Elvira Pinos de Rivadeneira.

Prior to college, He received a Magna Cum Laude International Baccalaureate (IB) degree and graduated in the top of his class. At Texas A&M University, He completed a Bachelor of Science degree in biological and agricultural engineering in May 2001. In the summer of 1998 he worked as an entry-level engineer and performed crude-oil and wastewater environmental remediation work in Ecuador with Texaco Petroleum Inc. During the summer of 2000, He worked as an intern in the Texas Agricultural Experiment Station and collected data to develop a groundwater estimates computer model in the Texas Edward's Aquifer.

In May 2005, he completed his M.S. degree in biological and agricultural engineering under the direction of Dr. Rosana Moreira. He successfully constructed, coordinated and developed the first electron-beam food irradiation research pilot-plant in the Department of Biological and Agricultural Engineering at Texas A&M University to perform irradiation research of agricultural products. He researched and developed a three-dimensional chemical sensor apple-phantom to optimize the use of electron-beam irradiation in apples through phantoms.

Author's permanent address:
Av. Granados y Shuara N40-54
Quito, Ecuador